KfK 4378
September 1990

Interactions in Zircaloy/UO_2 Fuel Rod Bundles with Inconel Spacers at Temperatures above 1200° C

(Posttest Results of Severe Fuel Damage Experiments CORA-2 and CORA-3)

S. Hagen, P. Hofmann, G. Schanz, L. Sepold
Hauptabteilung Ingenieurtechnik
Institut für Material- und Festkörperforschung
Projekt Nukleare Sicherheitsforschung

Kernforschungszentrum Karlsruhe

Kernforschungszentrum Karlsruhe
Hauptabteilung Ingenieurtechnik
Institut für Material- und Festkörperforschung
Projekt Nukleare Sicherheitsforschung

KfK 4378

Interactions in Zircaloy/UO_2 Fuel Rod Bundles with Inconel Spacers at Temperatures above 1200°C (Posttest Results of Severe Fuel Damage Experiments CORA-2 and CORA-3)

S. Hagen, P. Hofmann, G. Schanz, L. Sepold

Kernforschungszentrum Karlsruhe GmbH, Karlsruhe

Kernforschungszentrum Karlsruhe GmbH
Postfach 3640, 7500 Karlsruhe 1

ISSN 0303-4003

Wechselwirkungen in Zircaloy/UO_2-Brennstabbündeln mit Inconel-Abstandshaltern bei Temperaturen oberhalb 1200°C (Nachuntersuchungsergebnisse der Experimente CORA-2 und CORA-3)

Kurzfassung

Die CORA-Experimente, die in einer Out-of-pile Versuchsanlage des Kernforschungszentrums Karlsruhe (KfK) durchgeführt werden, sind Teil des sog. Severe-Fuel-Damage-Programms (SFD) zur Untersuchung schwerer Kernschäden in Leichtwasserreaktoren (LWR).

Mit Hilfe der CORA-Versuche sollen die Versagensmechanismen von LWR-Brennelementen im Temperaturbereich bis 2000°C und in einigen Fällen bis 2400°C ermittelt werden.

In diesen Versuchen werden Brennstabbündel, die aus 16 elektrisch beheizten Brennstabsimulatoren und neun unbeheizten Stäben bestehen, Temperatur-transienten mit langsamer Aufheizrate und in Dampfatmosphäre ausgesetzt. Damit wird ein Unfallablauf für einen LWR simuliert, der sich aus einem Kühlmittelverluststörfall durch Auftreten eines sogenannten kleinen Lecks entwickeln kann.

CORA-2 und CORA-3 waren die ersten Versuche des SFD-Programms, die mit UO_2-Pellets durchgeführt wurden, und zwar am 6. August 1987 und am 3. Dezember 1987. Beide Versuchsbündel enthielten kein Absorbermaterial, so daß die Versuche als Referenzexperimente für die zukünftigen CORA-Tests dienen können, bei denen der Einfluß vorhandener Absorberstäbe zu betrachten ist.

Ein Ziel von CORA-2 als erstem UO_2-Experiment war es, Erfahrungen bei der Versuchsdurchführung und bei der Abwicklung der Nachuntersuchung zu gewinnen. CORA-3 wurde als Hochtemperaturexperiment durchgeführt. Mit ihm konnten u.a. die Grenzen der elektrischen Leistungseinheit ermittelt werden.

Die anfänglichen Aufheizraten für beide Versuche betrugen wie geplant 1 K/s, bis die Temperatureskalation aufgrund der exothermen Zircaloy(Zry)-Wasserdampf-reaktion ab ca. 1000°C einsetzte. Die Höchsttemperaturen in den Versuchen CORA-2 und CORA-3 betrugen 2000°C bzw. 2400°C.

Nach den Versuchen zeigten die beiden Versuchsbündel starke Oxidation und teilweises Schmelzen des Hüllmaterials, chemische Auflösung von Brennstoff durch die Wechselwirkung Zry/UO_2, vollständige Zerstörung des Inconel Abstandshalters sowie Umverlagerung von Schmelzmassen und Bruchstücken in den unteren Teil des Bündels unter Bildung ausgedehnter Blockaden.

In beiden Versuchen begann die Stabzerstörung mit dem Auftreten erster Schmelzen aus der Wechselwirkung Inconel/Zircaloy. Der untere Zry-Abstandshalter fungierte als Auffänger für heruntergefallenes Material. Im Versuch CORA-2 ist während der Abkühlphase das UO_2 teilweise in feines Pulver zerfallen. In CORA-3 hingegen wurde keine Pulverisierung festgestellt.

Abstract

The CORA experiments carried out in an out-of-pile facility at the Kernforschungszentrum Karlsruhe (KfK), Federal Republic of Germany, are part of the "Severe Fuel Damage" (SFD) program.

The experimental program is to provide information on the failure mechanisms of Light Water Reactor (LWR) fuel elements in a temperature range from 1200°C to 2000°C and in a few cases up to 2400°C.

In the CORA experiments test bundles of usually 16 electrically heated fuel rod simulators and nine unheated rods are subjected to temperature transients of a slow heatup rate in a steam environment. Thus, an accident sequence is simulated, which may develop from a small-break loss-of-coolant accident of an LWR.

CORA-2 and CORA-3 were the first "Severe Fuel Damage" experiments of the program with UO_2 pellet material. The transient tests were performed on August 6, 1987, and on December 3, 1987, respectively. Both test bundles did not contain absorber rods. Therefore, CORA-2 and CORA-3 can serve as reference experiments for the future tests, in which the influence of absorber rods will be considered. An aim of CORA-2, as a first test of its kind, was also to gain experience in the test conduct and posttest handling of UO_2 specimens. CORA-3 was performed as a high-temperature test. With this test the limits of the electric power supply unit could be defined.

The transient phases of CORA-2 and CORA-3 were initiated with a temperature ramp rate of 1 K/s. The temperature escalation due to the exothermal zircaloy(Zry)-steam reaction started at about 1000°C, leading the bundles to maximum temperatures of 2000°C and 2400°C for tests CORA-2 and CORA-3, respectively.

The test bundles resulted in severe oxidation and partial melting of the cladding, fuel dissolution by Zry/UO_2 interaction, complete Inconel spacer destruction, and relocation of melts and fragments to lower elevations in the bundle, where extended blockages have formed.

In both tests the fuel rod destruction set in together with the formation of initial melts from the Inconel/Zry interaction. The lower Zry spacer acted as a catcher for

relocated material. In test CORA-2 the UO_2 pellets partially disintegrated into fine particles. This powdering occurred during cooldown. There was no physical disintegration of fuel in test CORA-3.

Contents:

1. Introduction

Safety studies have demonstrated that so-called small break loss-of-coolant accidents in Light-Water Reactors (LWR), in combination with failure of the required safety systems, can lead to overheating of the core and thus result in severe fuel damage (SFD) and fission product release.

In such an accident the nuclear fuel rods may be subjected to temperatures beyond the present design basis accident limit of 1200°C. The temperature transient, however, will not necessarily escalate to an uncontrolled core meltdown accident, as was learned from the TMI accident in 1979.

The transient of a SFD-type accident is initiated by a slow temperature rise in the order of 0.5-1.0 K/s, followed by a rapid temperature escalation (several tens of degrees Kelvin per second) due to the exothermal heat produced by the Zry cladding oxidation in steam environment. Besides oxidation and embrittlement of the fuel rod cladding, local melting of the cladding and an interaction between molten zircaloy and uranium oxide pellets will occur, leading to destruction of fuel rod elements and other core structure far below the melting point of the fuel. The concern with melting of fuel rod materials in a SFD accident is relocation, solidification, and therefore the formation of coolant channel blockages.

To investigate the relevant damage mechanisms acting with increasing temperature on an uncovered core, and to develop models for estimating core damage initiation and propagation, research programs have been defined in various countries. In these programs in-pile and out-of-pile experiments are being performed under severe fuel damage conditions, i.e. temperature escalation to about 2000°C with termination of the transient before complete core meltdown.

At the Kernforschungszentrum Karlsruhe (KfK) a series of out-of-pile experiments on SFD research is being performed in the CORA facility /1/. 15 tests have been planned with usually 25-rod bundles in different configurations and under various system atmospheres /2/. Besides the main test series with UO_2 pellets (see test matrix in Table 1) two experiments with Al_2O_3 as fuel simulator were performed as scoping tests /3/. Tests CORA-2 and CORA-3 were the first experiments with UO_2 as pellet material and were performed without absorber materials, i.e. as reference tests. All other CORA experiments are performed with

absorber materials. Two different absorber materials are used within different bundle configurations, i.e. (Ag,In,Cd) rods are to PWR (Pressurized Water Reactor) conditions whereas boron carbide refers to the experiments simulating BWR (Boiling Water Reactor) fuel elements. Pellets, claddings, and grid spacers are typical for those of commercial PWRs with respect to their chemical compositions and dimensions.

This report describes the results of the first SFD experiments using UO_2 as pellet material. The designations of these experiments are CORA-2 and CORA-3. CORA-2 and CORA-3 were performed on 6 August 1987 and on 3 December 1987, respectively.

Both experiments are considered reference tests to be compared to results from test CORA-5, which contains PWR absorber material, and test CORA-12, which contains also PWR absorber material, and which was additionally terminated by quenching instead of a slow cooldown, thus simulating a rising water level during a reflood phase.

2. Test Description

2.1 Description of the Test Facility

A detailed description of the CORA facility is given in reference /2/. In the axial cross section of Figure 1 the main components of the CORA facility are shown schematically. The test bundle is surrounded by a high-temperature shield which is insulated by ZrO_2 and Al_2O_3/SiO_2 fiber ceramics (Fig. 2). The fiber ceramics are proven to be excellent insulators with a low heat capacity due to the low density of the material.

The high-temperature shield is located within the pressure tube. Through a number of holes in the shield, the test bundle is being inspected during the test by several video and still cameras. The holes are also used for temperature measurements by two-color pyrometers complementing the thermocouple readings at elevated temperatures.

Steam generator and steam superheater are placed inside the CORA containment. Using the total electric power of the steam generator, a maximum steam temperature of more than 800°C can be reached. The maximum steam flow rate amounts to 33 g/s.

Two different condensers are installed in the CORA facility: A vent condenser and a surge condenser. Under normal operating conditions the steam which is not consumed by oxidation of the bundle, is condensed in two vent condenser units. The surge condenser is physically separated from the high pressure system by four rupture disks. In case of emergency, e.g. due to an extremely high evaporation rate caused by quenching of the bundle, the void volume of the surge condenser serves as a pressure suppression system.

The condensate from the vent condensers and -in the case of emergency- the excess spray water of the surge condenser are collected in the condensate tank. After each test the amount of water in the condensate tank is determined to perform a water mass balance.

To avoid any hazard of hydrogen formed during the zircaloy oxidation, the non-condensable gases are expanded and diluted in a mixing chamber (see Fig. 3). In particular the hydrogen is diluted to a concentration below explosion limits by adding compressed air to the gas.

The test facility has a quench capability which is activated by raising a water-filled quench cylinder into the test section at a controlled speed. After the test the high-temperature shield can be lowered into the quench unit without moving the bundle. So, the tested bundle can be inspected and photographed posttest in its original condition that existed at the termination of the transient.

2.2 Test Train Design

The test bundles CORA-2 and CORA-3 consisted of 25 fuel rod simulators arranged as shown in Fig. 4. 16 of the 25 fuel rods were electrically heated by using tungsten pins as heater elements (Fig. 4a). The heated rods (fuel rod simulators) were filled with annular UO_2 pellets whereas the unheated rods contained full UO_2 pellets of the same outer diameter.

The designation of the heated and unheated rods can be taken from Fig. 4b for CORA-2 and Fig. 4c for CORA-3. The design of both types of rods used in the CORA test bundle is given with Fig. 5.
The rods are surrounded by a shroud made of Zircaloy-4. The dimensions of the shroud can be taken from Table 2 and from the cross section in Fig. 6. In this figure the grid spacer is shown as well. The shroud itself is insulated with a 20 mm-thick layer of ZrO_2 fiber material to guarantee a uniform radial temperature distribution.

Three grid spacers of approximately 40 mm length were mounted below the heated region, in its center, and in the upper zone. The lower and upper grid spacers were made of Zircaloy-4 whereas the central spacer was of Inconel 718. Details on the location of the spacers and the fuel rod simulator design characteristics are given in Table 2.

The test train instrumentation comprised thermocouples and two-color pyrometers for the various temperature measurements. In both experiments the test section was instrumented with thermocouples (W/Re and NiCr/Ni type thermoelements) and two-color pyrometers to measure steam temperature, rod cladding temperature, shroud temperature, and insulation temperature. In both tests, CORA-2 and CORA-3, there were 34 thermocouples installed in the test section and 32 thermocouples at different elevations of the high-temperature insulation.

More details on the test train instrumentation are given in references /4/ and /5/. In addition, ten videoscopes were used in both tests to observe the materials behavior and the relocation of material during transient testing. A schematic of the videoscope system with video camera and 35-mm still camera is given with Fig. 7.

The operational data, e.g. voltage, current, electric power, pressure, and temperatures were recorded by a data acquisition system as were the temperatures of the test section.

The hydrogen produced during the test by the steam/Zr reaction is usually measured at two different positions, i.e. above the test section and in the mixing chamber (see Fig. 3).

A schematic of the probes, gas lines, and gas analysis system is provided with Fig. 8. To dilute the gas taken at the location above the test section a dilution chamber with flow meters is installed. The off-gas mixture which contains hydrogen among other gases is being transported to the spectrometer via capillary tubes. It is analyzed by two quadrupole mass spectrometers of the type Leybold PQ 100. The ion currents representing the concentrations of the respective gases are determined. From these data the mass production rate of hydrogen as well as of the other gases is calculated with the ratio of the partial pressure of the particular gas and that one of argon (carrier gas) and multiplied by the argon flow rate through the test bundle.

2.3 Test Conduct and Results

With tests CORA-2 and CORA-3 a basis for the conduct of the experiments was established. The subsequent tests were performed in the same way.

After a pre-heating period of 3000 s the transients of CORA-2 and CORA-3 were initiated. The target temperature of test CORA-2 was 1850-2000°C whereas CORA-3 was planned as a high-temperature test with a maximum of 2400°C. The initial heatup rate, i.e. the temperature rise up to the onset of the exothermal reaction, was about 1 K/s for both experiments.

The bundle heating power and coolant conditions as established during the transient tests CORA-2 and CORA-3 are given in Table 3. The power input history for both tests is provided with Fig. 9. The coolant data as argon flow, steam flow (provided as mass flow of the injected water into the evaporator), and inlet temperature of the argon/steam mixture is depicted in Figs. 10 and 11 for tests CORA-2 and CORA-3, respectively.

In CORA-2 the temperature escalation started at 4050 s when the rod temperature had reached about 1200°C (Fig. 12, temperature response of CORA-2 at 550 and 750 mm elevation. A complete set of temperature traces of test CORA-2 is given in reference /4/).

In test CORA-3 the bundle was held at temperatures above 2000°C for more than 10 minutes (Fig. 13). The limit of the electric power input was reached with 55 to 60 kW. This limit was indicated by breaks of all the individual power connectors due to overheating at the end of the transient. Overheating might have occurred since there was no essential heat exchange with the environment of the bundle due to the very effective thermal insulation of the shroud. Another reason for the break of the heated rods could be mechanical failure of the power connectors (electrodes of copper and molybdenum). In this case a blockage of solidified material could have created a fixed connection between rods and shroud and so could have led to axial stresses on the connectors. The temperatures measured during test CORA-3 are provided with reference /5/.

The amount of hydrogen produced during tests CORA-2 and CORA-3 cannot be given quantitatively but in relative units versus time (Figs. 14 and 15 from reference /8/). The H_2 data are derived from the ion current obtained from the gas probes at two different locations, i.e. at the outlet of the test section and in the mixing chamber.

From the temperature readings and the videoscope observation during the transient of CORA-2 it was learned that

- the axial temperature had its maximum at the bottom of the bundle after the onset of the transient (before the electrical heating was turned on), then the temperature had its maximum in the center region (between 550 mm and 700 mm) beyond 800°C.
- the first melt formation started at 4160 s when the temperature was approx. 1350°C. The first melt droplets originated from the Inconel grid spacer (448-488 mm) and were observed from 400 mm downward. The melt formation is caused by the eutectic alloy formation between the Fe, Cr and Ni of the spacer with the Zr of the fuel rod cladding.
- the meltdown of the Inconel spacer takes less than one minute (see Fig. 16).
- an enhanced melting in the midsection occurred at 4260 s shifting the axial hot spot to the bottom of the bundle
- some melt droplets solidified as soon as they passed a cold region, others burned for quite some time after deposition which might be an indication for continued oxidation of essentially metallic material
- the velocity of falling droplets amounted to approx. 3 m/s.

Results from temperature recordings and videotapes taken during test CORA-3 indicate that

- the axial hot spot was at 700 to 800 mm from 500°C upward.
- the melt formation started at the elevation of the Inconel grid spacer
- the melt relocation till 4700 s went in the same way as during the CORA-2 transient
- the first melt generated in the upper part of the bundle was observed after 4670 s at 700 mm elevation.
- there was an enhanced melt movement (rivulets) between 4700 s and 4900 s
- the last melt was visible at 4910 s.

3. Posttest Appearance of the Bundles

Test CORA-3 resulted in remarkably more severe damage than test CORA-2. This could be seen in the appearance of the shroud and the shroud insulation but also of the bundle itself.

3.1 Appearance after Test CORA-2

Fig. 17 gives an overview of bundle CORA-2 at four different orientations after removal of the shroud insulation. Figs. 18 through 20 provide more detailed photographs of the lower and central region of bundle CORA-2.

From the bottom to about 170 mm the shroud is of grey color indicating some oxidation. Above 170 mm the shroud is clearly deformed and extremely brittle. At several locations material of the test bundle was found "baked" to the shroud surface. Shroud material is missing between 280 mm and 420 mm allowing a look into the interior of the bundle. There are remnants of the shroud between 420 mm and 480 mm. From 490 mm to 600 mm the shroud is open so that the bundle can be viewed. Above 600 mm the shroud is intact but strongly deformed, particularly in the region between 600 mm and 960 mm. The color is light grey to dark grey. From 1070 mm to 1260 mm (above the heated zone, without shroud insulation) the shroud appears almost unoxidized.

The view of the bundle itself reveals solidified rivulets of melt ("candling") between 250 mm and 450 mm. These re-solidified droplets originate mainly from the central grid spacer made of Inconel. The droplets exhibit metallic (shiny) and ceramic melt.
Loose rubble of cladding and fuel fragments (Fig. 21) as well as fine particles of UO_2 (powder) were found at several locations within the bundle. The UO_2 powder (particle size analysis see section 4.2) must have formed during the cooldown phase of the test since it was located on top of the relocated materials.

Cross sections of the tested bundle CORA-2 (Figs. A-4 through A-18, Appendix) show that

- only a small amount of material has relocated below the heated region
- some material has deposited on the lower grid spacer. A small fraction of this material is solidified melt, the major portion is rubble

- the only cross section partly blocked by refrozen melt exists between 250 mm and 300 mm
- the Inconel grid spacer in the center of the bundle is completely gone; remnants of the molten spacer are deposited in the "blockage" area
- there are pieces of cladding and pellet relocated to the zone where the Inconel spacer was positioned
- "flowering" of the cladding can be observed (i.e. opening up as a consequence of a hoop stress in the cladding) at most of the rods from 380 mm to the upper end of the heated region.

Fig. 22 is an illustration of the posttest appearance of bundle CORA-2. A longitudinal section of CORA-2 from 136 mm to 253 mm elevation is depicted in Fig. 23. Different types of resolidified melts which have relocated at different times can be seen on this picture. Another vertical section (300 - 345 mm) in Fig. 24 demonstrates fuel rod failure and fragmentation.
The evaluation of the UO_2 distribution after test CORA-2 (from reference /9/) is given with Fig. 25. The pellet material dissolved in the upper portions of the bundle has relocated downward as can be seen in this figure.

3.2 Appearance after Test CORA-3

Fig. 26 is the overview picture of the bundle CORA-3 after the removal of the shroud. Details of the bundle appearance from the bottom to the top are provided with Figs. 27 through 30 taken at the 210° orientation.
The shroud and its insulation were broken down to about 250 mm elevation. The bundle is significantly bent into different directions. A massive block of previously molten material has formed from the bottom of the heated zone to about 150 mm elevation. In the region above 150 mm there is not much cladding material left besides a few heavily oxidized remnants at various locations, particularly at the observation windows (cold spots), e.g. at 30°, 500 mm. The extremely high temperature during the CORA-3 test must have caused melting of the fairly unoxidized cladding. Strongly oxidized (grey color) but unmelted cladding is present above the 1000 mm elevation. The UO_2 pellets in this region, however, have survived the exposure to temperature so that most pellet columns are intact though attacked by liquid Zry. The pellet stacks between 150 mm and 310 mm are baked together exhibiting an extension of the blocked area in the upward direction. Some melt left the interior of the bundle and solidified at cold spots outside as can be seen at 30° and 500 mm elevation.

No powderization of the UO_2 fuel pellets took place during cooldown of the CORA-3 bundle, similar to that observed during the test CORA-2.

The horizontal and vertical cross sections of test bundle CORA-3 are given in the Appendix, Figs. A-21 through A-31. An illustration of the posttest appearance of CORA-3 is depicted in Fig. 31.
The evaluation of the cross-sectional area of both test bundles (from reference /9/) is given in Fig. 32. The evaluation of the UO_2 distribution after test CORA-3 (Fig. 33) is based on the same reference. One can clearly see that the relocation of materials from the upper locations downward includes theUO_2 as well.

4. Investigation of Fragments Taken from the Test Bundles

4.1 Materials Taken from Bundle CORA-2

Specimen 101 is a piece of a melt rivulet of dark grey to black colour and blunt surface, which was broken at 300 mm elevation from another solidified melt. It consists of a metallic core of oval cross section in partially remaining contact with a fragment of thick oxide scale. The scale, showing columnar grains typical for ZrO_2, proved to be (Zr, U)O_2. The prior melt is multiphase metallic with a ceramic component (Fig 34). It was analyzed to be composed of the metallic phase (Zr, Cr, Fe, Ni) with U, of depleted Ni content in comparison to the Ni/Cr/Fe relation of Inconel, further the metallic phases (Zr, U, Ni, Fe) and (Zr, Ni, U) with Fe and the ceramic phase (Zr, U)O_2. The melt is thus indicating the interaction of Zry and Inconel with subsequent fuel attack and U pick-up by UO_2 dissolution.

Specimen 102 is a melt drop, wetting remnants of cladding, and was collected from 390 mm elevation. The cladding is found to be completely converted to oxide, whereas the melt shows regions with globular metallic inclusions in a two-phase ceramic matrix. The cladding was analyzed to have picked-up UO_2 to form (Zr, U)O_2. The analyzed region of prior melt consists of a matrix of (Zr, U, Cr) oxide phase primary crystals together with a small amount of a (Cr, Al) oxide phase with some Ti content. The metallic inclusions have the main components (Ni, Fe, Sn) and contain further some Mo and W. Thus the multicomponent interaction must have been followed by essentially complete oxidation.

Specimen 103 is a cladding tube fragment with a droplet of melt attached to it, which was found relocated to the 360 mm level. The optical microstructure resembles the one of specimen 102. Especially inclusion-rich zones of the melt are identified as a matrix of ZrO_2 containing particles of metallic (Sn, Ni) or (Sn, Ni, Fe) together with others of (Fe, Cr, Zr, Si) oxide and (Cr, Fe) oxide. Accordingly the melt was formed by Zircaloy-Inconel interaction.

Specimen 104, collected from 240 mm elevation, is, according to the optical microscopy, a piece of shroud, almost completely converted to oxide by double-sided oxidation. Except, some central zones of the wall and of an agglomeration of melt at such a mid-wall position contain metallic residues of an originally homogeneous melt. Within the wall a (Zr, U)O_2 phase with minor Cr content is the matrix of zones of residual metallic melt, decomposed into a (Sn, Ni, Fe) phase

with minor Mo content, and a (Ni, Fe, Sn) phase with some Mo. At the melt agglomeration the elemental analysis shows that a similar matrix of (Zr, U)O_2 contains zones with the three metallic phases (Sn, Ni) with some Fe and Cr, (Cr, Fe, Ni, Mo) with some Si and Sn, and (Fe, Ni, Cr) phase with some Sn, Mo and Si. Again a complex scheme of interaction between Zircaloy, UO_2 and Inconel has to be assumed for explanation.

Specimen 105 is a solid fuel pellet with cladding and melt residues attached to it, collected from 360 mm elevation. The pellet is intact, the cladding completely transformed to oxide and the melt shows a zone of pores and metallic inclusions (Fig. 35). The melt is (Zr, U)O_2 containing zones with (Sn, Ni) particles; the obviously reacted cladding is (Zr, U)O_2 as well. In another region, where the matrix contains some Cr and Fe, an oxide phase of (Cr, Fe, Al) type is also observed as precipitate.

Specimen 106, fragments of annular pellets from a corner rod together with cladding and melt relicts, were removed at 460 mm elevation. The pellets themselves show at the interior side, that especially intense interaction has taken place in contact with some originally present melt. The piece of cladding and the melt relicts in contact with it are converted to oxide, whereas locally metallic inclusions are agglomerated or droplets of metallic melt have remained. The melt at the interior pellet side was identified as (Zr, U)O_2 with a relation of ca. 80/20 (and some interdendritic W-rich particles), and the solid state reaction zone as (Zr, U)O_2 with the composition of ca. 60/40. The cladding was confirmed as ZrO_2, the metallic particles or droplets embedded or attached to it as (Ni, Fe) with Mo, Sn, Cr or (Ni, Fe, Mo), partly containing (Ni, Fe,Zr) precipitates with some Cr, Mo and Sn content, and thin surface zones of Cr oxide with some Al and Ti content. Again metallic material from the Inconel spacer grid is thus found after complex interaction with the Zircaloy cladding.

Specimen 107 is a fragment, combined of a piece of pellet, attached to originally molten material of mainly ceramic character, which was removed from the window at 200 mm elevation. Another fragment from the same position (107*) is obviously a piece of heated fuel rod (Fig. 36). The first fragment was identified to consist mainly of (U, Zr)O_2, and thus to originate from a pellet after interaction with cladding material. Dispersed phases identified at one position are (Zr, U)O_2, (U, Zr) and (Zr), at another one ZrO_2, (Zr, Sn) and a Cr containing (W, Zr) phase of metallic light optical appearance. Fragment 107* was identified to have been

modified by serious pellet cladding interaction and oxidation, so that $(Zr,U)O_2$ is the mainly present phase. At another analyzed position the pellet is in contact with originally molten material, which consists of the phases $(U, Zr)O_2$, (Zr, Sn) and (Zr, Ni, U, Fe) with some Cr.

Specimen 108, a cladding tube fragment from 900 mm elevation was found completely converted to oxide and therefore not further analyzed.

Specimen 109, a black and partly lustrous lump of melt, which had solidified as low as 80 mm in the bundle, shows in the light optical investigation a dendritic primary and interdendritic secondary phases. The essentially metallic fragment is covered by a thick oxide scale. The overall composition of the melt lump is Zr/U/Ni/Fe/Cr = 80/15/3/1/1. Its dendritic matrix is identified as (Zr, U, O), the interdendritic phases as ZrO_2, (U, Zr), (Zr, Sn) and (Zr, U, Ni, Fe) with Cr content. The oxide scale of $(Zr, U)O_2$ shows individual sub-layers of different composition.

In Tab. 4 the results of the fragments analysis, as described above are arranged in the following sequence: First, metallic melts are listed, which have decomposed into multi-phase matrices of mostly multi-component phases, which are the products of interactions between Zircaloy, Inconel and UO_2. Then, originally molten materials are described, which consist of matrices of the (Zr, U, O) or $(Zr, U)O_2$ type, and which contain minor phases resulting from an interaction with Inconel, the tungsten rods or their molybdenum electrodes.

4.2 UO_2 Powder of Bundle CORA-2

UO_2 powder was first observed during the visual inspection of the bundle after test CORA-2. The powder was randomly distributed throughout the bundle. Samples were taken from the videoscope port holes to be analyzed for chemical composition and particle size. The powder collected from two port holes H25 and H27 (at 200 mm and 300 mm elevation) consisted of UO_2 mainly as was determined by mass spectrometer analyses. The other components were as follows:

Position

H25 4.50 wt.% Zr, 0.06 % Fe, 0.11 % Sn, less than 0.05 % Mn, Cr, Ni.

H27 11.80 wt.% Zr, 0.06 % Fe, 0.14 % Sn, less than 0.05 % Mn, Cr, Ni.

(The contents of Zr stems from the ZrO_2 fiber insulation material).

Powder from the same port holes and from H37 (at 690 mm), in addition, was taken for the determination of the particle size. The particle size distribution was determined using a "Laser Granulometer type 715" which was especially designed for analyses of powder, i.e. for particle sizes < 192 µm. The suspension of particles in water is transmitted by a laser beam. The particle size distribution results from the analysis of the energy distribution of the diffraction pattern, i.e. the amount of diffracted light from a particle is proportional to the diameter of the projected area. The diameter is determined under the assumption of particles with a speric shape.

In Figs. 37 through 39 results from the particle size analyses for the three samples are presented. Plotted is the density distribution as a histogram and its integration (summation curve) for each sample. The mean diameters (50 % values) are as follows:

71.7 µm (H25)
58.7 µm (H27)
67.6 µm (H37).

These values are clearly above the original grain size of UO_2.

However, the shape of the three curves leads to an assumption that there might be two individual distributions mixed together. This could be the case if the "smaller" UO_2 distribution was polluted by a ZrO_2 contribution from the insulation material. Under this assumption the particle sizes would be

40 µm for UO_2
100 µm for ZrO_2.

This results would agree better with the findings from the microstructural analysis of the UO_2 pellets with respect to the grain size:

(a) Full UO_2 pellets
- after test CORA-2 up to 30 µm
- as-fabricated 8 to 20 µm

(b) Annular UO_2 pellets

- after test CORA-2 up to 32 µm
- as-fabricated 4 to 12 µm.

To the understanding of the cause of powdering:
UO_2 powdering, i.e. extensive grain boundary separation, has been observed where nuclear fuel rods were under film boiling conditions. Under these conditions the powdering could be explained by the combination of a severe loss of grain boundary strength (intergranular fracture) at elevated temperatures experienced under film boiling conditions and the high tensile stresses induced by a subsequent quenching /6/. Since the CORA-2 bundle experienced a different exposure without quenching another explanation for the disintegration of the UO_2 pellets is needed. One explanation is based on the observation that UO_2 became hypostoichiometric due to oxygen diffusion from the fuel into the cladding, as deduced from the presence of precipitates of oxygen-stabilized α-Zr(O) and metallic U within the fuel. Oxidative conditions for those precipitates during the further course of the test would result in their volume increase, internal stressing of the surrounding UO_2 matrix and eventually fuel fracturing /7/.

4.3 Materials Taken from Bundle CORA-3

Specimen 101 consists of solid pellets glued together to a rod fragment, which was removed from ca. 375 mm bundle elevation. The light optical investigation of a horizontal cross section through this rod seems to confirm, that (U, Zr) phase, which is tentatively identified by its characteristic staining behaviour during air exposure of the polished specimen, has penetrated deeply into the pellet. An externally sticking melt, however, indicates by its complex microstructure, that the reaction of the pellet might have been more complicated than a simple interaction with the cladding. Within this melt several types of angular or acicular crystals have grown or were formed during its solidification. The central channel through the pellet, equipped with a W/WRe thermocouple with duplex sheath of Ta + Zr and HfO_2 insulation, is found to be filled by a melt which has also decomposed into a complicated microstructure of several phases.

The energy-dispersive X-ray spectrometry by scanning electron microscopy (SEM-EDX) has been used to analyze the reacted pellet, the externally sticking melt and the melt in the TC bore: The melt, having penetrated into the pellet

(misinterpreted above as (U, Zr)) had been an alloy of Zr with Cu and Mo of the heater electrodes. It has picked up U from the pellet and has decomposed into a (Zr, Cu, Mo) phase, (Cu, Zr) phases with more or less oxygen content, and a (U, Mo, W, O) phase as minor constituent. The externally sticking melt of integral composition Zr/Cu/Mo/U = 46/40/8/6 has decomposed by growth of rectangular crystals of (U, Zr)O_2, smaller angular ones of (Zr, O), a (Cu, Zr, O) phase (stained by air exposure of the polished cross section), plates or needles of (Mo, Zr, W) phase, all within the remaining (Zr, Cu, U) matrix (Fig. 40). So each of the main components has been enriched in its special phase. The melt in the TC bore shows Ta-containing or even Ta rich phases in the vicinity and on the TC sheath, which shall only be mentioned here. Otherwise, this melt is similar in composition and phases as the external melt described above: Rectangular crystals are identified as UO_2, primary dendrites as (U, Mo, O) phase with some Zr, laces around UO_2 phase as (Zr, Mo, Cu), a minor constituent as (Zr, Sn, Cu) and the matrix as (Zr, Cu, Mo) with U.

The above described pellet column is not typical for the bundle elevation, where it was removed from. It might have fallen from the upper end of the bundle, where it could have reacted with melt, formed by reaction of Zircaloy cladding with Mo and Cu of the heater rods. Otherwise, such a melt could also have relocated down through the bundle.

Specimen 102 consists of fragments of annular pellets, removed at 300-350 mm elevation. They show that melting had occurred especially at the inner surface and dispersions of metallic phase are to be observed at several positions of the priorly molten ceramic material. The phase analysis shows, the melt to be (U, Zr)O_2 and the precipitates to be W, picked up from the heater.

Specimen 103 is a cladding fragment removed from 800 mm elevation. It exhibits a cross section of ZrO_2 with pellet remnants and some metallic inclusions on the internal side, which proved to be (Sn, Ni) phase in a (Zr, U)O_2 matrix. Specimen 104 consists of other cladding fragments from this elevation. They are found completely converted to oxide as well. The pellet-cladding reaction zone, (Zr, U)O_2 to (U, Zr)O_2, contains metallic particles of (Sn, Ni, Cu) phase.

Specimen 105 consists of melt drops solidified in contact with a heated rod at 500 mm elevation. They are of ceramic character, containing zones with metallic residues. The matrix of the specimen is ZrO_2 at cladding regions and (Zr,U)O_2 at

regions of prior melt, which contain certain colonies of the following precipitated phases: (Sn, Ni) phase with Fe, Cu-particles with Sn content, (Zr, U, O) or ZrO_2 phase with Cu content. However, the melt is essentially the product of pure pellet-cladding interaction and subsequent oxidation.

The specimens 106 and 107 are pieces of the shroud from 150 mm elevation. Specimen 107 was analyzed at the position, where the shroud was completely converted to oxide, to be ZrO_2. At the boundary to the duplex metallic-ceramic main region of this fragment (Zr, O) and (W, Zr, O) phase are identified as precipitated particles and in fine eutectic distribution. The duplex phase region is ZrO_2 and (Zr, O), the latter with precipitates of (W, Zr) with some Cr and Fe content (Fig. 41). A band of metallic character through this specimen is analyzed to consist of the matrix phases (Zr, Cu) with U content, (Cu, Zr, O) and some (Mo, Zr, W, O) precipitates. Externally attached metallic melt is of similar composition, (Cu, Zr, O) and (Zr, Cu, U) as matrix phases with (U, Zr)O_2 and (Mo, Zr, W, O) precipitates. So this region of the shroud must have reacted with steam, with melt from Zircaloy-UO_2 interaction and finally must have been modified by melt containing the components of the heater rods and their electrodes.

Specimen 106 is primarily of duplex type of several interpenetrating metallic and ceramic phases. The observations can be summarized for three investigated positions as follows: The main ceramic constituents are a (Zr, Cu) oxide phase or ternary compositions with variable U content as (Zr, U, Cu), (U, Zr, Cu) and (U, Cu, Zr), all as oxides. Further, Sn- and Mo-containing oxide phases of the (Zr, Sn, Cu) oxide and (Zr, Mo, Cu) oxide compositions are present as minor constituents. Other phases with smaller oxygen content can be denoted as (Zr, Cu, O), (with U content as well) and as less abundant constituents the Sn- and W-containing phases (Zr, Sn, Cu, O) and (Zr, W, Cu, O) and the Cu-rich (Cu, Zr, O). No or unimportant oxygen content seem to have (Zr, Cu) and the minor phase (W, Zr, Cu). This part of the shroud has obviously been more severely influenced than specimen 107 by melt containing heater components.

Specimen 108 consists of two "pillows" of melt, having accumulated and re-solidified at the window on 100 mm elevation plus fragments collected from there. One of the melt lumps was analyzed to consist of the matrix phases (Zr, O) with U, Sn and (U, Zr)O_2, together with traces of (W, Zr) precipitates with some Cr. The other lump was more U-rich, consisting of (Zr, U, O), (Zr, U)O_2 and two compositions of (U, Zr)O_2, again with traces of (W, Zr) with Cr. Both lumps are

found to be free of scales except local spots, which should have participated in the melt relocation, so that no detectable subsequent oxidation of the material has taken place. This can be understood by fast cooldown but also by a late formation of this melt. One of the collected fragments is identified as (Zr, U)O_2 of locally variable composition and traces of precipitated (W) phase.

Specimen 109 is a fragment, removed from 130 mm elevation, consisting of once-molten material of essentially metallic nature on an almost completely ceramic substrate. The latter was analyzed as (U, Zr)O_2 with an integral composition of U/Zr/Cu = 64/22/14 and the following types of precipitated phases: (Zr, O) with U and Cu, (Zr, Cu) and the oxides or the oxygen-containing phases (Zr, Cu, O) and (Cu, Zr, O). The prior melt (Fig. 42), analyzed at two positions, consists of the following matrix phases: (Cu, Zr, O) with U, (Zr, Cu) or (Zr, Cu, O) with some U content, and (Mo, Zr) or (Mo, Zr, O) with U, Cu and Cr as third phase. So each of the main components of the melt has been concentrated in its own phase during decomposition. Less abundant constituents are analyzed as (W, Mo) primary dendrites, (U, Zr)O_2 flakes, distributed in form of clouds, (Mo, Zr, O) and (Mo, W, Zr) phase.

In Tab. 5 the results of the fragments analysis as described above are arranged in a sequence of increasing interaction with the heater rods or the pick up of the elements Cu, Mo and W. In comparison, the interaction with the Inconel spacer grid was less important for the arbitrary and non-representative choice of investigated specimens.

5. Analysis of Cross Sections and Longitudinal Sections

After the visual inspection, photographic documentation, and collecting of fragments the test bundles were encapsulated in epoxy resin and sectioned according to the lists in Tables A-1 and A-2 (Appendix). The locations of the sections are illustrated in Figs. A-2 and A-19 (also in Appendix).

For encapsulation of the bundle the epoxy system Rütapox 0273 with the hardener designated LC (Epoxy resin and hardener manufactured by Bakelite GmbH, D-5860 Iserlohn 7) was chosen. The bundle was filled from the bottom, through the steam inlet line, to avoid air entrainment in the encapsulant (see Fig. A-1, Appendix). Approximately 13 kg were required to fill the bundle of 130 by 130 mm to an elevation above the top of the shroud. The epoxy showed some

heating during the curing stage but the shrinkage effect was negligible. After epoxying the bundle the resin was allowed to harden for one week.

A saw with a 2.3 mm-thick diamond blade (mean diamond size 138 μm) of 500 mm OD was used to do the cutting of the slab at 3200 rpm. The thickness of a slice from the epoxied bundle resulted in 13 mm corresponding to the distance of the marks of 15 mm.

Before grinding and polishing of the samples the selected cross sections were infiltrated by "Araldit" resin to close up residual pores.

The procedure of the preparation for the metallographic examination is given with Table A-3. The steps described in the list were performed using a semi-automatic machine with a closed water circuit for grinding and an automatic lubricant feeder for the polishing steps. The cross sections were studied in the as-polished condition.

5.1 Sections of Bundle CORA-2

5.1.1 Optical Microscopy Observations

In the following description of the status of the bundle the microstructural analysis of the individual cross sections is summarized according to the essential features of different axial zones. In addition some special characteristics of only minor or local importance and results of more detailed investigations are given.

Bottom of the heated zone, droplets and fragments

At the lower end of the heated zone of the bundle, at elevations around the Zry spacer grid and the steam inlet line, the bundle configuration remained unchanged and the individual rods essentially undamaged. As shown by Fig. 43, the cross section at the elevation of -13 mm, melt droplets have accumulated within the spacer grid and are in local contact with it and with the fuel rod cladding tubes. In addition some loosely lying rubble particles, obviously fuel rod fragments are observed.

The micrographs of Figs. 44 and 45 (corresponding to the positions 1 and 2 of Fig. 43) indicate, that the melt is of the (Zr, U, O) type, which, during solidification

and cooling has separated into a continuous metallic matrix phase and a dispersed ceramic phase. By local interaction with the melt the ZrO_2 scale of previously oxidized Zry components was modified or completely dissolved and a boundary layer of α-Zr(O) phase was retained between the partners of the interaction.

The Zry structures, which were partly molten (Fig. 44, Pos. 3; Fig. 45, Pos. 2), indicate that local temperature peaks above 1760°C occurred. In contrast the ZrO_2 scale thickness of only about 10 µm (Fig. 44, Pos. 5; Fig. 45, Pos. 3) for non-influenced structures allows to deduce, that, away from hot spots, a temperature of about 1000°C could have been exceeded for only a few minutes.

Considerable oxidation of the relocated melt is demonstrated by the presence of comparatively much thicker oxide scales (Fig. 44, Pos. 2). Crack formation across the solidified material indicates its brittle character due to an elevated content of dissolved oxygen.

In the upper region of the lower spacer grid and above more fuel rod fragments in addition to melt droplets have accumulated. The cross sections through those fragments exhibit the sequence of phases, known to be typical for Zry-UO_2 interaction and external Zry oxidation. In the direction from the oxidized Zry to the fuel the following layers are observed: ZrO_2, ZrO_2 + α-Zr(O), α-Zr(O), α-Zr(O) + (U,Zr), UO_2 + (U, Zr), UO_2 (Fig. 45, Pos. 5).

Zone of compact blockage

At elevations between ca. 150 and 270 mm a considerable amount of once molten and relocated masses have formed an almost compact blockage (Fig. 23). In the cross sectional area at 268 mm, which was investigated in detail, a coherent lump fills the inner part of the bundle almost completely (Fig. 46). The distribution of the melt masses reflect the known fact, that they have been built up by a multitude of single relocation events. A closer look on different regions of the blockage, as provided by Fig. 47, reveals local variations in the brightness of the colour and a pattern of gross cracks. The different reflectivities can be taken as an indication of variations in the composition; the crack system is typical for brittle material, here presumed to be rich in oxygen content. In Fig. 48 two different melt regions are compared in their microstructure. Whereas the one is essentially of metallic character with ceramic precipitates, the other is a duplex

mixture of metallic and ceramic phases. Both melts are products of the reactions of Zircaloy-4 with steam and fuel and are of the (Zr,U,O) type.

Further observations on the bundle behaviour at the blockage elevation are illustrated for the positions 1 to 3, as given in Fig. 49, and in magnified detail in Figs. 50 to 52:

Freely steam-exposed Zircaloy is found completely converted to oxide (Fig. 50). In the shown example internal reaction with the fuel and relocation of the thus modified molten cladding has left empty volumes behind (through which steam might have invaded as well). Residual metallic material, analysed to be enriched in tin and the components of Inconel, has resisted to oxidize.

Where the cladding was getting surrounded by melt it was more protected from fast steam oxidation. But an interaction between the pre-existing oxide scale and the melt proceeded. In parallel, the internal reaction with the fuel went on. Fig. 51 and 52 show different stages of cladding destruction under both-sided attack. The variations in the extent should reflect local temperature differences and the history of the melt relocation. For an interaction of cladding and fuel in the solid state, the formation of the already mentioned layer sequence at the interface is typical (Fig. 51), whereas liquid phase interaction is combined with local melt relocation and void formation (Fig. 52). As both types of features were found, the peak temperature of this level of the bundle must have been around the melting temperature of Zircaloy. This is in agreement with the fact, that the (Zr, U, O) melt type, which has a similar or higher melting range, has re-solidified here.

The fragmentation of the fuel pellets and the formation of rubble beds of those fragments, which are also seen in this elevation (Figs. 51, 52) have been separately discussed.

Cladding oxidation and interaction with the fuel

In correspondence to the axial temperature profile during the test, the external oxidation of the cladding and its internal interaction with the fuel are expected to intensify with increasing elevation. It is observed that already above ca. 100 mm the steam oxidation and the fuel interaction of the cladding have become essential, and that the destruction of the fuel rods is initiated above ca. 140 mm.

Fig. 53 illustrates, at the zone of compact blockage, that the UO_2 pellet stack is attacked by (Zr, U, O) melt, which has filled the space between neighbouring pellets and the gap to the original cladding. The microstructures demonstrate, that some melt had already high contents of dissolved oxygen, and continued to oxidize on free surfaces.

The cross section at 298 mm elevation, which has also been analyzed in detail, makes obvious that the bundle still retained its original configuration, but that individual rods are seriously damaged by cladding oxidation, melt formation and fuel dissolution (Fig. 54). Whereas molten material has partly relocated to lower regions, rubble fragments have been collected from above. It is obvious, that the melting range of the metallic part of oxidizing Zircaloy, 1760°C (for oxygen-free Zircaloy) to 1975°C (for α-Zr(O)) was reached at this elevation.

As illustrated by Fig. 55 the fuel interaction could proceed therefore by intimate contact with already melted cladding material. The molten phase has deeply penetrated into the attacked fuel pellets and partly dissolved them at positions, where the reaction was strong and continuous. On the other hand, the pellet surfaces were only modified, where the partners of the reaction became separated by melt relocation, by which empty volumes were filled, and others were left behind. Accordingly a broad range of compositions is to be expected for the (Zr, U, O) melt. An original (Zr,O) melt might even have avoided any contact with fuel.

Relocation of molten material was found to proceed in the following steps (Fig. 56): Local pools of melt tend to form by adherence to solid structures and by filling closely neighboured gaps. Melt, which is still confined within the fuel rod, redistributes, presumably to form larger pools below, and leaves the observed void volumes behind. Another path for long range melt relocation is opened by failure of the ZrO_2 scale. In Fig. 56 positions are shown, where the oxide scale was thinned or breached under the chemical attack of metallic melt. Some melt has penetrated through the breach. At this position of the bundle, however, the breach was closed again during the ongoing oxidation, so that the originally metallic material was further confined and is finally found in form of a ceramic of (Zr, U)O_2 type. Oxide scale failure, possibly as the combined effects of chemical attack from the melt and mechanical forces, is required for the observed melt relocation by candling and free falling of droplets.

The destruction of the fuel rods is even more advanced at the elevations above the cross section, which was just described. The melt, which has formed the compact blockage had its main source here and only limited amounts of once molten material remain as residues near their original elevation. Other residues are pellet fragments glued together by adherent originally melted (Zr, U, O) reaction products. Cladding fragments have to be mentioned as the last type of residues, which are completely converted to oxide.

Pellet disintegration

At elevations above 380 mm the unheated rods are the first for which a decay is observed: The already de-clad pellet stacks seem to have fractured into pieces of a broad range of sizes which have partly fallen downward during the transient or during the cooldown of the test.

At the 298 mm elevation the pellets essentially remain at place, although they are already weakened by systems of gross cracks and a multitude of fine fissures which are concentrated within certain areas, as visualized in Fig. 57 (top, left) for the example of the annular pellet of a heated rod. The still uncracked areas of the fuel pellets show precipitates, which are rich in uranium but of metallic character. The occurrence of this (U, Zr) phase indicates the reducing effect of interaction with the molten cladding.

A very similar microstructure was found for the 268 mm level as already shown in Fig. 51. Here a solid pellet in contact with a (Zr, U, O) melt is being destroyed by grain boundary cracking into fine particles. The still compact part of the pellet shows the same (U, Zr) precipitates as mentioned above. At another zone in this elevation UO_2 particles are the main component of the rubble bed shown in Fig. 52.

Accordingly fragmentation of the fuel is observed both for the solid and the annular pellets at a stage, where the fuel had already interacted with (Zr, U, O) melt, had been submitted to the transient, and possibly also of importance, was exposed to the atmosphere.

Inconel spacer grid

The position of the grid spacer of Inconel 718 in the axial center of the bundle is covered by the cross section at 480 mm elevation (Figs. 58 to 60). The videoscope system had allowed to observe, that this structure melted away in the course of the test within a few seconds. It is known that Zr in metallic contact with Fe or Ni, respectively, is able to form melts already at temperatures above ca. 950°C by eutectic interaction. From temperature measurements and observations it was deduced in the present case, that a melt, formed by eutectic interaction, has seriously attacked the cladding tubes in the elevation of the spacer at about 1450°C. Melt formation can be understood to initiate in turn, at least for the localized contact regions, an early attack of the fuel. It cannot be demonstrated that the fraction of dissolved fuel was increased, but it cannot be ruled out as well, that premature melting and melt relocation as consequences of the eutectic interaction between cladding and spacer might have influenced the disintegration of the bundle even over longer distances. In any case, the relocation of melts observed in this test had its origin at the elevation of the spacer and could only be pursued below that level.

Typical for the elevation of the central spacer is, that the cladding material as well as originally metallic melt are found completely converted to oxide (Fig. 59). In contrast, fuel rod fragments often show metallic or partly metallic components, namely re-solidified Zircaloy or (Zr, U, O) melts from the interaction with the fuel. Those fragments must have fallen from more elevated original positions of less severe temperature history (Fig. 60). Since they are not typical for their final position, they must have broken down rather late in the transient or even during the cooldown phase of the test.

Top of the heated zone

At the elevation of the upper grid spacer of Zircaloy-4 at the 870 mm cross section, the destruction of the bundle is less advanced (Figs. 61, 62). The prevailing mechanisms for the damage are still the oxidation of the cladding and the spacer material and their interaction with the fuel under formation of (Zr, U, O) melt. However, the high temperatures required for that reaction can have been reached for only very short periods. Otherwise the oxidation of spacer, cladding and melt should have proceeded more than observed. The typically

measured ZrO_2 layer thickness of ca. 100 µm would be reached within few minutes at about 1500°C (Fig. 62). It is plausible, that some limitation of the steam supply became effective in the upmost zone of the bundle, which can be expected to have contributed to a moderation of the temperature excursion. Steam starvation is also deduced for this elevation from a special investigation of the oxidation behaviour and the deformation of the cladding material in test CORA-2 /11/.

5.1.2 Results of Scanning Electron Microscopy Analysis

Selected positions of the bundle and molten materials were investigated by use of the scanning electron microscope (SEM) and analyzed with energy dispersive X-ray spectrometry (EDX) for the overall composition and the element content of the different phases. Some wave length dispersive measurements (WDX) were also performed, in order to confirm oxygen content observations.

At the cross section of -13 mm elevation a separately-lying lump of melt (Fig. 63) was identified to originate from Zry-UO_2 interaction and mainly consisted of a (Zr, U, O) phase and an (U, Zr)O_2 phase. For details of the integral composition and the phase analyses obtained in this and the following cases see Tab. 6 and 7.

A small melt droplet (Fig. 64) was found to contain, in addition to the main components Zr,U and O, some material from the central spacer grid of Inconel. Its microstructure was analyzed to be composed of a (Zr,U, O) phase surrounded by a seam, containing considerable amounts of Ni, Fe and Cr, here denoted as (Zr, U, Inc), further a (U, Zr)O_2 phase, and some (Zr, Sn, Ni) grains (Fig. 65).

Melt in contact with a cross of the Zry spacer grid (Fig. 66) was analyzed to be composed of three different types, an (Inc, Zr) type melt, almost without U, but with some Mo from the heater electrode, further a (Zr, U, O) type of melt with some content of Inconel components, and finally a (Zr, Sn) type of melt. The contact region between the (Inc, Zr) and the (Zr, U, O) melts was analyzed at two positions (Fig. 67). Multiphase microstructures, in one case of the metallic phases (Zr, Inc), (Zr, Ni, U) and (Zr, Ni, Sn, U) together with some precipitated ZrO_2 were found. In the other case the phases are interpreted as metallic (Zr, Inc, U) and (Zr, Ni, U) and ceramic (Zr, U)O_2, containing some Inconel components. In these notations "Ni" stands for an enrichment in this element in relation to Cr and Fe, which are included if present in traces when compared to the original

composition of Inconel, otherwise "Inc" denotes Cr, Fe and Ni roughly in their original relation.

In order to draw a complete picture, an only locally observed type of melt in external contact with a fuel rod is mentioned, which was analyzed to be of ceramic nature and to combine the components of cladding, fuel, tungsten heater and Inconel grid spacer. This melt can only have formed very late in the test, when sections of heater rods got uncovered. A fuel rod fragment was also analyzed for the cladding fuel interaction, which went on before the fragment fell down.

Summarizing the observations, the molten masses found at the lower bundle end can be interpreted to originate from Zircaloy - UO_2 interaction, Inconel interaction with Zircaloy and from alloying of non-oxidized residual metallics.

Within the blockage zone (268 mm elevation), as indicated by the integral analysis, Zry-UO_2 interaction resultant melt with traces of tungsten has accumulated. The melt has decomposed into a (Zr, U, O) phase with (U, Zr)O_2 precipitates, two different compositions of (U, Zr)O_2 type and a (W, Zr, U, Cr) oxide as trace constituent. Typical for the whole blockage is the weight relation U/Zr = 54/46, which is the average of several integral analyses performed at this cross section.

At the position of Fig. 50 the area between ZrO_2 and UO_2, where residual melt has resisted oxidation, was also analyzed (Fig. 68). The fuel pellet was found contaminated by a Cr-rich interaction layer. The cladding and a boundary layer towards the residual melt is transformed into two different (Zr, U)O_2 compositions. The melt region is composed of metallic Inconel, modified by some Sn content, a metallic (Sn, Ni) phase and an inclusion of (Zr, U)O_2 phase with balanced Zr/U relation and some Inconel contribution. The fuel pellet also contained this latter phase as minor constituent together with two different compositions of (U, Zr)O_2 phase, (U, Cr, Zr) oxide and (Cr, U, Zr, W) oxide as reaction layers.

Summarizing the observations on this elevation, the blockage, which has the average composition U/Zr = 54/46, is mainly the result of relocation of material from cladding-fuel interaction and cladding melting. The identification of only modified Inconel melt could eventually indicate, that the central grid spacer was

not completely dissolved by eutectic interaction with the cladding, but that residues finally melted down. The alloying of residual metallic melts is again observed, which tend to enrich in oxidation resistant metals. In contrast, reactive elements tend to enrich in scales and ceramic interaction layers.

At the 480 mm elevation a fragment of originally molten material on a fuel pellet fragment was identified to originate from cladding-fuel interaction. According to the gross analysis the Zr/U relation was about 70:30 close to the pellet and about 85:15 more apart. At both positions the microstructure was identified to consist mainly of dendrites of (Zr, O) phase, mostly with U and often with some Sn content. Two interdendritic phases were identified as metallic (U, Zr) and ceramic (U, Zr)O_2. A (Zr, Sn) phase occurred as minor constituent (Fig. 69). Another fragment of essentially metallic character and in contact with a pellet fragment was also identified as melt from Zry-UO_2 interaction. The integral Zr/U relation was roughly 2:1, the dendritic phase was identified as (Zr, U, Sn) and the interdendritic phase as (U, Fe, Zr). Some grains of (Zr, Sn) phase could also be found.

An isolated solid pellet showed a broad surface zone of interaction, which gave a gross analysis of the Zr/U relation of 60:40. Within this region U-rich zones interpenetrated into others of roughly balanced Zr/U relation. The originally molten materials have become completely ceramic in the course of oxidation.

Finally for this elevation, positions were anlyzed on a heated rod, at which melts in between pellet and cladding or pellet and heater rod, respectively, had formed. Those were analyzed to be of the (Zr, U)O_2 or (U, Zr)O_2 type with only minor attack of the heater by the latter (Fig. 70). So it can be assumed, that the melts were subsequently oxidized and the temperatures had not been extreme enough to result in eutectic melting of oxide.

As a summary for this elevation, melts from Zry-UO_2 interaction and locally of some content of dissolved Inconel spacer material are found, still in partly metallic condition or subsequently transformed to oxide.

At the 870 mm elevation still metallic melt near the contact with a solid UO_2 pellet was analyzed to consist of (Zr, O) phase primary crystals together with a fine eutectic distribution of (U, Zr)O_2 particles in the above-mentioned matrix.

This microstructure is typical for the quasi-binary eutectic system observed for the cut from α-Zr(O) to UO_2 through the Zr-U-O system.

A partly once-molten fragment was analyzed in the metallic and the ceramic regions. The metallic material is a (Zr, O) phase with (Zr, Mo) phase precipitates. In the adjacent oxide ZrO_2 contains (Zr, Mo) oxide particles, deeper in the oxide ZrO_2 and (Zr, U)O_2 form a matrix, containing zones with finely dispersed (Zr, Mo) oxide. The fragment is thus to be interpreted as the remnant of an annular pellet with internally adherent (Zr, U) melt, which has picked up Mo from the upper electrode of the heater.

With this fragment an interference with the W of the heater rods or Mo of their electrodes has been reported, repeatedly. However, this does not mean that those reactions were of general or essential influence for the behaviour of the bundle. They are over-represented in the description given above, since complicated, strange and unknown microstructures have been preferred in the analysis, in comparison to the other interactions, which are better known from separate-effects investigations.

5.2 Sections of Bundle CORA-3

Bundle CORA-3 has been cut into a multitude of horizontal slabs and vertical sections, especially in order to show the degree of blockage by agglomerated melt and of destruction of the original arrangement of fuel rods. They were evaluated in the as-cut condition, while three of them were metallographically prepared for the detailed microstructural investigation, which is reported below.

In the course of the experiment melt has found its way down even below the heated part of the bundle, where the fuel rods have remained intact, except the cladding tubes, which got embedded into the contacting melt. At 35 mm elevation already one half of the bundle cross section is blocked by solidified melt. Pellet-cladding interaction obviously has proceeded here as an in-situ process. Above 50 mm the cladding tubes became dissolved into the molten masses. The vertical section between 67 and 184 mm contains a complete blockage of the empty volume of the bundle.

Above this blockage some rubble of agglomerated fragments is observed. The central Inconel spacer grid left no detectable traces behind. The fuel rods are

heavily destroyed over the whole heated length and even above. The fuel rod cladding which became seriously oxidized, cracked and deformed by the "flowering" process, seems to be the first rod component to have failed. The fuel pellets have been partly dissolved by chemical interaction with the molten cladding. The pellets are often cracked as well. Where pieces of annular pellets have broken off, the bare tungsten heater rods have become exposed. The remaining bundle configuration seems to be glued together and thus to be stabilized by a flux of melt. Residues of this melt can be found in form of lumps of essentially metallic nature.

Three of the cross sections of bundle CORA-3 have been investigated in detail, the horizontal cross sections at 20 mm and at 798 mm elevation (sections 3-1 and 3-14) and the vertical section from 67 to 184 mm through the massive blockage (section 3-b).

Section 3-1 at 20 mm elevation, below the main part of the blockage, shows, that about one half of the flow channel area between the fuel rods and a part of the additional area around the bundle is filled by dense, originally molten material. The light optical macrographs indicate, that the material is of primarily metallic nature (Fig. 71).

Where the space between the fuel rods was not completely filled, bridges of melt between neighbouring rods indicate good wetting behaviour. At other positions, however, the wetting of the rods has been poor. Another part of the melt has here no contact with rods. The observed differences might reflect the variation in the temperature of the locally agglomerating melt and the conditions of the rods at that time. For example, an early-relocated or superheated melt might easily dissolve the still relatively thin oxide layer of a cladding tube, wet it and react with it, whereas a later-arrived, cooler fraction could show poor wetting. Isolated melt might have dropped down, instead of rinsing down along rods, to form a separate lump.

Oxide scales of ca. 130-270 µm local thickness have been formed on steam-exposed parts of the cladding tubes, which have retained their integrity. Where the rods became embedded into melt, the cladding was modified at the contact zone but not completely melted. Its essentially single-phase microstructure can be still distinguished from that of the melt, which has decomposed into a primary matrix phase and secondary constituents from the solidification of residual melt

in between those primary crystals (Fig. 71). The microstructure of the melt shows considerable variations along the cross section, but it can be recognized, that it must have resulted from pellet-cladding interaction, because this reaction is found to have proceeded with similar resulting microstructures at this elevation as well. Whereas the in situ reaction has formed only metallic phases, a part of the melt contains ceramic phase in addition, and thus indicates a higher overall content of oxygen in the respective zones. Free surfaces of the melt are covered by an oxide scale of ca. 200 µm from steam exposure after relocation.

Details of the microstructure will be described now, together with the results of the phase analysis by SEM-WDX evaluation.

At the steam-exposed side of a partially melt-embedded unheated fuel rod the material in between the oxide scale of the cladding and the solid pellet has been analyzed (Fig. 72). Below the ZrO_2 an external (Zr, O) layer is identified. An internal (Zr, O) layer with some Sn and U content and a few (U, Zr)O_2 precipitates contacts the pellet (Fig. 73 bottom). A central zone in between both (Zr, O) layers (Fig. 73 top, right) is composed of (Zr, O) phase with Sn and U as primary phase matrix and additional (U, Zr, O) melt being decomposed into (Zr, O) and (U, Zr, O). This zone contains angular crystal plates of (Zr, Sn) as third phase and a (Zr, U, Ni) phase with Fe, Cr content as minor constituent. The integral composition of another analyzed region of this type is Zr/U/Ni/Fe/Cr/Sn = 47/44/5/2/1/1. Both analyses prove, that melt, which already contained the components of the Inconel spacer grid in considerable amount, must have penetrated into the attacked cladding of the fuel rod. Other pellet-cladding and pellet-melt interaction zones show either aspects of solid state interaction or melting of the attacked cladding.

The microstructure of several investigated positions deep within the melt can be discussed as follows: Everywhere at this elevation metallic (Zr, O) is the matrix, the primary or dendritic phase. Other phases are (U, Zr) with typical staining behaviour during air exposure of the polished specimen, and (U, Zr)O_2 at many regions in the melt. Angular crystals of (Zr, Sn) and (Zr, U, Ni) are restricted to some zones and found to be less abundant even there.

A statistically relevant series of integral analyses of the melt composition at various positions has demonstrated two types of melt in this bundle elevation: The majority of the melt contains only some material from the Inconel spacer, as

an average composition Zr/U/(Ni + Fe + Cr) = 81/18/1 was found. A separate melt lump had the average composition Zr/U/Ni/Fe/Cr = 71/19/5/3/2, which indicates more pronounced alloying with Inconel.

At one position of this melt lump primary crystals of (Zr, O) with U, secondary (Zr, U, O) phase and plates of (Zr, Sn) can be distinguished. A band through this region consists of (Zr, O) with U and contains aligned (U, Zr)O_2 particles. This observation is discussed as relict of an originally free and thus oxidized surface of melt, which became embedded into a growing melt pool.

Vertical section 3-b is a cut through a row of three unheated fuel rods between 67 and 184 mm elevation, where melts have formed a massive and compact blockage of the whole bundle. The rods have remained as free-standing UO_2 pellet columns with clearly visible dishing volumes, some of them partly filled by penetrated melt. At some positions a more essential attack or even the partical dissolution of submerged pellets is obvious. A stratification of the melt is indicated by local differences in the reflectivity of the polished specimen: The lower half of the blockage has a rather uniform grey tint (Fig. 74), whereas the upper half consists of intermixed zones of darker and brighter colour (Fig. 75 and 76). It is assumed, that the brighter zones, embedded by darker ones, have solidified relatively late, since they were able to form an almost flat free surface of melt, solidifying within a crucible of already re-frozen material. The porosity observed in the zone directly below this surface is shrinking volume. It is also mentioned, that a crack system across the blockage, which also penetrates straight into and through the fuel pellet stacks, is arrested around the bright zones of prior melt, which are uncracked. Above the blockage some fragments have agglomerated and are partly glued together by prior melt. Residues of the shroud wall complete the overall picture.

A detailed investigation and SEM-WDX analysis were performed at many selected positions, which is reported in the following:

The grey zone of melt in the lower half of the blockage can be understood at first sight as (Zr, O) primary matrix phase and eutectic melt, which has decomposed into (Zr, O), (U, Zr) and (U, Zr)O_2 (Fig. 74). The WDX analysis confirms Zr with considerable U and small oxygen content. As an average integral composition the relation Zr/U = 84/16 was observed for this metallic melt type.

At one position where somewhat darker looking melt seems to have flown down into the grey zone, this variant of melt has decomposed into (Zr, U)O_2 grains showing precipitated needles of (Zr, U, O) and into other eutectically decomposed grains of (Zr, U, O). The integral composition of this ceramic melt is determined as Zr/U = 80/20.

At all of the other investigated positions of the dark zones of melt, the ceramic (U, Zr)O_2 phase is typically the main constituent and metallic (Zr, U, O) the dispersed phase (Fig. 75). As an average integral composition for this ceramic melt type the relation U/Zr = 82/18 was calculated. Individual measurements showed variations between 90/10 and 74/26. The oxygen content corresponds to an essentially ceramic character of this "dark" type of melt.

At some positions in this type of melt a minor content of the elements of the heater rods has been detected. This holds for the contact zones with the pellets as well and even for the reaction zones within the pellets. Normally (U, Zr) and (Zr, O) are identified as grain boundary phases precipitated between the UO_2 grains. At some positions one or two other phases are present. As an example, a pellet surface position of the integral composition U/Zr/W = 86/12/2 contains UO_2 together with (Zr), containing U, (U, Zr, Mo) oxide and a metallic (Zr, Mo, W) with Cu and U. At another position metallic melt, which partly fills a dishing volume is analyzed as dendritic (U, Zr, Mo) or (U, Zr, Mo, O) phase and interdendritic (Zr, Cu) with Fe and U, with some (Zr, Sn, Cu) minority phase and (U, Mo, Zr) oxide in contact to the pellet.

It can be assumed therefore, that the dark melt has been contaminated in the intimate contact and intermixing with the bright type of melt, which is to be described below, and which is an artifact of the out-of-pile experimentation and therefore not reactor-typical (Fig. 76):

At a low position, a zone of bright melt was analyzed integrally as Mo/W/Zr/U = 36/25/23/16. At a higher position another zone had the integral composition U/Mo/W/Zr = 30/25/23/22 (Fig. 77, top), which means that a similar (Mo, W, Zr) melt has dissolved more U here. The phase analysis identified (U, Mo, Zr) or (U, Mo, Zr, O), (Zr, W, U) oxide with Cu, and (Mo, Zr, W). The surface zone of pellets, being in contact with this melt contains the above characterized phases (U, Mo, Zr) and (Mo, Zr, W) as well. The microstructure of the decomposed melt of this bright type is very complex. Often dominate block-shaped and angular crystals

within a two-phase matrix. At one position at least two block-shaped constituents three phases of dendritic morphology, two matrix phases or compositions together with an angular ceramic phase of characteristic morphology, which also occurs in form of skeleton crystals or which is even dispersed into flakes, is observed (Fig. 77, bottom). In the vicinity of a pellet this latter phase is typical for the pellet dissolution microstructure and the angular variant of this phase for the crystallisation of U rich phase from the melt. This phase has been analyzed as (U, Zr, O) (Fig. 77, bottom). This type of crystals has been found in other CORA bundles and in TMI specimens as well.

At the porous surface zone of the melt the central rod has leached out two neighbouring pellets at the dishing between them, which is filled by ceramic material. Between this and the metallic melt the integral analysis U/Zr/Cu = 49/37/14 was obtained. In this region dendrites of (W, Mo, Cu, O) are identified together with (Cu, Zr, W) oxide and (Mo, Zr, W, O) phase with minor Cu, Sn, Ti, Cr content.

Extremely thick oxide scales up to about 3000 µm are observed at some positions of the free surface of the melt blockage, which cannot be understood by subsequent oxidation of relocated melt, but must result from completely oxidized constituents as shroud or cladding fragments.

Section 3-14 at 798 mm elevation exhibits the bundle in a strongly destroyed status (Fig. 78). From the central part only the heater rods remain, bare or glued together by some melt. The fuel pellets are partly in good condition, others have been attacked by interaction with the cladding or deeply dissolved by some melt. The remaining Zircaloy material is completely converted to oxide.

A melt lump between a solid fuel pellet and bare heater rods has been analyzed for elemental and phase composition. Near to the attacked pellet the obtained integral analysis is Zr/Mo/Cu/U/W = 50/27/12/7/4 (Fig. 79, top). The phases (U, Zr)O_2 and (Zr, U)O_2 form a double reaction layer on the pellet and dendrites of (Mo, W, Zr) interlink the ceramic interaction zone with the metallic zone of the prior melt. This melt has the integral composition Cu/Mo/Zr/W/U = 48/25/21/3/3 more apart from the pellet and consists of a matrix of (Cu) phase with a system of unidirectionally solidified lances of (Cu, Zr, O) with U, angular precipitates of (U, Zr, O) with Cu and (Zr) with Cu, and finally a dendrite system of (Mo, W, Zr) with Cu (Fig. 79, bottom).

The above mentioned dendrites are also found at melt-attacked pellets with residual converted and reacted cladding. In a region of integral composition Zr/Mo/W/U = 69/17/8/6, near an annular pellet, dendrites of (Mo, W) with Zr intersect the (Zr, U)O_2 interaction zone together with colonies of unidirectionally solidified rods or wires of presumably the same phase, which have been formed by solidification of melt with eutectic composition.

Finally, the sequence of phases identified between the ZrO_2 scale of the prior cladding tube and a solid fuel pellet is a (Zr, U)O_2 layer, interlinked by (Mo, W, Zr) dendrites with prior melt, which has decomposed further into the matrix phases (Cu, Zr, O) and (Zr, Cu) with U plus the minority phase (U, Cu, Zr) oxide.

All of the phases observed at the three sections, which were extensively investigated, are listed in Tab. 8.

6. Materials Interaction Processes; Separate-Effects Tests

In parallel to the integral CORA experiments extensive separate-effects tests have been performed. The objective of these experiments is to obtain information on typical microstructures of the various bundle components and the reaction products in dependence on temperature and time and to determine quantitatively the extent of the chemical interactions between the bundle components under well defined test conditions. Since the results of these laboratory experiments have been published elsewhere /15, 18-22/, only the main results will be briefly described.

6.1 Zircaloy Cladding High-Temperature Oxidation

In the LWR safety analysis the oxidation of Zry cladding in steam is a most important factor. It deserves consideration because the oxidative cladding tube wall consumption determines cladding embrittlement, competes with fuel/cladding interaction and is accompanied by release of hydrogen and exothermal reaction heat.

Numerous and world-wide investigations have been performed towards the understanding of Zry cladding high-temperature behaviour and oxidation kinetics. The results are based on laboratory-scale exposure of short tube sections to steam of generally atmospheric pressure, performed under isothermal and temperature-transient conditions, and evaluated for specimen mass increase, ZrO_2 scale and α-Zr(O) layer growth and microstructural observations.

Below 1000°C the oxidation kinetics can be described by cubic rate equations for oxygen uptake and layers growth, until a transition to non-protective scale growth with roughly linear rate occurs, beyond a temperature dependent critical scale thickness. This long-term behaviour is complicated by influences of phase transformations of Zircaloy and its oxide, and accompanied by considerable hydrogen uptake. This oxide growth regime is of limited importance in the present context, since only a slow transient would reach it, and even then would resume normal, protective scale growth slightly above 1000°C, where this field is known to terminate (Fig. 80) /12/.

Above 1000°C parabolic rate laws describe the oxygen uptake and the layers growth in a simple way until the total oxidative consumption of the matrix is

approached. At about 1525°C an abrupt, almost step-wise increase to the parabolic reaction rates observed above that boundary temperature can be explained by formation of an additional subscale of cubic ZrO_2 phase below the tetragonal oxide modification /12/. In contrast, no discontinuity of this kind seems to exist at the melting temperature of Zircaloy (1760°C) and at the stability limit of the tetragonal ZrO_2 phase (2285°C) /13/. Experimental limitations are growing seriously with increasing temperature, since the dramatic reaction heat evolution disturbs temperature control and the reaction time period is shortened. Correction of the results on the basis of a more sophisticated oxidation model becomes essential in the evaluation:

The high-temperature oxidation of Zry cladding can be described by diffusional oxygen transport in a multi-layered system of finite thickness, in which the oxygen concentrations at the phase boundaries remain at equilibrium values and the boundary movement is calculated with finite difference methods /14, 15/. Such a code can be used to refine the evaluation of experimental results, since the total oxidative consumption of the material is included in the model. After the verification of the materials data base of the code in comparison with experimental results, any ramp or more complicated temperature cycle can be calculated.

Additional parameters interfere as follows: Pre-existing scales from normal reactor operation are expected to loose their protective influence during the accidental transient, as this was observed for simulated scales above 1100°C /16/. A direct influence of steam pressure on the oxidation seems not to exist; an indirect effect was only observed at 905°C in connection with the α/β phase transformation of the material, but not at 1100°C /17/. Another indirect influence of steam pressure (or steam velocity) may seem to exist in case of a serious lack of oxidant supply. However, under those steam starvation conditions the ZrO_2 scale growth rate is reduced simply according to the limiting rate of gaseous transport of steam molecules to the surface of the exposed material. In the same sense, inert gas and even hydrogen in mixed atmosphere do not influence the oxidation. Under steam starvation conditions hydrogen, however, was found to act as competing reactant and is picked up by Zircaloy until the solubility limit is reached. This limit increases with the square root of the hydrogen partial pressure in the atmosphere, but decreases with increasing temperature /16/. This is why its influence on cladding oxidation is unimportant at the high temperatures, which are considered here.

6.2 Chemical Interactions between UO_2 and Zircaloy

6.2.1 Interactions up to the Melting Point of Zircaloy

The chemical interactions between UO_2 fuel and Zircaloy-4 cladding up to the melting point of Zircaloy (Zry) were investigated under possible severe fuel damage (SFD) conditions /15, 18, 19/. Under these conditions a combined external and internal oxidation of the fuel rod cladding takes place due to a reaction with steam or oxygen on the outside surface and the UO_2 fuel on the inside surface. These reactions result in the formation of oxygen stabilized α-Zr(O) phases, ZrO_2 and a (U,Zr) alloy. The tests were conducted in inert gas (1 to 80 bar) /18, 19/ or in an (Ar + 25 vol.% oxygen) environment /15/ with 10 cm long Zry cladding specimens filled with stoichiometric UO_2 pellets. The reaction kinetics has been studied with both isothermal /18/ and transient temperature /15, 19/ experiments up to 2000 °C. The annealing period varied between 1 and 150 minutes.

The extent of the internal cladding interaction depends decisively on whether or not good solid contact between UO_2 and Zry has been established. If solid contact exists, Zry reduces the UO_2 to form α-Zr(O) and uranium metal. The uranium reacts with Zr low in oxygen to form a (U,Zr) alloy rich in uranium. The (U,Zr) alloy, which is liquid above 1150 °C, lies between two α-Zr(O) layers. The affinity of Zr for oxygen, which results in an oxygen gradient across the cladding, is the driving force for the reaction. The UO_2/Zry reaction obeys initially a parabolic rate law. The degree of chemical interaction between UO_2 and Zry is determined by the extent of oxygen diffusion into cladding, and hence by the temperature, time and the oxygen uptake from the outside. Since the oxygen potential (partial pressure) on the outside (H_2O) is higher than on the inside (UO_2) of the cladding the UO_2/Zry growth rates decrease after some time and finally come to a stop.

The external cladding oxidation with oxygen or steam results in the formation of α-Zr(O) and ZrO_2. The reaction obeys initially a parabolic rate law. After some time, the growth rates of the various phases increase due to the finite cladding wall thickness and the internal oxygen uptake from the UO_2 /15/. The final stable reaction products are ZrO_2 and a ceramic $(U,Zr)O_2$ compound.

The growth of the reaction layers can be represented in an Arrhenius diagram (Fig. 81). The UO_2/Zry reaction occurs as rapidly as the steam/Zry reaction above about 1100 °C. The extent of the interaction is independent of the external pressure above about 10 bar at 1400 °C and 5 bar at 1700 °C. If there is no external

oxygen uptake from the steam, the maximum measured oxygen content of the cladding is about 6 wt.%, which corresponds approximately to oxygen saturated α-Zr(O). Up to 9 vol.% of the UO_2 can be chemically dissolved by the Zry. In an actual fuel rod, complete release of the volatile fission products in this region of the fuel must therefore be assumed since the UO_2 crystalline structure is totally destroyed by chemical interaction with the Zry /15, 19/.

To describe the chemical interaction of Zry with UO_2 fuel and oxygen a computer model, called PECLOX (Pellet Cladding Oxidation) has been developed for the calculation of the internal and external Zry cladding oxidation /15/. The numerical model PECLOX solves the Fick and Stefan equations. It predicts the formation, growth and disappearance of the various interaction layers which form as a result of the chemical interactions of the Zircaloy cladding with the UO_2 fuel and oxygen or steam and it calculates the corresponding oxygen profiles as functions of temperature and time. In addition, PECLOX determines the expansion or shrinkage of the fuel rod geometry due to the chemical interactions. The diffusion of oxygen into the Zircaloy cladding is assumed to be the rate-determining step for the growth of the interaction layers. PECLOX has an option for limiting the oxygen flux on the outer cladding surface, for example, due to steam starvation in the coolant channel /15/.

6.2.2 Dissolution of Solid UO_2 by Molten Zircaloy

The solid UO_2 fuel can be liquefied at temperatures far below ($\approx$ 1100 K) its melting point by dissolution in molten Zircaloy. For this reason, the reaction kinetics of molten Zircaloy with solid UO_2 have been investigated /20/. The liquid Zircaloy dissolves chemically the solid UO_2 under formation of a metallic (Zr,U,O) melt which decomposes on cooldown into α-Zr(O), a (U,Zr) alloy and, at higher oxygen concentrations, a ceramic $(U,Zr)O_2$ phase. Microstructures of solidified (Zr,U,O) melts of different initial chemical compositions (20, 40, 60, 80 wt.% UO_2 dissolved in molten Zry) are shown in Figure 82. One can recognize the two metallic phases and the ceramic phase. The ceramic phase forms only at initial UO_2 concentrations of $\geq$ 35 wt.%. In addition, other molten UO_2/Zry mixtures of various UO_2/Zry ratios were prepared and the resulting microstructure has been used to quantify the extent of UO_2 fuel dissolution in the separate-effects tests and in the integral CORA experiments.

The dissolution-time dependence of the $(U,Zr)O_2$ phase portion is obtained for the various test temperatures and was used to quantify the dissolution process.

The chemical interaction between UO_2 and molten zircaloy obeys a parabolic rate law. The dissolution rate is found to have an Arrhenius dependence on temperature, indicating that the rate controlling process is thermally activated with an unexpected high activation energy. The UO_2 dissolution rate by molten Zircaloy is shown as function of the reciprocal temperature in Figure 83 /20/.

The dissolution of solid UO_2 by molten Zircaloy has been described by a model /20/. Since an analytical solution for this problem can be very difficult a numerical solution (code) was developed: LISI (Liquid Zircaloy - Solid Uranium Oxide Interaction). One of the essential assumptions of the model is that the UO_2 dissolution by molten Zircaloy is controlled by an oxygen diffusion process in the liquid. The solid UO_2/molten Zircaloy reaction interfacial area increases due to UO_2 dissolution and disintegration. To simulate this process an artificially high equivalent oxygen diffusion coefficient was considered in the liquid near the interface. The equivalent oxygen diffusion coefficient approaches its true physical value in the molten Zircaloy far away from the solid/liquid reaction interface. The high activation energy involved in the UO_2/molten Zircaloy interaction is correlated with the increased oxygen diffusion coefficient near the UO_2/Zircaloy interface. The code LISI can determine the oxygen concentration profile and the interface position at every time and is able to predict the dissolution rate of UO_2 at each temperature.

6.3 Dissolution of Solid ZrO_2 by Molten Zircaloy

Molten Zry cladding chemically interacts with both solid UO_2 and solid ZrO_2 which forms during heatup in an oxidizing atmosphere. For this reason, it is also important to know the dissolution rate of solid ZrO_2 by molten Zry. The liquid Zry dissolves the ZrO_2 about 1000 K below its melting point under formation of a (Zr,O) melt. Depending on the oxygen concentration of the melt it forms on cool-down metallic oxygen stabilized α-Zr(O) or it decomposes at higher oxygen concentrations, into α-Zr(O) and ceramic ZrO_{2-x} phase /21/. The ceramic phase portion was used to quantify the extent of ZrO_2 dissolution. The dissolution obeys a parabolic rate law. The ZrO_2 dissolution rate by molten Zry is shown versus the reciprocal temperature in Figure 83 in comparison with the UO_2 dissolution rate. The activation energy for both processes is very similar. The ZrO_2 dissolution rate is a factor of about 5 slower than the UO_2 dissolution rate. The low-temperature liquefaction of both UO_2 and ZrO_2 provide mechanisms for their relocation in a molten state much below their melting points. This will enhance core melt progression in a severe reactor accident.

6.4 Chemical Behavior of Inconel Spacer Grids at Higher Temperature

The CORA experiments showed by visual observation and temperature measurements that the Inconel spacer grid fails due to liquefaction below its melting point (around 1450 °C) as a result of eutectic reactions of nickel and other alloy components with zirconium. To determine the reaction kinetics and the onset temperature of liquid phase formation interaction experiments between Inconel 718 and Zircaloy cladding (Zry) have been performed between 1000 and 1400 °C /22/. The Zry cladding was used in the as-received condition and in the pre-oxidized (10, 20, 45, 100 µm oxide layer thicknesses) condition. An oxide layer on the surface of the Zry can initially prevent the interaction with Inconel, but the oxide is rapidly dissolved in the Zry at higher temperatures, during an incubation period, t_0.

The eutectic interactions between the Inconel 718 spacer grid and the Zry cladding can be described by parabolic rate laws. Liquid phases form around 1000 °C and a fast and complete liquefaction of both components occurs above 1250 °C, about 200 °C below the melting point of Inconel. Only small amounts of Inconel are necessary to dissolve great amounts of Zry. Thin ZrO_2 layers on the Zry surface delay the chemical interactions of Zry with Inconel, but cannot prevent them. The ZrO_2 layer must be dissolved before chemical interactions can take place. The required incubation period, t_0, depends on temperature and time. Dissolved oxygen in the Zry, forming oxygen stabilized α-Zr(O), reduces the reaction rates with Inconel and shifts the liquefaction to higher temperatures. In Figure 84 the reaction rates between Inconel and Zry are plotted versus the reciprocal temperature for various oxide layer thicknesses. The thicker the initial ZrO_2 layer the larger is the incubation period t_0 /22/. No interactions take place at 1000 °C for initial oxide layers ≥ 20 µm for the maximum annealing times of 3 hours examined.

7. Interpretation of CORA Results

The tests CORA-2 and CORA-3 have been successfully conducted, accompanied by measurements and visual observations and evaluated by microstructural and compositional analyses. On the basis of this information and the expertise from separate-effects investigations the following interpretation of the sequence of mechanisms during the degradation of the bundles is given.

As already observed in previous tests /3/ the temperature traces recorded during the tests CORA-2 and -3 indicate an increase in the heatup rate above 1000°C. This temperature escalation is due to the additional energy input from the exothermal Zry/steam oxidation, the strong increase of the reaction rate with increasing temperature, together with the excellent thermal insulation of the bundles. An effectively moderated escalation would be observed for smaller initial heatup rates, because the growth of protective scale during steam exposure counteracts by decreasing the oxidation rate of the material.

This explains the observation that the temperature escalation starts at the hottest position in the bundle, at an elevation above the middle. From there, slowly moving fronts of bright light, which illuminated the bundle, were seen, indicating the spreading of the temperature escalation upward and downward. It is reasonable to assume, that the violent oxidation essentially consumed the available steam, so that time-limited and local steam starvation conditions, which cannot be detected in the post-test investigation, should have occurred.

A first melting process starts already at about 1250°C at the central grid spacer of Inconel, due to diffusive interaction in contact with Zry cladding material, by which the melting temperatures of the interaction partners (ca. 1760°C for Zry, ca. 1450°C for Inconel) are dramatically lowered towards the eutectic temperature, where a range of molten mixtures solidifies. (This behaviour is similar to that of the binary eutectic systems Zr-Ni and Zr-Fe with eutectic temperatures of roughly 950°C).

Relocation of thus formed Zry-rich Inconel-containing melt was observed at temperatures above 1500°C and resulted in a wide-spread distribution within the lower half of the bundles. It alloyed with the cladding of contacted fuel rods and initiated a premature dissolution of UO_2 fuel, as indicated by often considerable

contents of uranium and oxygen, before it finally solidified. Most of this melt accumulated in local blockages within the lower Zry spacer grid.

It is to mention that the information from the analysis of the bundles is not sufficient to rule out that residues of unreacted Inconel spacer material might have melted down at about 1450°C. (Such material could have alloyed with Zry melt later on. The only once observed zirconium-free metallic Inconel melt drop in a fuel rod of CORA-2 could, however, be explained also by selective oxidation of an originally present Zry content).

In a temperature range still below the melting point of the cladding Zry begins to react with a considerable rate in solid state contact with UO_2 fuel under growth of a series of interaction layers. Where such a contact is not provided, the external oxidation in steam, by which the ZrO_2-scale and the intermediate α-Zr(O) layer are formed on β-phase Zry, is the only reaction to be considered, when cladding failure mechanisms are discussed. The brittleness of those oxygen-rich layers together with internal stresses built-up during oxidation (and possibly also applied stresses) are factors contributing to a potential of early cladding failure. Cladding deformation and rupture under internal pressure as well as circumferential temperature differences will complicate the stress field around a cladding tube. An assumed axially oriented crack through the tube wall or the rupture opening of a burst tube will provide access for steam to the inner surface. The scale growth on this side is delayed against the external oxidation and will consequently induce an outward bending and flattening of the split tube section, by which the further access of steam is promoted. The tube splitting process will proceed in axial direction.

This is a reasonable explanation for the observed "flowering" phenomenon, if it should have occurred under solid conditions. Shroud deformations can also be explained by similar argumentation. However, the microstructural investigation of the bundles has shown that the discussed mechanisms of cladding disintegration have only contributed to others, which are based on partially molten cladding.

When a fuel rod with still intact cladding reaches 1800°C, slightly more than the melting temperature of Zry, the cladding melt, originally low in oxygen content, is confined within the still solid external layers α-Zr(O) plus ZrO_2 and the UO_2 fuel. Melt relocation within the fuel-rod, by which the observed voids are formed,

closes the gap to the UO_2 pellet and thus increases the original areas of direct contact, where solid state Zry/UO_2 interaction has taken place already. Here, the liquid state Zry/UO_2 interaction proceeds dramatically by dissolution of increasing amounts of fuel, when the temperature increases further. (Should the temperature stagnate, the melt would finally re-solidify with excessive contents of uranium and oxygen).

Simultaneously and in competition the degradation of the external melt confinement proceeds: An internal dissolution into the melt competes with a continued growth tendency under steam. Steam starvation conditions would contribute to reduce the growth rate of the oxide barrier. Further, a new melt front is formed in between ZrO_2 and α-Zr(O) above 1900°C, the eutectic temperature of this system. At 1975°C α-Zr(O) is completely molten.

Oxide scale perforation is assumed as the result of the described weakening tendencies in combination with mechanical loads. Melt may either re-solidify and close a perforation again, because it gets oxidized in contact with steam, or it may flow out to initiate the major melt relocation events observed in the tests.

Cladding melt and mostly modified melt from fuel dissolution are distributed downward in the bundle by droplets and rivulet formation. Although free falling droplets are observed early, rivulet movement is the prevailing transport mechanism. It might require some incubation period to improve the wetting between melt and already oxidized fuel rod. Droplets typically fall through long distances and resolidify quickly in their relatively cool new environment. Rivulets tend to vary in the velocity and the mass flux of transported material, or even re-solidify and get re-melted, until the material agglomerates at its final elevation. So, some melt reaches the lower spacer grid and most of it re-solidifies into an extended blockage above the spacer. Early melts are of the (Zr, O) and mostly the (Zr, U, O) types and of metallic character. Late relocation of molten material of almost the ceramic composition (U, Zr)O_2 was found in test CORA-3, where it solidified on top of metallic melt. (A further formation of melt in CORA-3 was caused by the destruction of the upper heater rod electrode zone due to superheating at the end of the test. It relocated in form of different alloys of the component metals Cu, Mo and W, dissolved residual fuel in the upper half of the bundle and was caught by the melt pool in the blockage).

Relocation of solid fragments became essential only very late in the tests, probably during the cooldown phase. Most of this material forms a bed of rubble above the blockage. It consists of fragments of cladding and shroud transformed to ZrO_2, fuel rod fragments, fuel pellet fragments and, in case of CORA-2, fine fragmented fuel (powder). Information from further CORA tests is required to confirm the understanding of this fuel fragmentation in dependence of the individual test conditions.

It is instructive to compare the limitations and advantages of the out-of-pile experimentation in the CORA facility with the respective potential of in-pile testing. The extensive instrumentation and the real-time inspection of the bundles have given valuable complementary results to those of the post-test analysis. On the other hand, the general limitation of out-of-pile tests is the requirement of a heat source simulation. CORA-specific is that tungsten heater rods tend to dissipate more energy where a hot spot has formed, since the electric resistivity increases with temperature. This should have supported and has possibly accelerated the development of the oxidation-induced temperature escalation, after the bundle was heated homogeneously. Also with respect to chemical and mechanical behaviour the influences of the heater rods remained quite limited, so that only the constraint exposed on the reactor materials is worth to be mentioned. The similarity between the behaviour of heated simulators and that of unheated rods in the tests indicates that the interference of the heater rods is an unimportant and understood feature of the generally well-simulated picture of reactor core degradation.

In both CORA tests it was not intended to simulate pre-formed scale and crud on the cladding from reactor normal operation, fuel pre-conditioning, as well as fission product release. In those respects the tests are not claimed to be representative.

In general as well as in many details of other special phenomena excellent comparability of CORA results with that of in-pile tests and TMI core observations has been observed.

8. Summary and Conclusions

The CORA-2 and CORA-3 test bundles of fuel rods and electrically heated simulators, which are the first ones of the CORA series to contain UO_2 pellets, were heated with an initial rate of 1 K/s. In CORA-2 and CORA-3 the temperature escalated to peak values of roughly 2000 and 2400°C, respectively.

The integral CORA tests have been accompanied by separate-effects tests in which the chemical interactions of the various bundle components with each other have been studied under well defined boundary conditions to obtain information on the appearance of reaction products, reaction kinetics, and onset of liquid phase formation.

Observations during the CORA tests, the post-test evaluation of the severely damaged bundles, and information from separate effects investigations are the basis of the following conclusive summary:

- The temperature escalation develops in the upper middle of the bundles, from where escalation fronts are moving upward and downward. Local steam starvation conditions remain temporary.
- At the Inconel grid spacer at the middle elevation eutectic melting is initiated at roughly 1250°C by interaction with Zircaloy. Visible relocation of this Zr-rich metallic melt takes place at about 1400°C. The melt is distributed within the lower half of the bundles. Droplets mainly solidify accumulated in local blockages within the lower Zry spacer grid, which acted as a catcher.
- The Inconel/Zry melt interacts with the fuel rod cladding and dissolves some UO_2, even below the melting point of Zry.
- Localized failure of the cladding by axial splitting under oxidation-induced and external stress, by which steam access to the internal tube surface is provided, is one mechanism to explain "flowering", the observed outward bending and flattening of cladding tubes. At higher temperatures, however, other failure mechanisms become important.
- At about 1800°C molten cladding material which is still confined between intact external layers and the fuel, initiates localized melt relocation within the fuel rod and thereby increases the contact area to the fuel pellets. Dramatic UO_2 dissolution takes place in competition to the interaction of the melt with the α-Zr(O) layer and the ZrO_2 scale. By this "chemical weakening", in combination with mechanical loads, and influenced by other conditions as

temperature and local steam supply, oxide scale perforation is assumed to occur, thus opening up further paths for melt relocation.

- Cladding melt (Zr, O) and modified melt from fuel dissolution (Zr, U, O) is relocated by droplets and mainly by rivulet formation. The masses of melt are transported either in localized, individual events or more continuously. The melts agglomerate within the bundle to an extended blockage above the lower spacer grid. The relocated materials are of metallic character.
- Higher temperatures applied in test CORA-3 result in an extended destruction of the bundle with stronger melt formation, relocation, and a complete blockage of the bundle cross-section. Blockage formation in test CORA-2 is much less.
- In CORA-3 considerable amounts of uranium - and oxygen-rich melt of a (U, Zr)O_2 composition and ceramic character relocate and solidify on the metallic melt blockage (crust), when the temperature increases further in this test.
- Only residues of fragmented fuel pellets and completely oxidized cladding remain at the hottest upper elevation of the bundles. Rubble particles fall down and accumulate above the blockage, essentially during the cool-down phase of the tests.
- The understanding of the powderization of fuel, as observed in CORA-2, needs confirmation from further tests.
- In the general behaviour of the bundles as well as in many details of special phenomena, the tests CORA-2 and CORA-3 have proved to simulate LWR core degradation reliably. They will provide the reference for all the following CORA tests, in which the presence of absorber material in a fuel rod bundle is considered.

9. References

/1/ A. Fiege, "Severe Fuel Damage Investigations of KfK/PNS", KfK-3431B (1983).

/2/ S. Hagen, K. Hain, "Out-of-pile Bundle Experiments on Severe Fuel Damage (CORA-Program): Objectives, Test Matrix, and Facility Description", KfK-3677 (1986).

/3/ S. Hagen et al., "Interactions between Aluminium Oxide Pellets and Zircaloy Tubes in Steam Atmosphere at Temperatures above 1200°C (Posttest Results from the CORA Tests B and C)", KfK-4313 (1988).

/4/ S. Hagen, W. Hering, K. Vogel, "CORA-2 Test Results Report", KfK-4342 (to be published).

/5/ S. Hagen, W. Hering, K. Vogel, "CORA-3 Test Results Report", KfK-4402 (to be published).

/6/ A.W. Cronenberg and T.R. Yackle, "An Assessment of Intergranular Fracture within Unrestructured UO_2 Fuel Due to Film Boiling Operation", NUREG/CR-0595, TREE-1330, EG&G Idaho (USA), 1979.

/7/ H. Rosinger, private communication, 1988

/8/ H. Ruhmann, unpublished results, 1988

/9/ F. Nagase, unpublished results, 1989

/10/ W. Hering, unpublished report, 1989

/11/ K. Minato and W. Hering, unpublished results, 1990

/12/ S. Leistikow, G. Schanz, H. v. Berg, A. E. Aly, "Comprehensive Presentation of Extended Zircaloy-4/Steam Oxidation Results 600-1600°C", Proc. OECD-NEA-CSNI/IAEA Spec. Meeting on "Water Reactor Fuel Safety and Fission Product Release in Off-Normal and Accident

Conditions", Risø (Denmark) May 16-20, 1983, IAEA-Summary Report IWGFPT/16 (1983) 188-199.

/13/ J. L Prater and E. L. Courtright, "High-Temperature Oxidation of Zircaloy-4 in Steam and Steam-Hydrogen Environments", NUREG/CR-4476, PNL-5558 (1986).

/14/ S. Malang, "SIMTRAN I - A Computer Code for the Simultaneous Calculation of Oxygen Distributions and Temperature Profiles in Zircaloy during Exposure to High-Temperature Oxidizing Environments", ORNL-5083 (1975).

/15/ P. Hofmann, H. J. Neitzel, E. A. Garcia, "Chemical Interactions of Zircaloy-4 Tubing with UO_2 Fuel and Oxygen at Temperatures between 900 and 2000 °C; Experiments and PECLOX Code, "KfK-4422 (1988).

/16/ S. Leistikow, G. Schanz, "Oxidation Kinetics and Related Phenomena of Zircaloy-4 Fuel Cladding Exposed to High-Temperature Steam and Hydrogen-Steam Mixtures Under PWR Accident Conditions", Nuclear Engineering and Design 103 (1987) 65-84.

/17/ R. E. Pawel, J. V. Cathcart, J. J. Campbell, S. H. Jury, "Zirconium Metal-Water Oxidation Kinetics, V. Oxidation of Zircaloy in High Pressure Steam, "ORNL/NUREG-31 (1977).

/18/ P. Hofmann, D. K. Kerwin-Peck, "UO_2/Zircaloy-4 Chemical Interactions and Reaction Kinetics from 1000 to 1700 °C under Isothermal Conditions", KfK-3552 (1983).

/19/ P. Hofmann, D. K. Kerwin-Peck, "UO_2/Zircaloy-4 Chemical Interactions and Reaction Kinetics from 1000 to 1700 °C under Isothermal and Transient Conditions", J. Nucl. Mater. 124 (1984) 80-105.

/20/ P. Hofmann, H. Uetsuka, A. N. Wilhelm, E. A. Garcia, " Dissolution of Solid UO_2 by Molten Zircaloy and its Modelling", Int. Sympos. an Severe Accidents in Nuclear Power Plants, Sorrento, Italy, 21-25 March 1988 (IAEA-SM-2986/1).

/21/ P. Hofmann et al., "Dissolution of Solid ZrO_2 by Molten Zircaloy", KfK-4100 (1987) 4200/9.

/22/ P. Hofmann, M. Markiewicz, "Compatibility Experiments between Inconel Spacer Grids and Zircaloy Cladding", KfK-4729 (1990).

10. Acknowledgements

Various kinds of support of the experimental program and its evaluation is gratefully acknowledged. The test rods were assembled by Mr. E. Mackert, the test bundles by Messrs. H. Giesmann and Ph. Pfann. The authors would like to thank Messrs. K. Vogel, H. Benz, O. Heil, W. Rötzel, and H.J. Röhling for the preparation for the test and the test conduct. Messrs. H. Malauschek and K.P. Wallenfels are acknowledged for arrangement of camera and video systems to observe the bundle behavior during the transient test. Mr. W. Rötzel's effort in the post-test photography is greatly appreciated. A special acknowledgement is due to Mr. H. Benz for the encapsulation procedure of the tested bundle. The authors thank Mr. L. Anselment for the sectioning of the bundle and for the preparation of the metallographic samples, Mr. H. Metzger for the investigation of the metallographic samples by optical microscope, and Mr. J. Burbach for the SEM investigations.

Thanks also to Mr. W. Hering for the critical review of this report.

11. List of Tables

Appendix:

Table 1: CORA Test Matrix

Test No.	Max. Cladding Temperatures	Absorber Material	Other Test Conditions *)	Date of Test
B	≈ 2000°C	-	Scoping test, Al_2O_3 pellets	Sept. 3, 1986
C	≈ 2000°C	-	Scoping test, Al_2O_3 pellets	Feb. 2, 1987
2	≈ 2000°C	-	UO_2 refer., inconel spacer	Aug. 6, 1987
3	≈ 2400°C	-	UO_2 refer., high temperature	Dec. 3, 1987
5	≈ 2000°C	Ag, In, Cd	PWR absorber	Febr. 26, 1988
12	≈ 2000°C	Ag, In, Cd	quenching	June 9, 1988
16	≈ 2000°C	B_4C	BWR absorber	Nov. 24, 1988
15	≈ 2000°C	Ag, In, Cd	rods with internal pressure 60 b	March 2, 1989
17	≈ 2000°C	B_4C	quenching	June 29, 1989
9	≈ 2000°C	Ag, In, Cd	10 bar system pressure	Nov. 9, 1989
7	≈ 1800°C	Ag, In, Cd	large bundle (52 + 5 rods)	Feb. 22, 1990
18	≈ 1800°C	B_4C	large bundle (48 + 11 rods)	June 21, 1990

*) Test characteristics are:

Initial heat-up rate: = 1.0 K/s;

Steam flow rate PWR: 6 g/s, BWR: 2 g/s;

Quench rate (from the bottom) = 1 cm/s

Table 2: Design characteristics of the fuel element simulators used in CORA-2 and CORA-3

Bundle size:			25 rods
Number of heated rods:			16
Pitch:			14.3 mm
Rod outside diameter:			10.75 mm
Cladding material:			Zircaloy-4
Cladding thickness:			0.725 mm
Rod length:			2175 mm
Heated length:			1000 mm
Fuel pellets	- heated rods:		UO_2 annular pellets
	- unheated rods:		UO_2 full pellets
U-235 concentration			0.2 wt%
Pellet outer diameter (nominal)			9.1 mm
Heater material:			Tungsten (W)
Heater diameter:			6 mm
Grid spacer	- material:		Zircaloy-4, Inconel 718
	- length:	Zry	42 mm
		Inc.	38 mm
	- location:	lower (Zry)	- 5 mm (a)
		center (Inc.)	+ 488 mm
		top (Zry)	+ 880 mm
Shroud	- material		Zircaloy-4
	- wall thickness		1.2 mm
	- outside dimensions		86 x 86 mm
	- elevation	CORA-2	36 mm - 1204 mm
		CORA-3	36 mm - 1264 mm
	- insulation material		ZrO_2 fiber
	- insulation thickness		20 mm

(a) Elevations are meant for the top of the grid spacers and are referred to the bottom of the heated zone (0 mm = EL 5121)

Table 3: CORA-2 and CORA-3 event sequences

CORA-2

- Up to	3000 s:	160 W power, 10 g/s argon flow
- from	3000 s:	power linearly increased from 5 kW to 28 kW (max.)
- from	3300 s:	from 10 g/s Ar changed to 4 g/s Ar plus 6 g/s steam
- at	4600 s:	steam flow turned off, argon flow increased to 10 g/s
- at	4800 s:	power (maximum) reduced to 50 %
- at	4900 s:	power shut off, cooldown

CORA-3

- Up to	3000 s:	400 W power, 6 g/s argon flow
- from	3000 s:	bundle power linearly increased from 6 to 60 kW
- from	3300 s:	onset of steam flow of 6 g/s in addition to 6 g/s Ar
- at	4000 s:	18 kW bundle power
- at	5050 s:	60 kW maximum bundle power reached
- at	5100 s:	reduction of electric power

Table 4: Analysis of Fragments Taken from Bundle CORA-2

Specimen	Description	Composition in wt.-%	Major Phases	Minor Phases
101	melt rivulet + fragment of thick scale		melt: (Zr, Cr, Fe, Ni) with U, (Zr, U, Ni, Fe), (Zr, Ni, U) with Fe, (Zr, U)O_2 scale: (Zr, U)O_2	
107*	pellet cladding interaction zone		melt decomposed into (U, Zr)O_2, (Zr, Sn), (Zr, Ni, U, Fe) with Cr	
106	oxidized cladding with metallic melt inclusions and melt droplets		melt: (Ni, Fe) with Mo, Sn, Cr, or (Ni, Fe, Mo) cladding: ZrO_2	precip. of (Ni, Fe, Zr) with Cr, Mo, Sn, scales of Cr-oxide with Al, Ti
109	melt lump with oxide scale	melt: Zr/U/Ni/Fe/Cr = 80/15/3/1/1	(Zr, U, O), dendritic	(U, Zr), ZrO_2, (Zr, Sn), (Zr, U, Ni, Fe) with Cr
102	melt drop + cladding	melt: Zr/Cr/U/Ni/Fe/Ti = 71/13/7/5/3/1 as oxides relations	melt: (Zr, U, Cr)-oxide cladding: (Zr, U)O_2	(Cr, Al)-oxide with Ti, (Ni, Fe, Sn) with Mo, W
104	shroud with melt zones in wall center		wall center: (Zr, U)O_2 with Cr melt agglomerate: (Zr, U)O_2	(Sn, Ni, Fe) with Mo, (Ni, Fe, Sn) with Mo (Sn, Ni) with Fe, Cr, (Cr, Fe, Ni, Mo) with Si, Sn, (Fe, Ni, Cr) with Sn, Mo, Si
105	melt in contact with fuel pellet and reacted cladding		melt: (Zr, U)O_2, in zones with Cr, Fe	(Sn, Ni), in zones (Cr, Fe, Al)-oxide
103	tube fragment + clad melt		melt: ZrO_2	(Sn, Ni) or (Sn, Ni) with Fe, (Fe, Cr, Zr, Si)-oxide, (Cr, Fe)-oxide
106	internally reacted annular pellet	ZrO_2/UO_2 = 80/20 ZrO_2/UO_2 = 60/40	melt: (Zr, U)O_2 contact zone: (Zr, U)O_2	W-rich interdendritic particles
107	seriously reacted pellet		(U, Zr)O_2	(Zr, U)O_2, (U, Zr), (Zr) or (Zr, Sn) or ZrO_2, locally (W, Zr) with Cr (as oxide?)

Element contents below 5% are indicated by "with"

Table 5: Analysis of Fragments Taken from Bundle CORA-3

Specimen	Description	Composition in wt.-%	Major Phases	Minor Phases
108	melt "pillow"		(Zr, O) with Sn, U, (U, Zr)O_2	(W, Zr), traces
	other melt pillow		(Zr, U, O), (Zr, U)O_2, two (U, Zr)O_2 compositions	(W, Zr), traces
	fragment		(Zr, U)O_2	(W), traces
107	piece of shroud with melt		shroud scale: ZrO_2	(Zr, O), (W, Zr, O) with Cr, Fe precipitates and eutectic
			once molten shroud: ZrO_2, (Zr, O)	(W, Zr) with Cr, Fe in metallic phase
			band of metallic melt: (Zr, Cu) with U, (Cu, Zr, O)	(Mo, Zr, W, O)
			attached metallic melt: (Cu, Zr, O), (Zr, Cu, U)	(U, Zr)O_2, (Mo, Zr, W, O)
106	melt at piece of shroud		(Zr, Cu) oxide to (Zr, U, Cu) oxide types, (U, Zr, Cu) oxide and (U, Cu, Zr) oxide types, (Zr, Cu, O), with U as well, ZrCu	(Zr, Sn, Cu) oxide, (Zr, Mo, Cu) oxide, (Zr, Sn, Cu, O), (Zr, W, Cu, O), (Cu, Zr, O) (W, Zr, O)
109	ceramic substrate with metallic melt	substrate: U/Zr/Cu = 64/22/14	(U, Zr)O_2	(Zr, O) with Cu, U, (Zr, Cu)
			melt: (Zr, Cu) or (Zr, Cu, O) with U, (Cu, Zr, O) with U, (Mo, Zr) with Cu, Cr, U	(Zr, Cu, O) and (Cu, Zr, O) or (Zr, Cu) oxide and (Cu,Zr) oxide (W, Mo) dendrites, (U,Zr)O_2 flakes, (Mo, Zr, O) and (Mo, W, Zr)

Specimen	Description	Composition in wt.-%	Major Phases	Minor Phases
101	pellet stack with TC remnant		pellet: UO_2	(U, Mo, W, O) with Zr, Cu, (Zr, Cu, Mo) with U or W, U, (Cu, Zr) with W, U, (Cu, Zr, O) with U
		external melt: Zr/Cu/Mo/U = 46/40/8/6	$(U, Zr)O_2$, (Zr, O), (Cu, Zr, O) with U, (Zr, Cu, U) (Mo, Zr, W) internal melt: UO_2 rectangular particles, lace of (Zr, Mo, Cu) with Ta, W, U, (Zr, Cu) or (Zr, Cu, Mo) with U or (Zr, Cu, Mo, W)	(Zr, Sn, Cu), dendrites of (U, Mo, O) or (U, Mo, Zr, O) with W, (Mo, Zr, Ta) with U, Cr, "asterisks" of (Ta, Mo) or (Ta, W, Mo)
102	internally reacted annular pellets		melted reaction zone: $(U, Zr)O_2$	(W), traces
103	cladding fragment		(Zr, U) O_2	(Sn, Ni)
104	cladding fragment		$(Zr, U)O_2$ to $(U, Zr)O_2$	(Sn, Ni, Cu)
105	melt drops		$(Zr, U)O_2$	(Sn, Ni) with Fe, (Cu) with Sn, ZrO_2 with Cu, prior (Zr, U, O)

Element contents below 5% are indicated by "with"

Table 6: Melts from Zircaloy-UO_2 interaction, CORA-2

Elevation	Description	Composition in wt.-%	Major Phases	Minor Phases
- 13 mm	separate lump of melt	Zr/U = 54/46	(Zr, U, O), (U, Zr)O_2	-
- 13 mm	small melt droplet	Zr/U/Inc = 62/33/5	(Zr, U, O), (U, Zr)O_2	seam of (Zr, U, Inc), (Zr, Sn, Ni)
- 13 mm	region of melt in spacer cross	Zr/U/Inc = 78/18/4	(see next table)	
268 mm	compact blockage	U/Zr = 54/46	(Zr, U, O), two diff. (U, Zr)O_2 compositions	(W, Zr, U, Cr)-oxide
480 mm	melt near pellet fragment	Zr/U = 71/29 (close) = 85/15 (apart)	(Zr, O), mostly with U, partly with Sn, as dendritic phase, (U, Zr) and (U, Zr)O_2 as interdendritic phases	(Zr, Sn)
480 mm	melt near pellet fragment	Zr/U/Sn + Fe = 66/31/3	(Zr, U, Sn) as dendritic, (U, Fe, Zr) as interdendritic phase	(Zr, Sn)
480 mm	reacted solid pellet surface (ceramic)	Zr/U = 60/40	(U, Zr)O_2, (Zr, U)O_2 with Zr/U = 1/1	
480 mm	melt between annular pellet and cladding (ceramic)	Zr/U = 68/32	(Zr, U)O_2	
870 mm	melt on solid pellet (metallic)	Zr/U = 89/11	primary (Zr, O), (Zr, O)-(U, Zr)O_2 eutectic	

Inc: Ni, Cr, Fe in relation roughly as in Inconel 718 (Ni/Cr/Fe = 76/16/8
Ni: Ni strongly enriched in comparison to Cr, Fe

Table 7: Residual metallics from Zircaloy cladding and Inconel spacer interaction, CORA-2

Elevation	Description	Composition in wt.-%	Major Phases	Minor Phases
- 13 mm	region of melt in spacer cross	Zr/Sn = 98/2	(Zr, O), (Zr, Sn)	
- 13 mm	other region of melt in spacer cross	Inc/Zr/U = 82/17/21		
- 13 mm	as above at contact to (Zr, U, O) melt region	Zr/Inc/U = 52/46/2 Zr/Inc/U = 66/25/9	1. pos.: (Zr, Inc), (Zr, Ni, U), (Zr, Ni, Sn,U) 2. pos.: (Zr, Inc, U), (Zr, Ni, U), (Zr, U)O_2 with some Inc	ZrO_2
268 mm	residual melt between cladding and fuel	Ni/Fe/Sn = 54/23/19	residual melt: (Inc) with Sn, (Sn, Ni) cladding: two diff. (Zr, U)O_2 compositions fuel pellet: (U, Zr)O_2	(Zr, U)O_2 with Inc (Zr/U = 1/1) (Zr, U)O_2 as above, (U, Cr, Zr) and (Cr, U, Zr, W) as oxide layers

Inc: Ni, Cr, Fe in relation roughly as in Inconel 718
Ni: Ni strongly enriched in comparison to Cr, Fe

Table 8: Compositional Analysis of Cross Sections through Bundle CORA-3

Cross Section	Description	Composition in wt.-%	Major Phases	Minor Phases
1 (20 mm)	solid pellet-cladding interaction zone	Zr/U/Ni/Sn/Fe/Cr = 71/21/3/2/2/1 (Zr/U/Ni/Fe/Cr/Sn = 47/44/5 /2/1/1):	zone near pellet: (Zr, O) with Sn, U central zone (Zr, O) with U, Sn, (U, Zr, O) - (Zr,O) eutectic zone near ZrO_2 scale: (Zr, O)	$(U, Zr)O_2$ (Zr, Sn), (Zr, U, Ni) with Fe, Cr
1	melt, alloyed with Inconel	Zr/U/Ni/Fe/Cr = 71/19/5/3/2 (average)	(Zr, O) with U, (Zr, U, O) or (U, Zr) band in melt: (Zr, O) with U	(Zr, Sn) aligned (U, Zr, O) particles
1	melt with some Inconel	Zr/U/Ni + Fe + Cr = 81/18/1 (average)		
b (67 to 184 mm)	"grey" zone of melt, lower half of blockage	Zr/U = 84/16 (average) metallic	(Zr, O), eutectic of (Zr, O), (U, Zr) and $(U, Zr)O_2$	
b	darker spot in "grey" zone of melt	Zr/U = 80/20 (average) ceramic	$(Zr, U)O_2$, (Zr, U, O) eutectically decomposed	(Zr, U, O) neddles in $(Zr, U)O_2$ grains
b	"dark" zone of melt, upper half of blockage	U/Zr = 82/18 (average) ceramic	$(U, Zr)O_2$ matrix, (Zr,U,O) as second phase	(Zr,U,O) precipitates
b	pellet surface contacting Mo, W, C contaminated "dark" melt	U/Zr/W = 86/12/2	UO_2	(Zr) with U, (U, Zr, Mo) oxide (Zr, Mo, W) with Cu, U
b	dishing between two solid pellets contacting "dark" melt		(U, Zr, Mo, O) dendrites, interdendritic (Zr, Cu) with Fe, U	(Zr, Sn, Cu), (U, Mo, Zr) oxide in contact with UO_2 pellet

Cross Section	Description	Composition in wt.-%	Major Phases	Minor Phases
b	"bright" melt, low position	Mo/W/Zr/U = 36/25/23/16		
b	"bright" melt, elevated position	U/Mo/W/Zr = 30/25/23/22	(Zr, W, U) oxide, (U, Mo, Zr, O), (Mo,Zr, W) contacting pellet surface zone: UO_2	angular (U, Zr, O) crystals (U, Mo, Zr, O), (Mo, Zr, W)
b	dissolution zone at dishing between two solid pellets	U/Zr/Cu = 49/37/14	(Cu, Zr, W) oxide, (Mo, Zr, W, O) with Cu, Cr, Sn	dendrites of (W, Mo, Cu, O)
14 (798 mm)	reaction zone of solid fuel pellet	Zr/Mo/Cu/U/W = 50/27/12/7/4	UO_2, (U, Zr)O_2 layer, (Zr, U)O_2 layer	(Mo, W, Zr) dendrites
14	melt, further apart of pellet	Cu/Mo/Zr/W/U = 48/25/21/3/3	(Cu) matrix with lances of (Cu, Zr,O) with U, angular crystals of (U, Zr, O) with Cu, (Zr) with Cu	dendrites of (Mo, W, Zr) with Cu
14	reaction zone near annular pellet	Zr/Mo/W/U = 69/17/8/6	(Zr, U)O_2	dendrites of (Mo, W) with Zr needles
14	reaction zone in between ZrO_2 and solid pellet		(Zr, U)O_2 layer, melt decomposed into (Cu, Zr, O) and (Zr, Cu) with U	dendrites of (Mo, W, Zr), (U, Cu, Zr) oxide

12. List of Figures

23. CORA-2, longitudinal section 136 mm - 253 mm

24. Longitudinal section of the test bundle CORA-2 depicting fuel rod failure and fragmentation

25. Damage profile of UO_2 pellets after test CORA-2 /9/

26. CORA-3; Posttest appearance at different orientations

27. Posttest view of bundle CORA-3 at 210° orientation (1)

28. Posttest view of bundle CORA-3 at 210° orientation (2)

29. Posttest view of bundle CORA-3 at 210° orientation (3)

30. Posttest view of bundle CORA-3 at 210° orientation (4)

31. Illustration of the posttest appearance of test bundle CORA-3

32. Profiles of the cross-sectional areas before and after tests CORA-2 and CORA-3 /9/

33. Damage profile of UO_2 pellets after test CORA-3 /9/

34. Re-solidified rivulet of melt from Zircaloy-Inconel-UO_2 interaction (specimen 101 of CORA-2)

35. Microstructures of solid UO_2 pellet and attached cladding fragment

36. Microstructures of annular UO_2 pellet, Zircaloy cladding and solidified melt

37. Particle size distribution (density function and sum) of the powder taken from observation window H 25

38. Particle size distribution (density function and sum) of the powder taken from observation window H 27

39. Particle size distribution (density function and sum) of the powder taken from observation window H 37

40. Multicomponent melt around the relocated fuel pellet stack fragment 101 of CORA-3, originating from interaction with heater and electrode materials

41. Typical part of shroud specimen 107 of CORA-3; Zry melt, contaminated by interference with heater and Inconel spacer materials

42. Prior melt of fragment 109 of CORA-3, formed by multicomponent interaction

43. CORA-2 bundle cross-section number 4 (-13 mm). The lower spacer grid acts as catcher for relocated solid and liquid materials.

44. Microstructures of CORA-2 bundle cross-section number 4 (-13 mm). The relocated (Zr, U, O) melt indicates a large amount of dissolved UO_2.

45. Microstructures of CORA-2 bundle cross-section number 4 (-13 mm). The relocated melts interact with the Zircaloy cladding and partially dissolve it.

46. CORA-2 bundle cross-section number 6 (268 mm). The relocated once molten material forms the large blockage of this elevation.

47. Microstructures of CORA bundle 2 vertical cross-section A (axial elevation 136-253 mm). Various solidified (Zr,U,O) melts containing different quantities of dissolved UO_2.

48. Microstructures of CORA bundle 2 vertical cross-section A. Details of Figure 47.

49. CORA-2 bundle cross-section number 6 (268 mm). Strong UO_2 attack by molten Zircaloy.

50. Formation of voids due to relocation of molten cladding (see. Fig. 68).

51. Microstructures of CORA-2 bundle cross-section number 6 (268 mm)

52. Microstructures of CORA-2 bundle cross-section number 6 (268 mm). Accumulation of rubble.

53. Microstructures of CORA bundle 2 vertical cross-section A (axial elevation 136-253 mm). Onset of UO_2 fuel dissolution by molten Zircaloy.

54. CORA-2 bundle cross-section number 8 (298 mm). Strong Zircaloy cladding disintegration.

55. Microstructures of CORA-2 bundle cross-section number 8 (298 mm). Strong UO_2 fuel dissolution by molten Zircaloy.

56. Microstructures of CORA-2 bundle cross-section number 8 (298 mm). Attack of the UO_2 and ZrO_2 on cladding surface by molten Zircaloy.

57. Microstructures of CORA-2 bundle cross-section number 8 (298 mm). Crack pattern in UO_2 pellets.

58. CORA-2 bundle cross-section number 12 (480 mm). Strong damage of the fuel rods

59. Microstructures of CORA-2 bundle cross-section12 (480 mm). Relocation of molten Zircaloy and "liquefied" UO_2; formation of large voids.

60. Microstructures of CORA-2 bundle cross-section12 (480 mm). Oxidation of the Zircaloy by steam and attack of the UO_2 by the Zircaloy.

61. CORA-2 bundle cross-section number 18 (870 mm). Strong damage of the fuel rods and spacer grid.

62. Microstructures of CORA-2 bundle cross-section 18 (870 mm). Details of Figure 61.

63. Integral analysis and microstructure of melt lump at lower spacer grid elevation, resulting from Zry-UO_2 interaction

64. Integral analysis of melt droplet, alloyed with some Inconel

65. Phase analysis of Inconel-alloyed melt droplet

66. Global analysis of melt at Zry spacer grid cross; agglomerate of three different types

67. Integral analysis of melt of (Inc, Zr) type near contact to attached melt of (Zr, U, O) type

68. Residual metallic melt in between attacked fuel pellet and transformed cladding (see Fig. 50).

69. Typical melt from Zry-UO_2 interaction, decomposed into (Zr,O), (U, Zr), (U, Zr)O_2 and (Zr, Sn).

70. Heated rod after internal and external fuel dissolution by subsequently oxidized metallic melts (see Fig. 59)

71. Relocated melt and dissolution of embedded fuel rod at cross section 1 of CORA-3

72. In situ Zry-UO_2 interaction plus interference with Inconel-containing melt at cross section 1 of CORA-3

73. Melt, containing Inconel spacer material after penetration between cladding and pellet of a partially embedded fuel rod

74. Zr-rich ("gray") melt of (Zr, U, O) type and pellet attack at longitudinal section b of CORA-3

75. U-rich ("dark") melt of (Zr, U, O) type and pellet attack at longitudinal section b of CORA-3

76. Mo- and W-rich ("bright") melt, from interference with heater rod electrode, and pellet attack at longitudinal section b of CORA-3

77. Analysis of melt from interference with material of heater rod and electrode. Identification of UO_2 dissolution and (U, Zr, O) growth.

78. Macrograph of cross section 14 (798 mm) of CORA-3

79. Late melt formation from interference with heater and electrode materials

80. High-temperature oxidation of Zircaloy-4 cladding material in steam; ZrO_2 scale growth kinetics (600-1600°C, 2 min-25h)

81. Comparison of the growth rate equations for reaction systems UO_2/Zircaloy, (Ar + 25 vol.% O_2)/Zircaloy and steam/Zircaloy

82. Microstructure of molten UO_2/Zr reference specimens for four different initial UO_2 concentrations. Depending on the UO_2 concentration either two metallic or two metallic and one ceramic phase form on cooldown.

83. Dissolution rates for solid UO_2 and solid ZrO_2 by molten Zircaloy-4

84. Reaction rates for the system Inconel 718/Zircaloy-4. Influence of oxide layers on the Zircaloy surface.

Appendix:

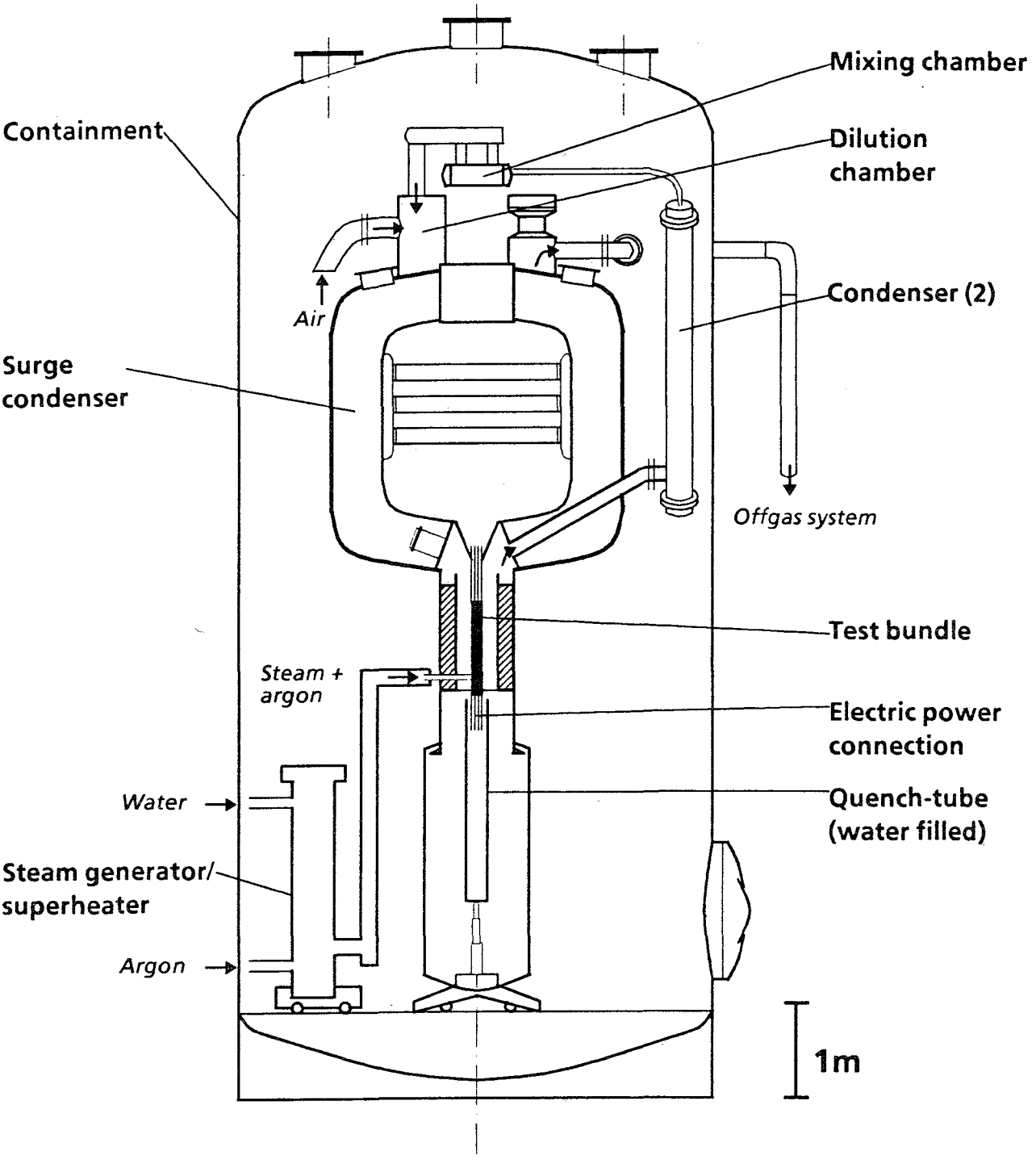

Fig. 1. SFD test facility CORA, main components

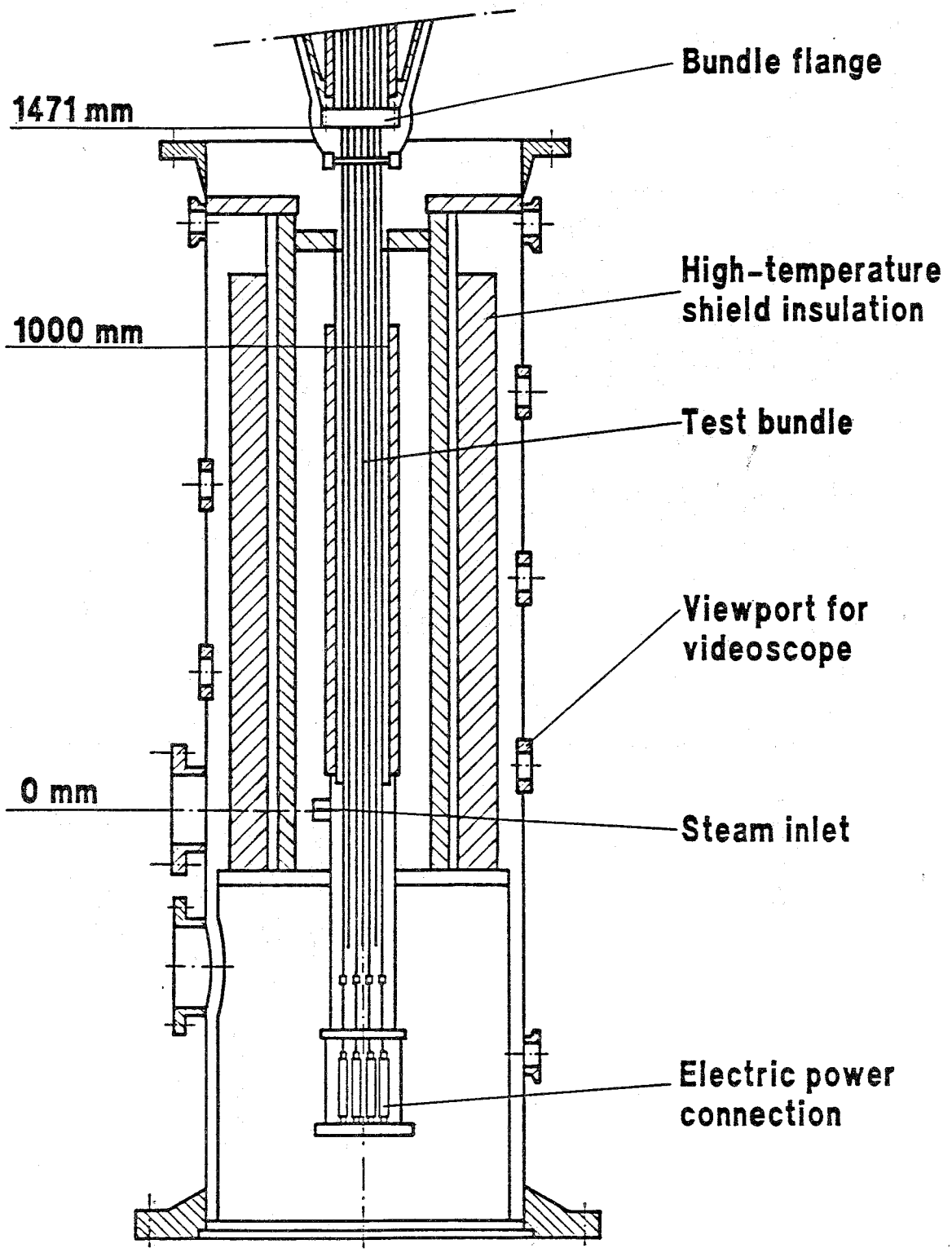

Fig. 2. CORA test section

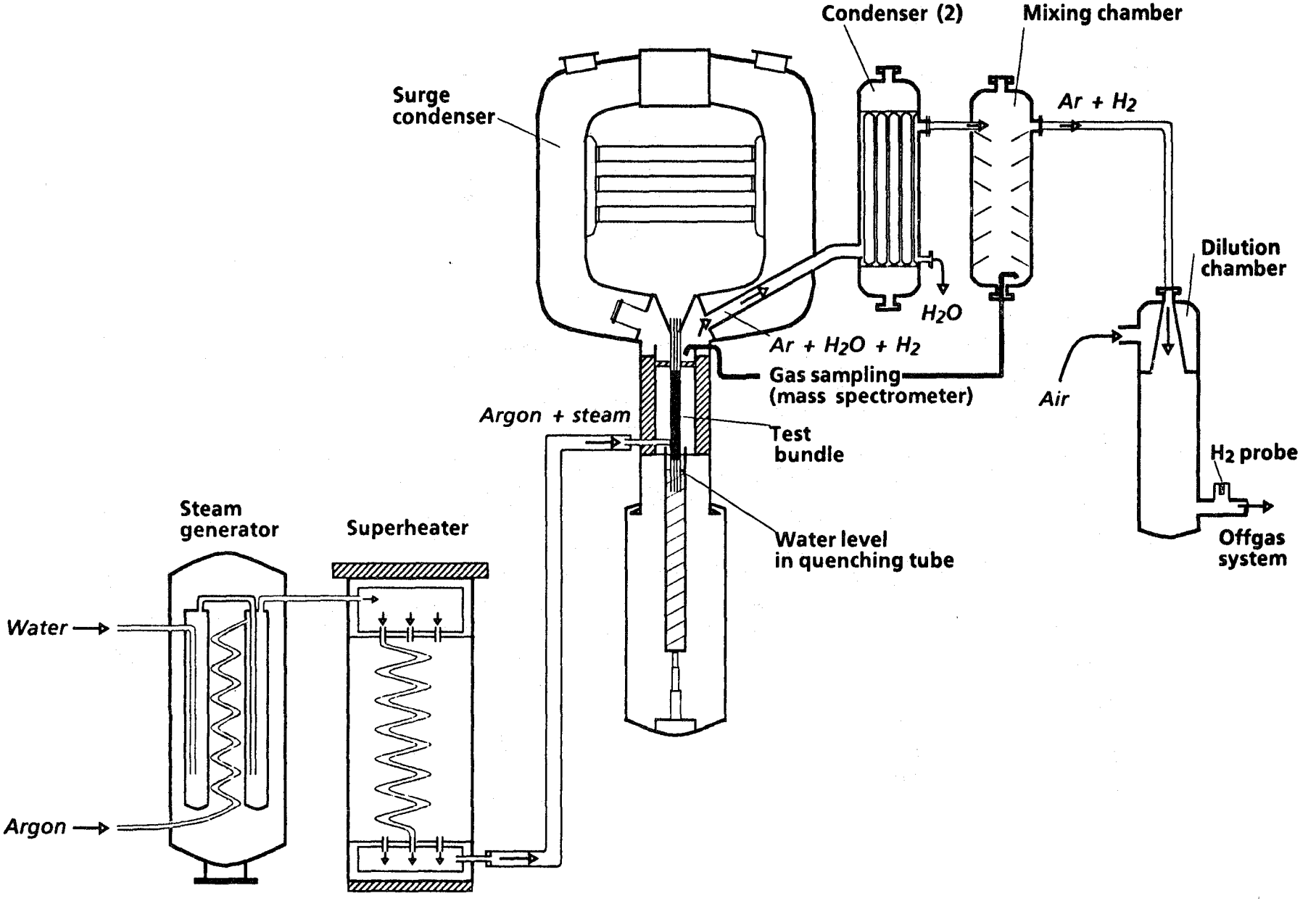

Fig. 3. SFD-Test facility, simplified flow diagram

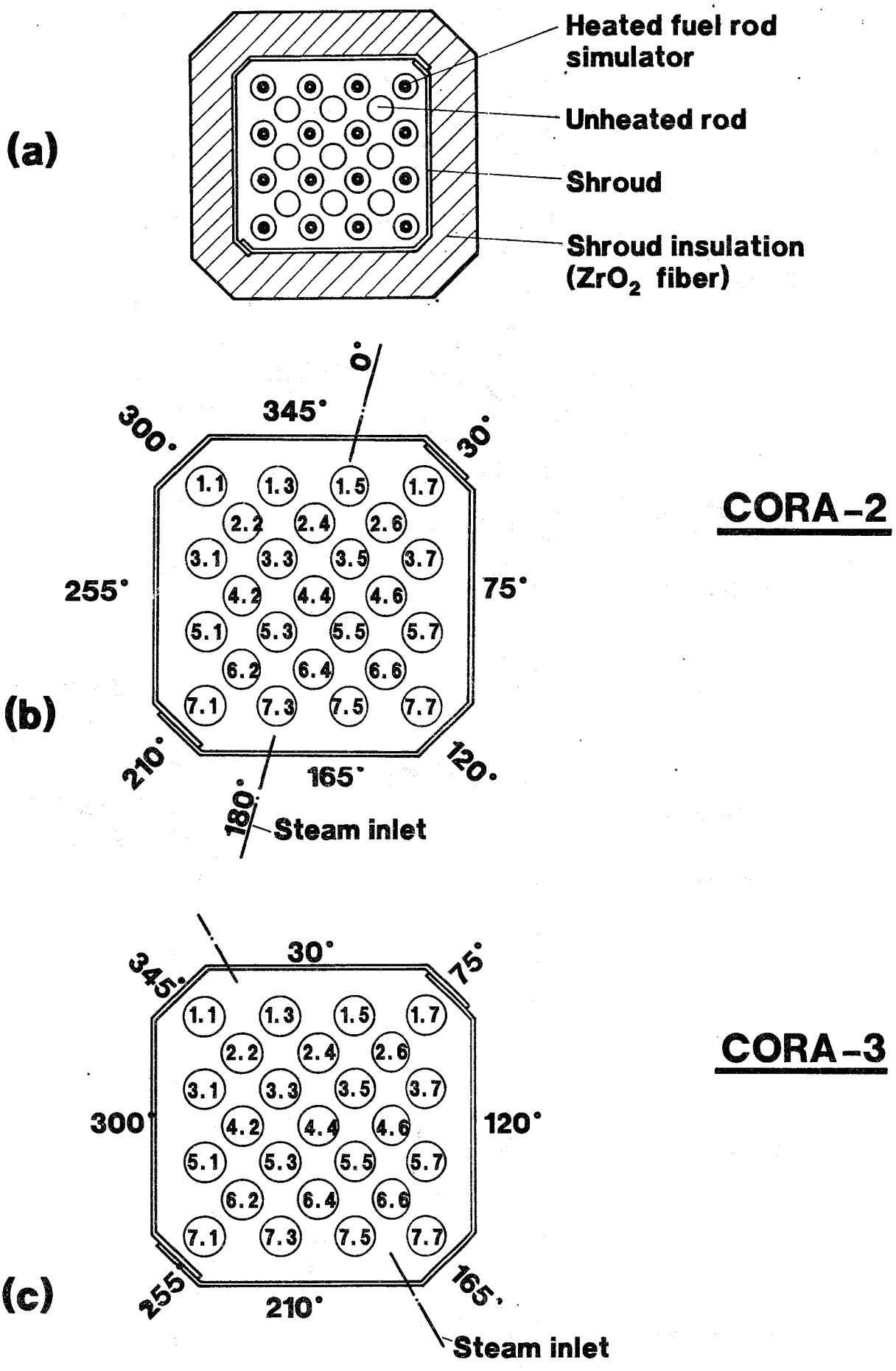

Fig. 4. Test rod arrangement (a) and rod designation for CORA-2 (b) and CORA-3 (c)

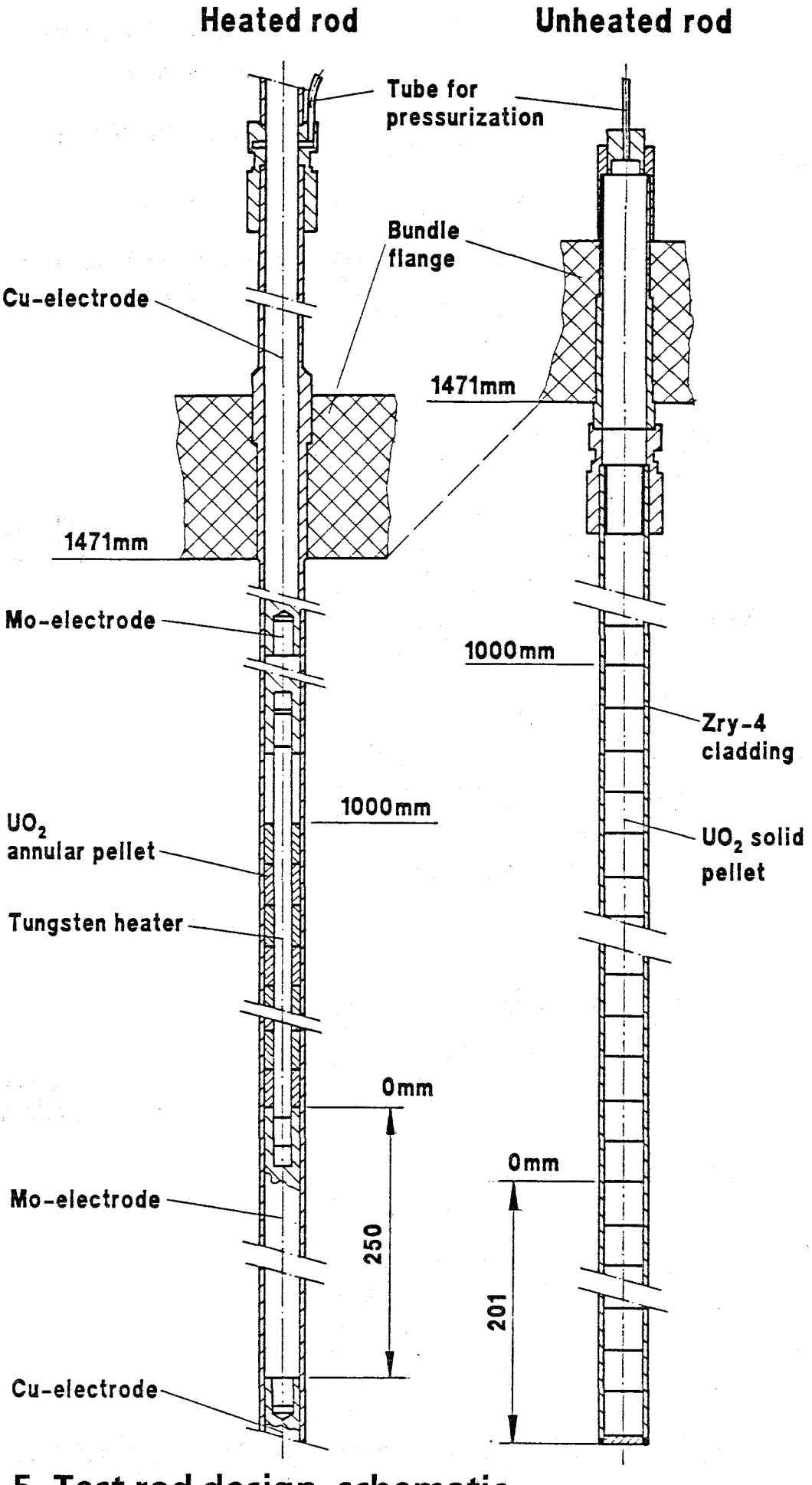

Fig. 5. Test rod design, schematic

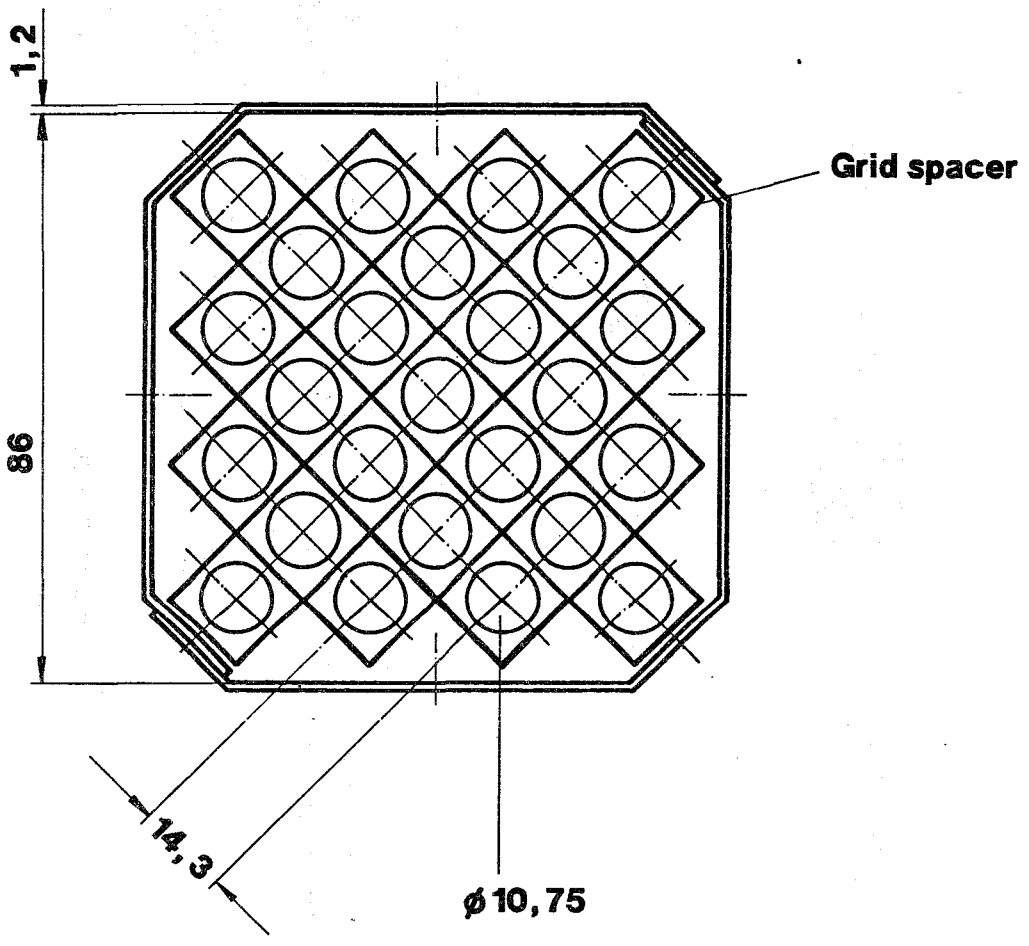

Fig. 6. Cross section of the CORA bundle with shroud and grid spacer

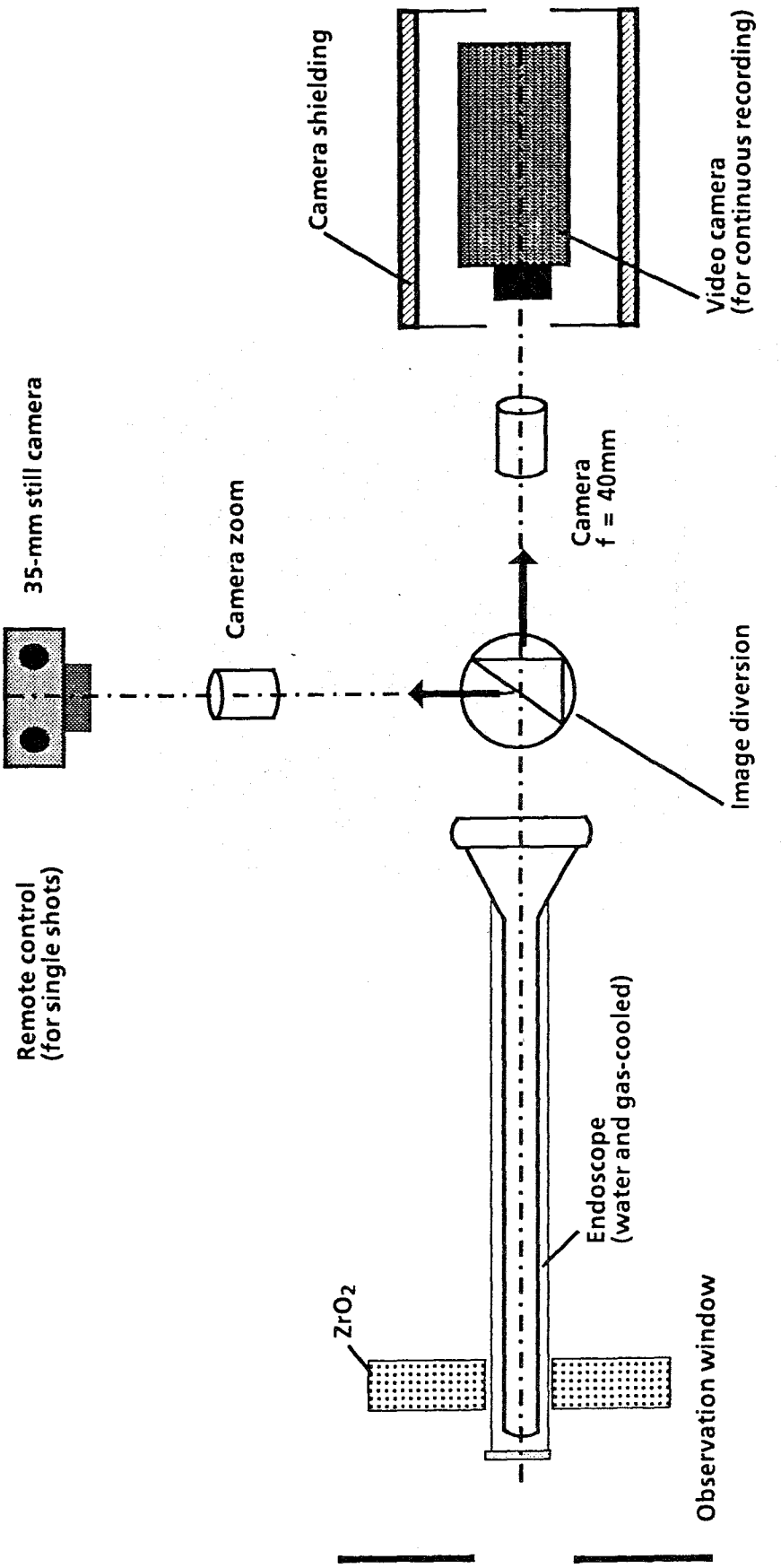

Fig. 7. Videoscope system for the CORA test bundle, schematic

(a)

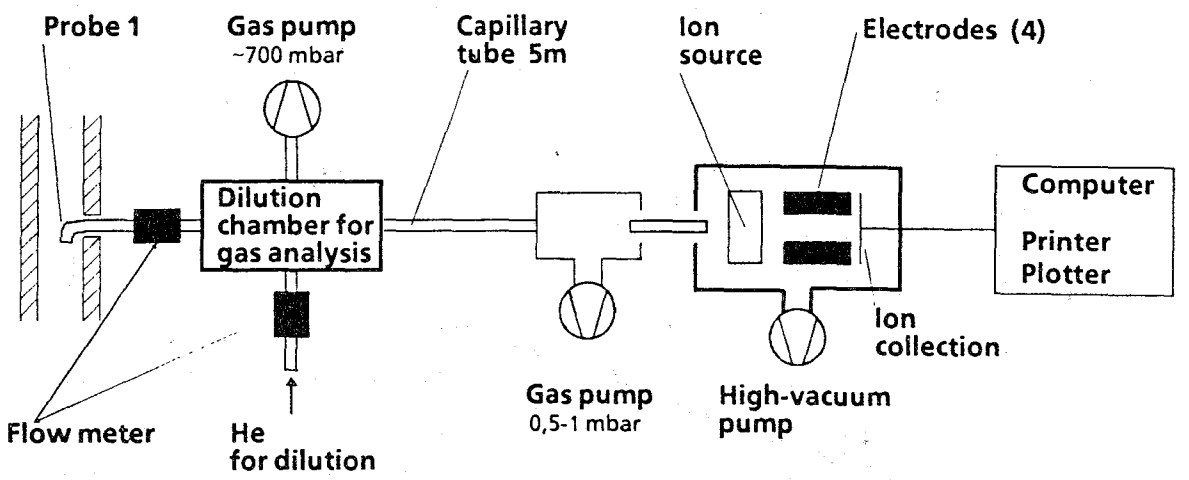

(b)

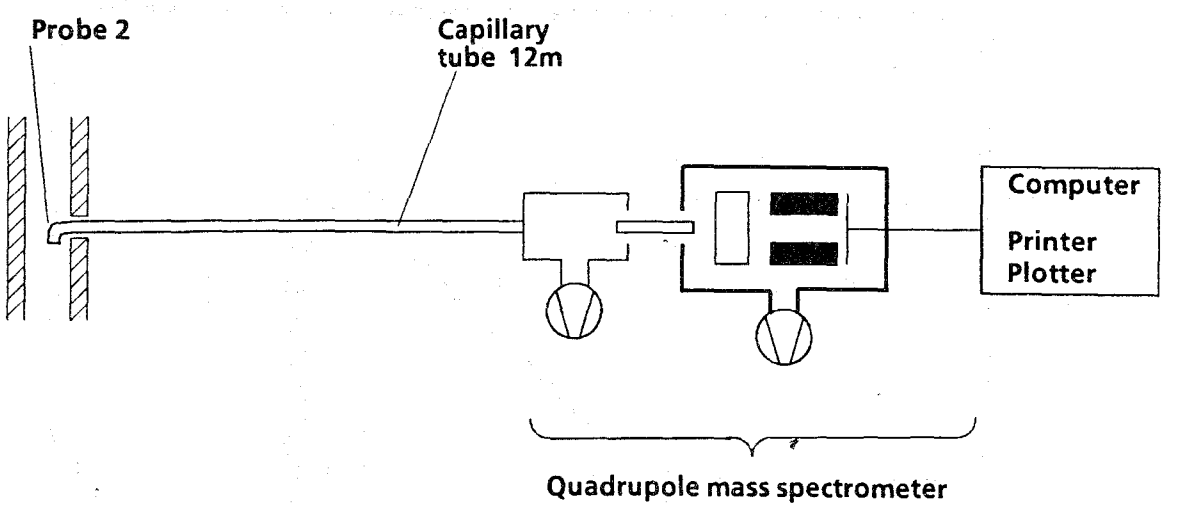

Location (a): Outlet of test section

Location (b): Mixing chamber

Fig. 8. Hydrogen probing at two locations of the CORA facility (see also Fig. 3). Gas analyses are performed by quadrupole mass spectrometer

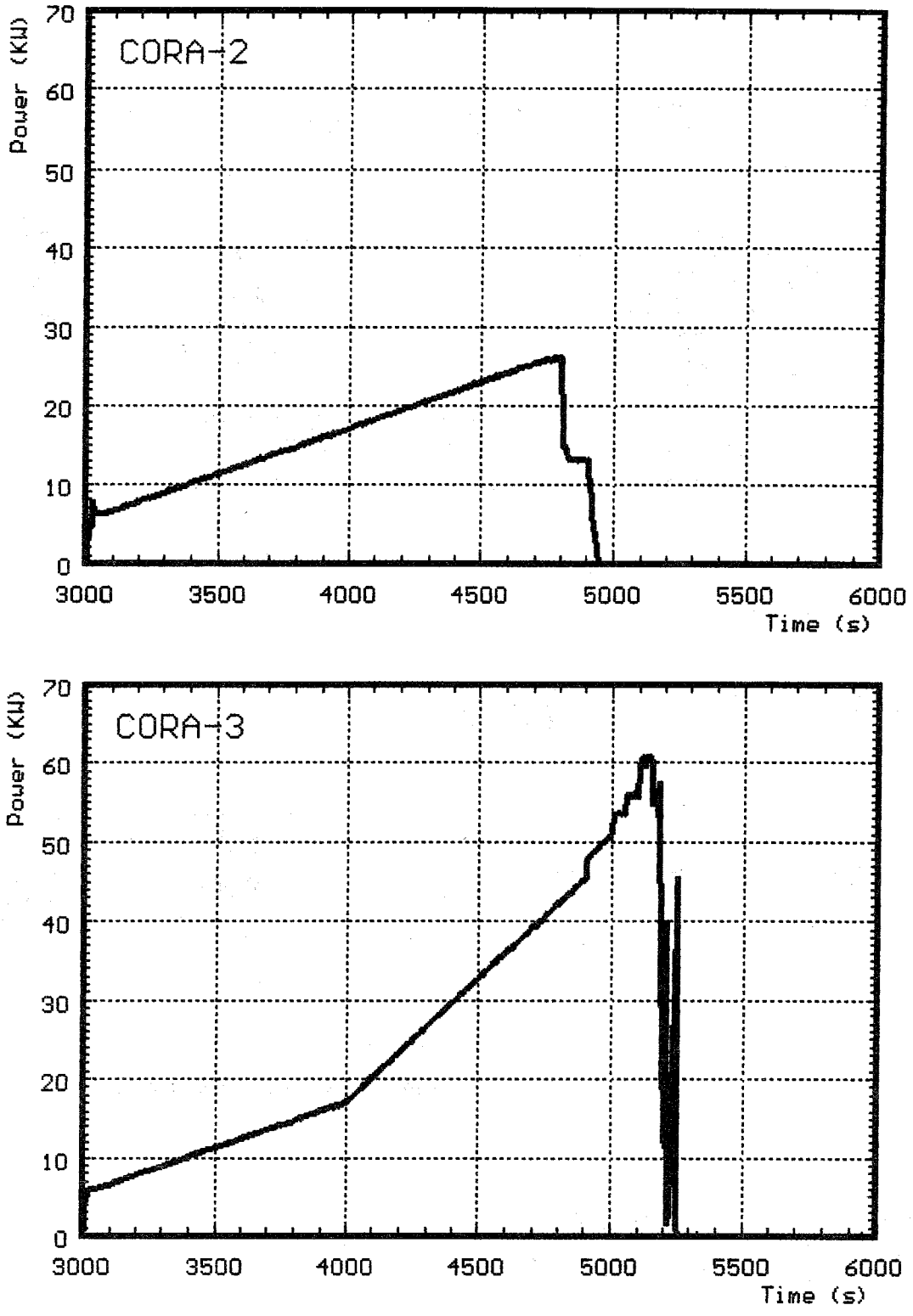

Fig. 9. Power input histories of tests CORA-2 and CORA-3

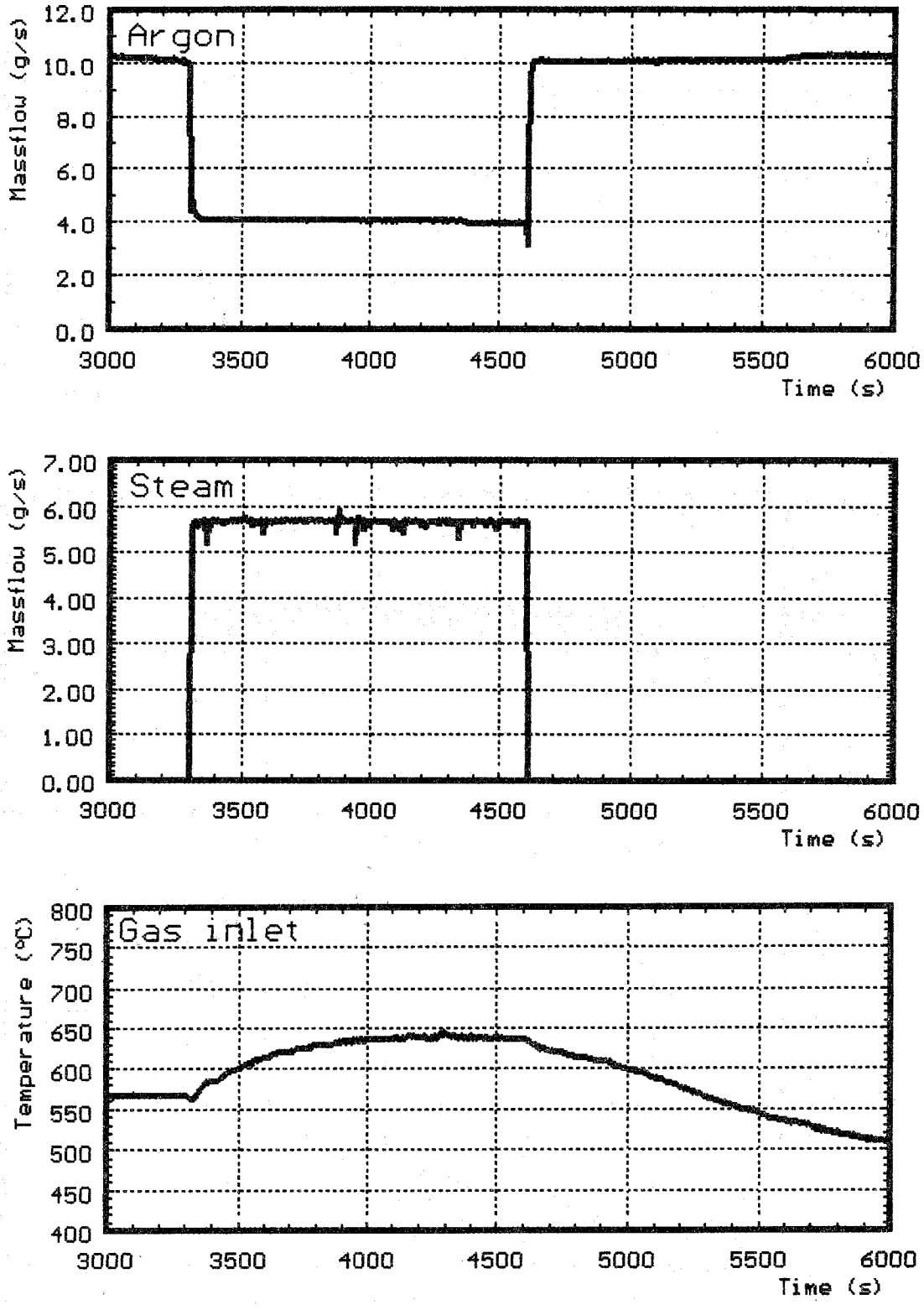

Fig. 10. Argon flow rate, steam flow rate (water injection into evaporator) and gas inlet temperature during test CORA-2

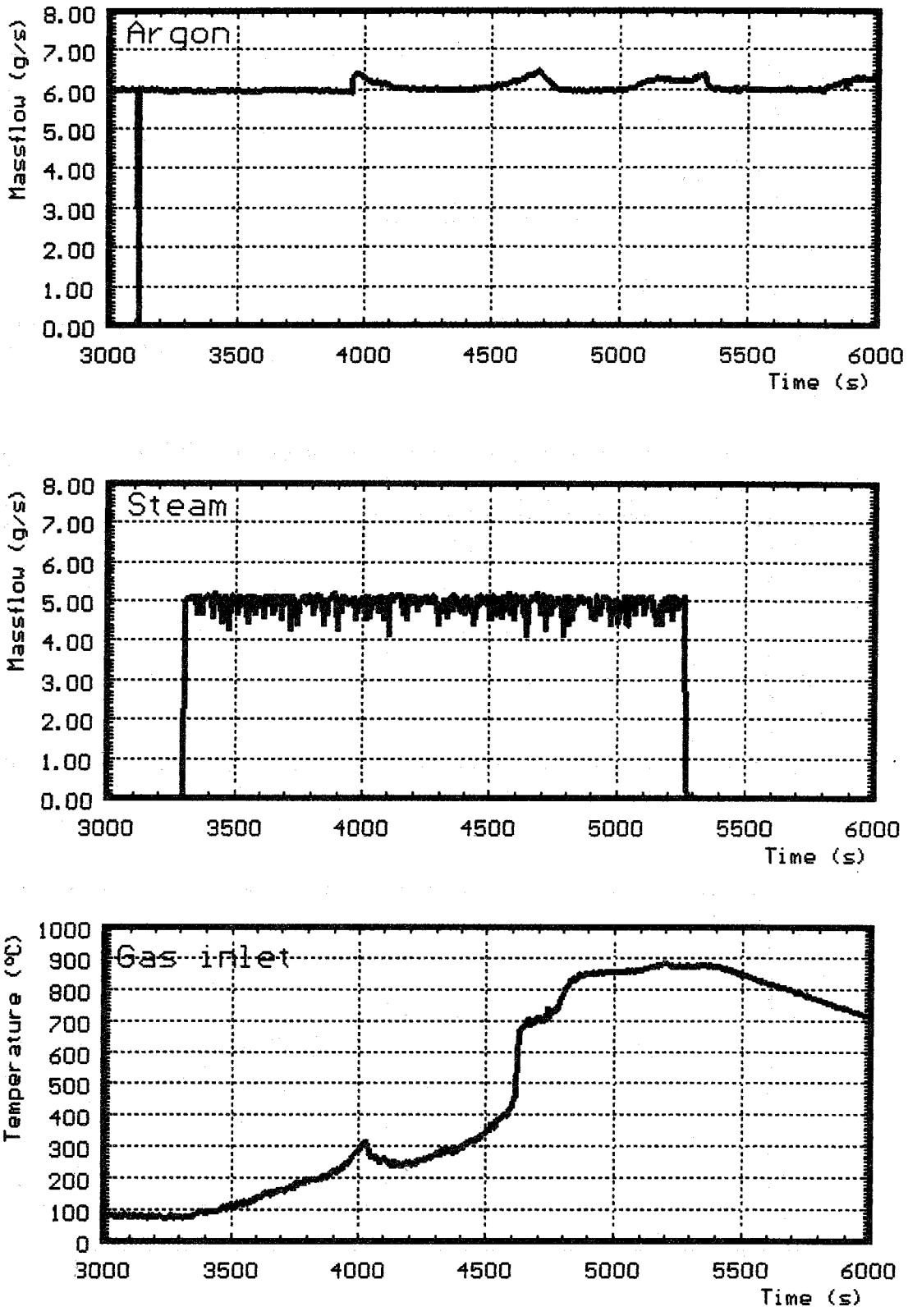

Fig. 11. Argon flow rate, steam flow rate (water injection into evaporator) and gas inlet temperature during test CORA-3

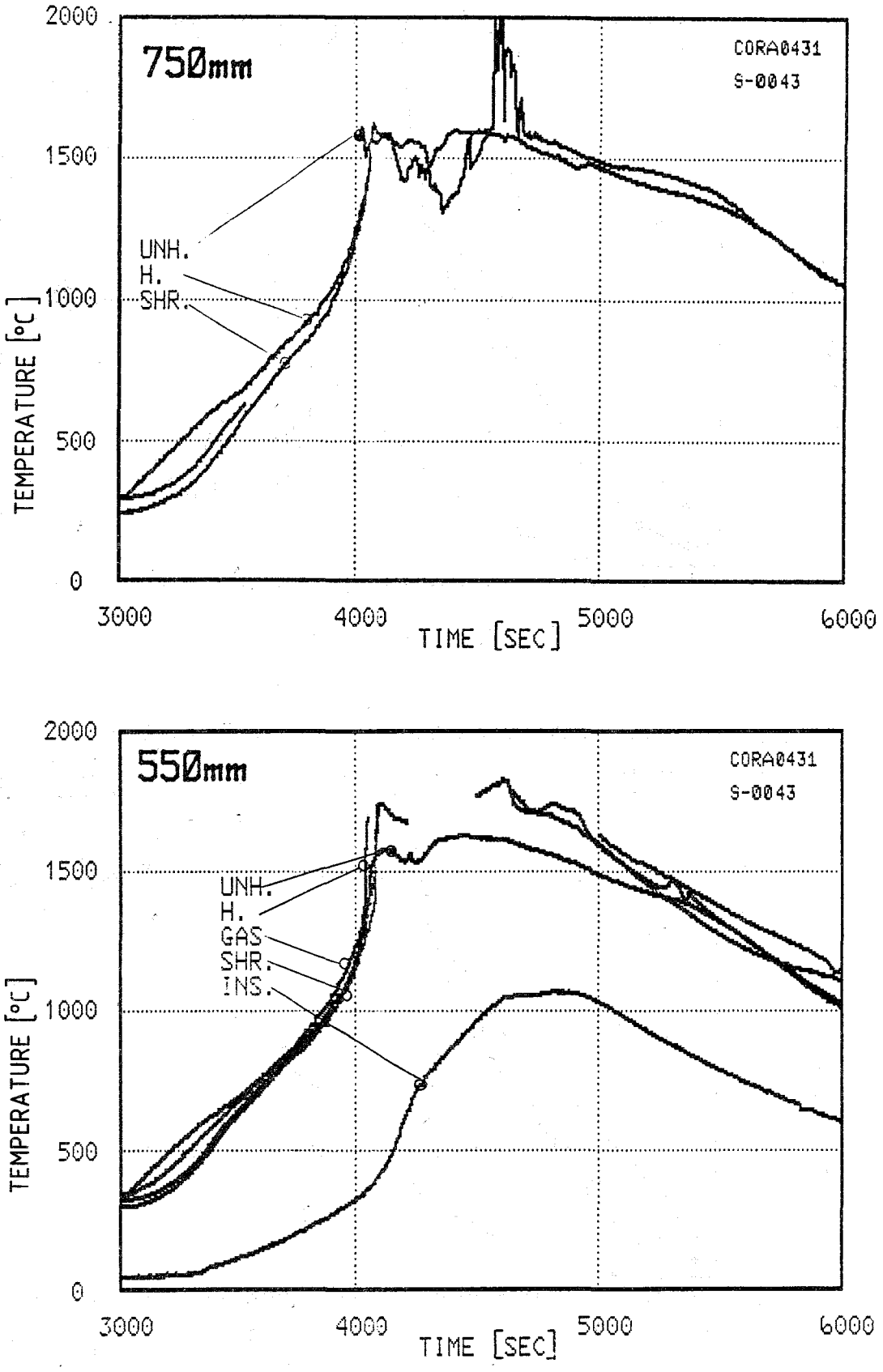

Fig. 12. Temperatures during test CORA-2 at 500 mm and 750 mm elevation. Temperatures of heated (H) and unheated rod (UNH), atmosphere (gas), shroud (SHR), and outer surface of shroud insulation (INS)

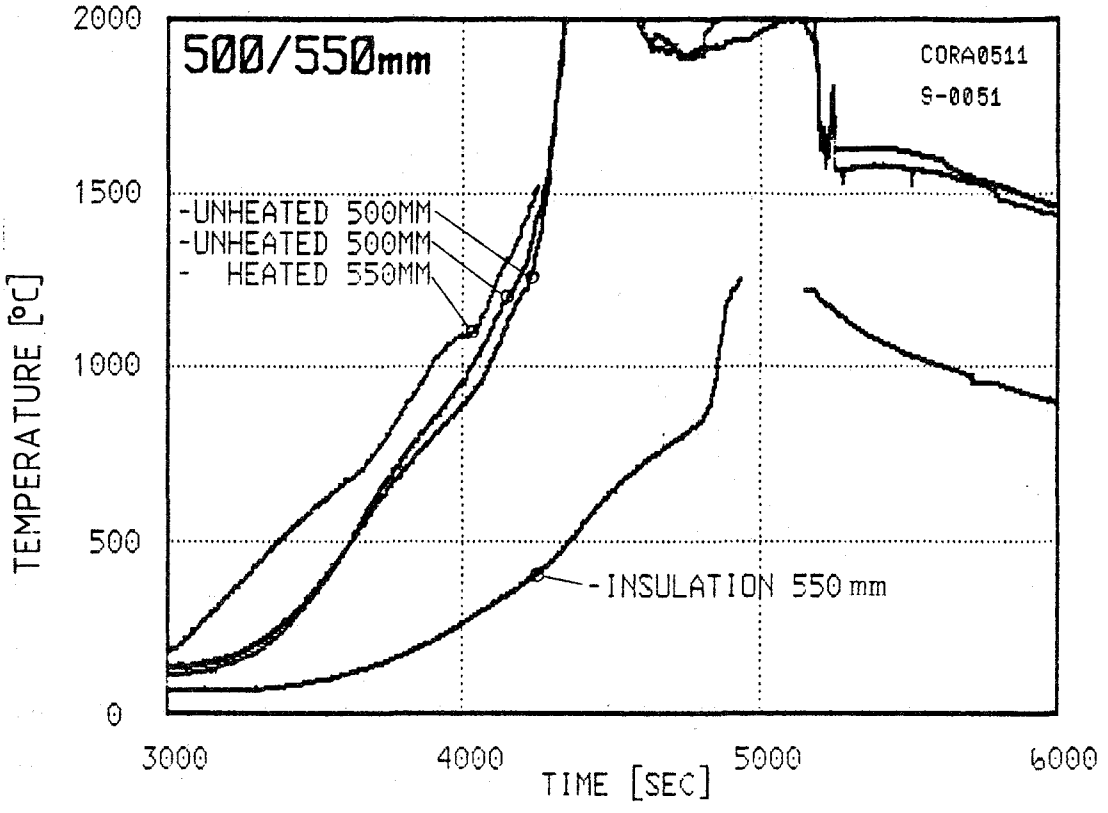

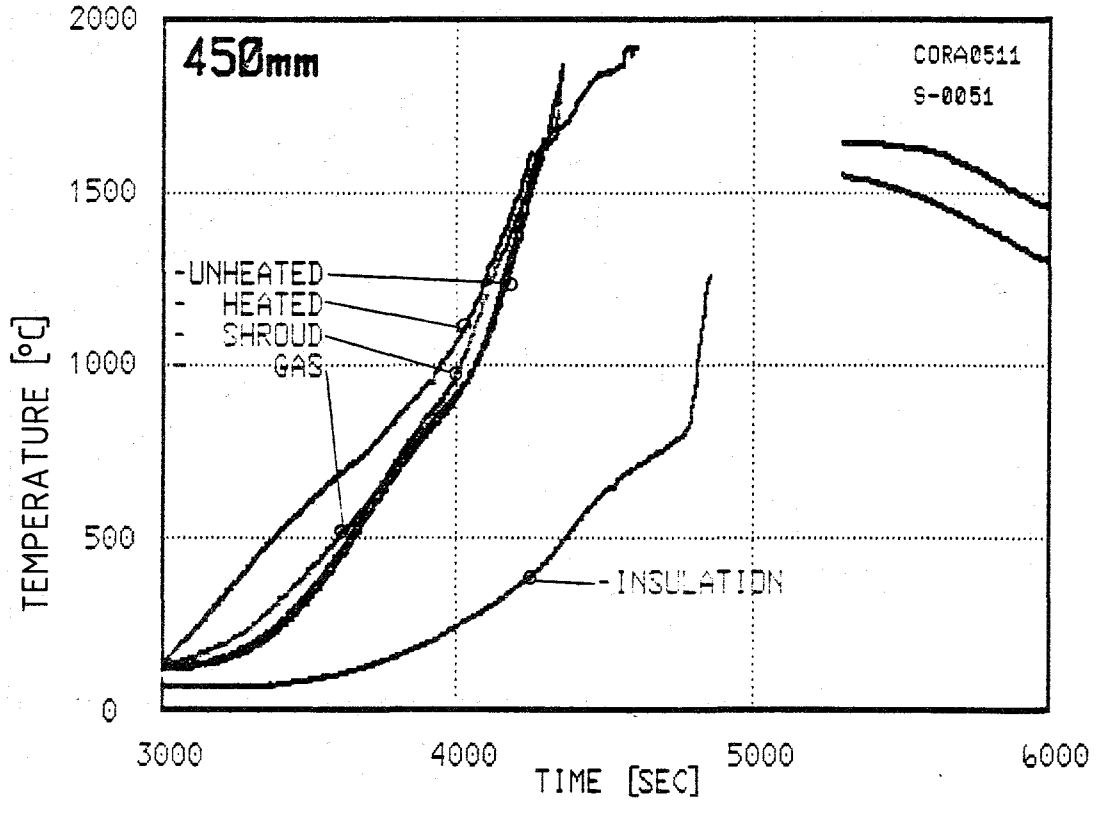

Fig. 13. Temperatures measured during test CORA-3 at 450 mm and 550 mm elevation

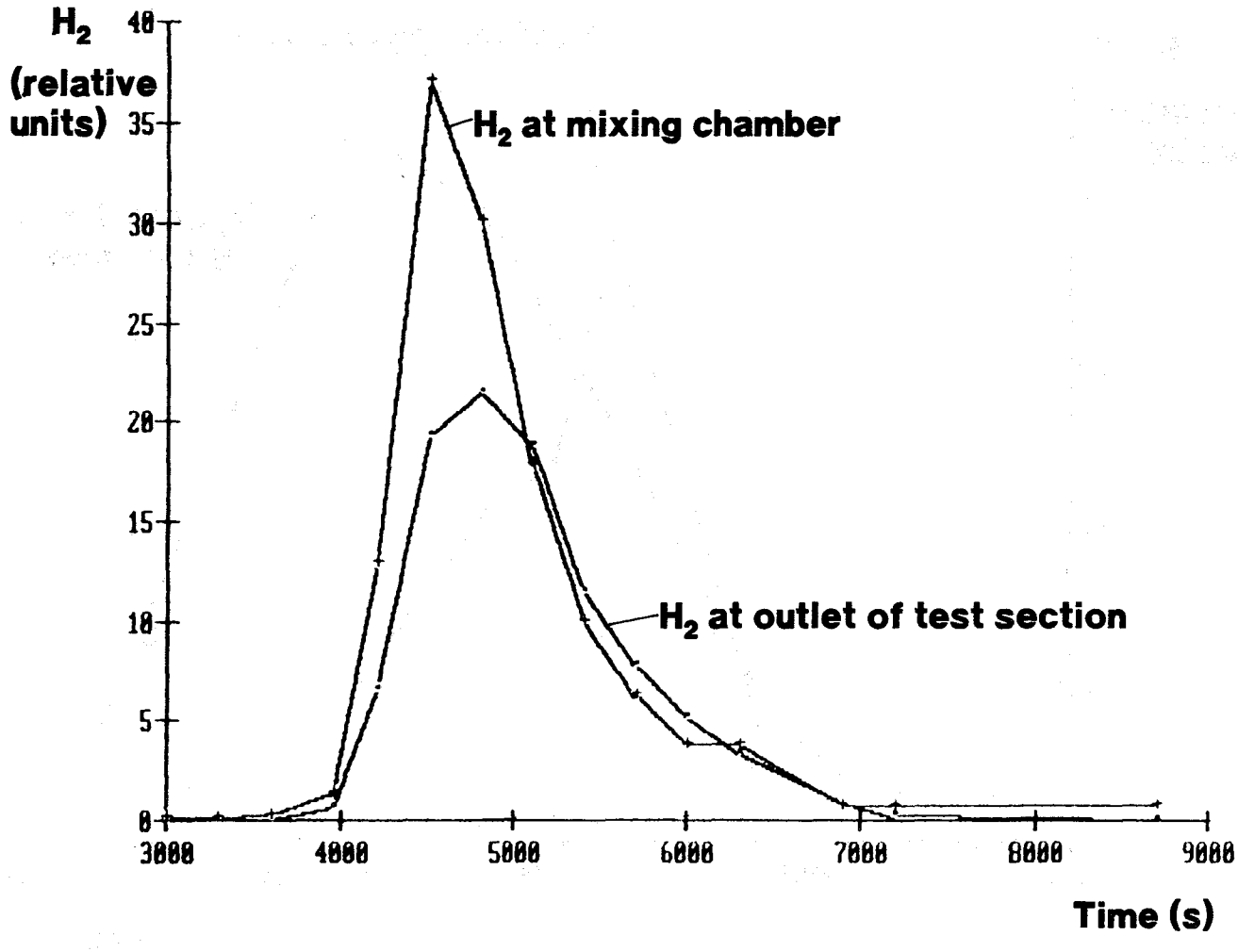

Fig. 14. Hydrogen generation rate at two different locations during test CORA-2 /8/

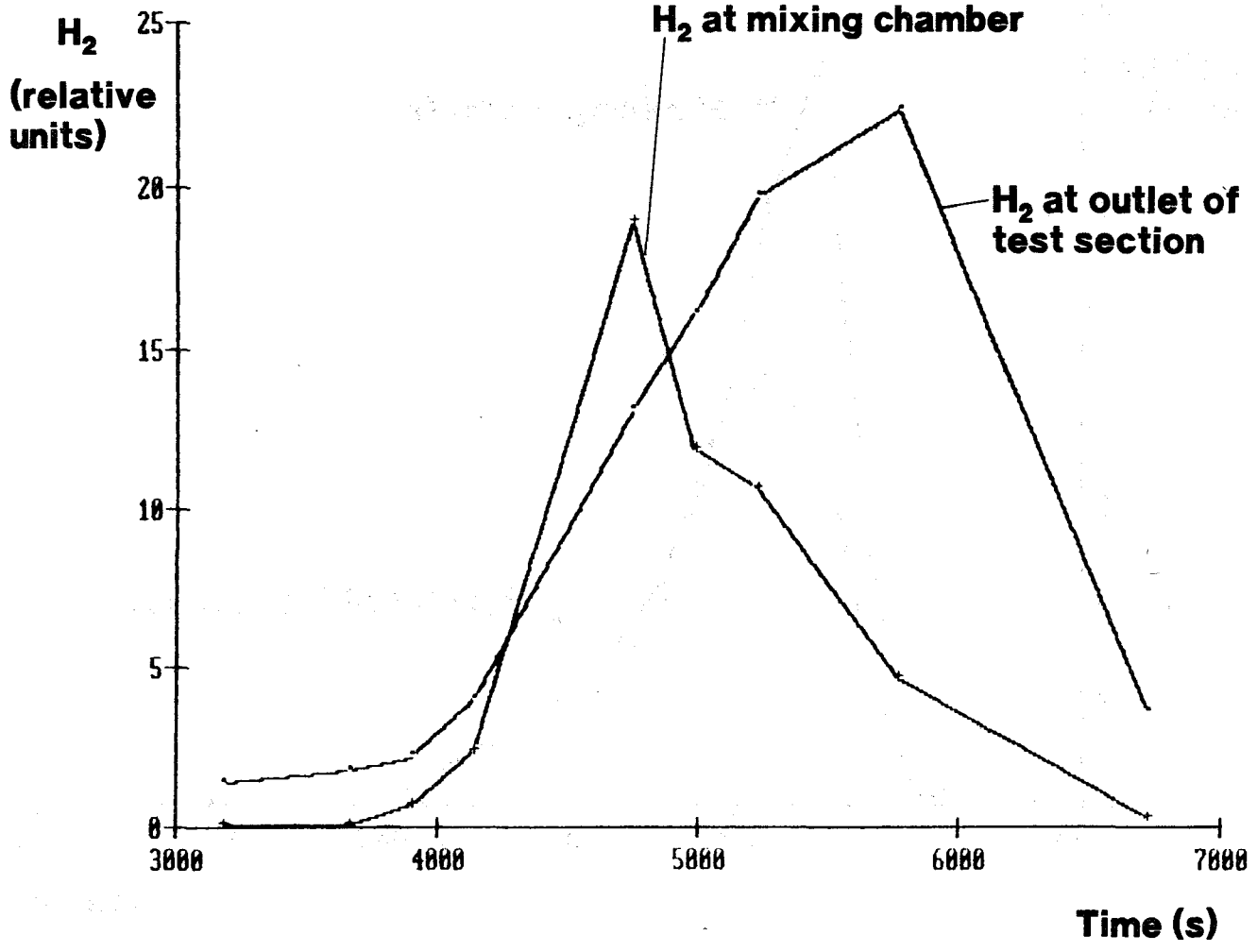

Fig. 15. Hydrogen generation rate at two different locations during test CORA-3 /8/

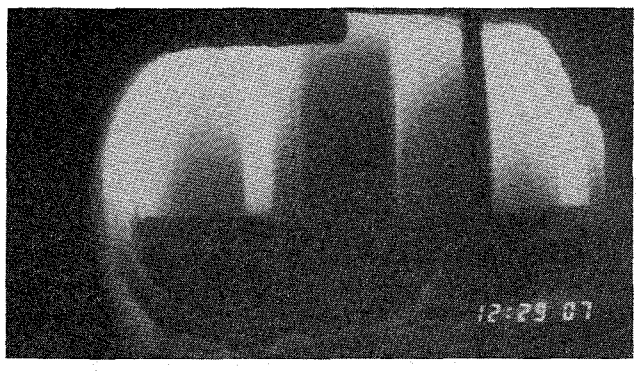

4147 sec

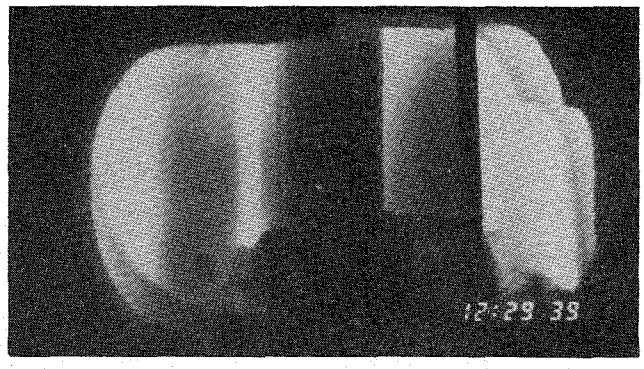

4179 sec

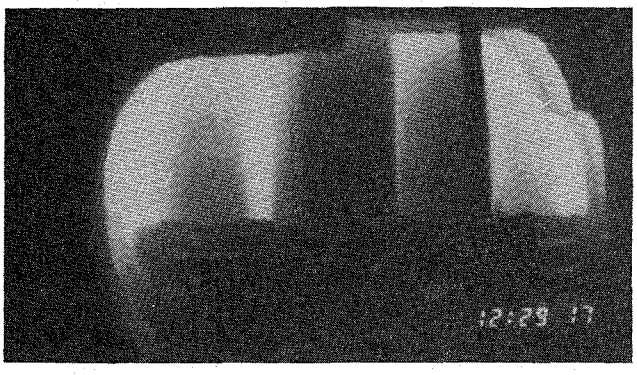

4157 sec

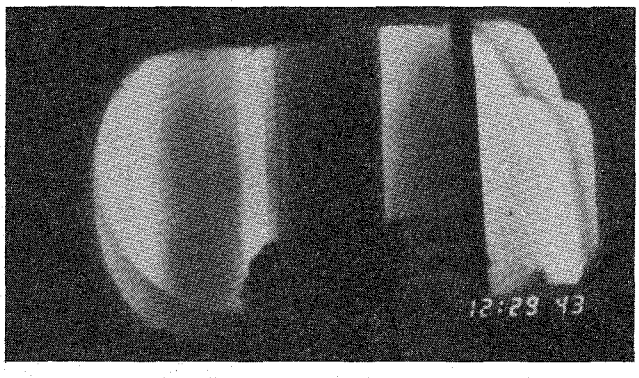

4183 sec

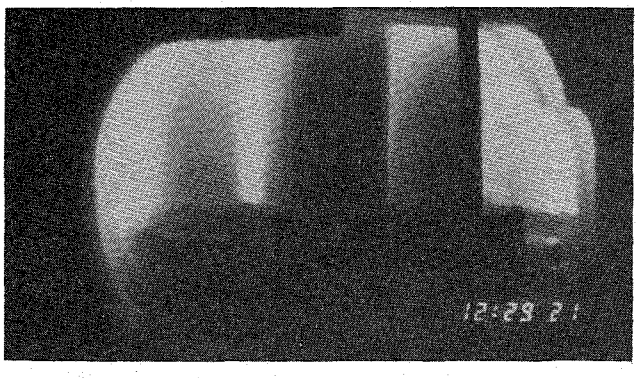

4161 sec

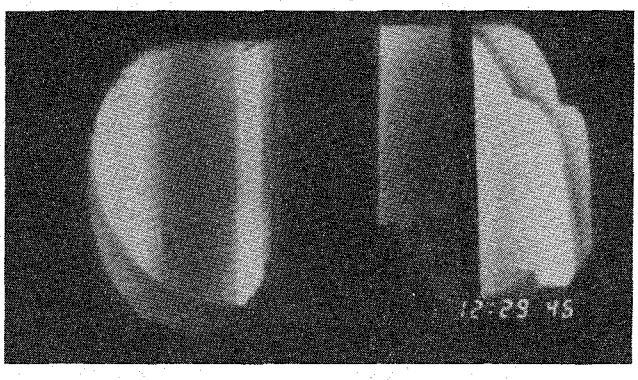

4186 sec

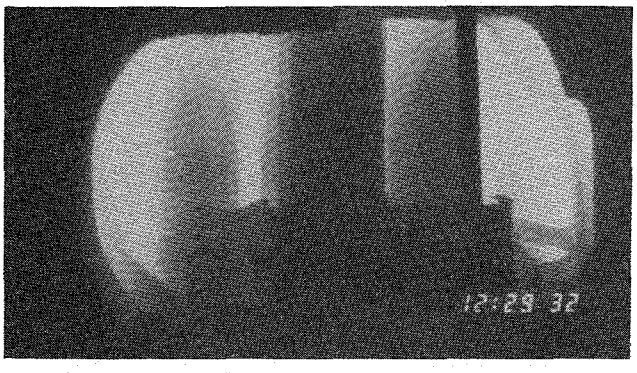

4172 sec

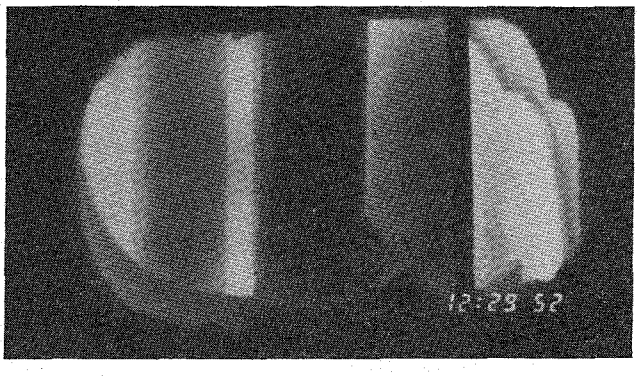

4192 sec

Fig. 16. Melting of the Inconel spacer during test CORA-2 seen by the videoscope at 500 mm elevation

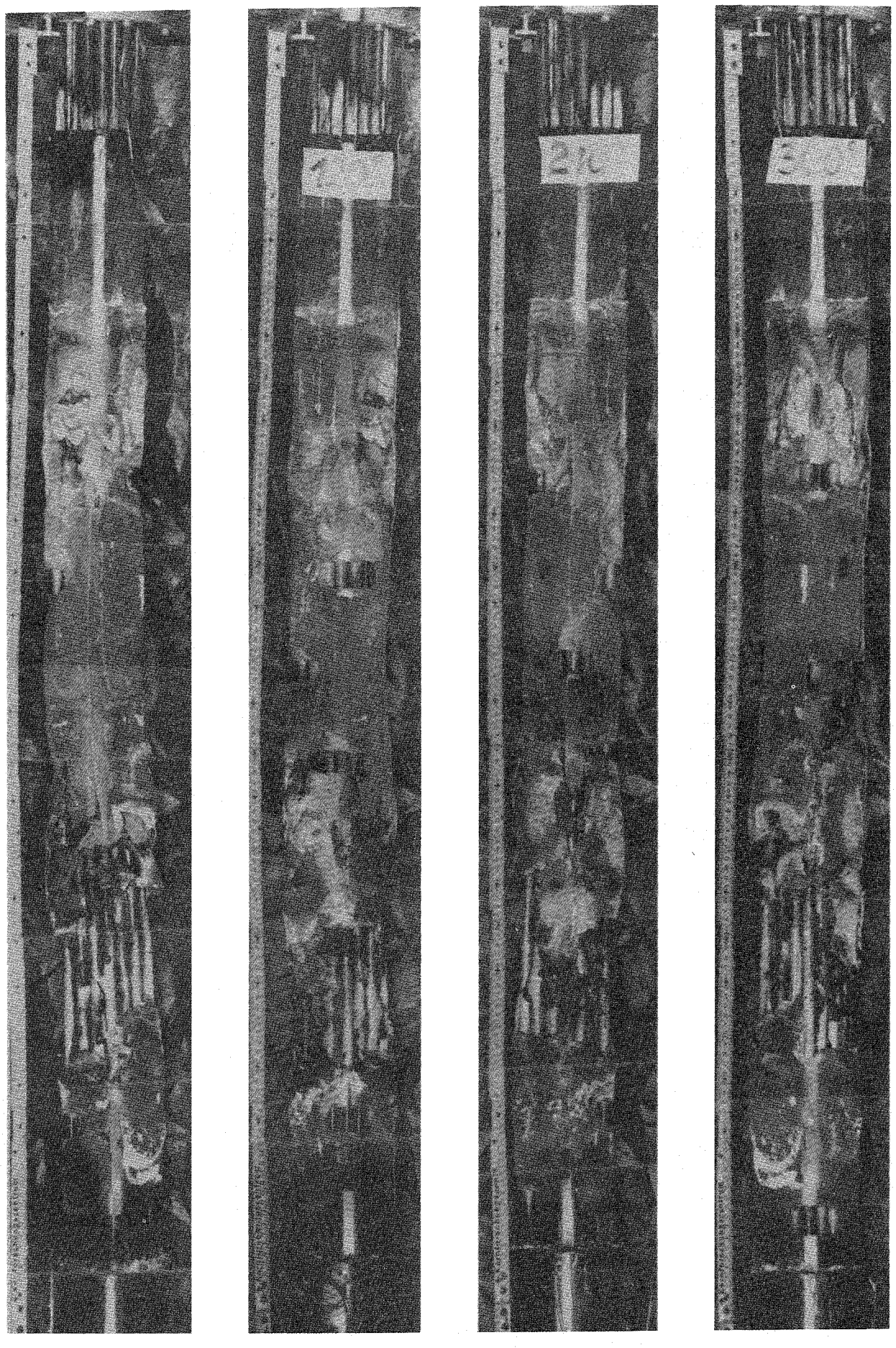

Fig. 17. Posttest appearance of CORA-2 bundle

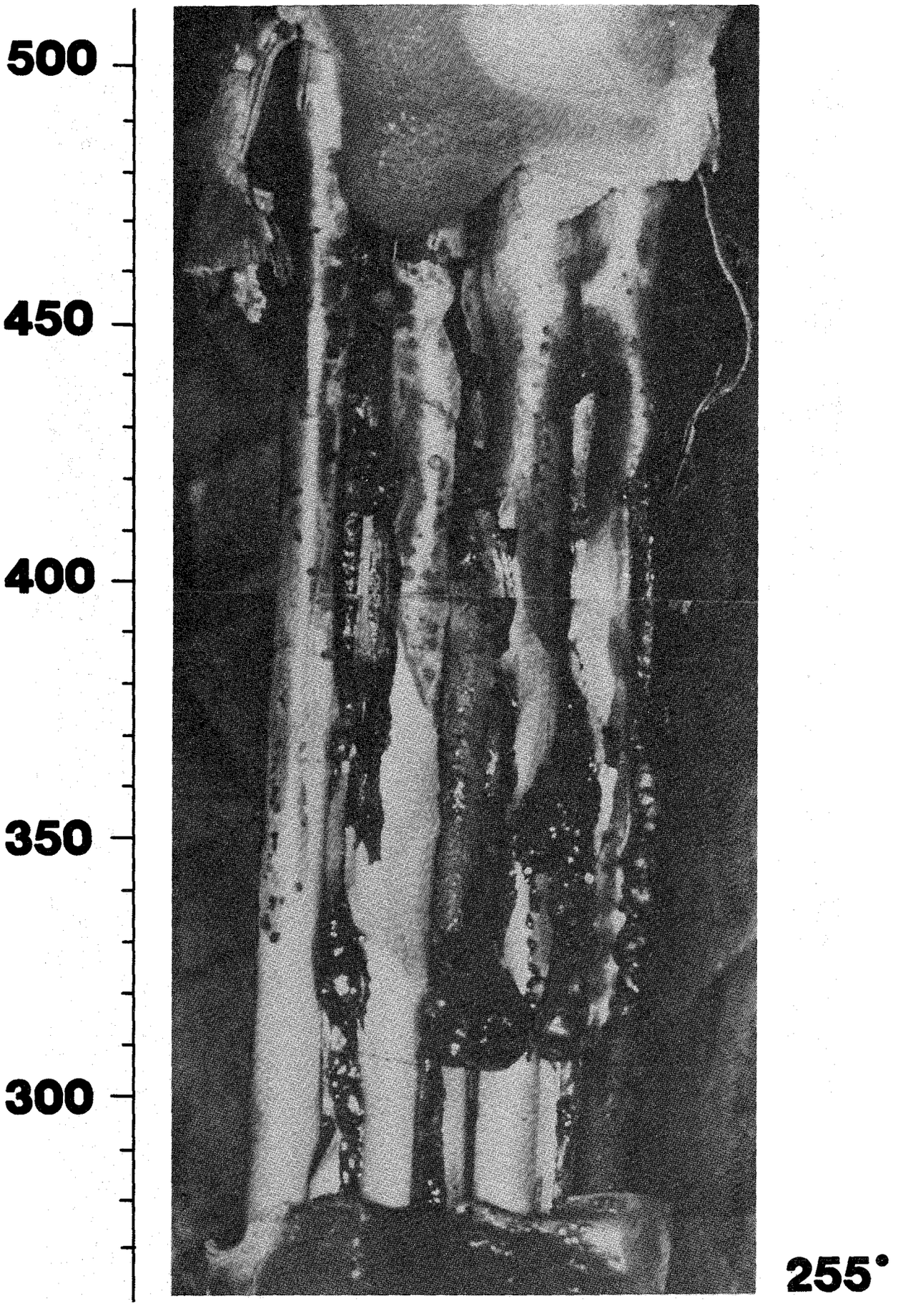

Fig. 18. Melt formation in the lower part of test bundle CORA-2

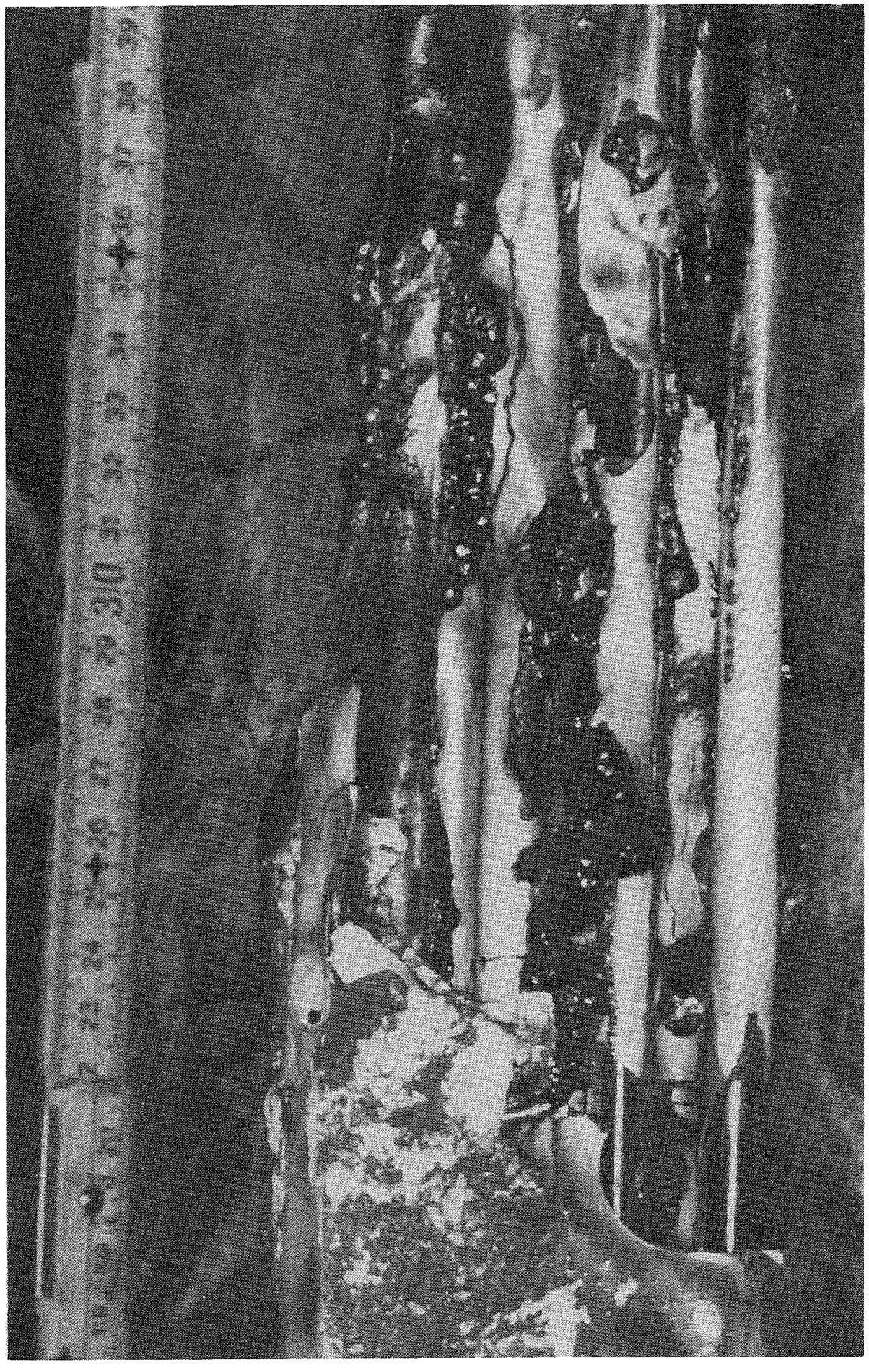

Fig. 19. Posttest appearance ot test bundle CORA-2 (160° orientation)

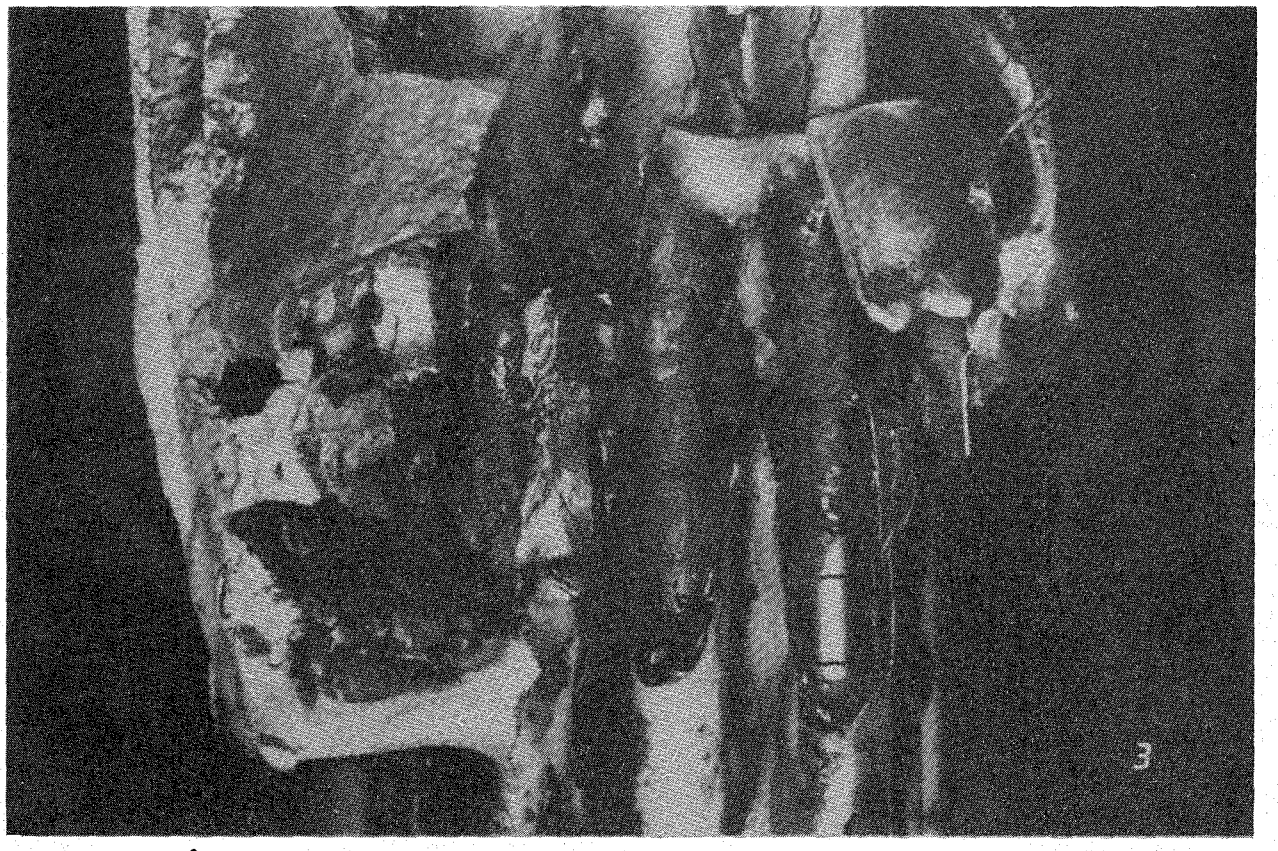

75° ; 400-500 mm elevation

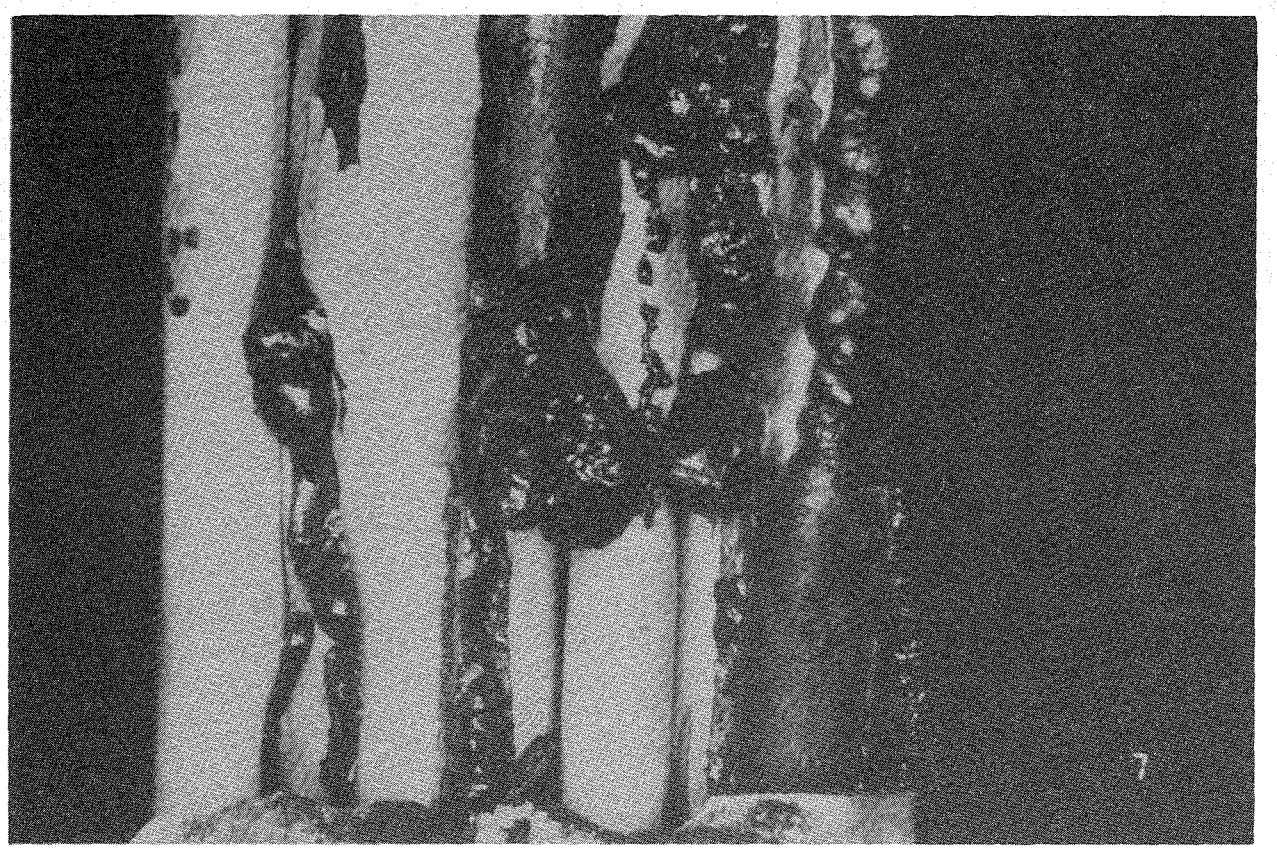

255° ; 280-350 mm elevation

Fig. 20. Solidified melt of test bundle CORA-2

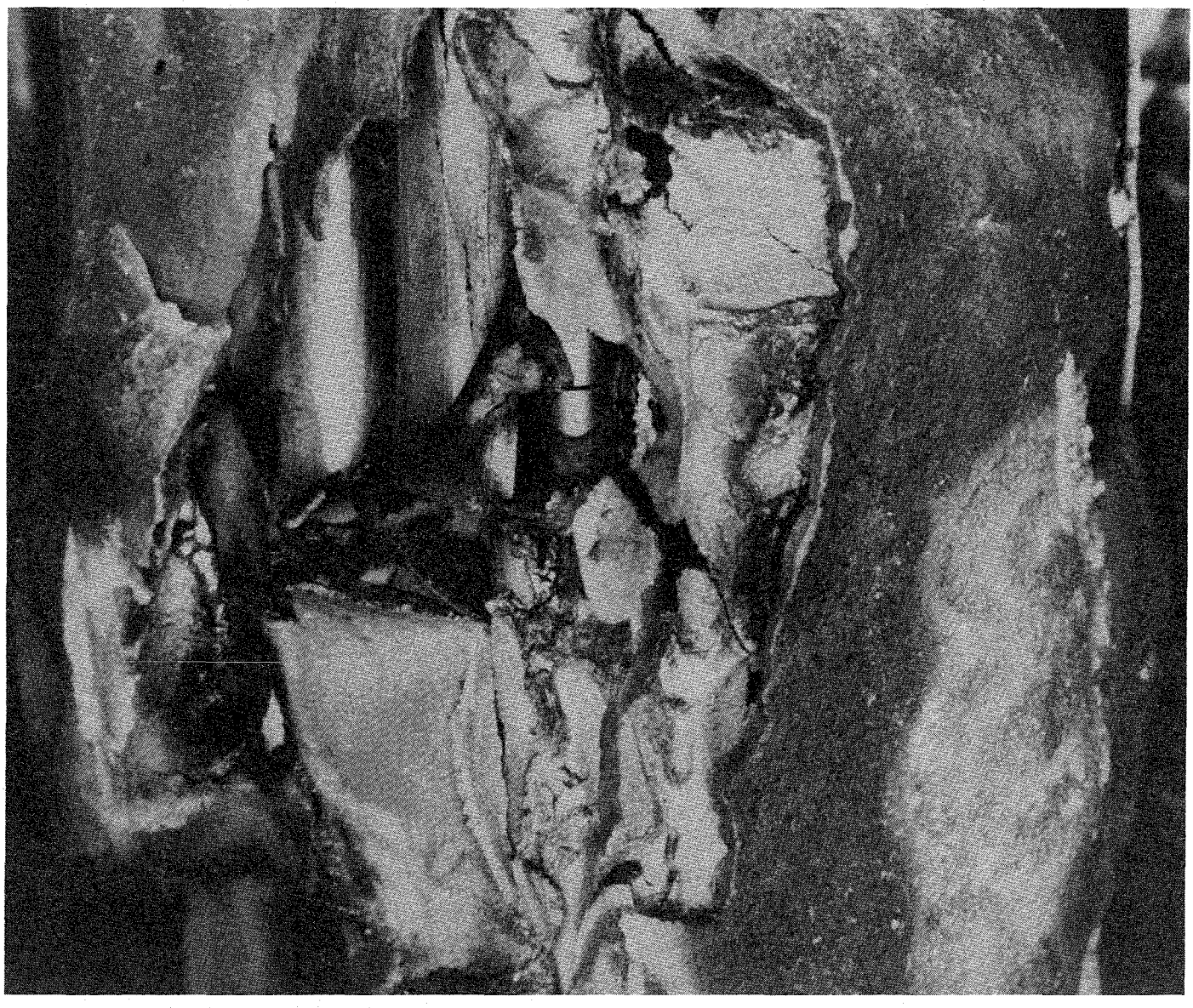

Fig. 21. Rubble formed during cooldown of test CORA-2 (490-600 mm elevation; 300° orientation)

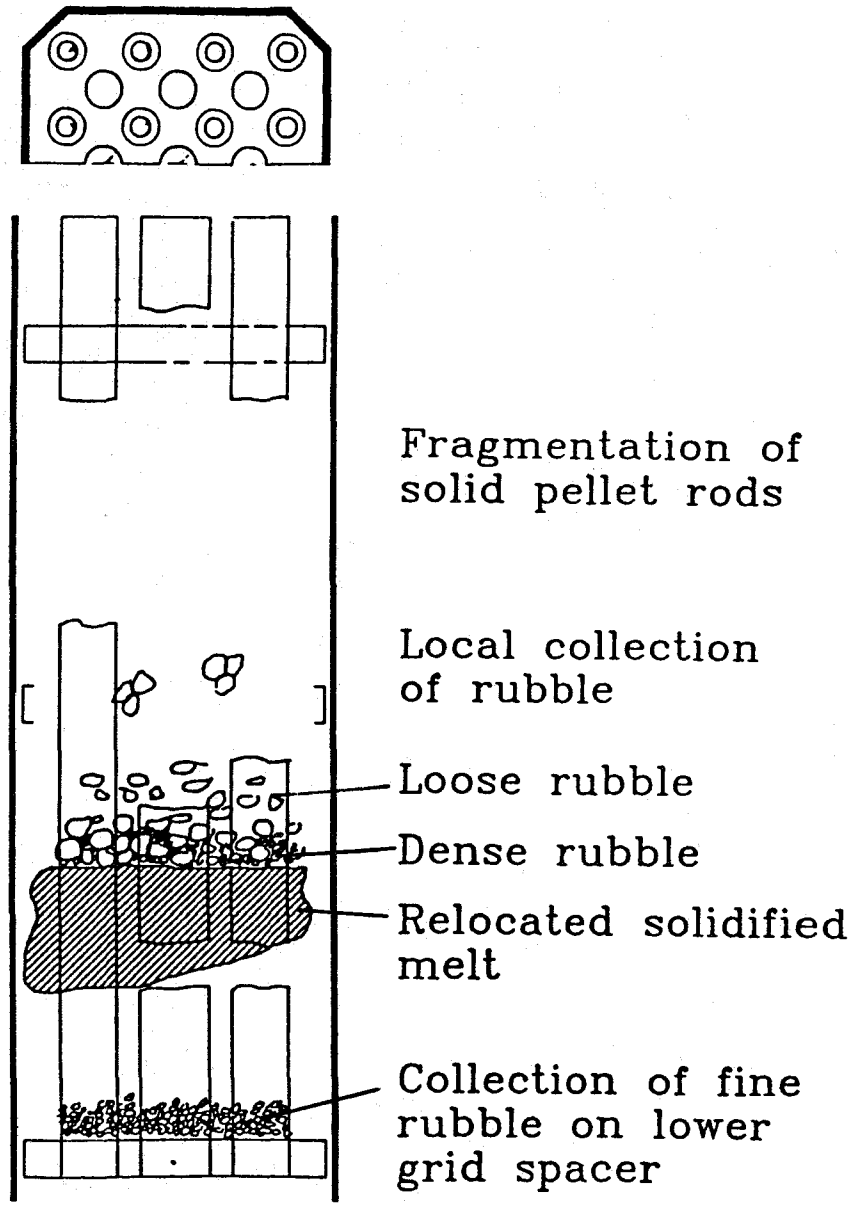

Fig. 22. Illustration of the posttest appearance of test bundle CORA-2

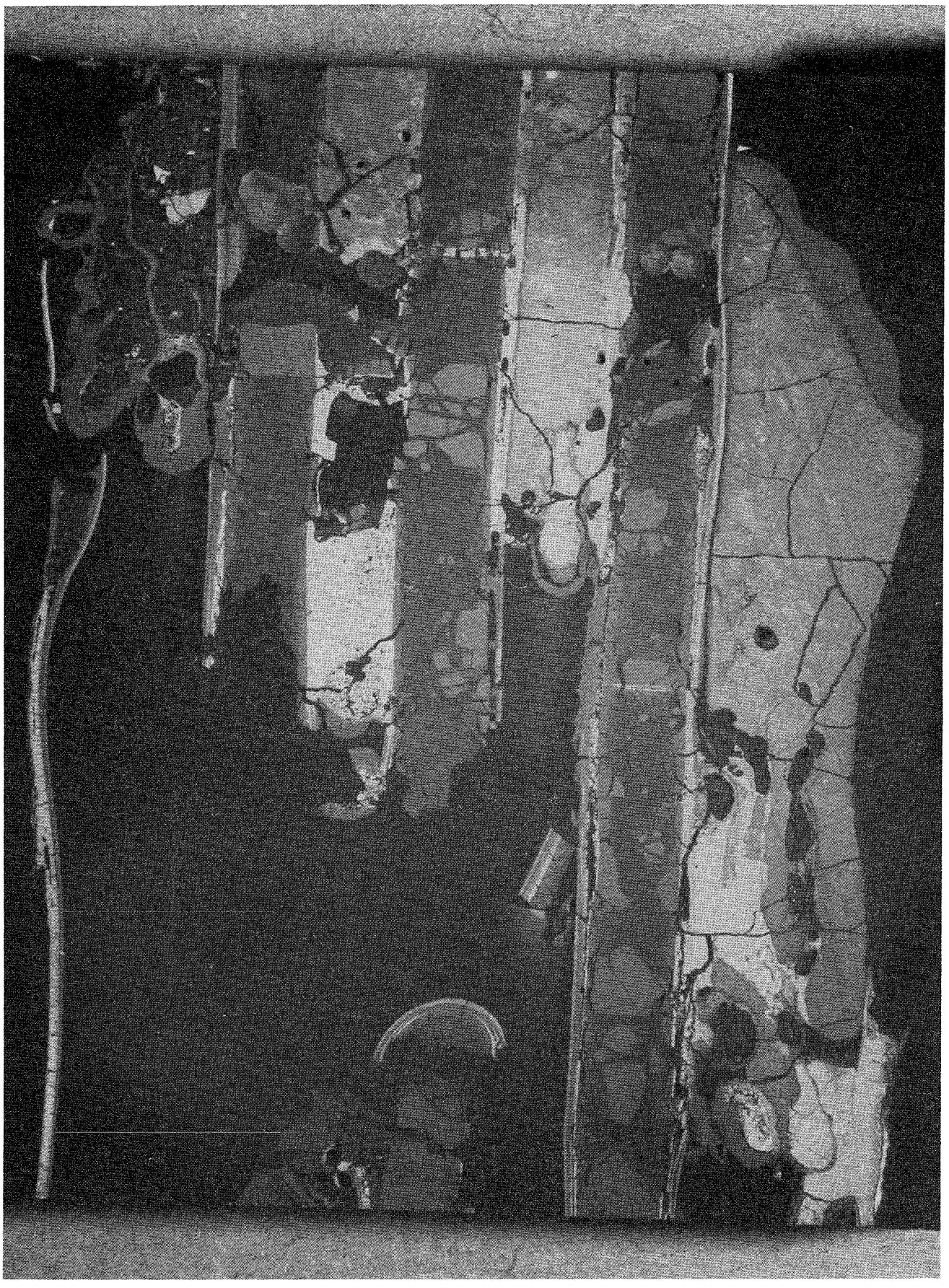

Fig. 23. CORA-2, longitudinal section 136 mm - 253 mm

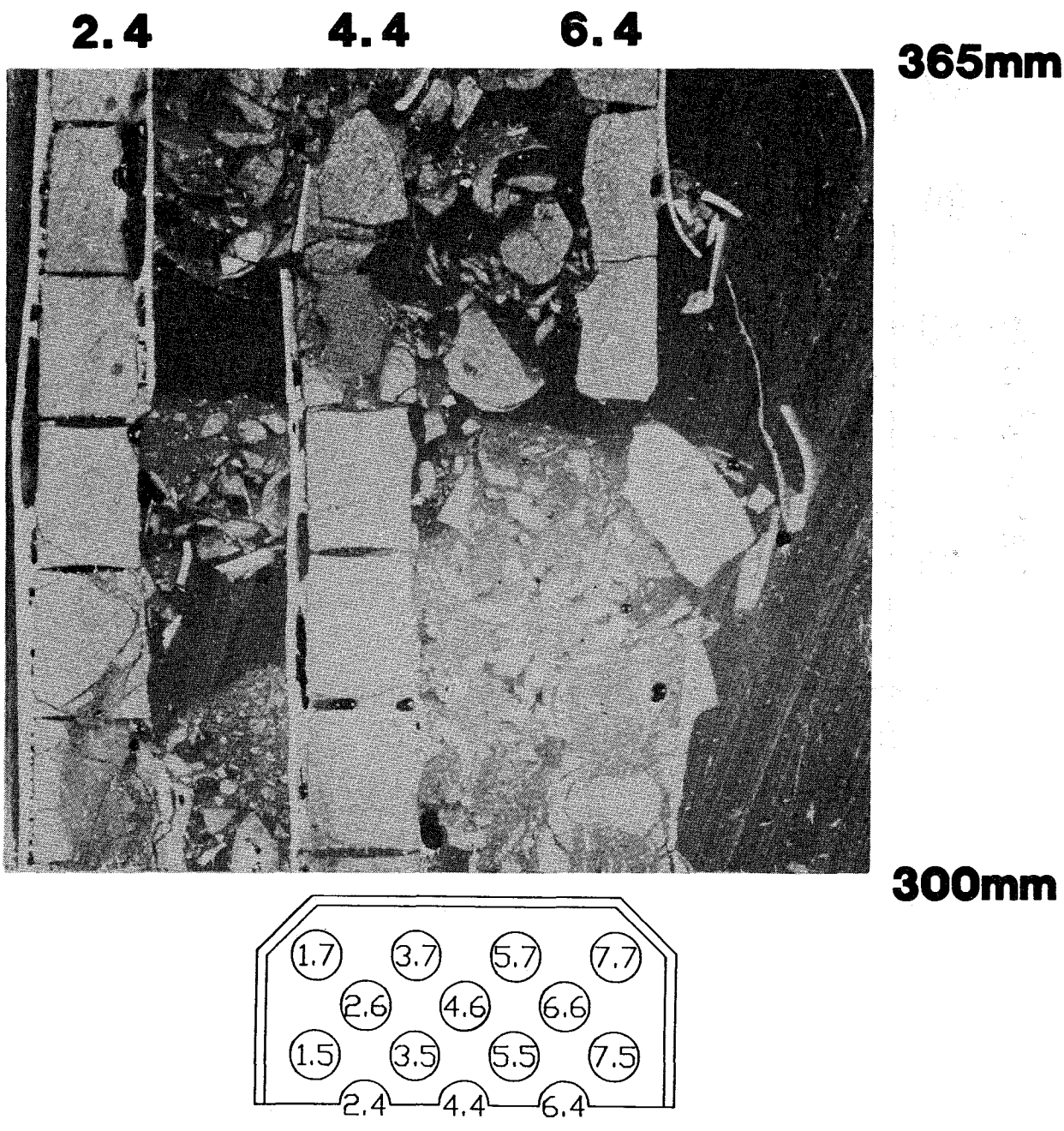

Fig. 24. Longitudinal section of the test bundle CORA-2 depicting fuel rod failure and fragmentation

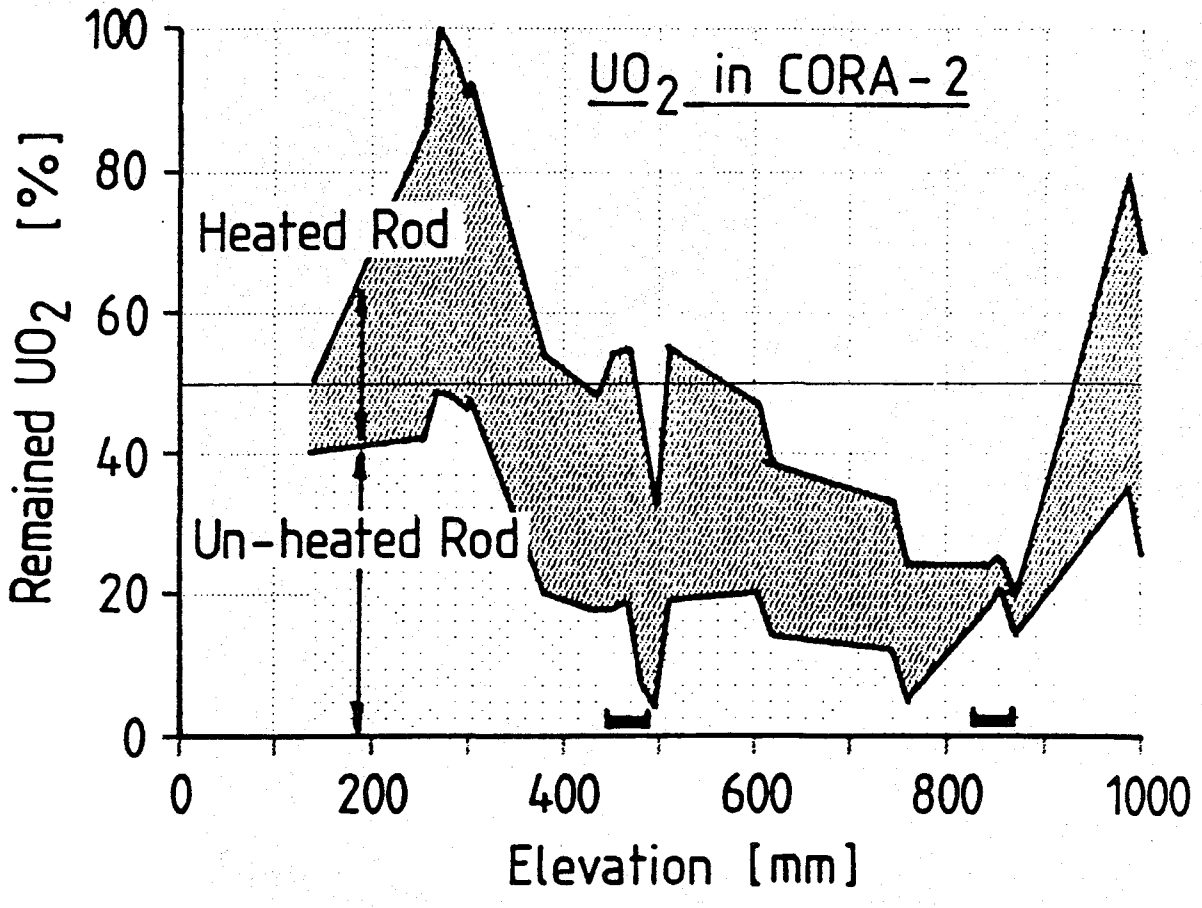

Fig. 25. Damage profile of UO_2 pellets after test CORA-2 /9/

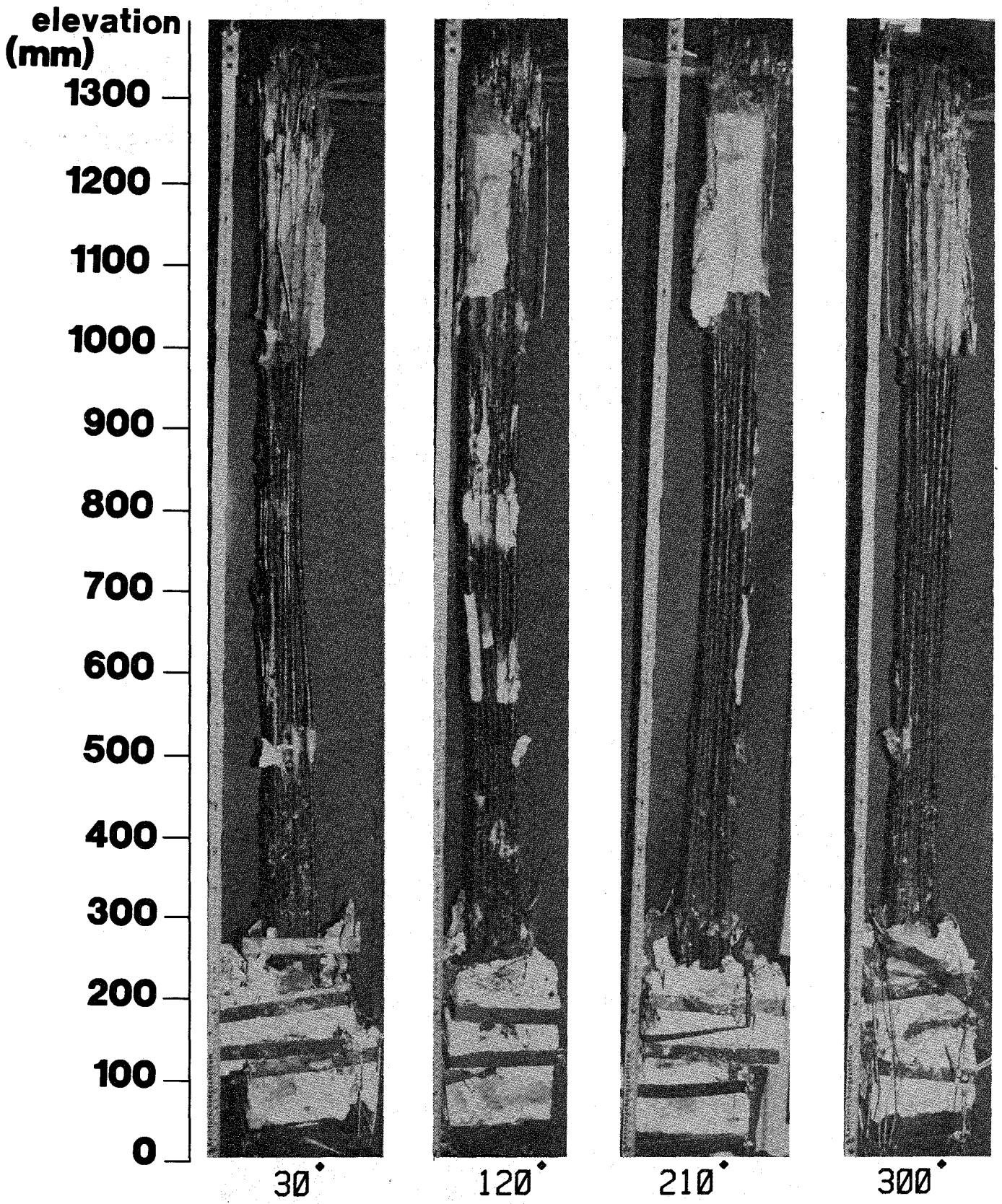

Fig. 26. CORA-3; Posttest appearance at different orientations

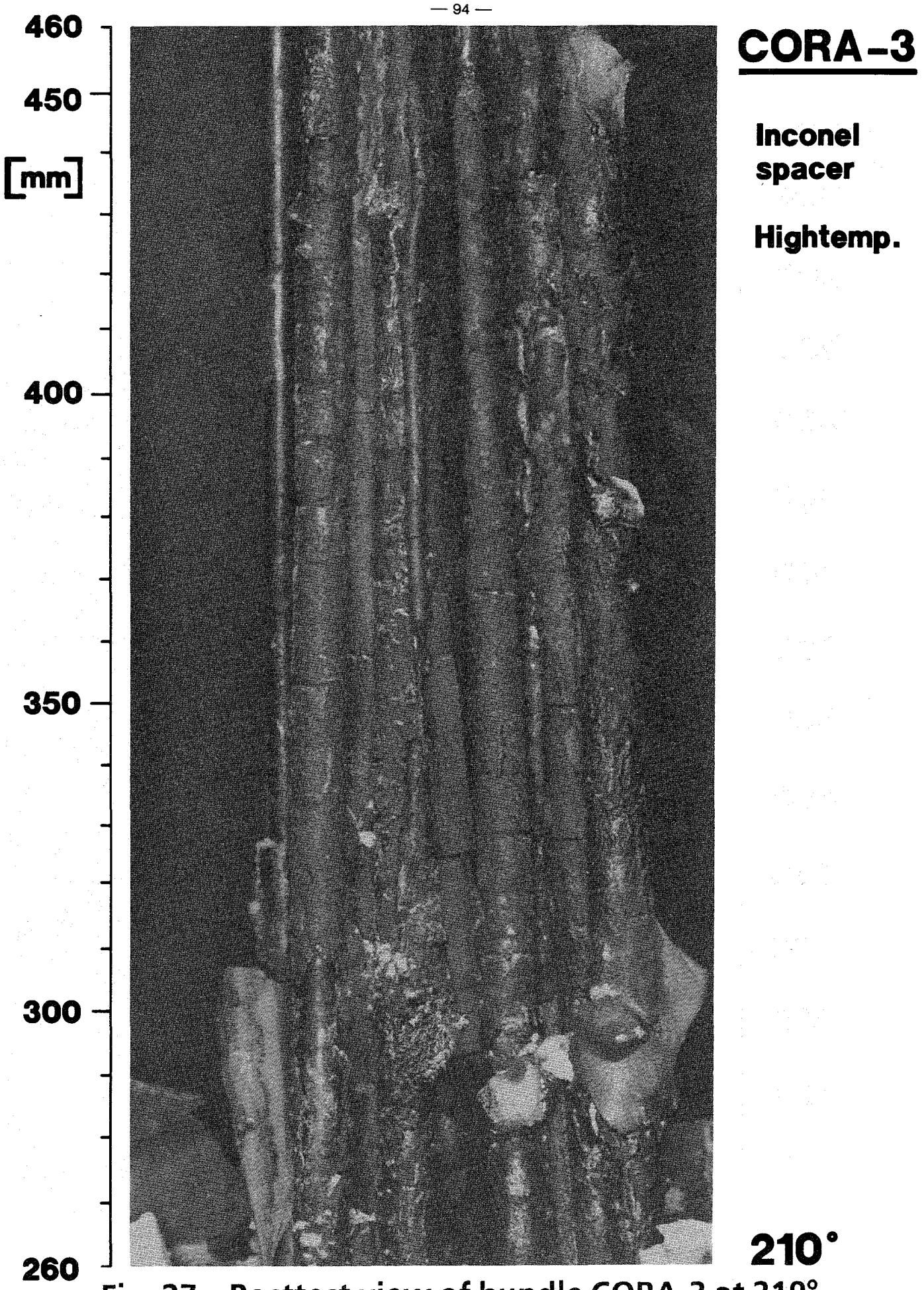

Fig. 27. Posttest view of bundle CORA-3 at 210° orientation (1)

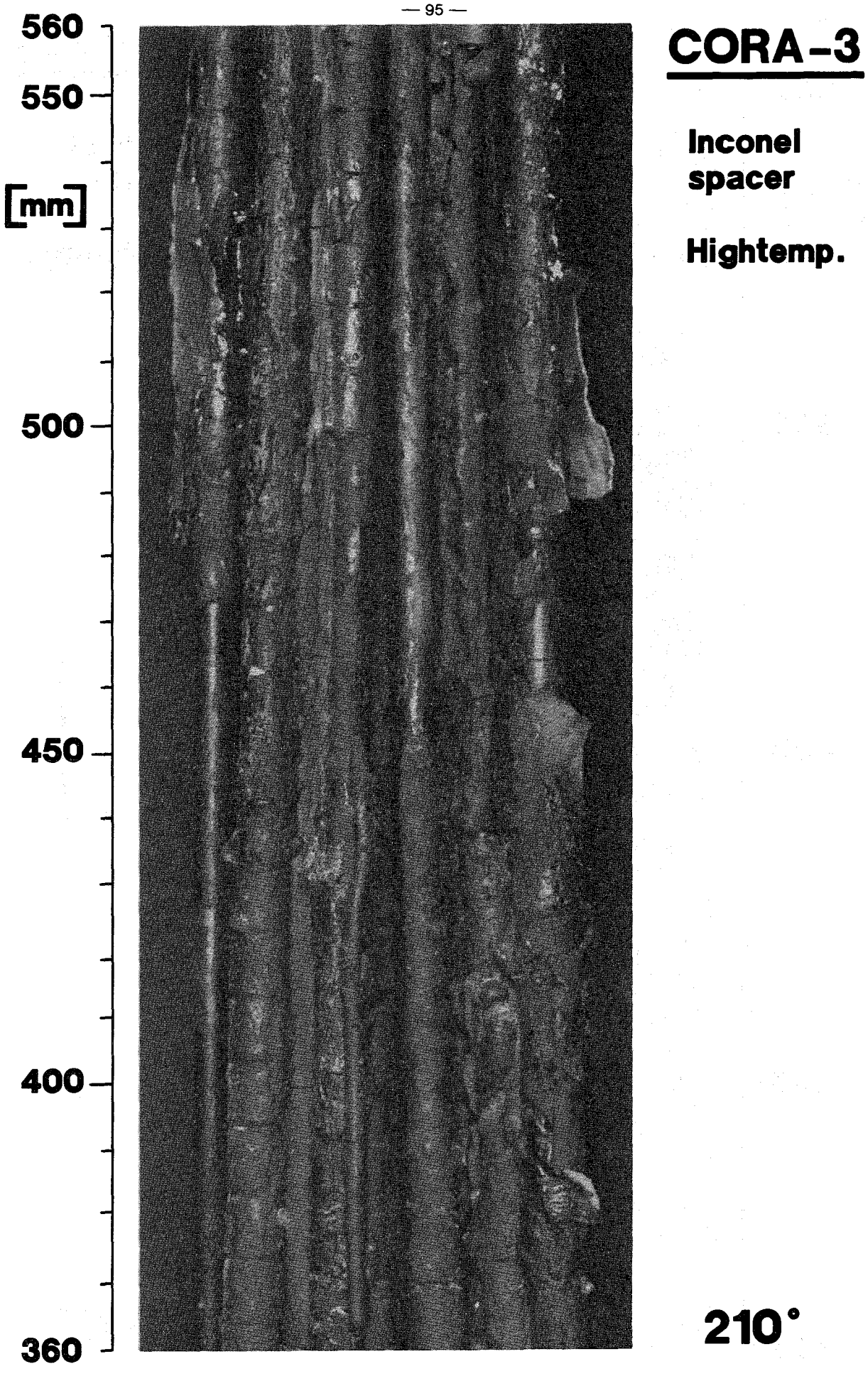

Fig. 28. Posttest view of bundle CORA-3 at 210° orientation (2)

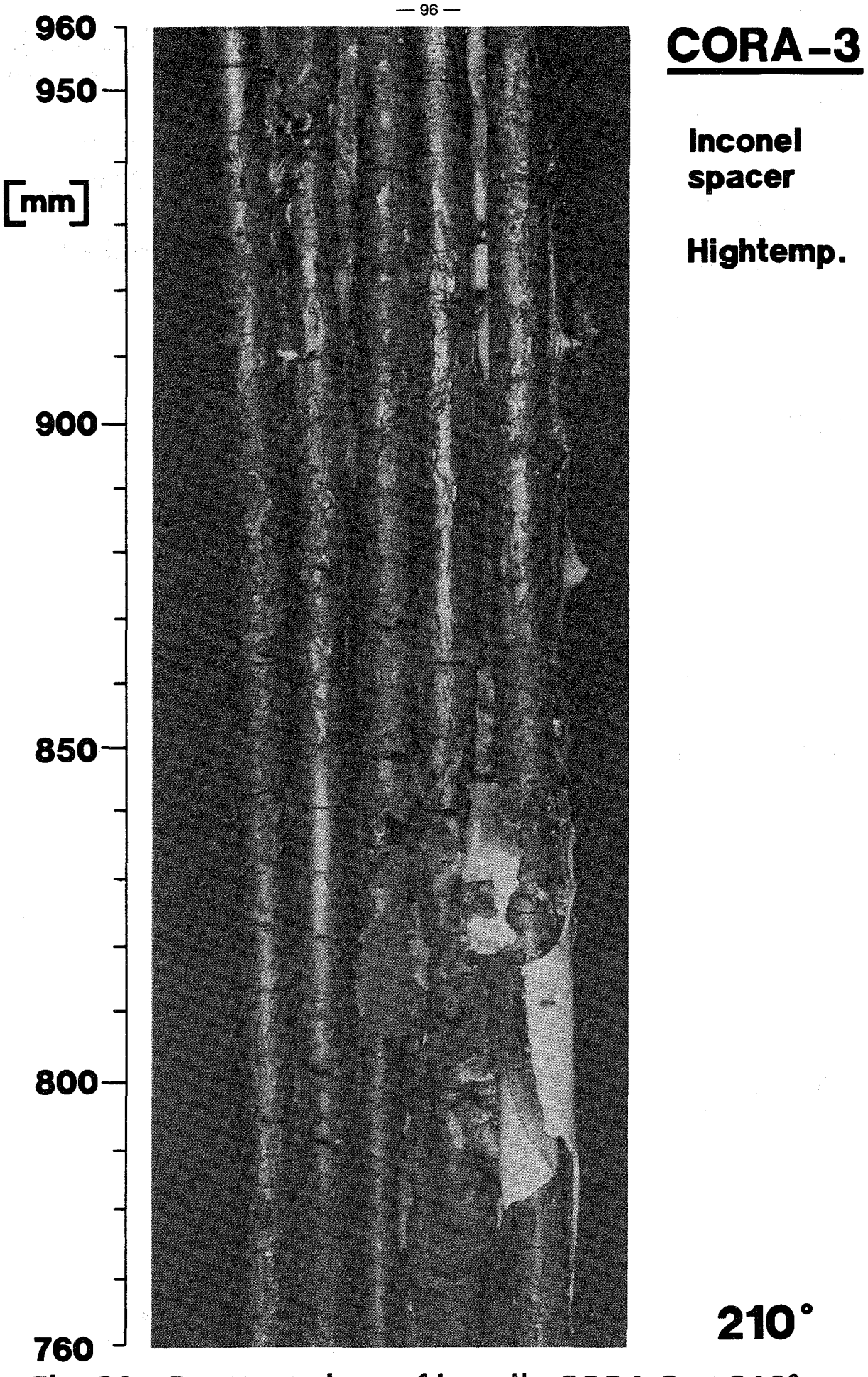

Fig. 29. Posttest view of bundle CORA-3 at 210° orientation (3)

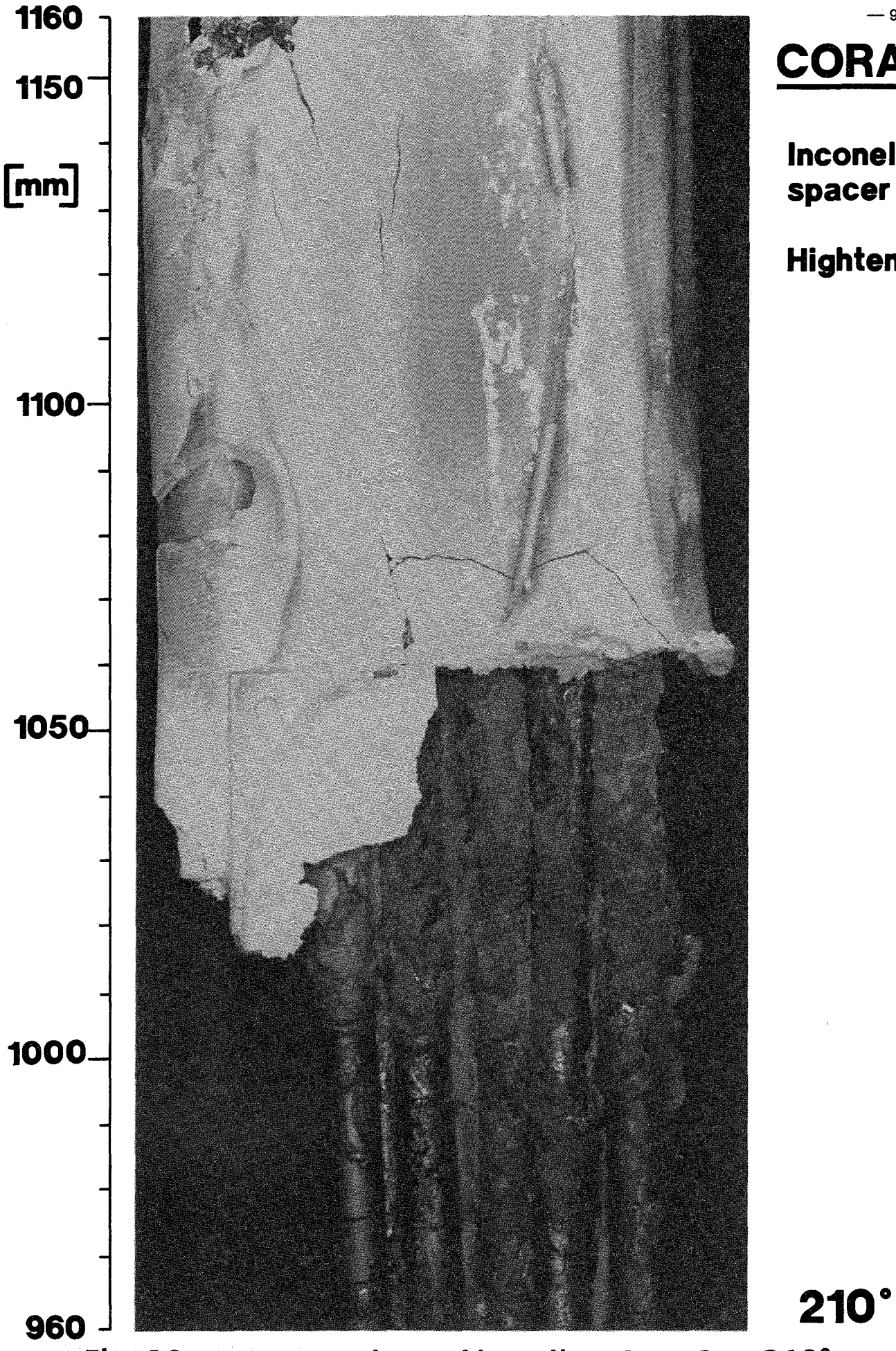

Fig. 30. Posttest view of bundle CORA-3 at 210° orientation (4)

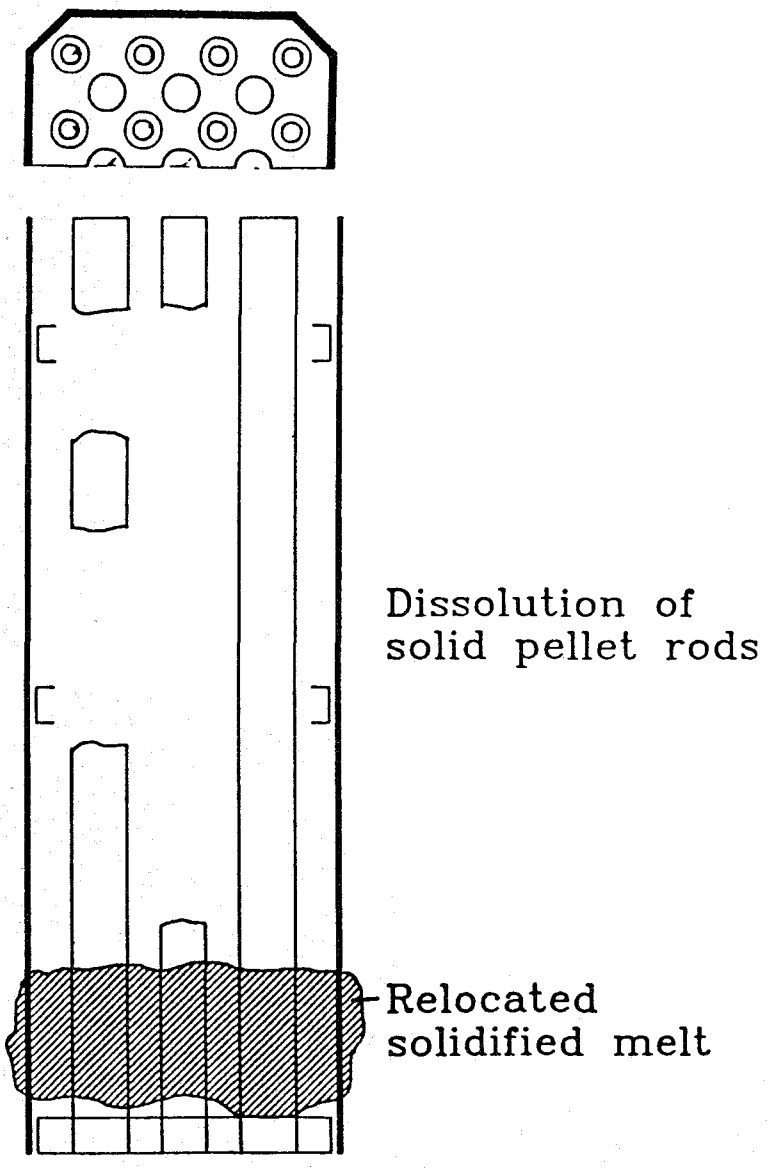

Fig. 31. Illustration of the posttest appearance of test bundle CORA-3

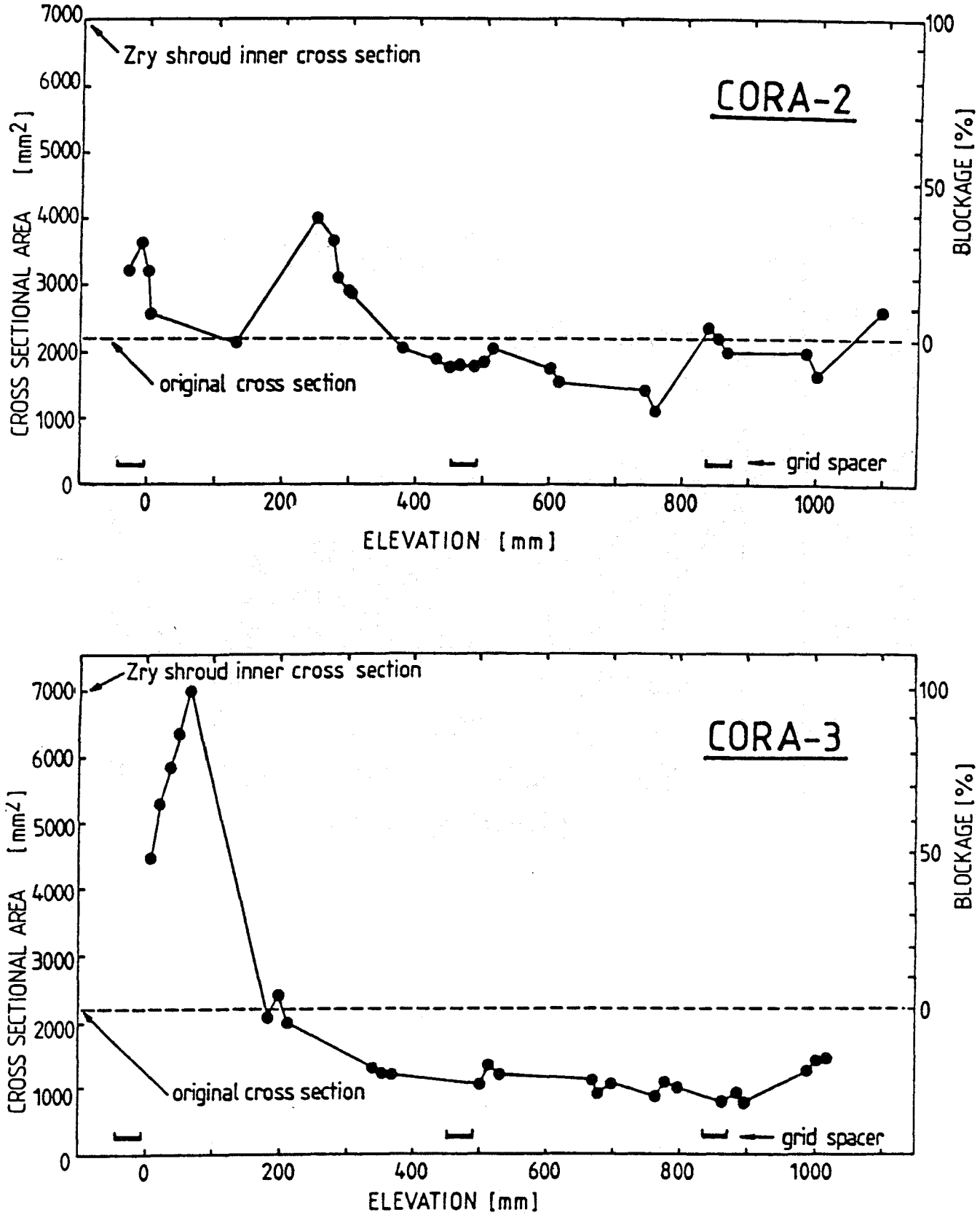

Fig. 32. Profiles of the cross-sectional areas before and after tests CORA-2 and CORA-3 /9/

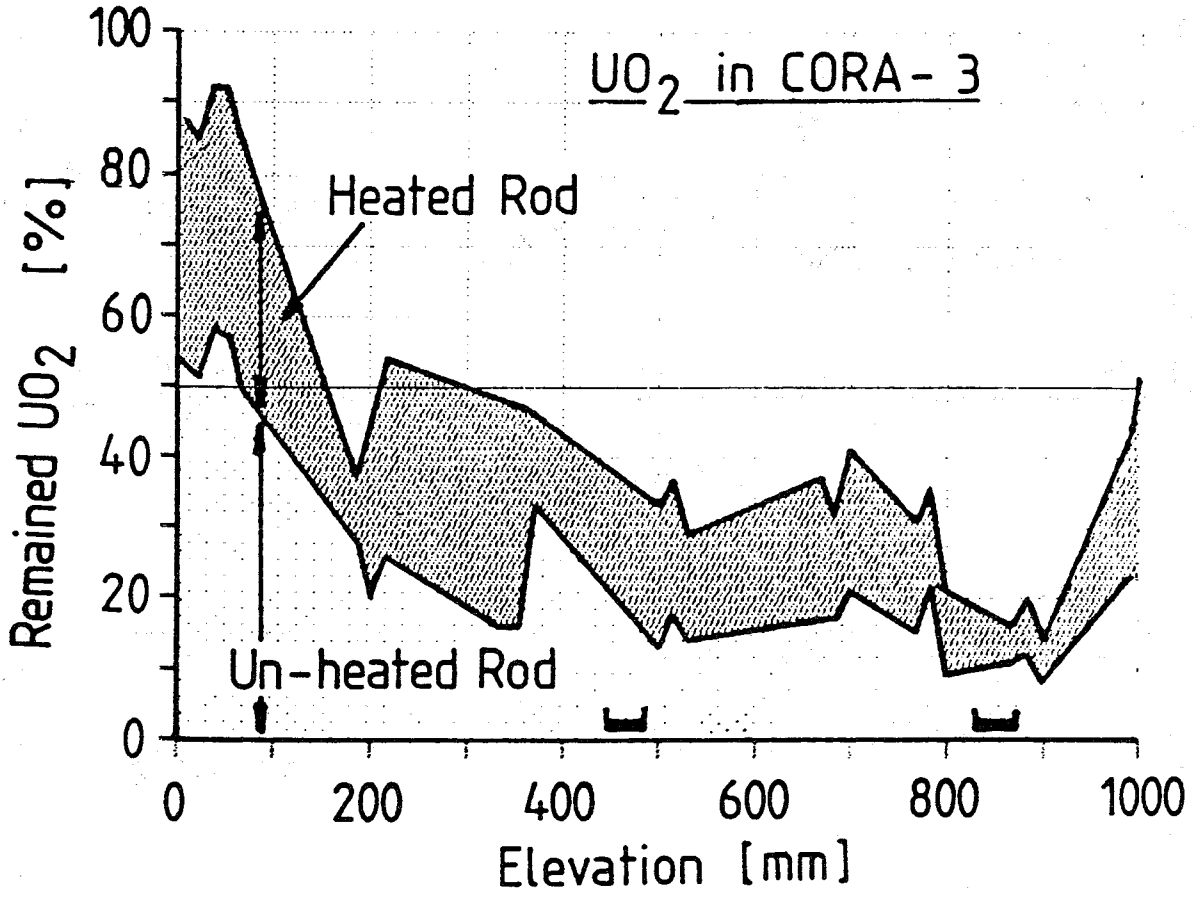

Fig. 33. Damage profile of UO_2 pellets after test CORA-3 /9

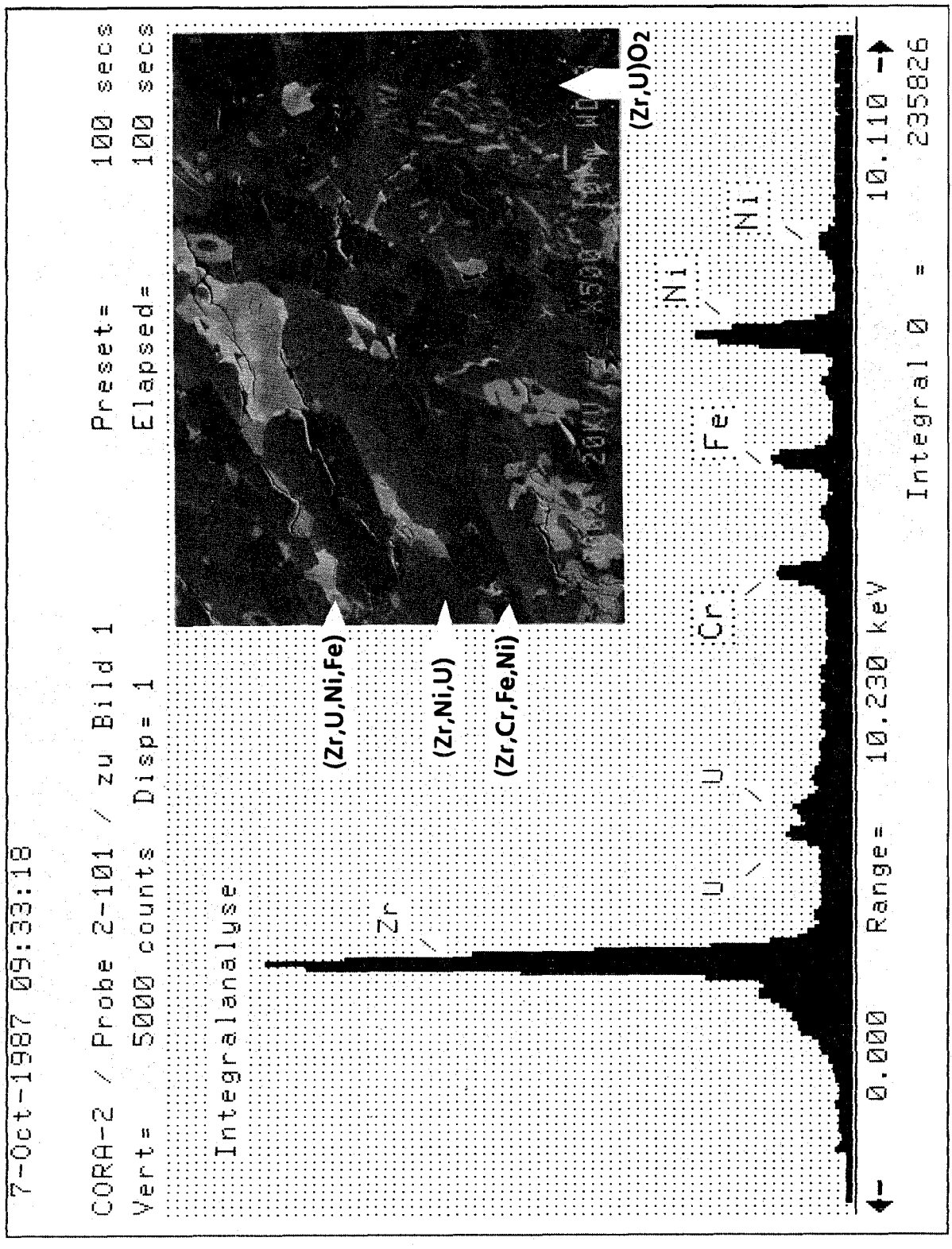

Fig. 34. Re-solidified rivulet of melt from Zircaloy-Inconel-UO_2 interaction (specimen 101 of CORA-2)

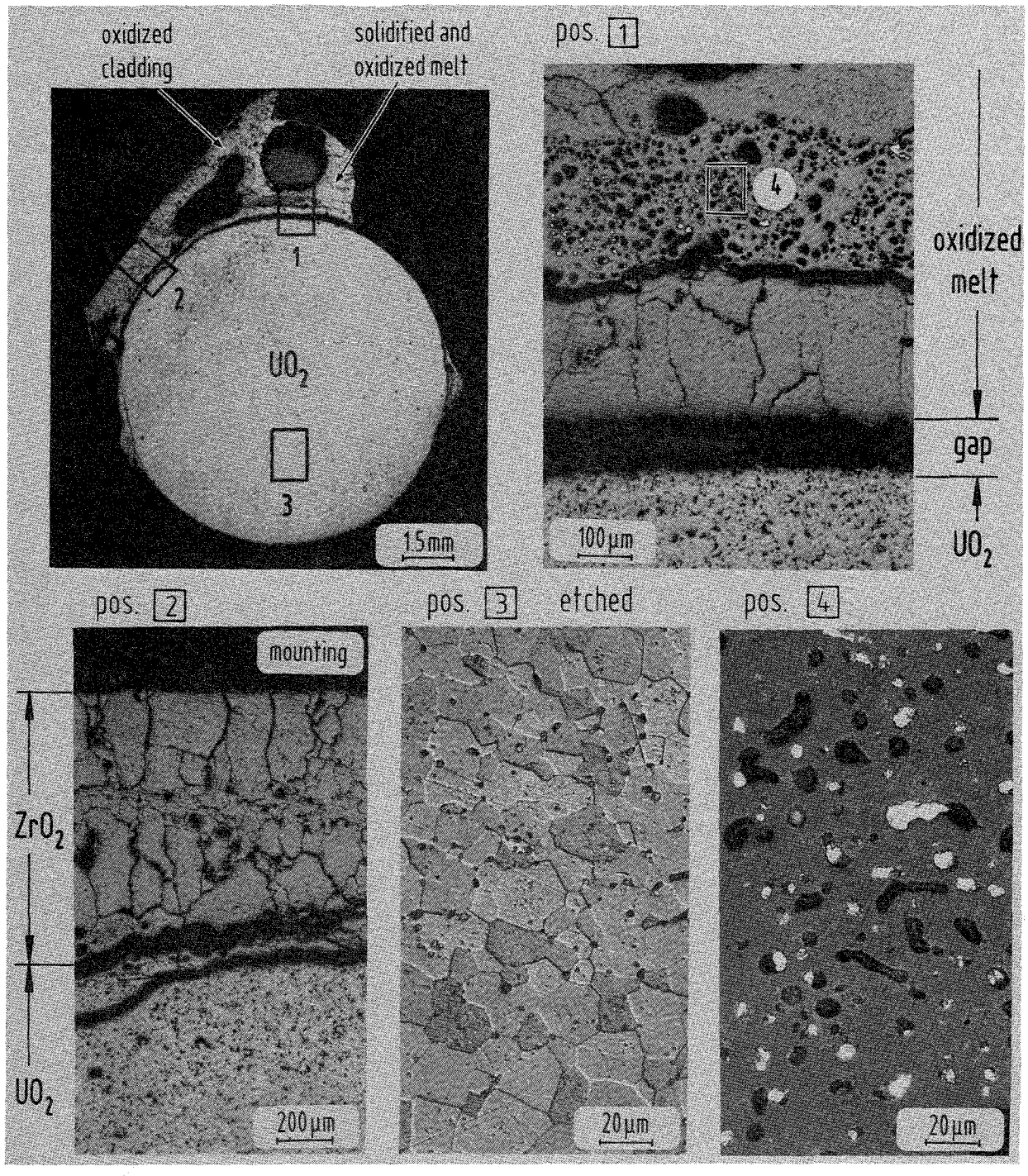

Fig. 35. Microstructures of solid UO_2 pellet and attached cladding fragment

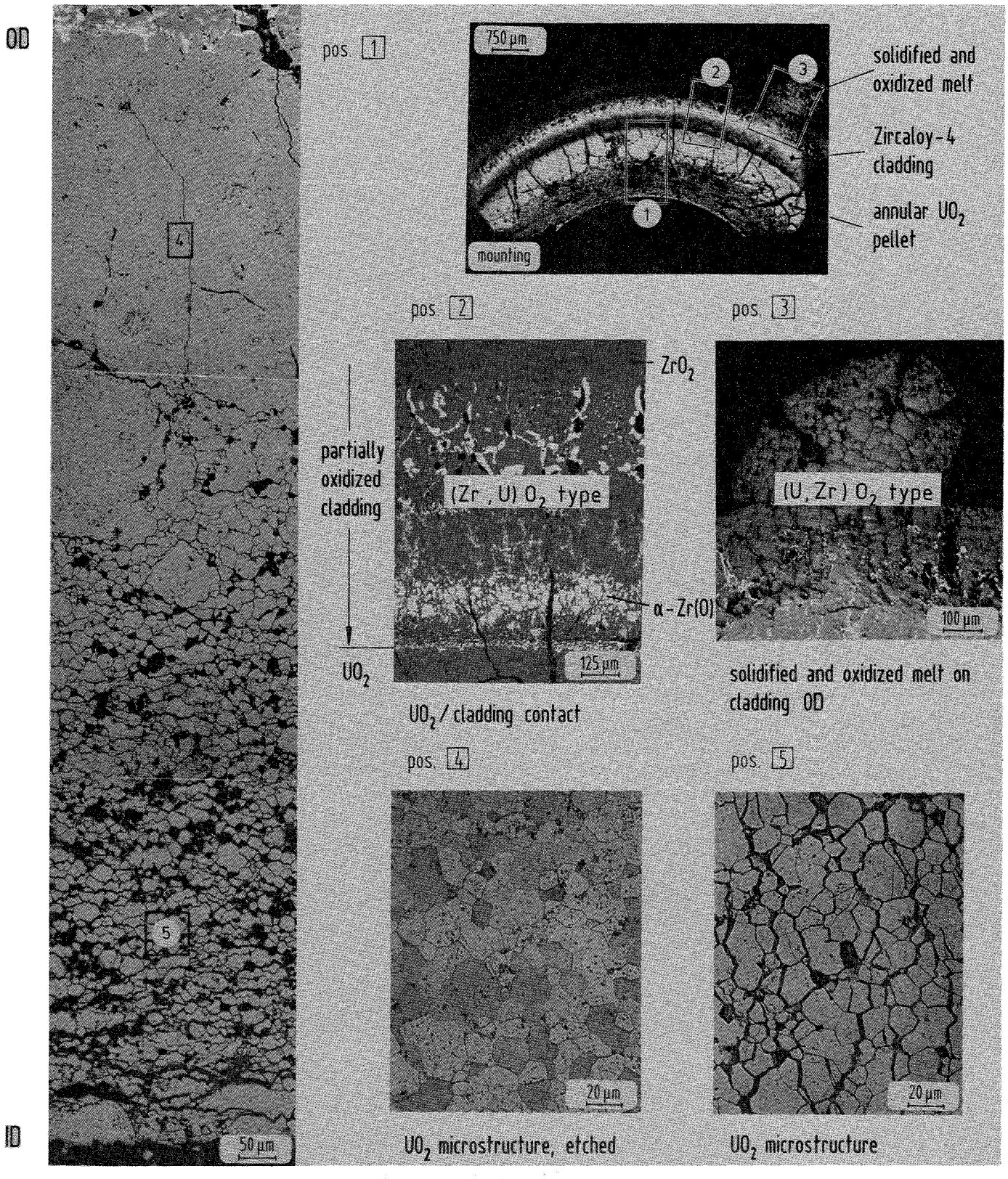

UO_2 pellet fragmentation;
metallic U can be detected within the UO_2

CORA 2-107

KfK IMF I, PRS

Fig. 36. Microstructures of annular UO_2 pellet, Zircaloy cladding and solidified melt

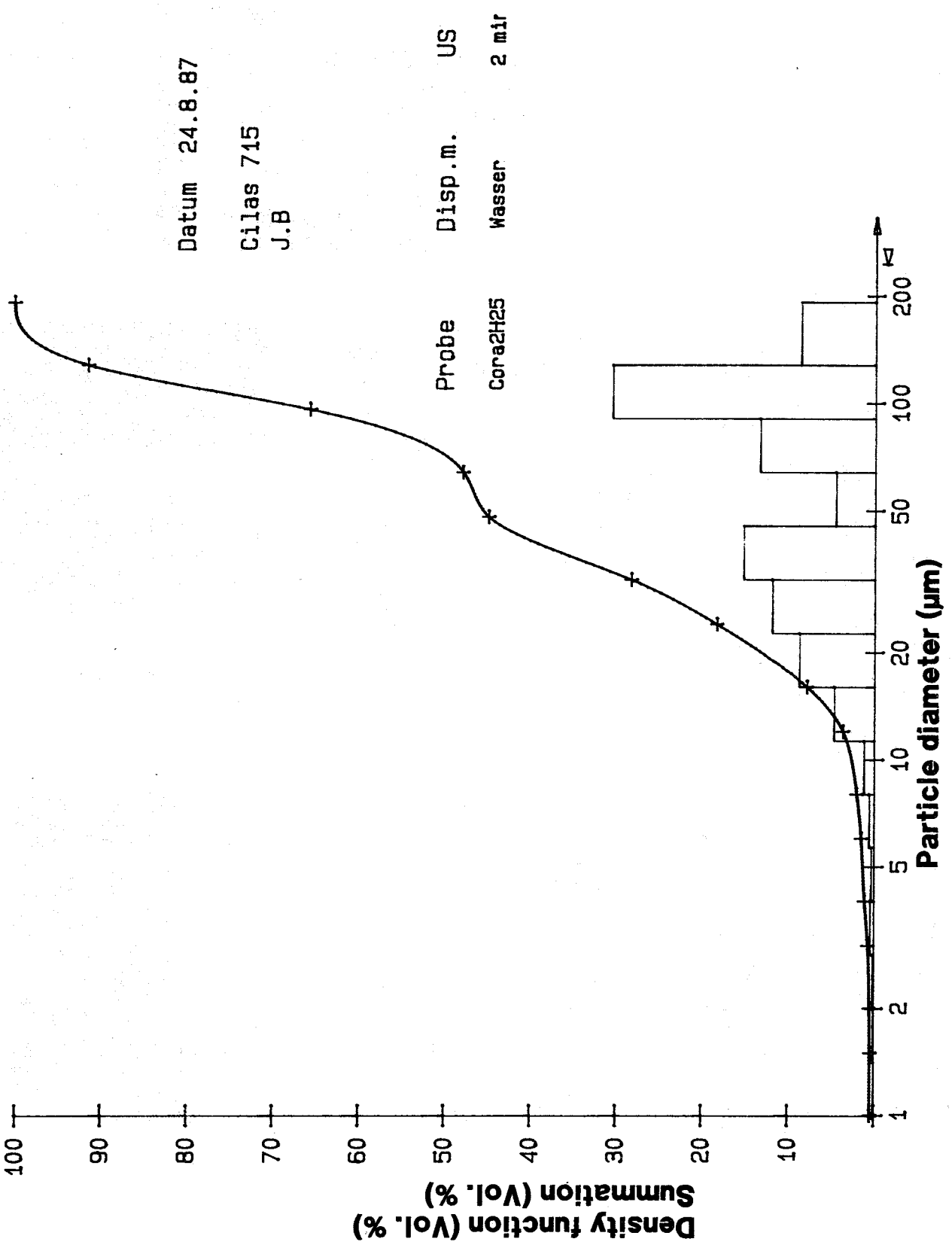

Fig. 37. Particle size distribution (density function and sum) of the powder taken from observation window H 25

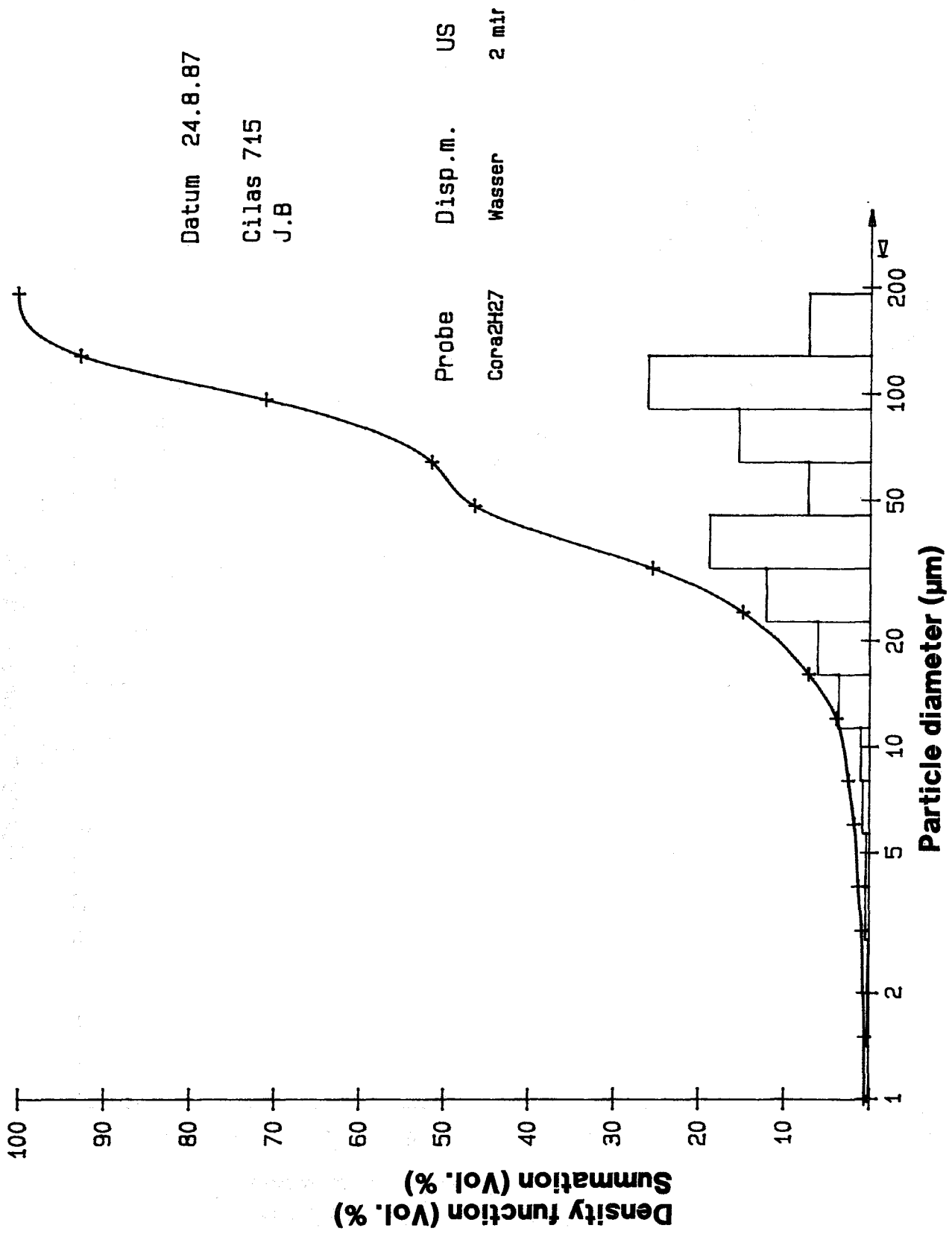

Fig. 38. Particle size distribution (density function and sum) of the powder taken from observation window H 27

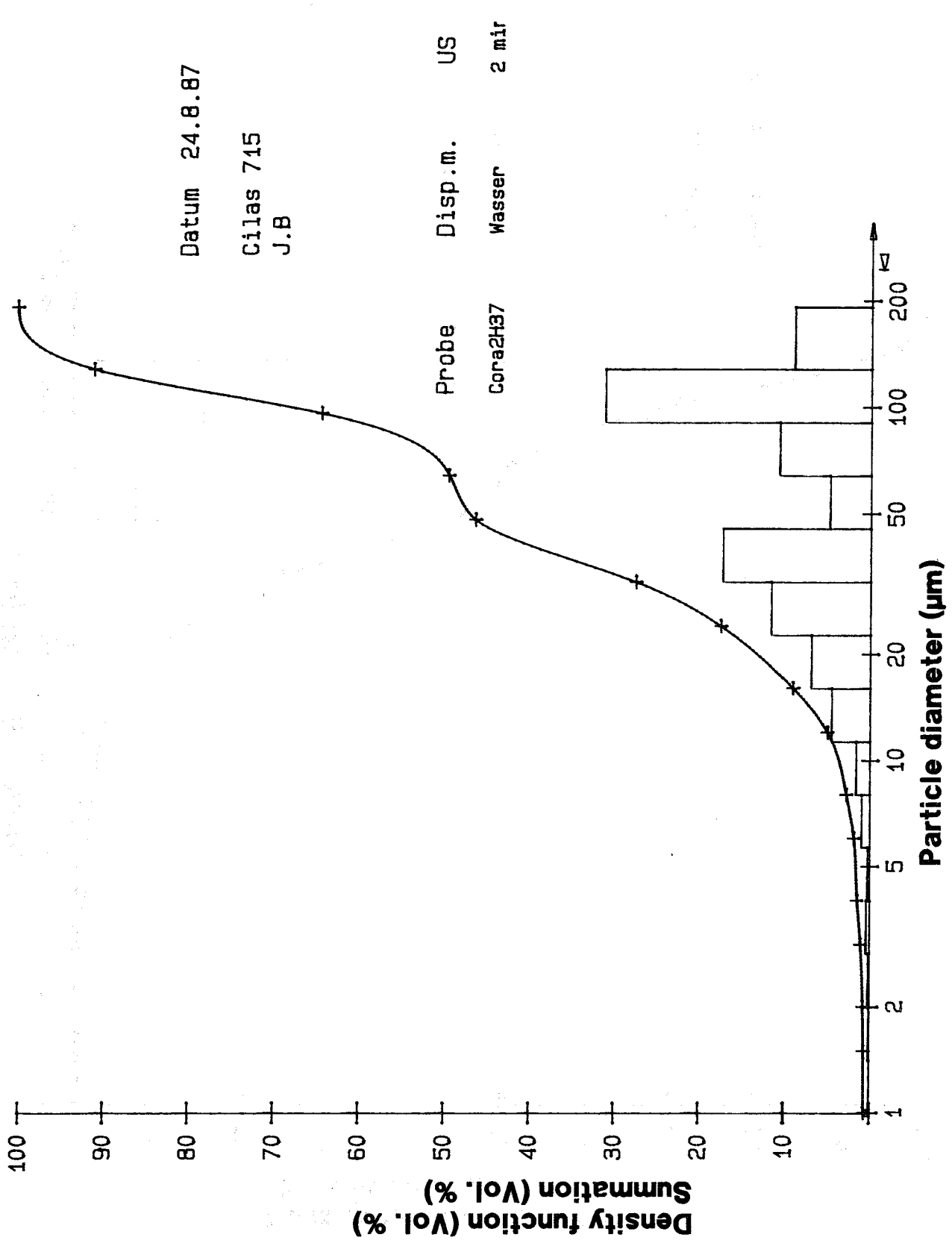

Fig. 39. Particle size distribution (density function and sum) of the powder taken from observation window H 37

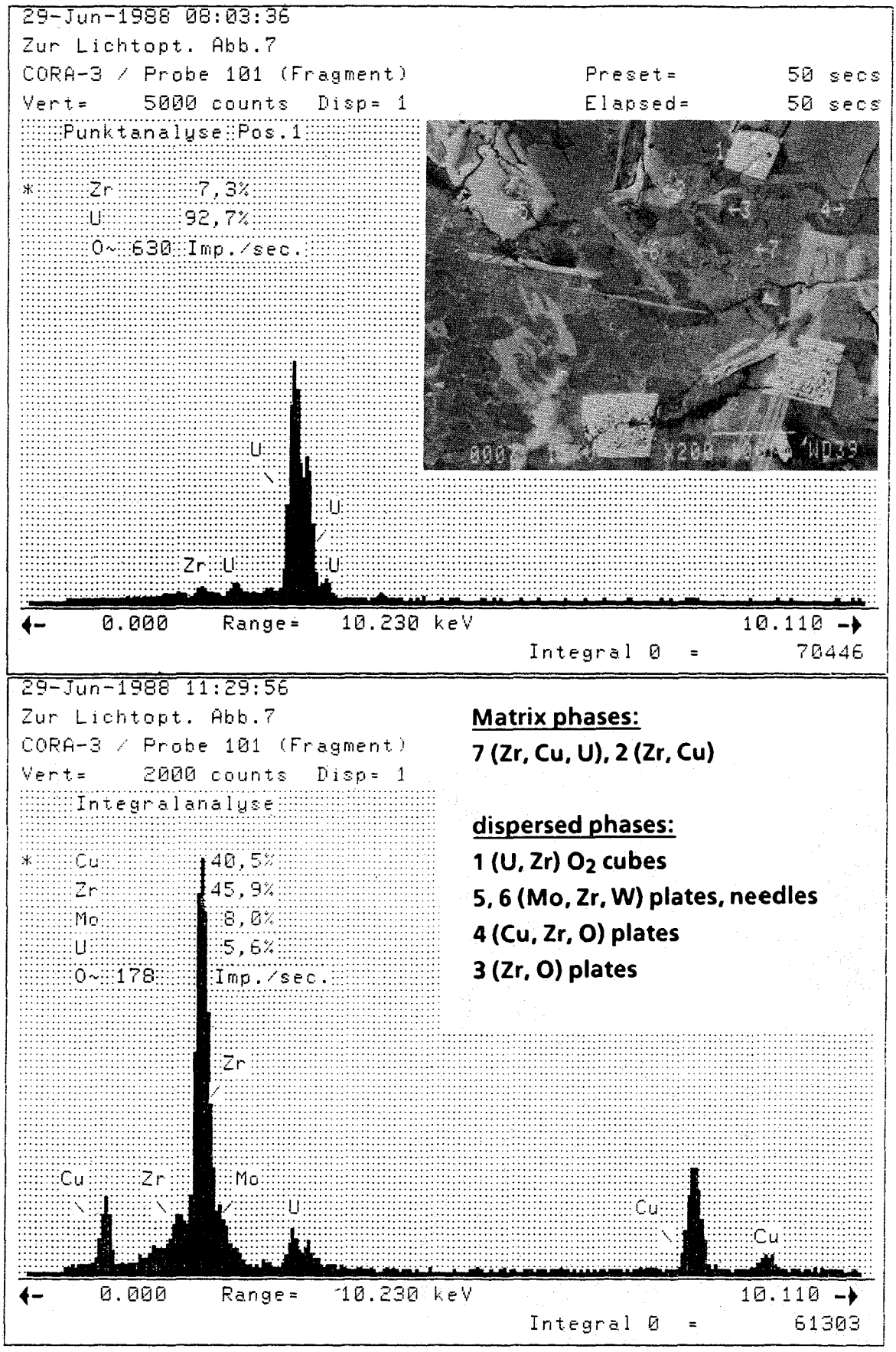

CORA-3

Fig. 40. Multicomponent melt around the relocated fuel pellet stack fragment 101 of CORA-3, originating from interaction with heater and electrode materials

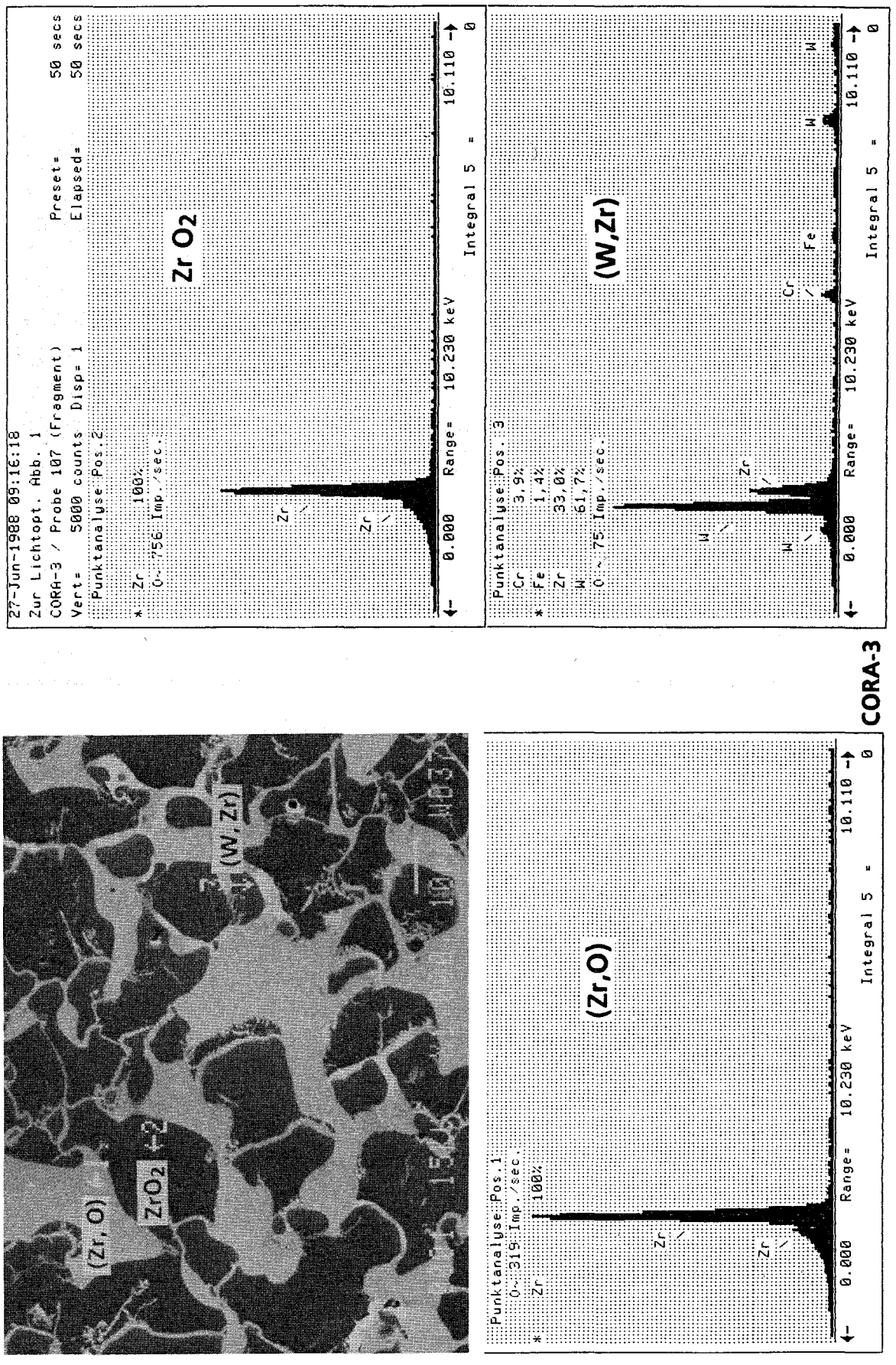

Fig. 41. Typical part of shroud specimen 107 of CORA-3; Zry melt, contaminated by interference with heater and Inconel spacer materials

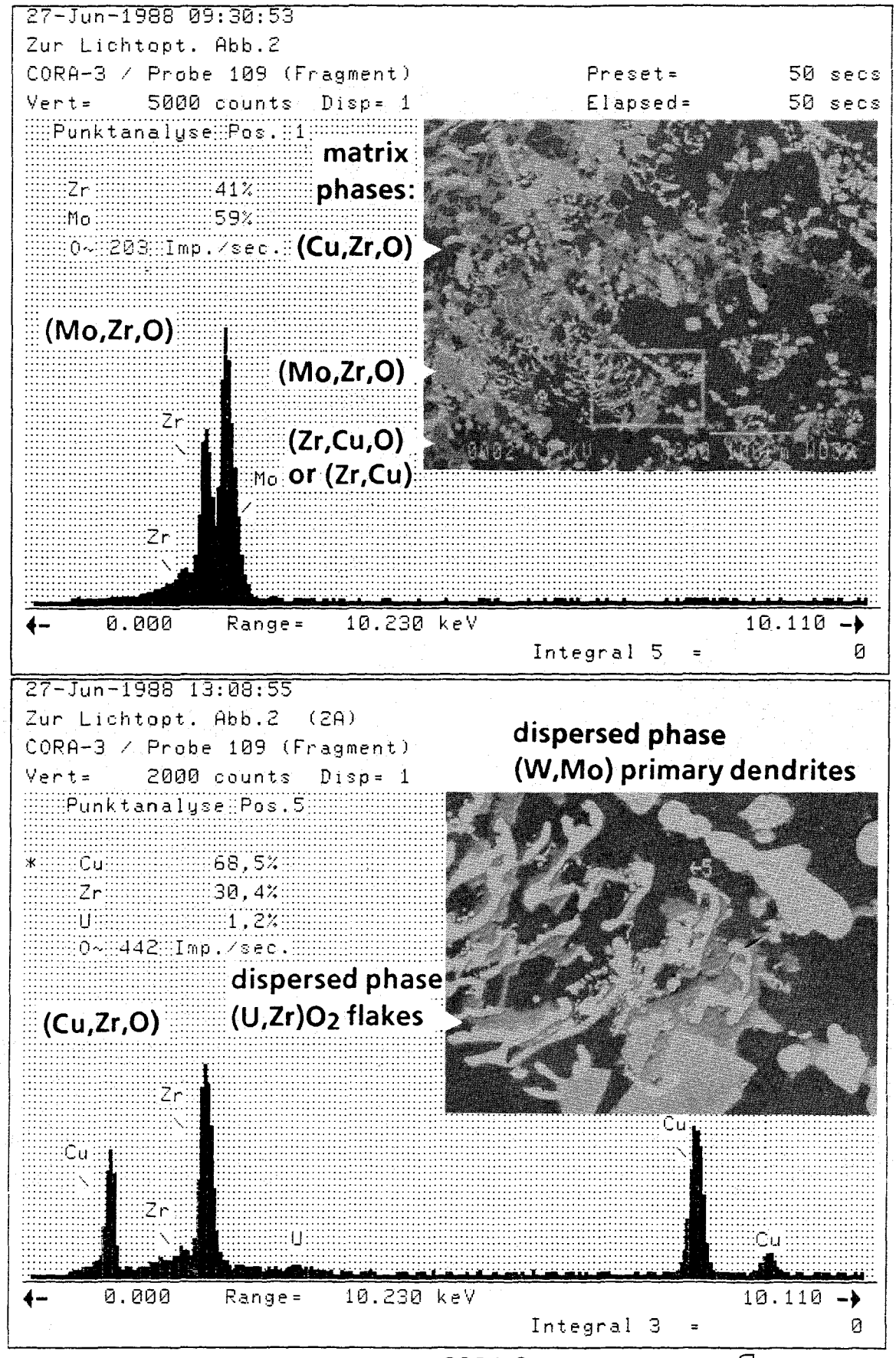

Fig. 42. Prior melt of fragment 109 of CORA-3, formed by multicomponent interaction

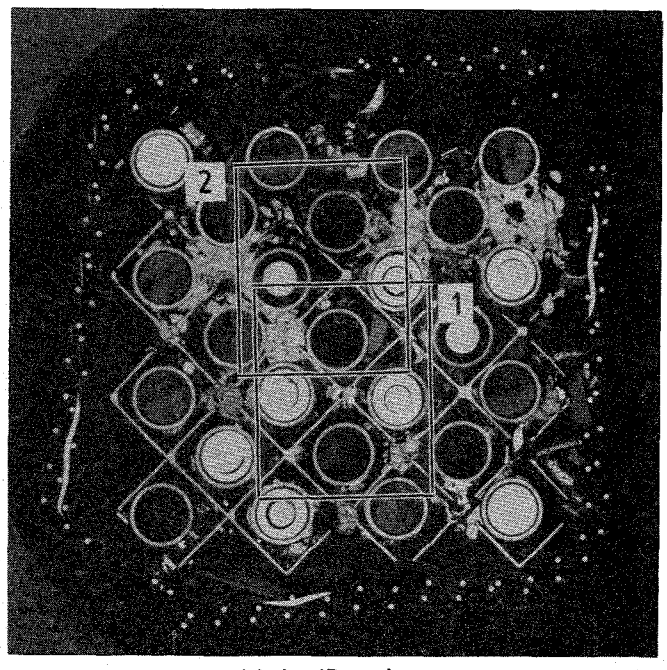

lower spacer grid (-13mm)

1 relocated metallic melt

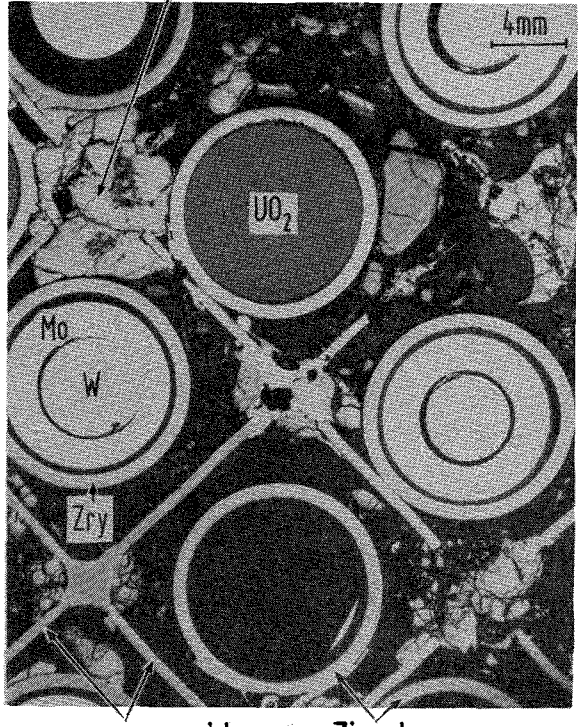

2

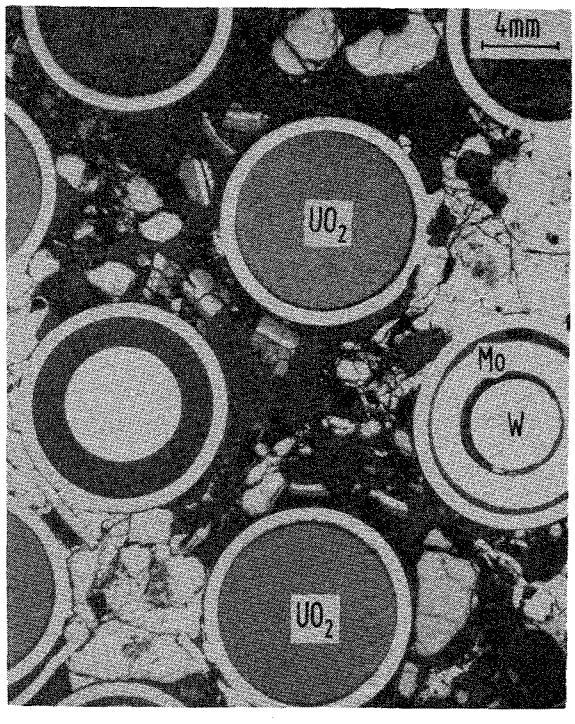

spacer grid Zircaloy

CORA bundle 2

KfK IMF I, PRS

Fig. 43. CORA-2 bundle cross-section number 4 (-13 mm). The lower spacer grid acts as catcher for relocated solid and liquid materials.

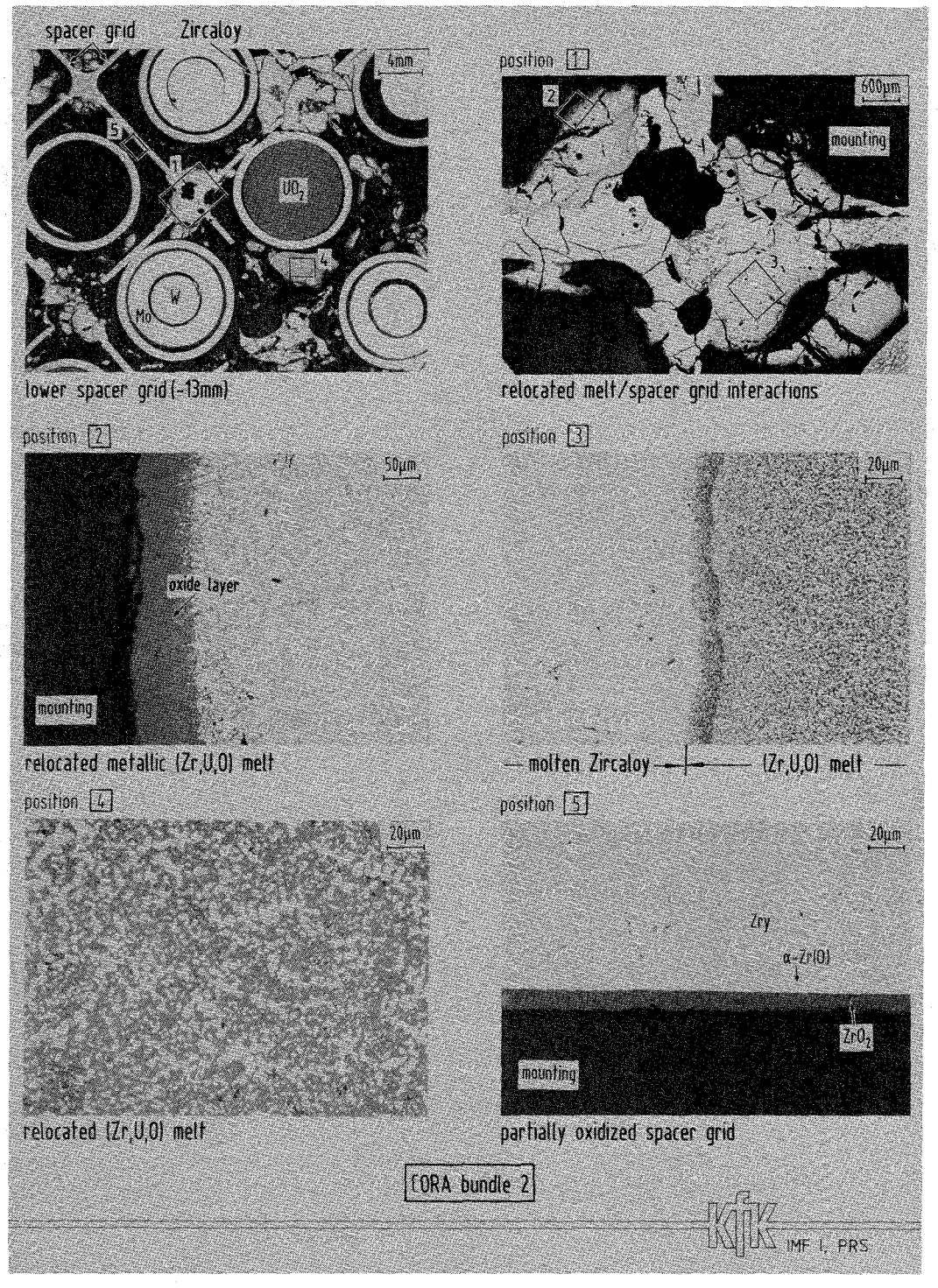

Fig. 44. Microstructures of CORA-2 bundle cross-section number 4 (-13 mm). The relocated (Zr, U, O) melt indicates a large amount of dissolved UO_2.

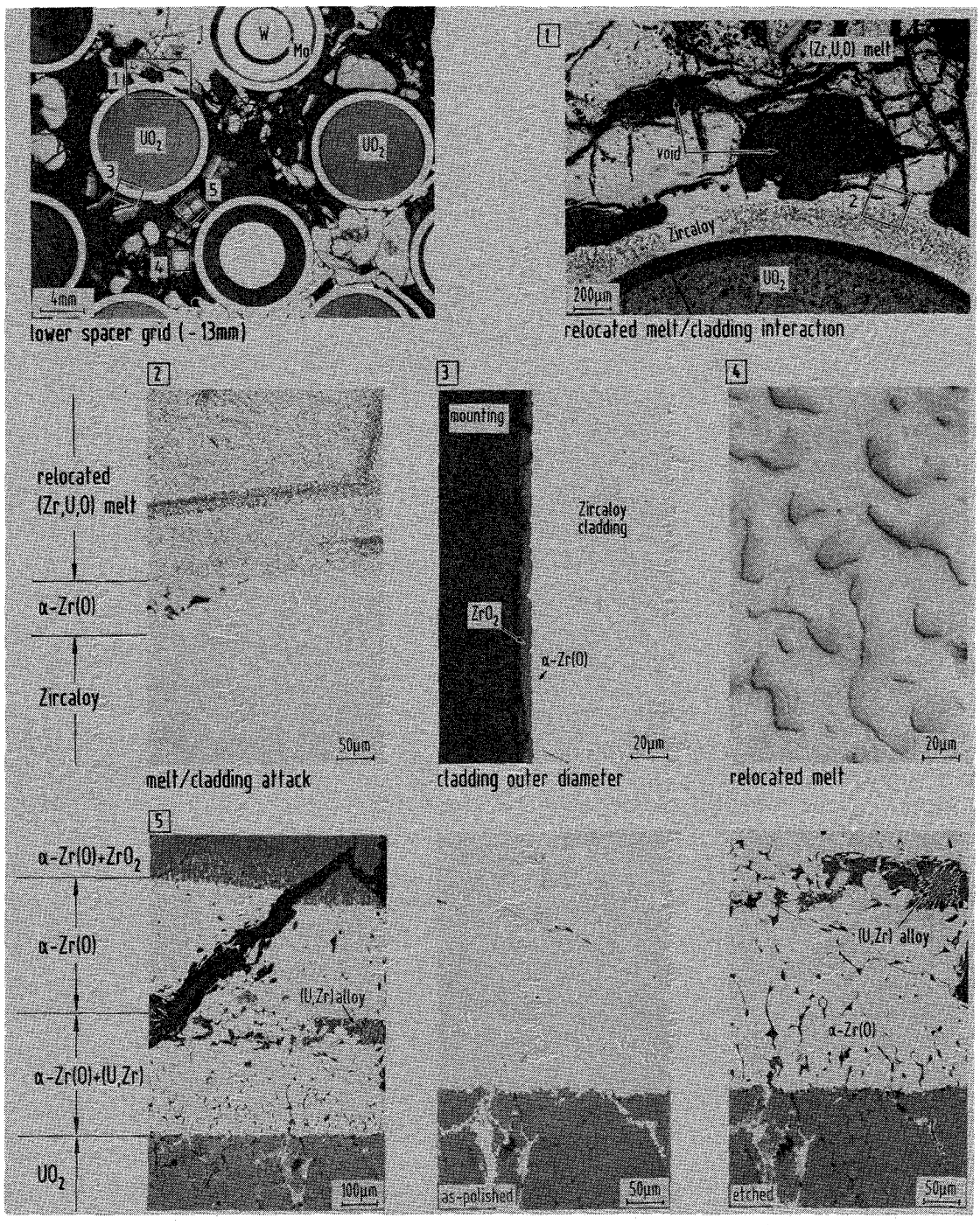

Fig. 45. Microstructures of CORA-2 bundle cross-section number 4 (-13 mm). The relocated melts interact with the Zircaloy cladding and partially dissolve it.

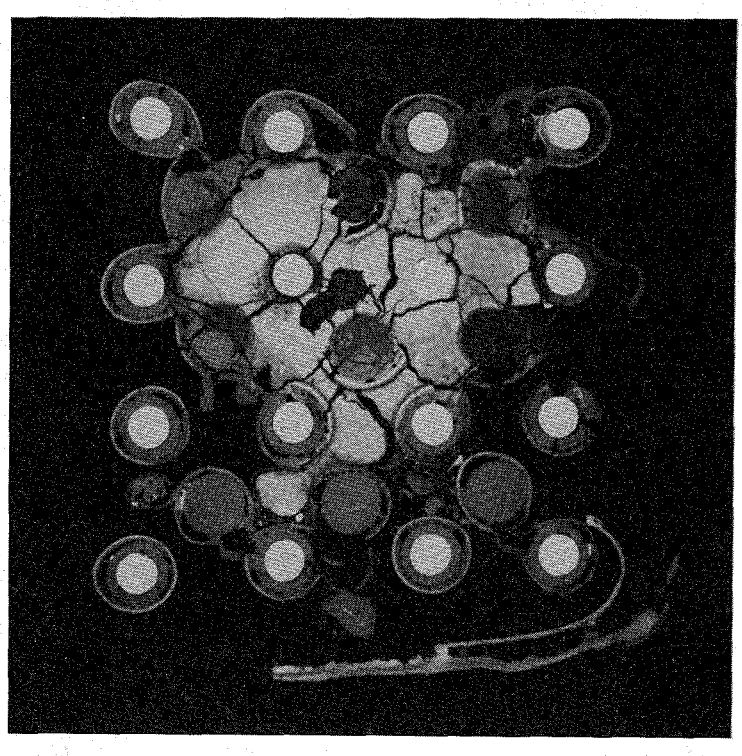

polished

10 mm

CORA bundle 2

KfK IMF I, PRS

Fig. 46. CORA-2 bundle cross-section number 6 (268 mm). The relocated once molten material forms the large blockage of this elevation.

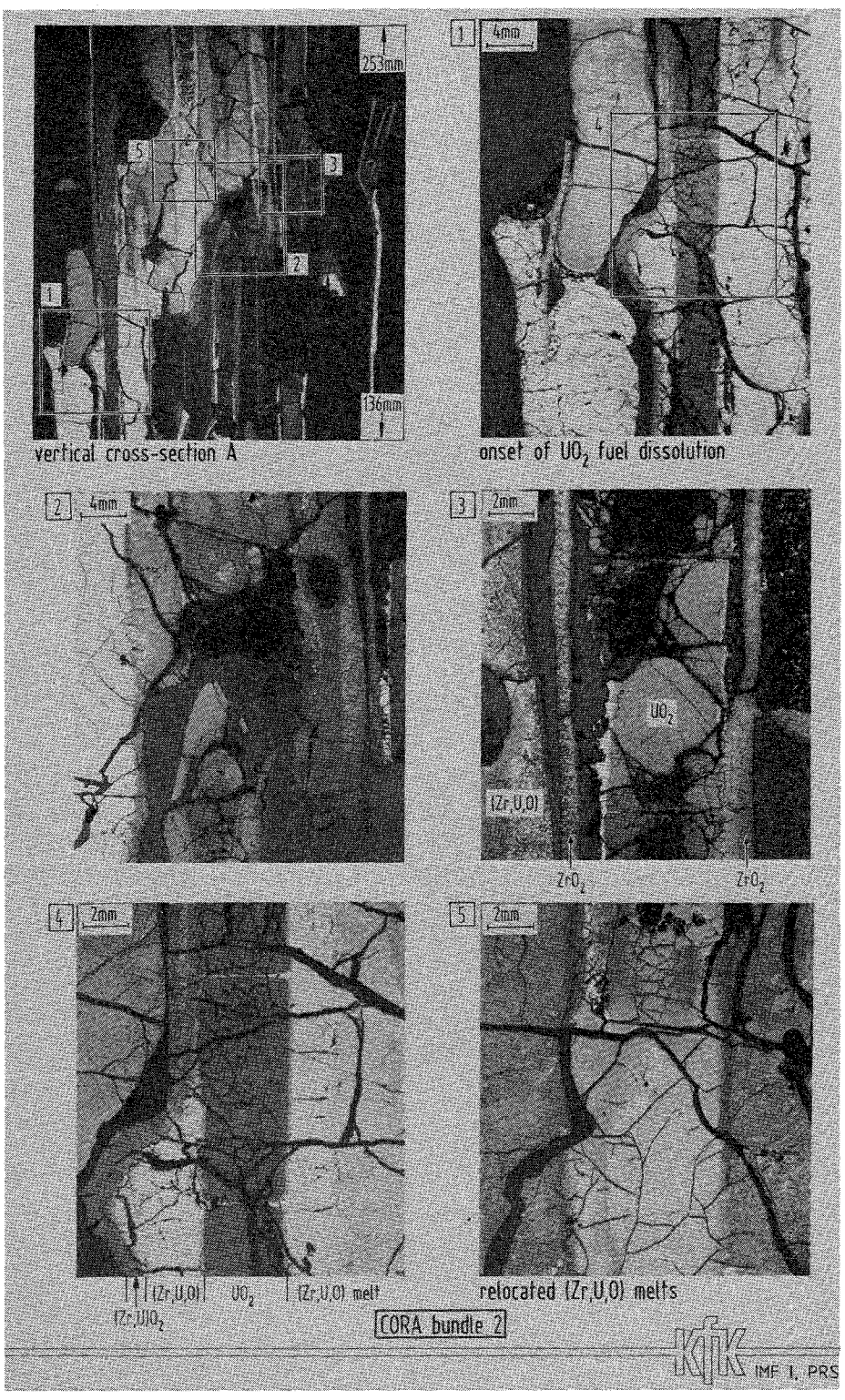

Fig. 47. Microstructures of CORA bundle 2 vertical cross-section A (axial elevation 136-253 mm). Various solidified (Zr,U,O) melts containing different quantities of dissolved UO_2.

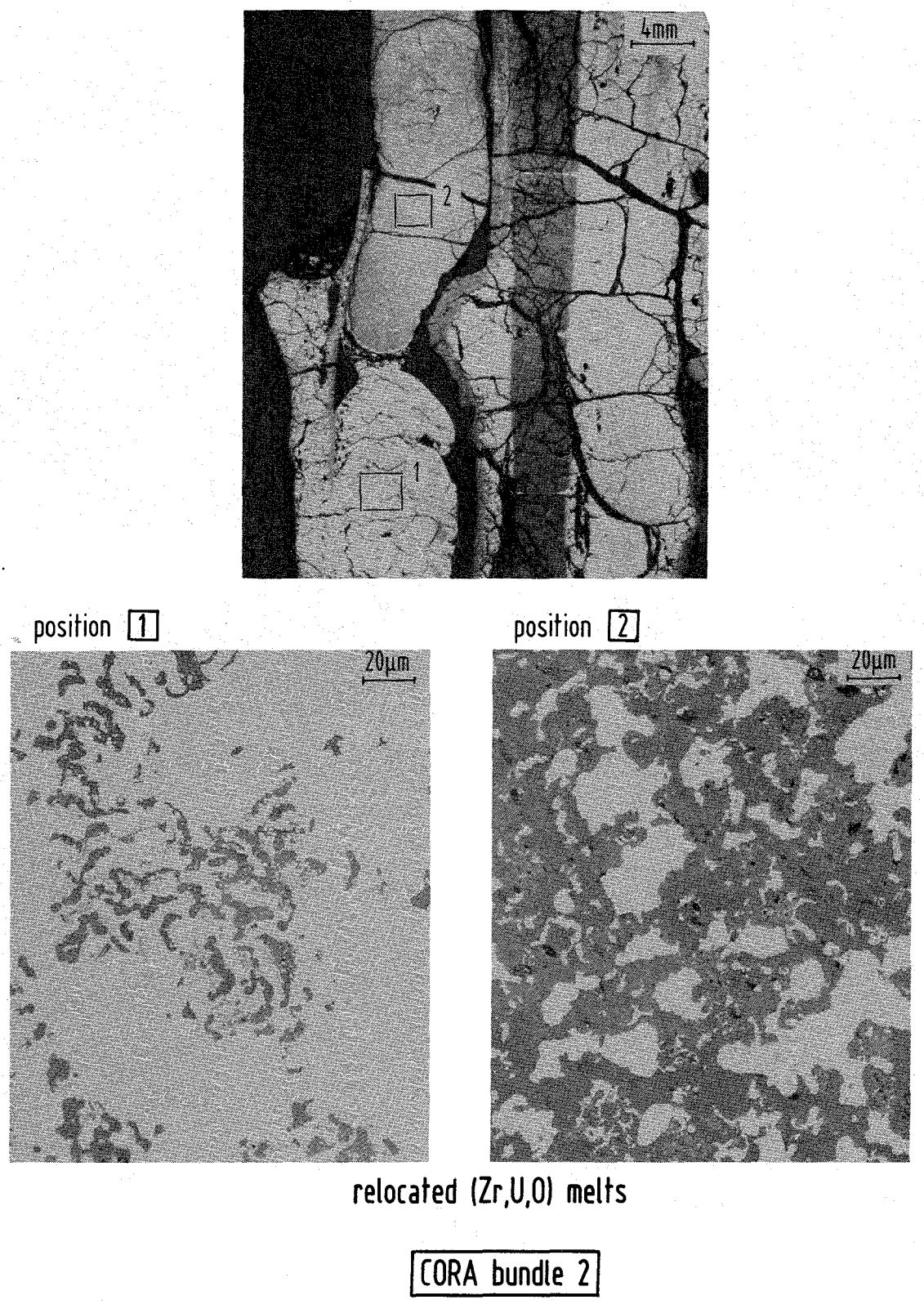

Fig. 48. Microstructures of CORA bundle 2 vertical cross-section A. Details of Figure 47.

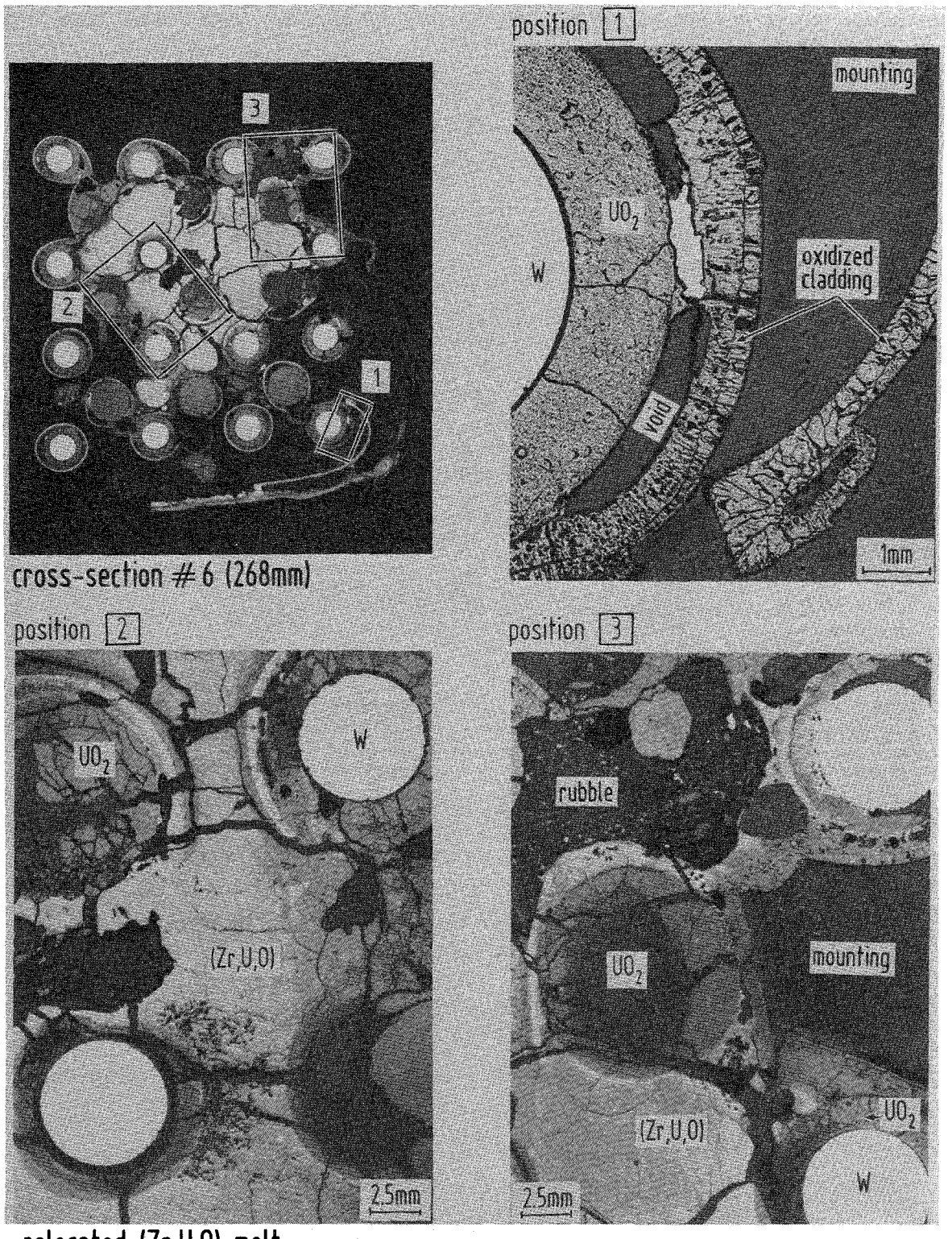

Fig. 49. CORA-2 bundle cross-section number 6 (268 mm). Strong UO_2 attack by molten Zircaloy.

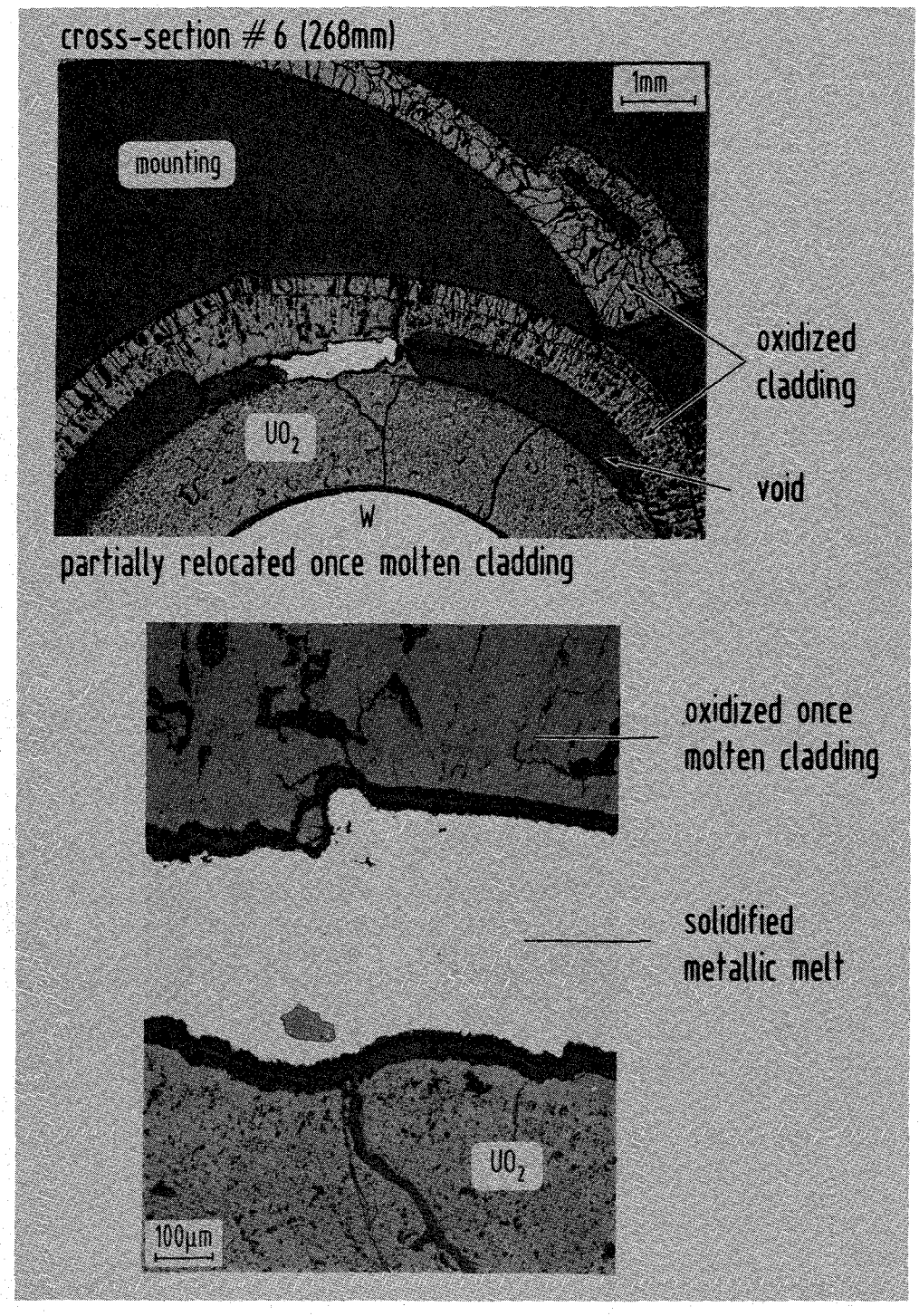

Fig. 50. Formation of voids due to relocation of molten cladding (see. Fig. 68).

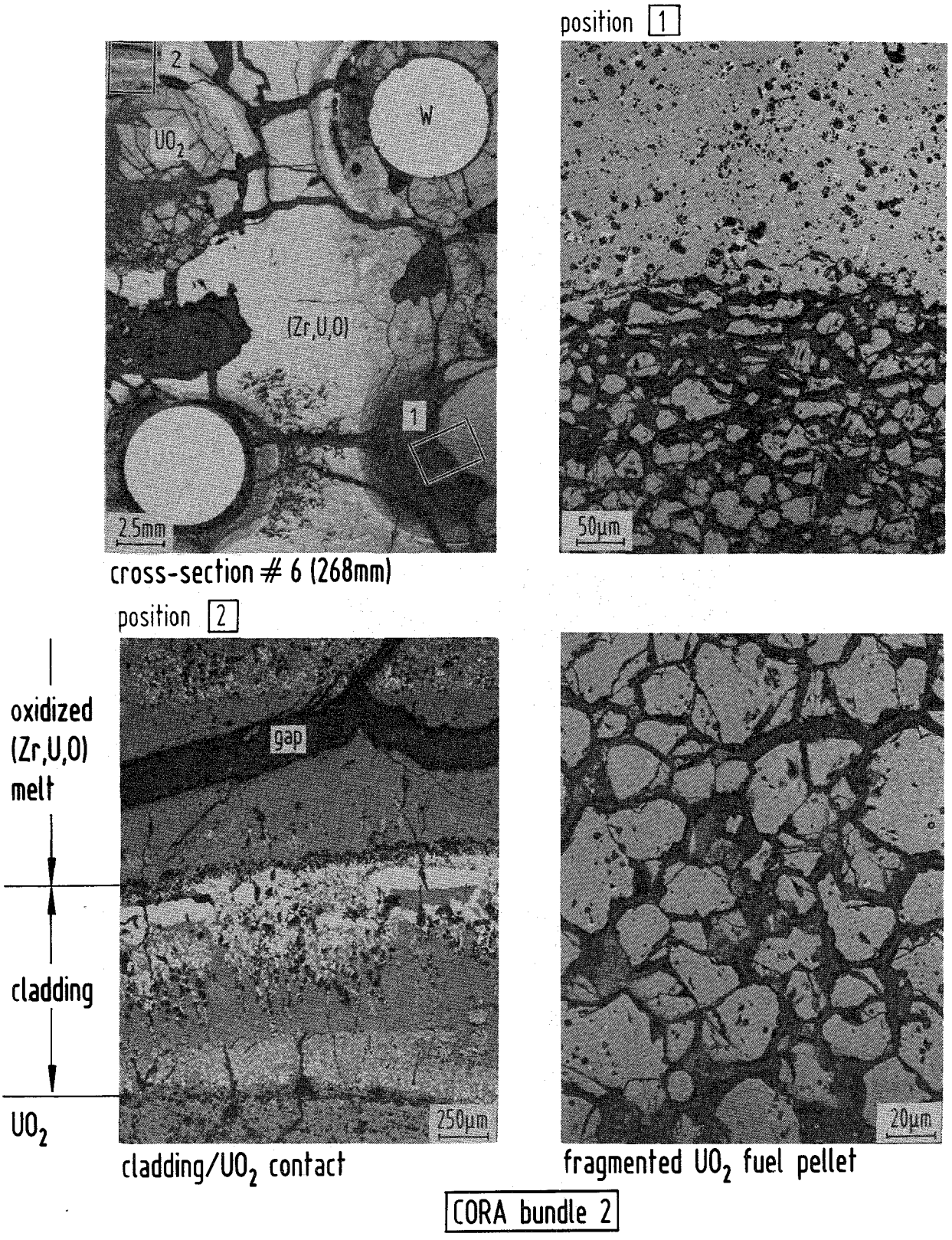

Fig. 51. Microstructures of CORA-2 bundle cross-section number 6 (268 mm)

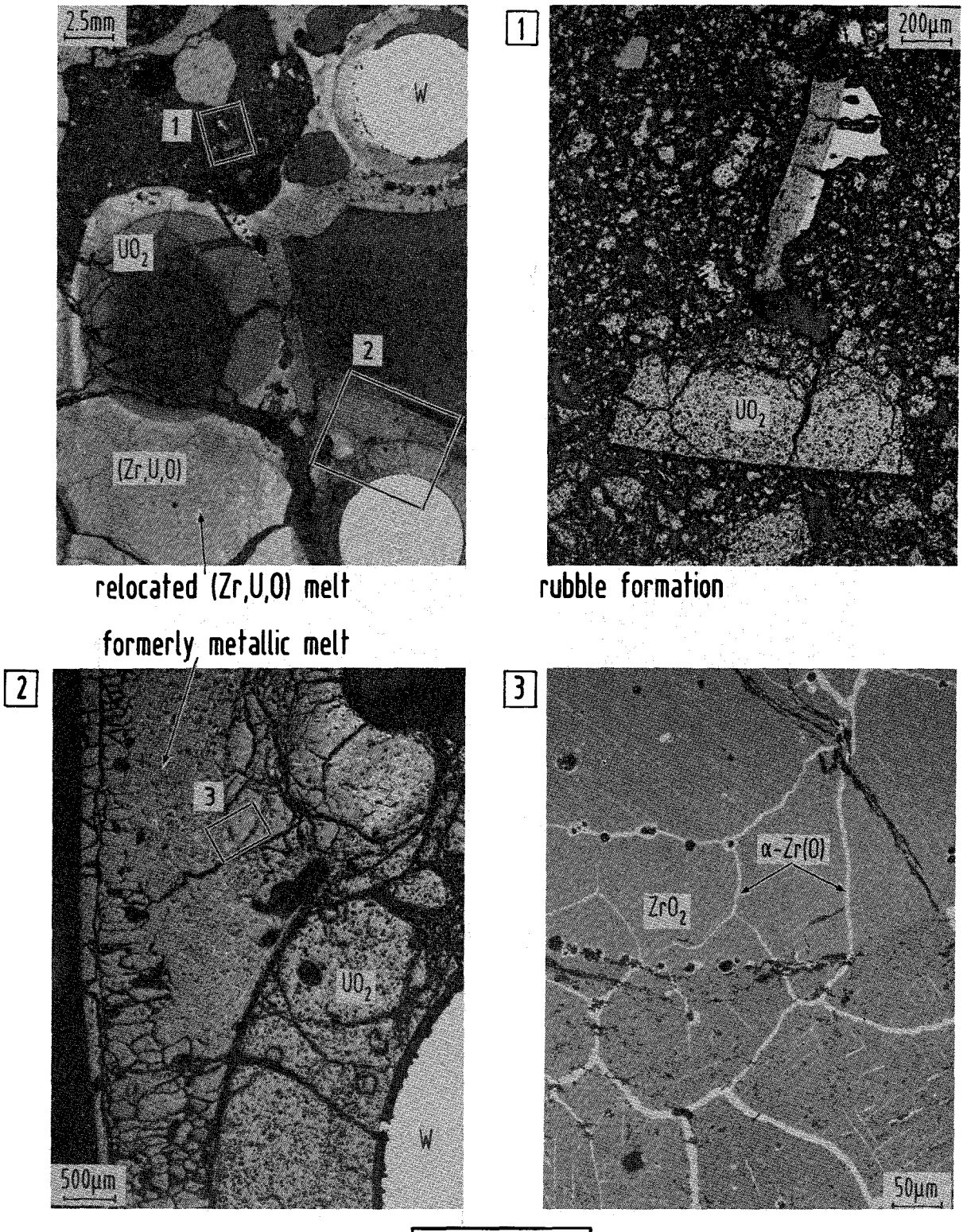

Fig. 52. Microstructures of CORA-2 bundle cross-section number 6 (268 mm). Accumulation of rubble.

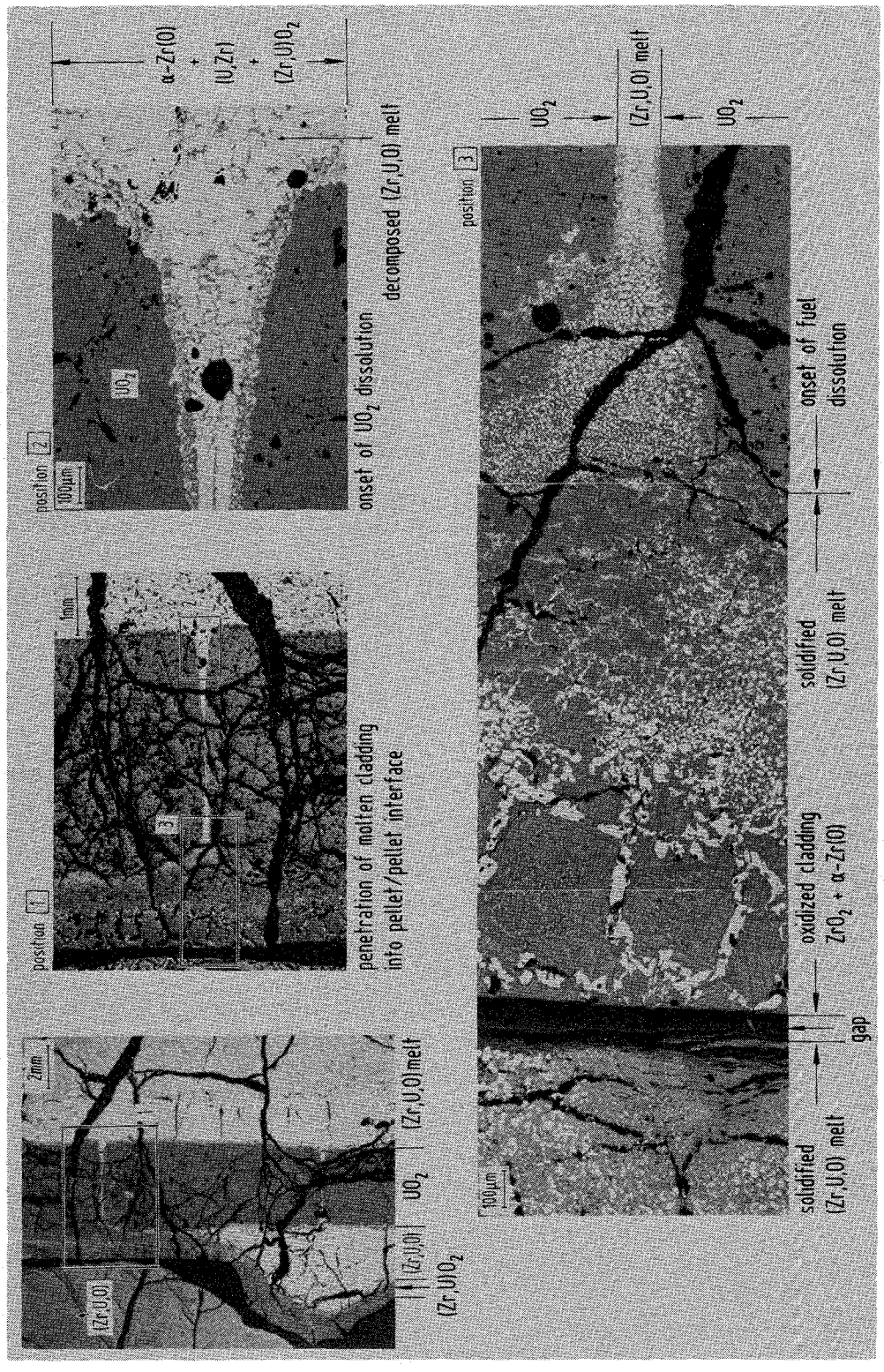

Fig. 53. Microstructures of CORA bundle 2 vertical cross-section A (axial elevation 136-253 mm). Onset of UO_2 fuel dissolution by molten Zircaloy.

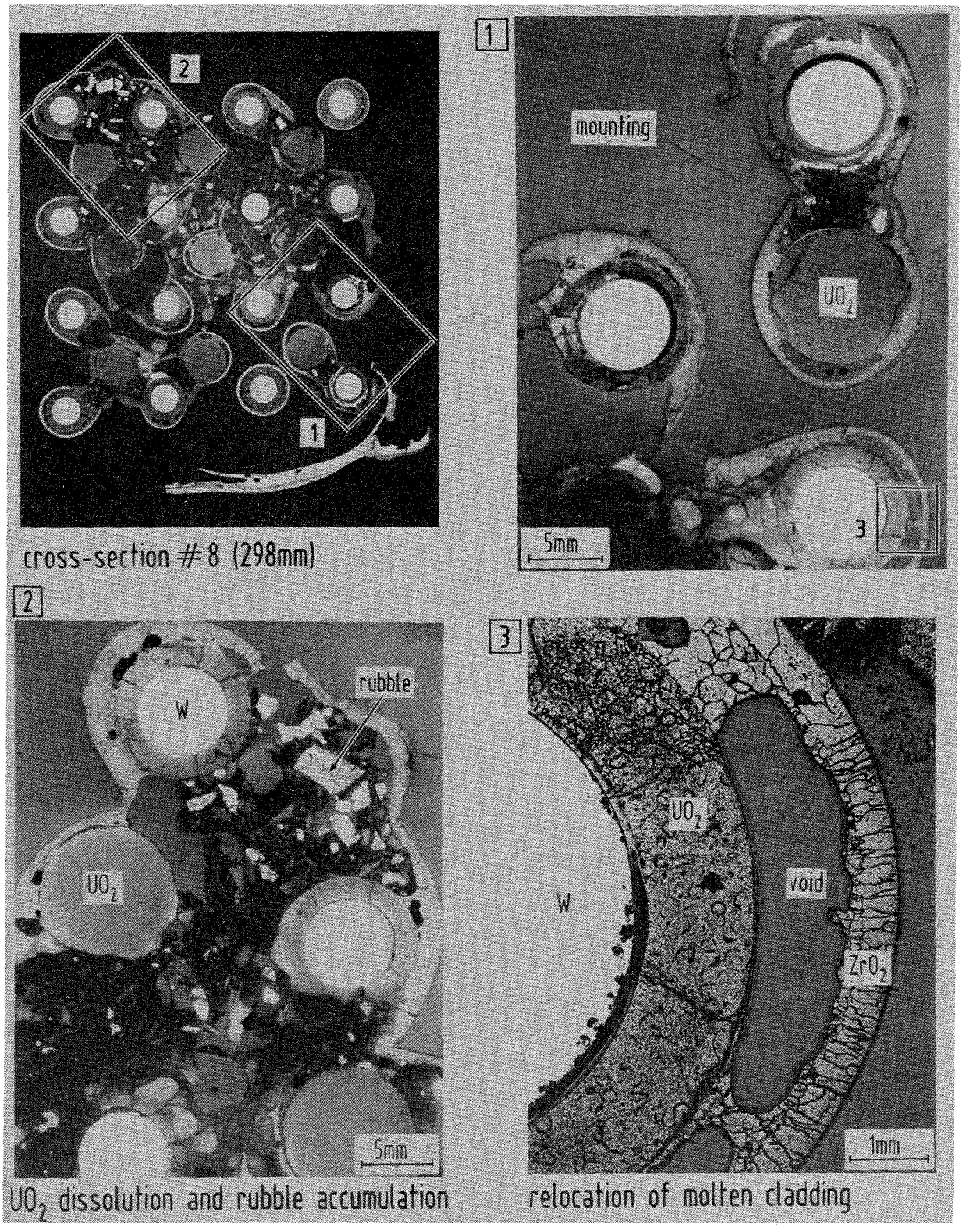

Fig. 54. CORA-2 bundle cross-section number 8 (298 mm). Strong Zircaloy cladding disintegration.

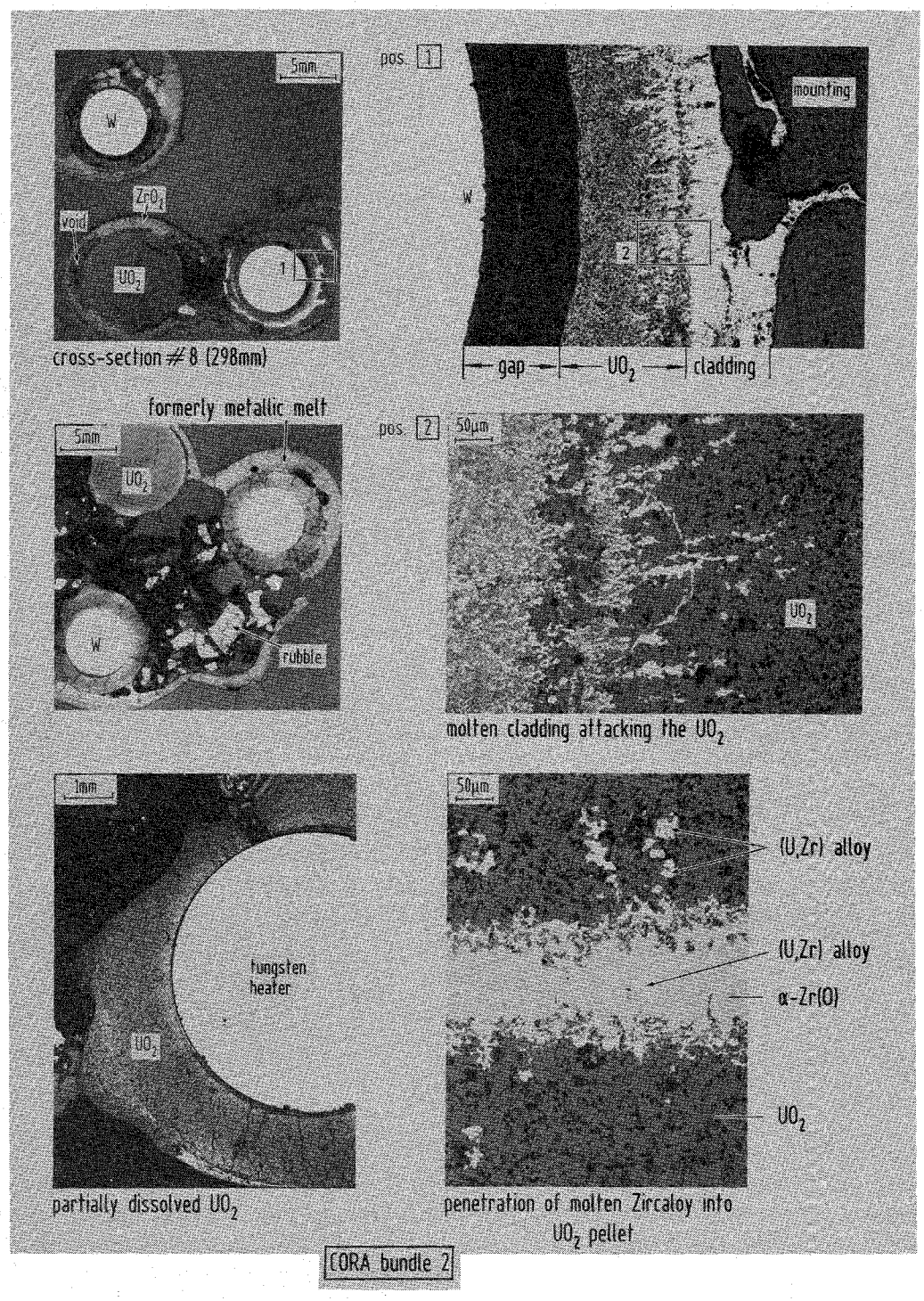

Fig. 55. Microstructures of CORA-2 bundle cross-section number 8 (298 mm). Strong UO_2 fuel dissolution by molten Zircaloy.

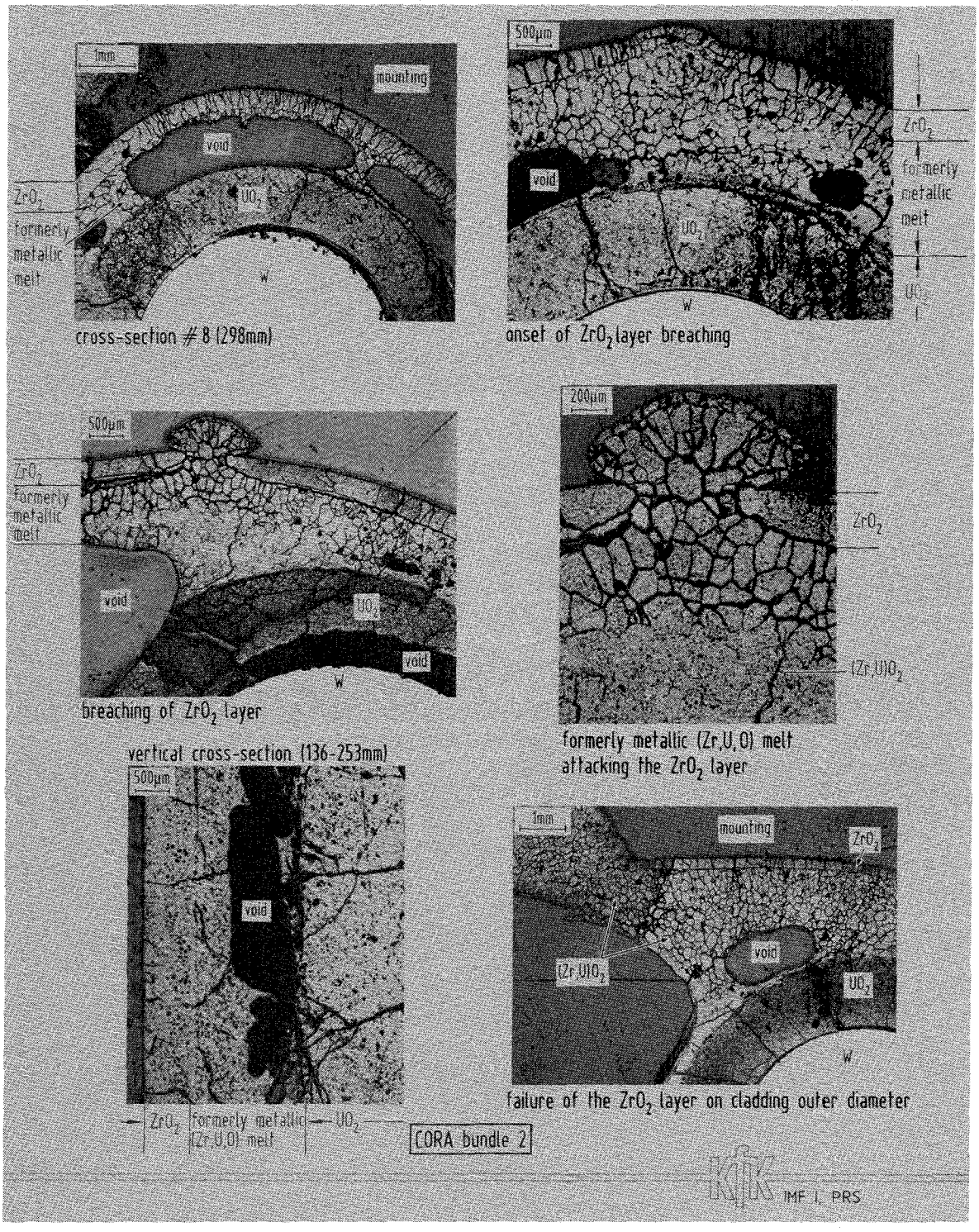

Fig. 56. Microstructures of CORA-2 bundle cross-section number 8 (298 mm). Attack of the UO_2 and ZrO_2 on cladding surface by molten Zircaloy.

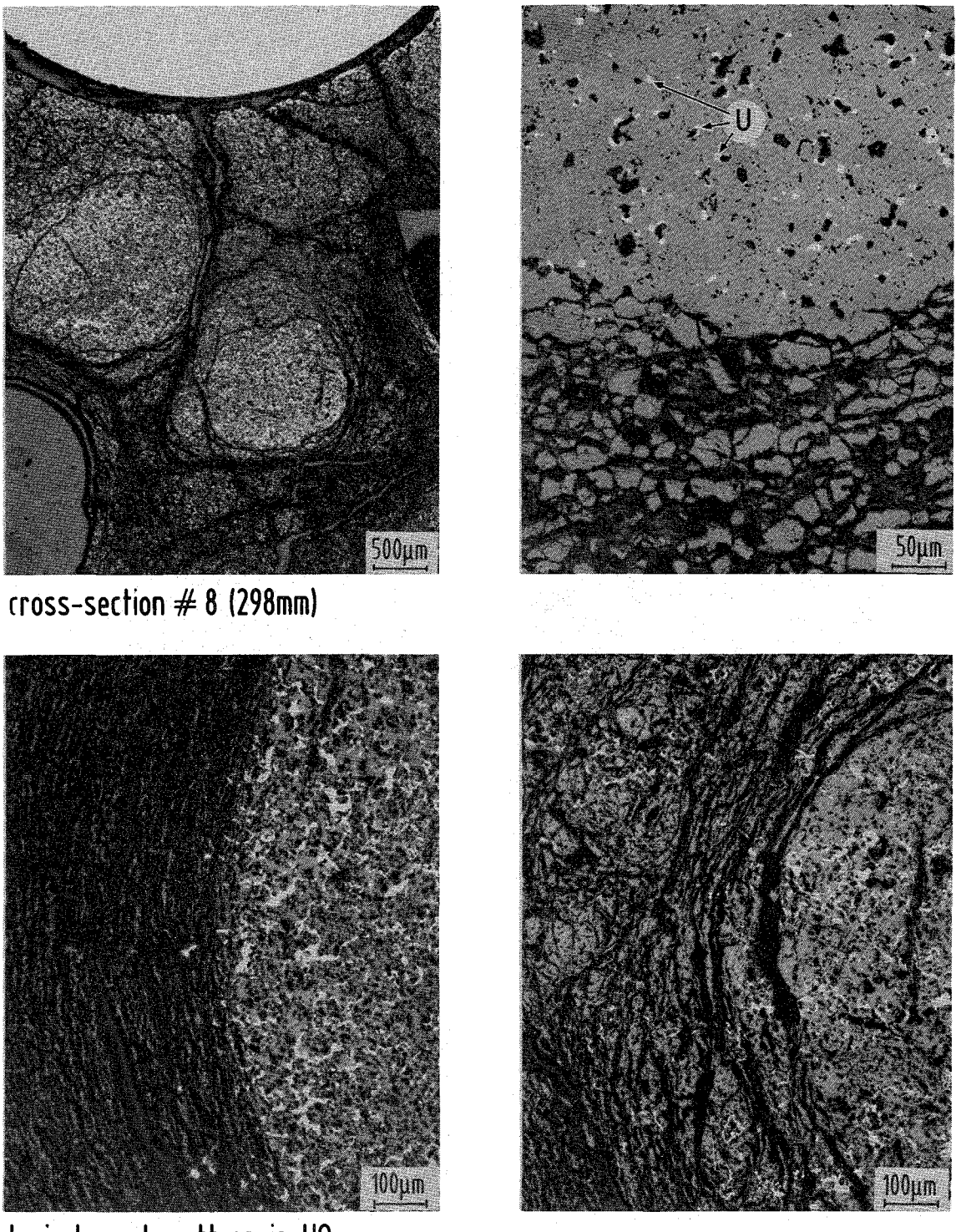

Fig. 57. Microstructures of CORA-2 bundle cross-section number 8 (298 mm). Crack pattern in UO_2 pellets.

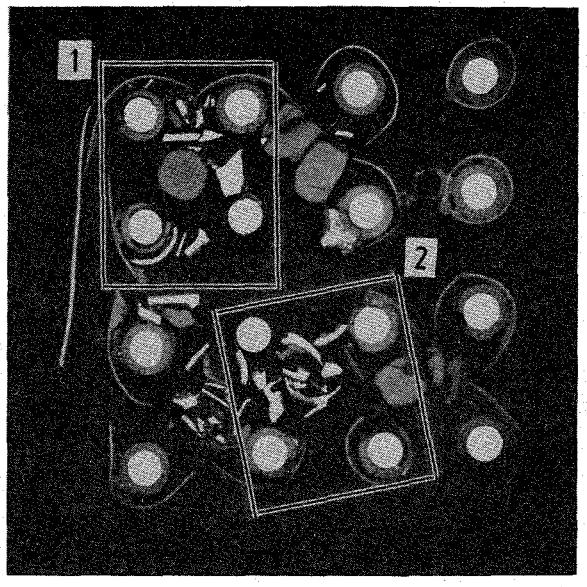

cross-section # 12 (480mm)

position 1

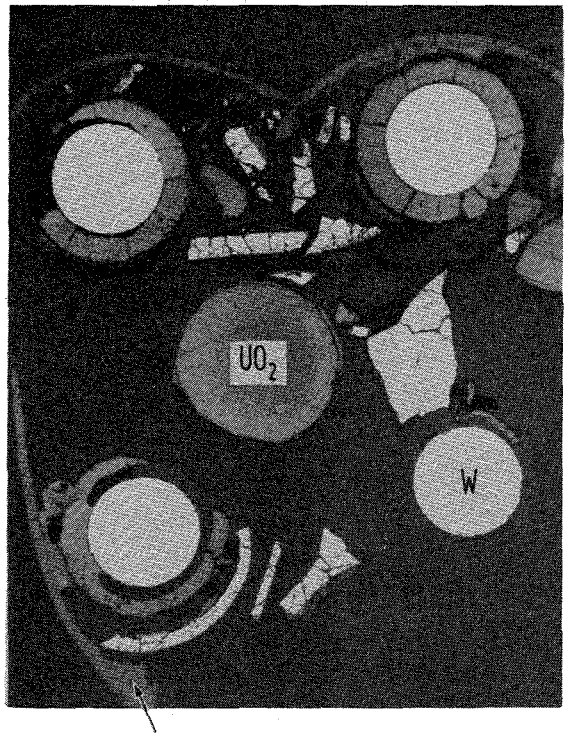

oxidized cladding

position 2

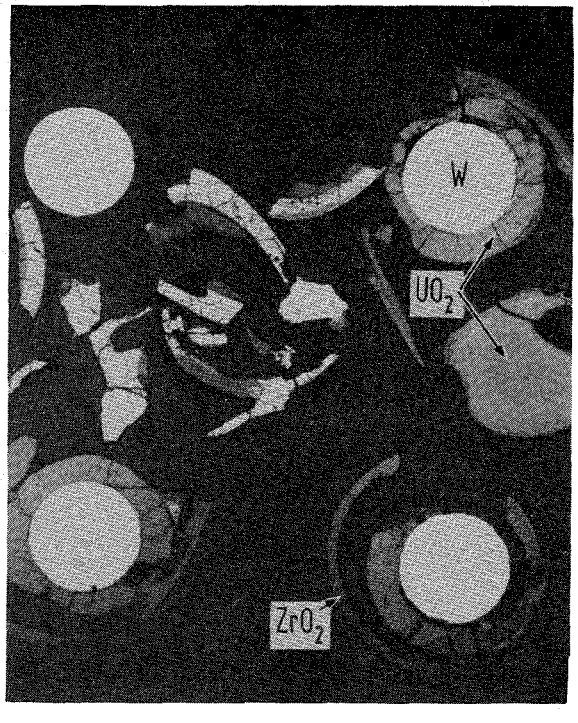

CORA bundle 2

Fig. 58. CORA-2 bundle cross-section number 12 (480 mm). Strong damage of the fuel rods

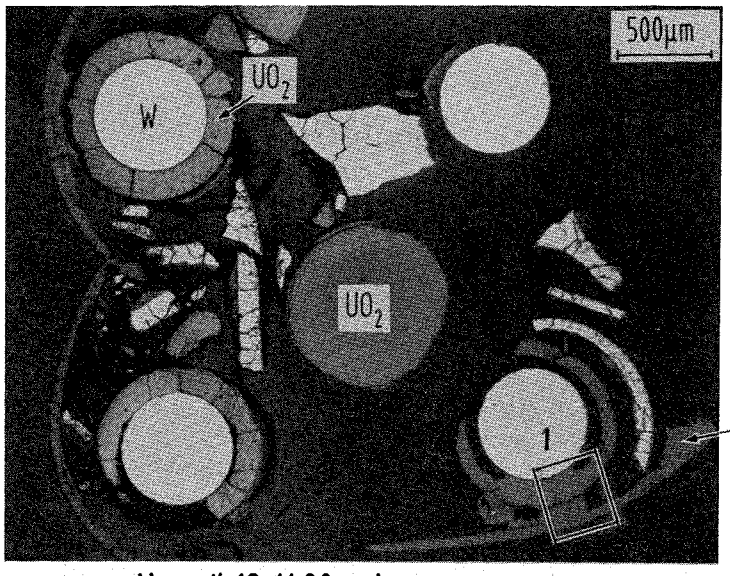

cross-section # 12 (480mm)

position [1]

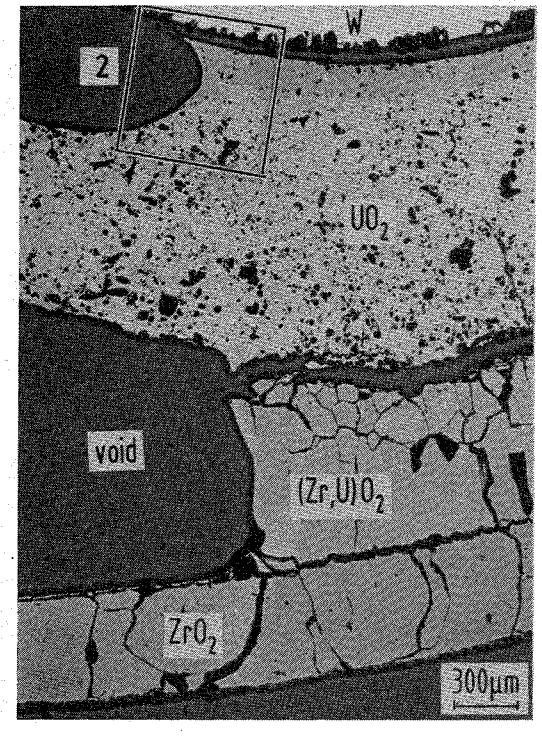

position [2]

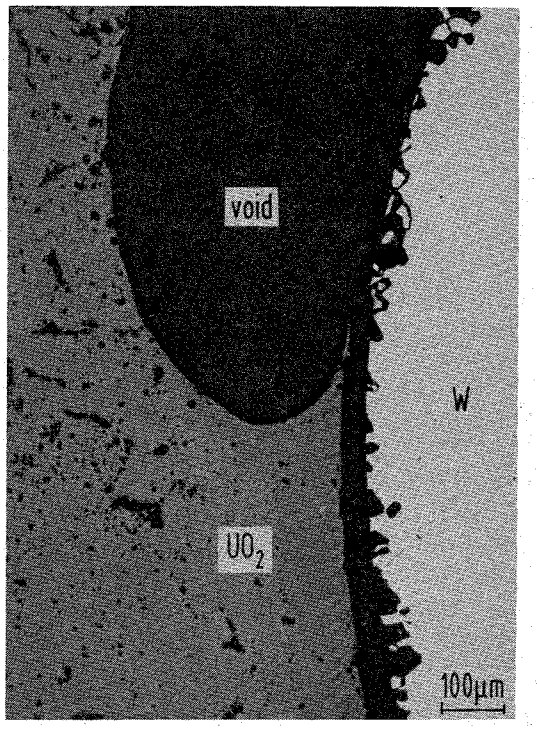

CORA bundle 2

KfK IMF I, PRS

Fig. 59. Microstructures of CORA-2 bundle cross-section12 (480 mm). Relocation of molten Zircaloy and "liquefied" UO_2; formation of large voids.

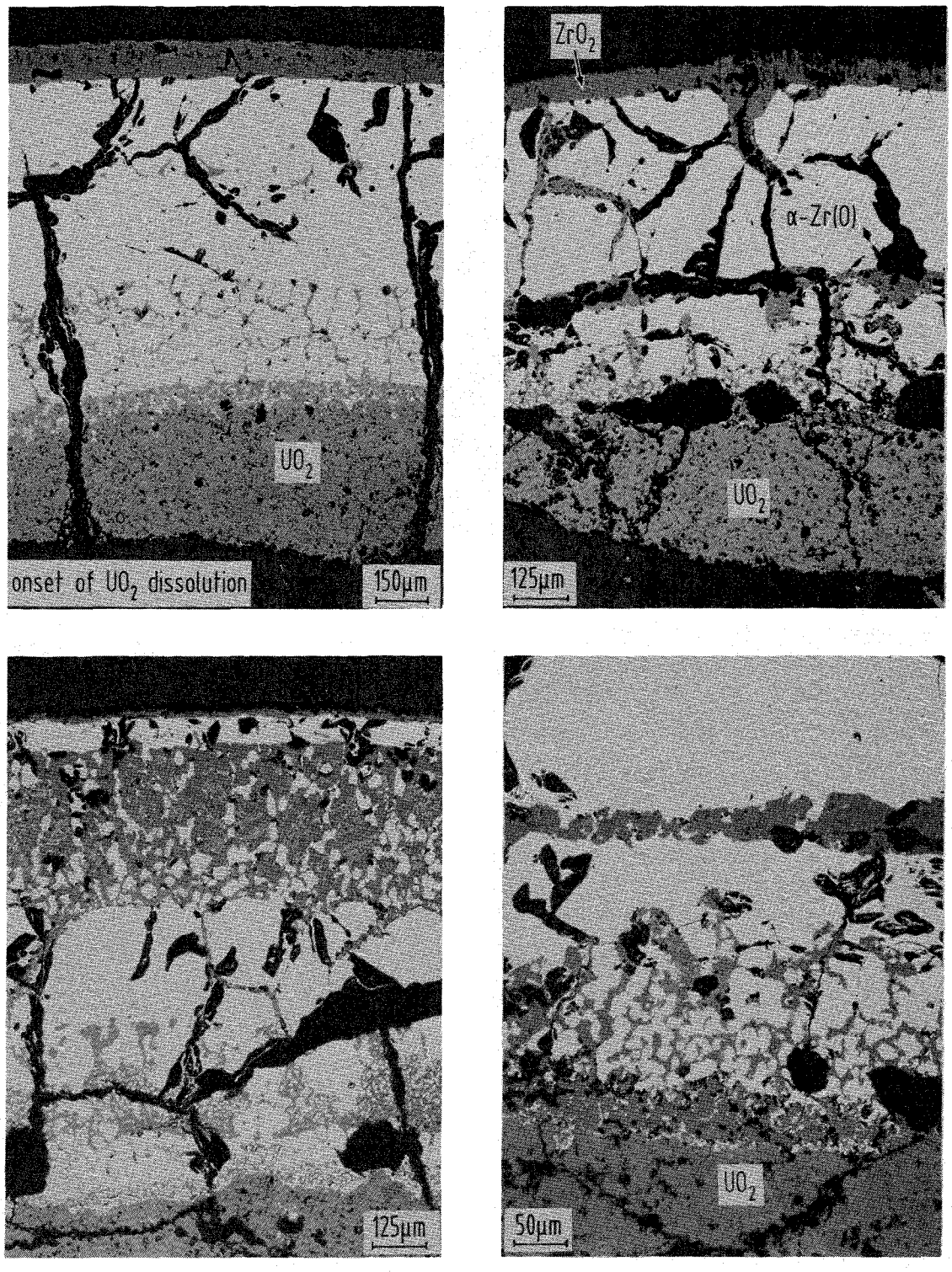

Fig. 60. Microstructures of CORA-2 bundle cross-section12 (480 mm). Oxidation of the Zircaloy by steam and attack of the UO_2 by the Zircaloy.

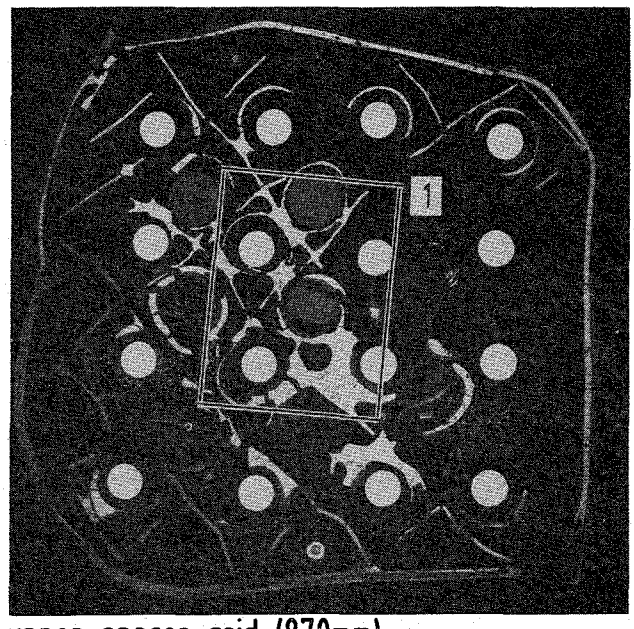

upper spacer grid (870mm)

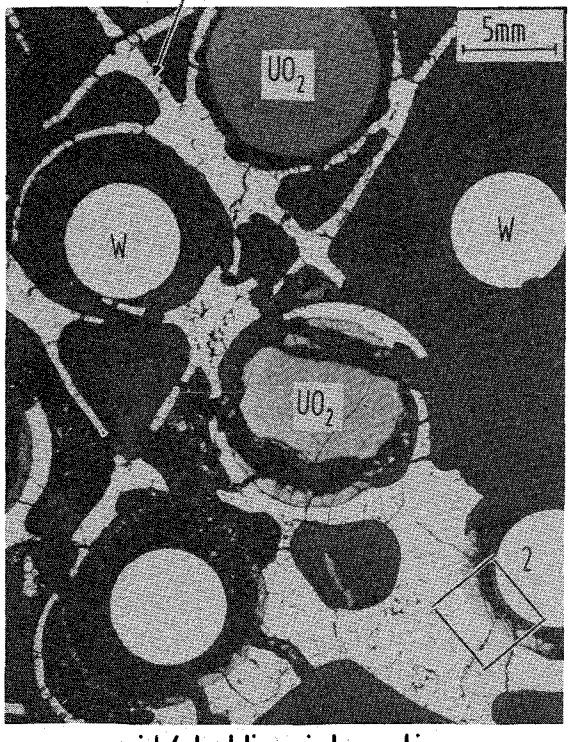

spacer grid/cladding interactions

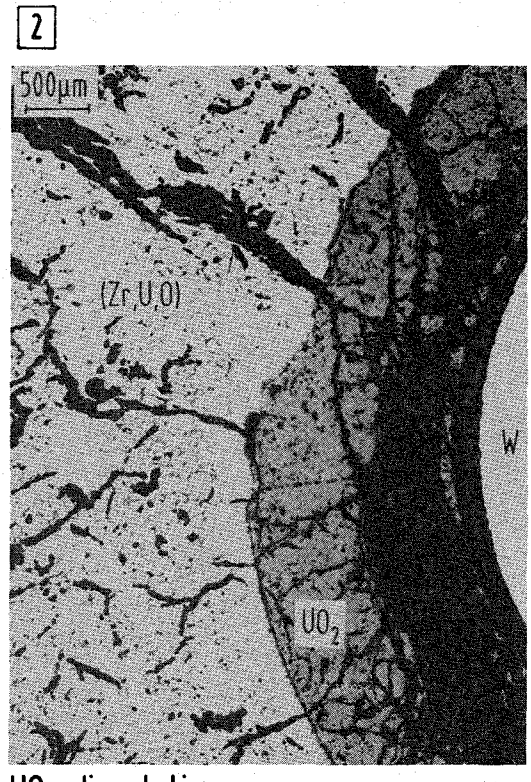

UO_2 dissolution

Fig. 61. CORA-2 bundle cross-section number 18 (870 mm). Strong damage of the fuel rods and spacer grid.

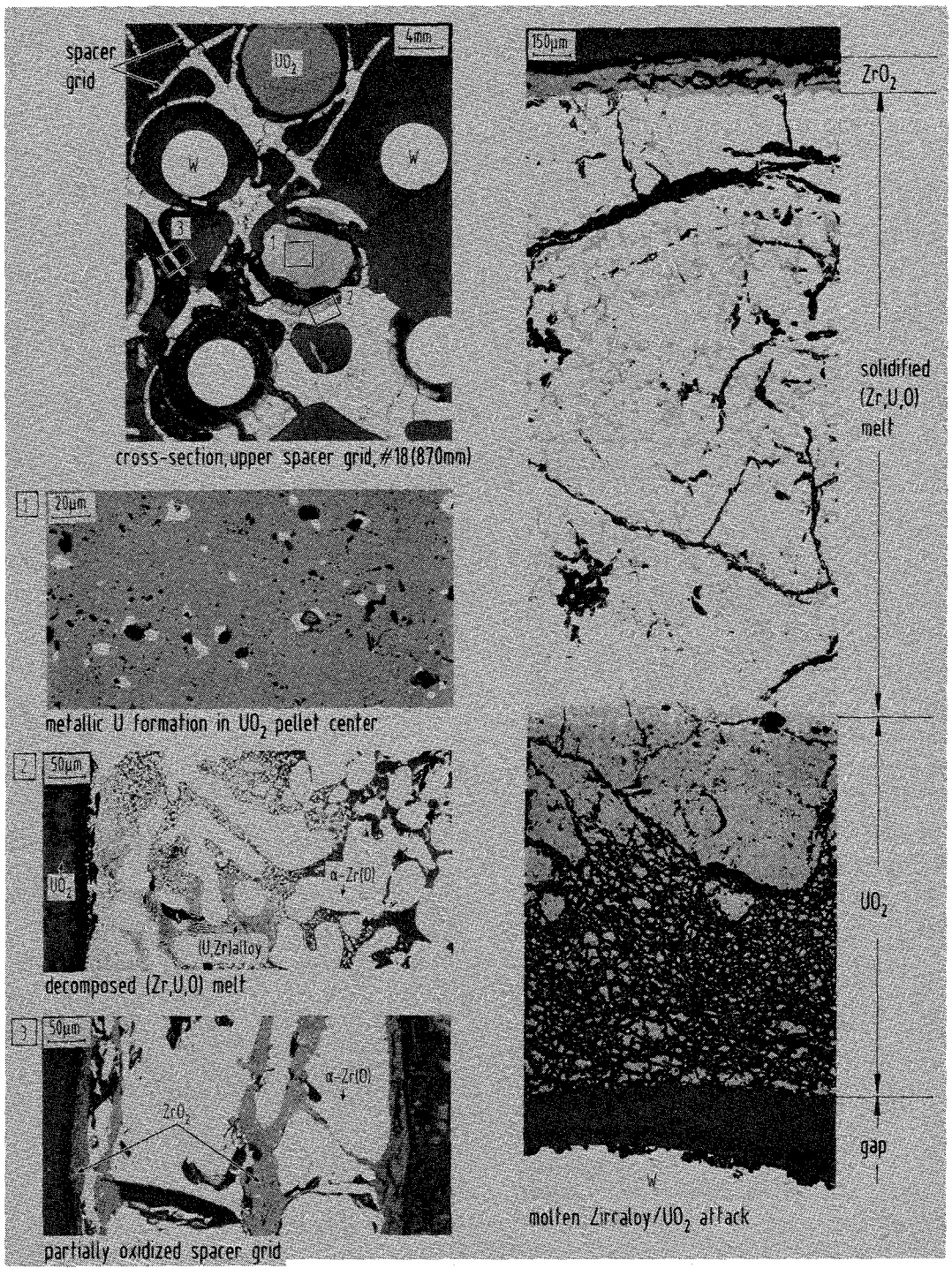

CORA bundle 2

Fig. 62. Microstructures of CORA-2 bundle cross-section 18 (870 mm). Details of Figure 61.

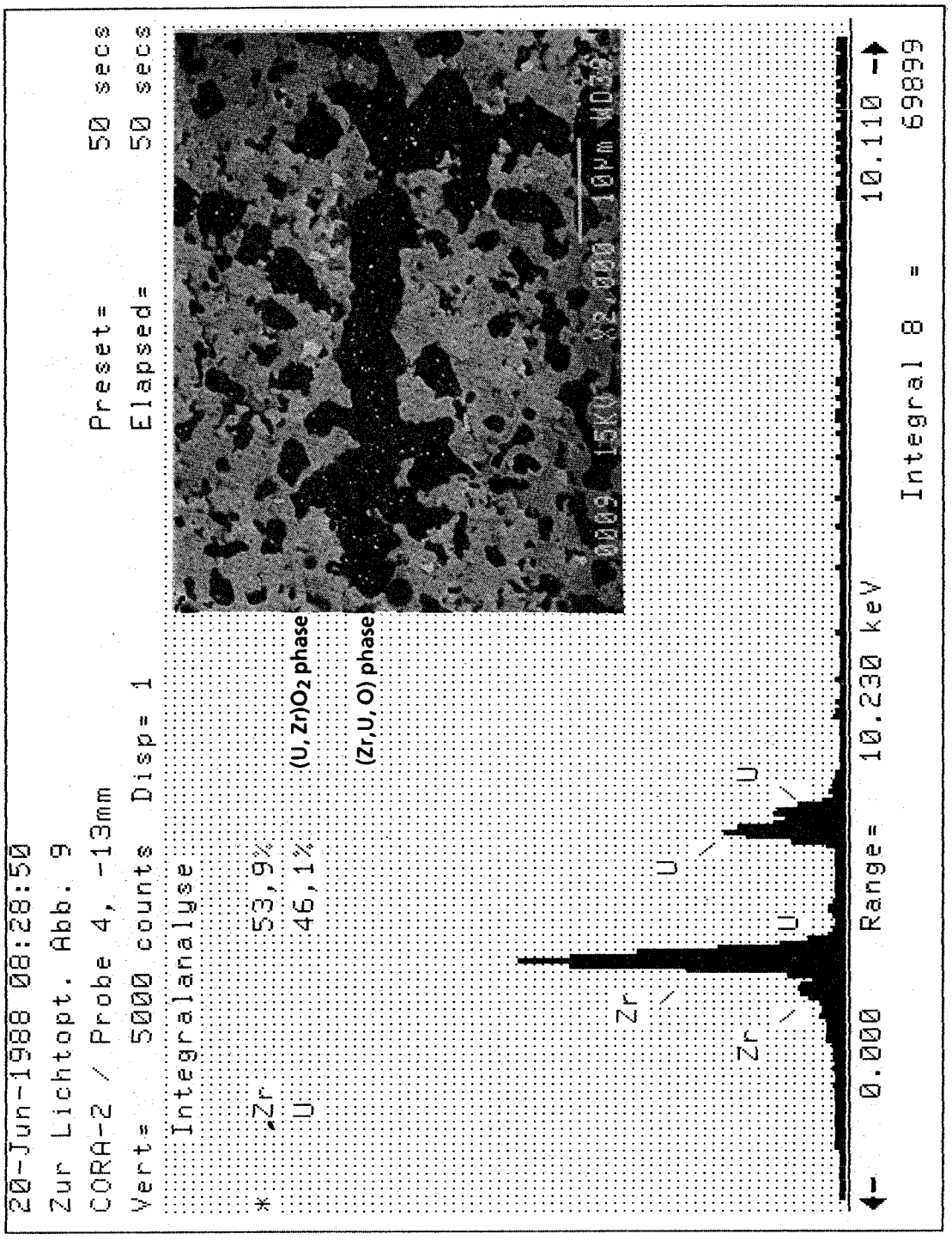

Fig. 63. Integral analysis and microstructure of melt lump at lower spacer grid elevation, resulting from Zry-UO_2 interaction

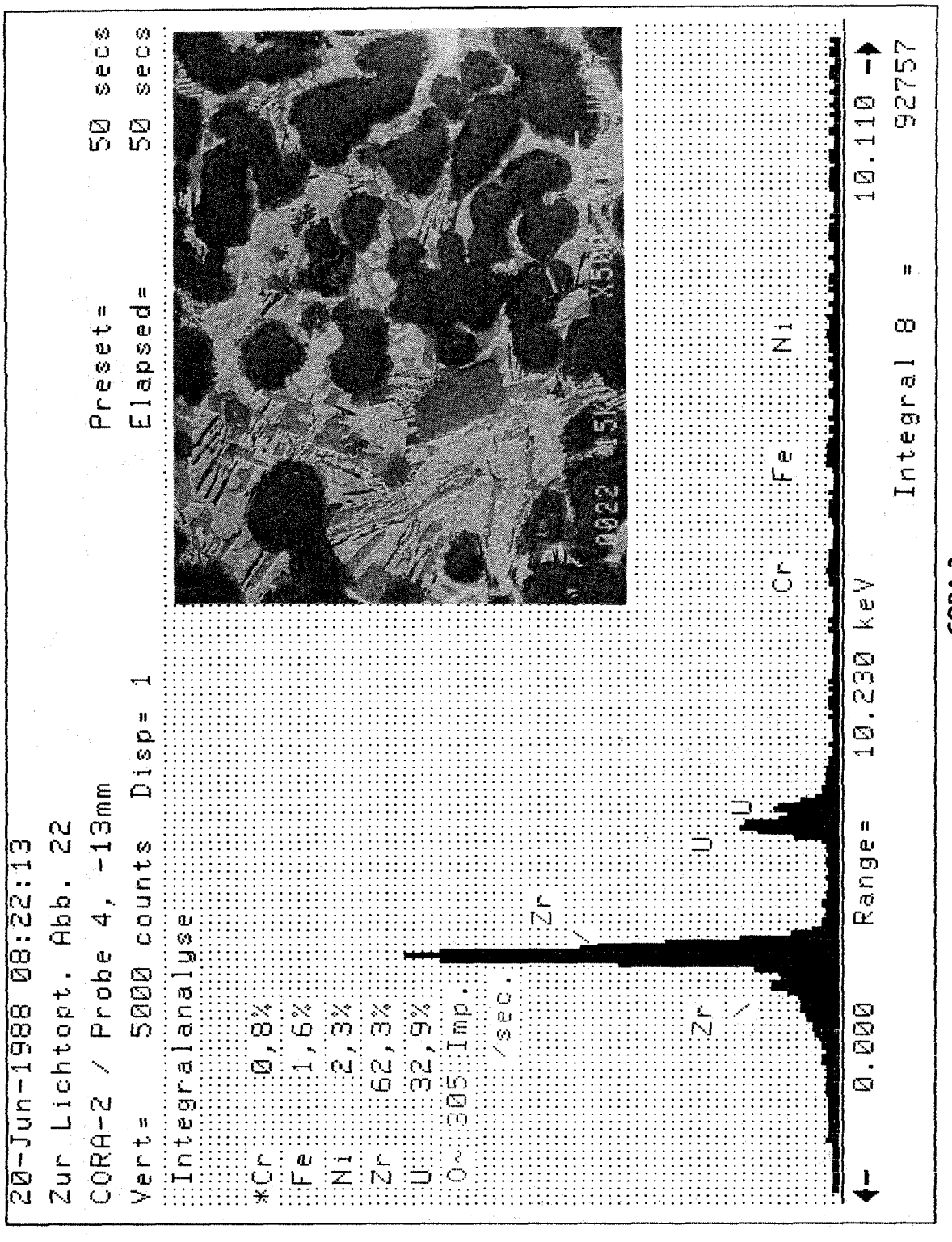

Fig. 64. Integral analysis of melt droplet, alloyed with some Inconel

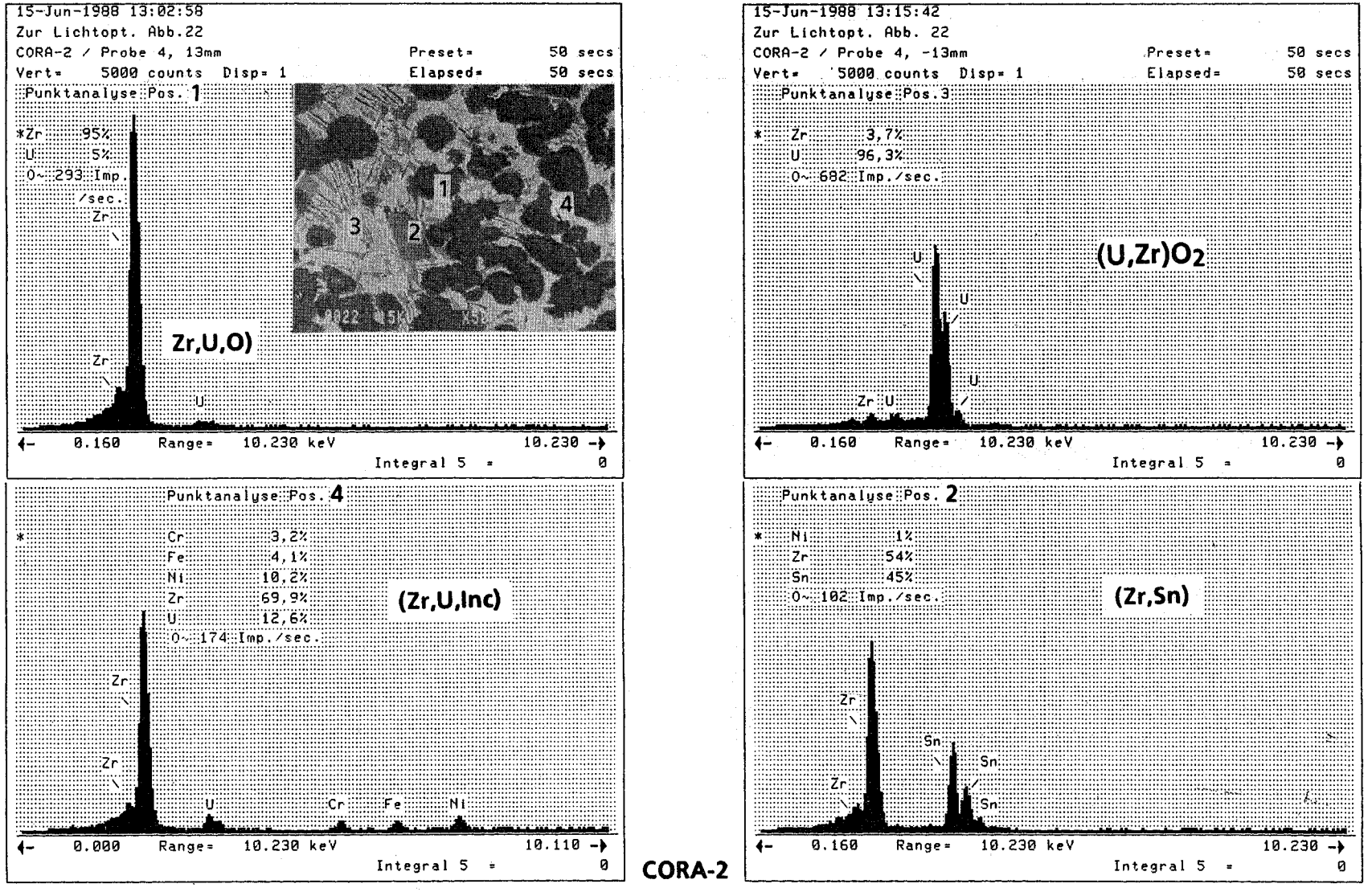

Fig. 65. Phase analysis of Inconel-alloyed melt droplet

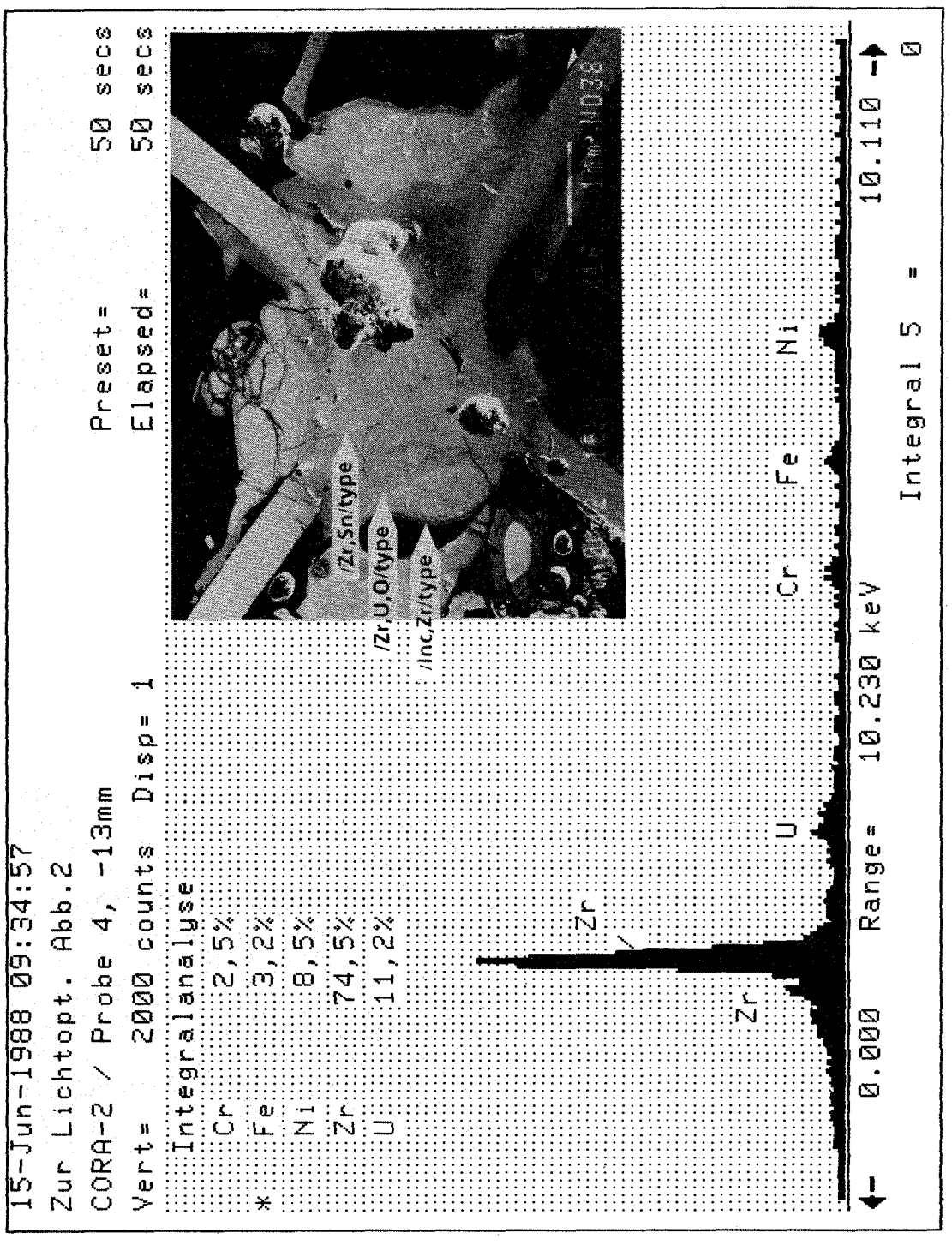

Fig. 66. Global analysis of melt at Zry spacer grid cross; agglomerate of three different types

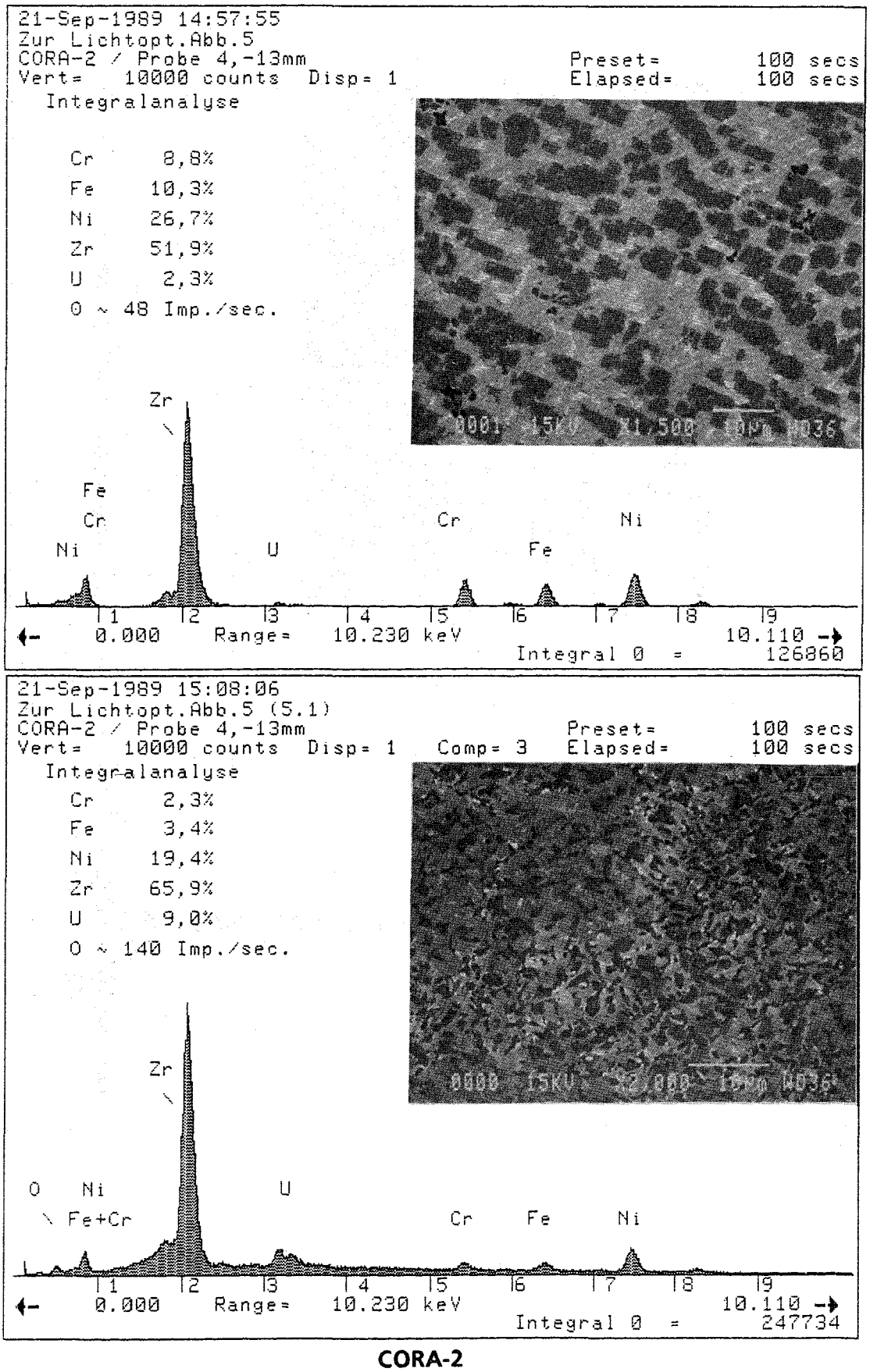

CORA-2

Fig. 67. Integral analysis of melt of (Inc, Zr) type near contact to attached melt of (Zr, U, O) type

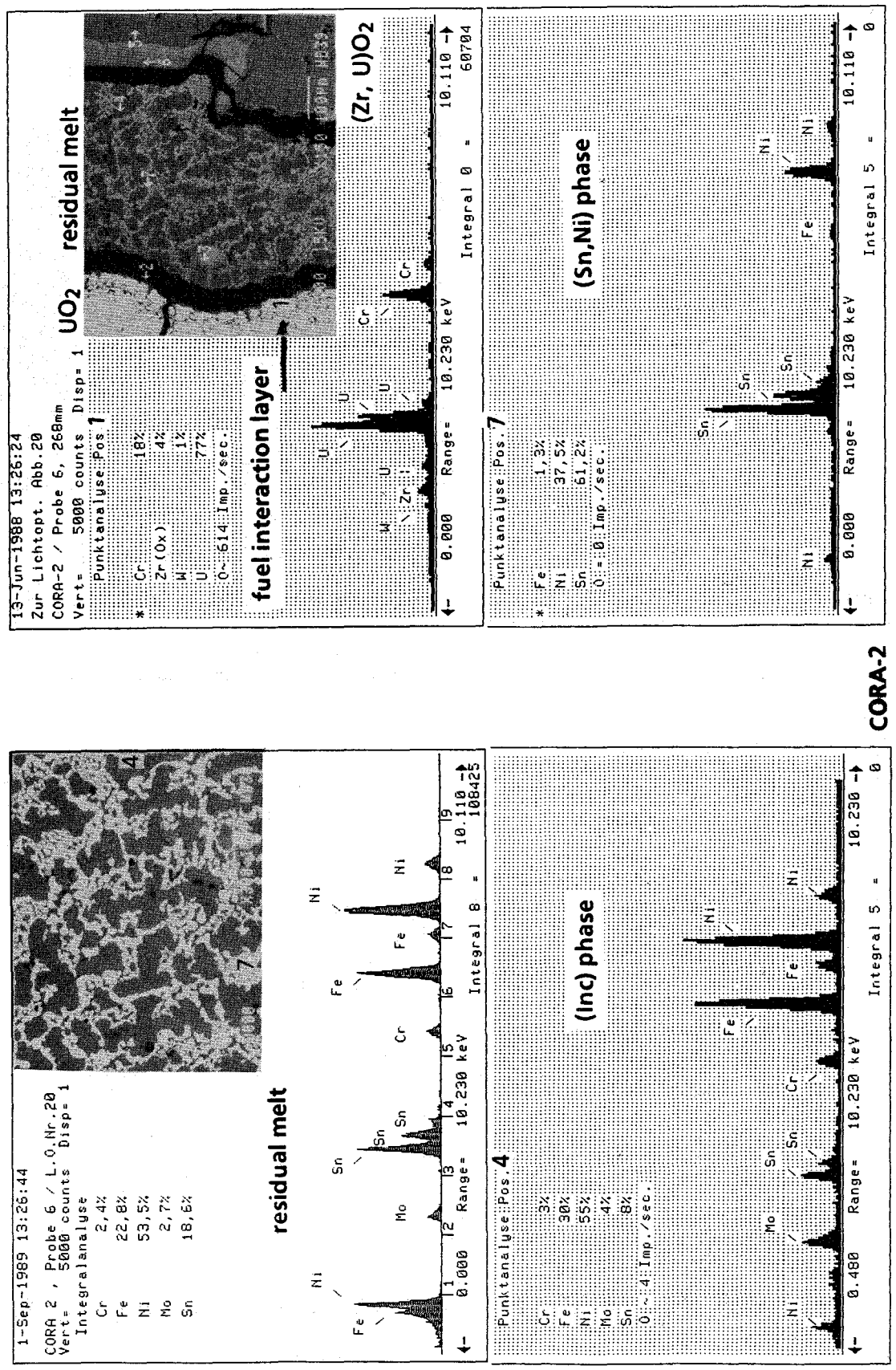

Fig. 68. Residual metallic melt in between attacked fuel pellet and transformed cladding (see Fig. 50).

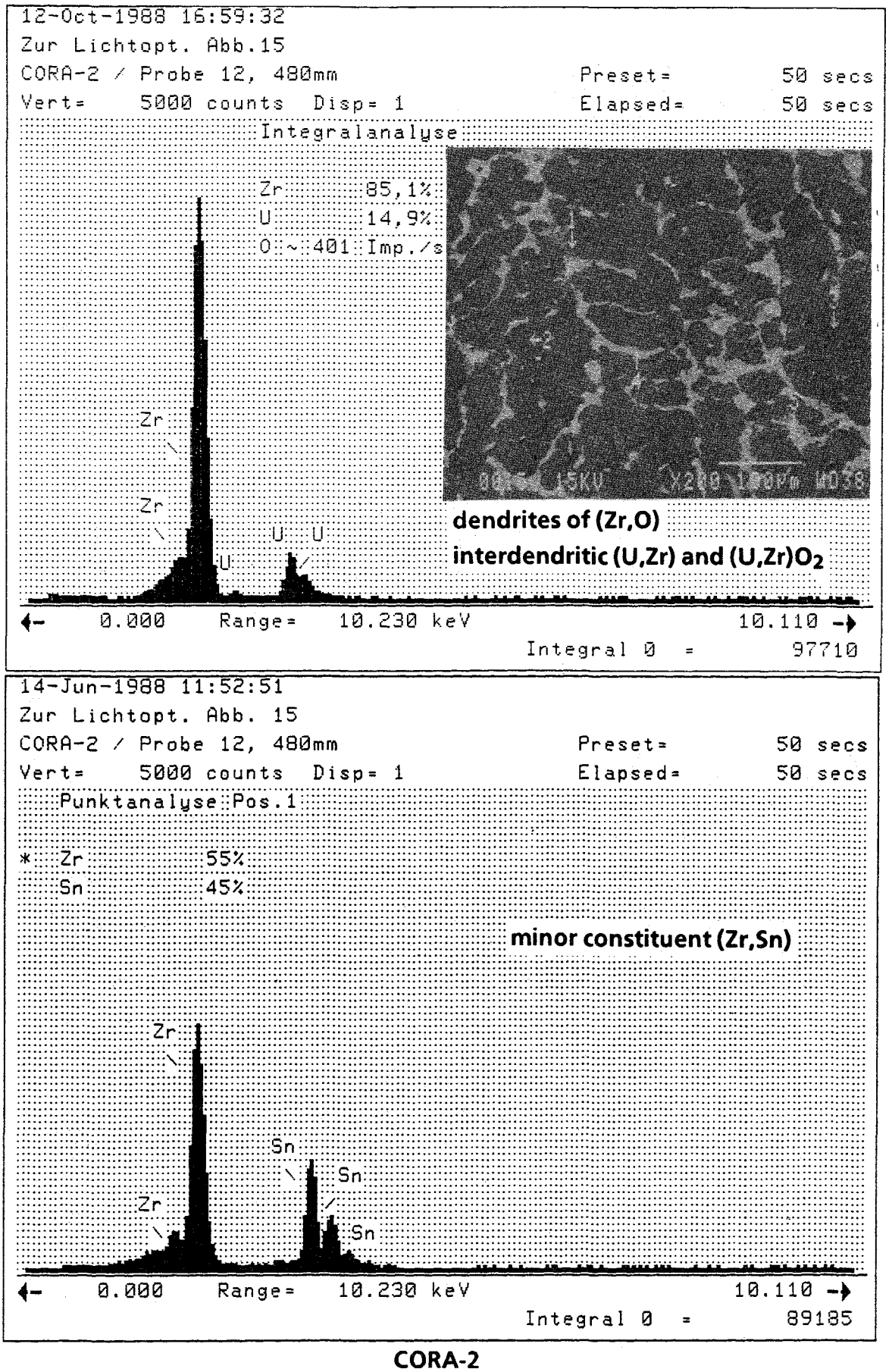

Fig. 69. Typical melt from Zry-UO_2 interaction, decomposed into (Zr,O), (U, Zr), (U, Zr)O_2 and (Zr, Sn).

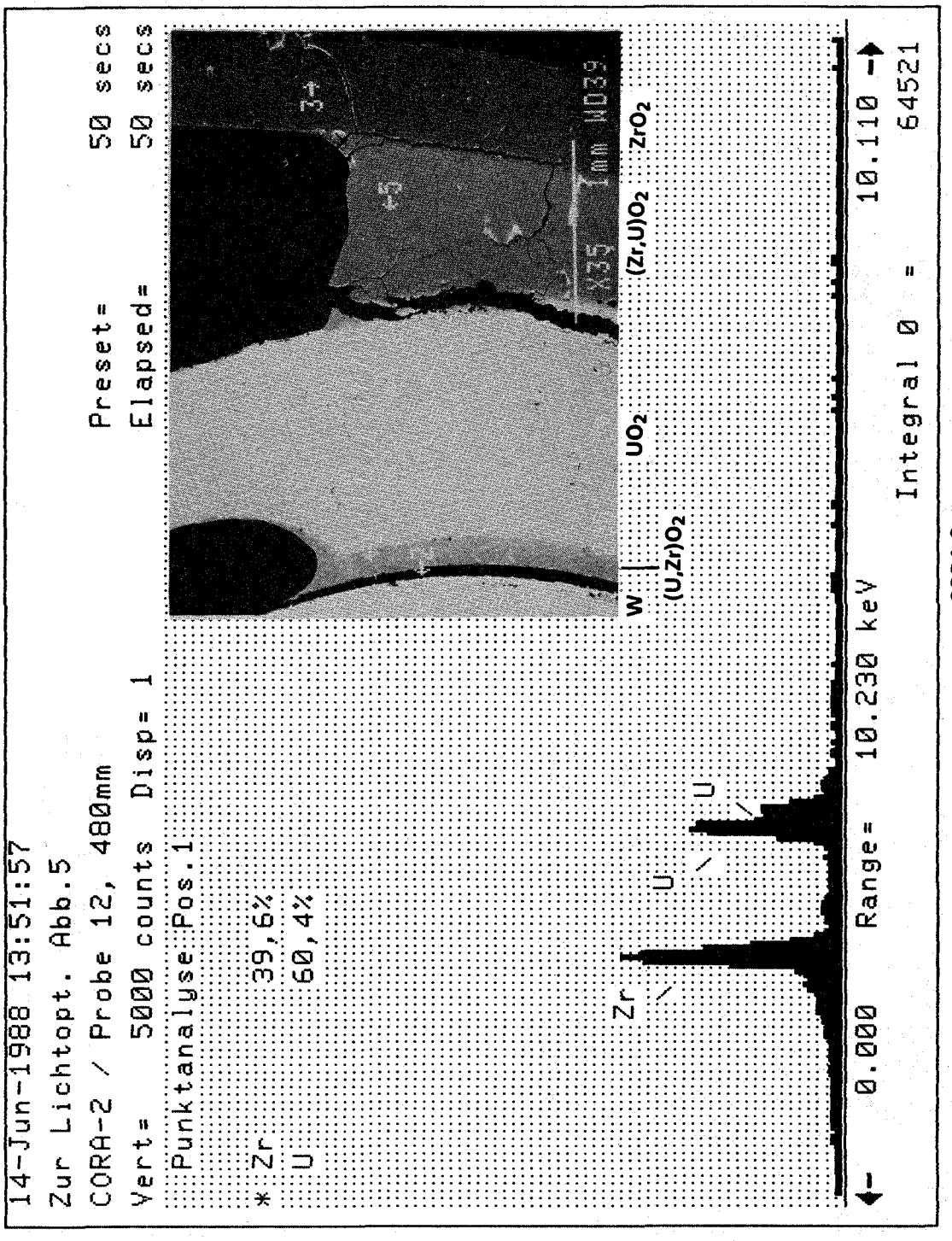

Fig. 70. Heated rod after internal and external fuel dissolution by subsequently oxidized metallic melts (see Fig. 59).

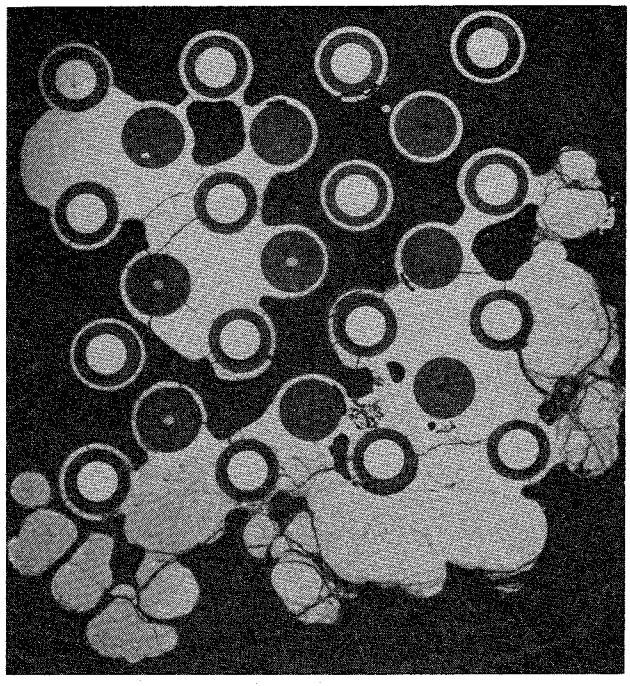

cross section 1 (20 mm) ⟷ 10 mm

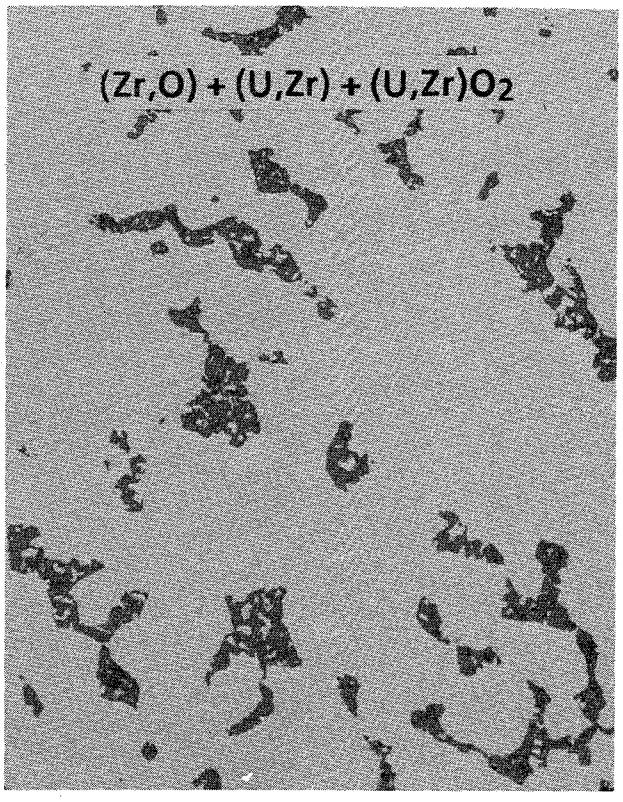

relocated melt ⟷ 20 µm

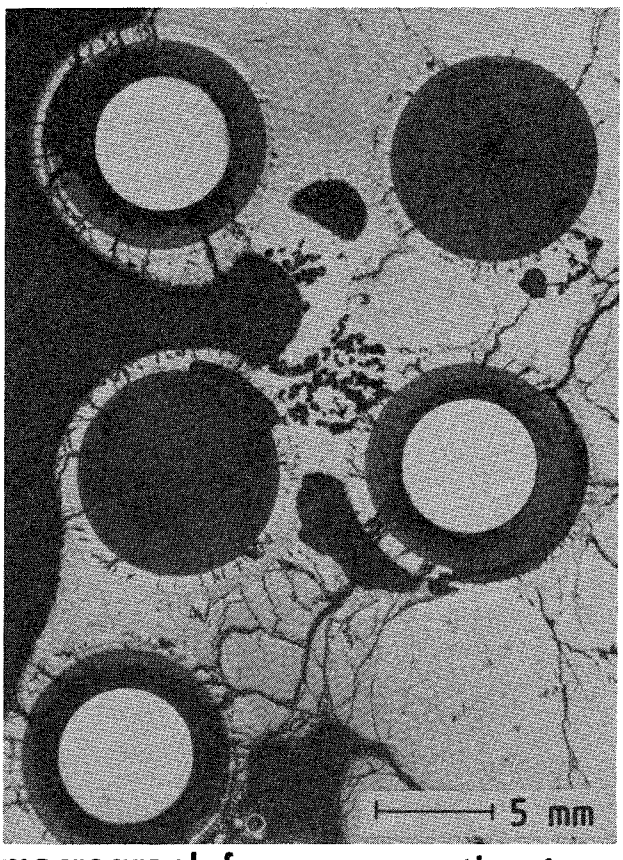

macrograph from cross section 1

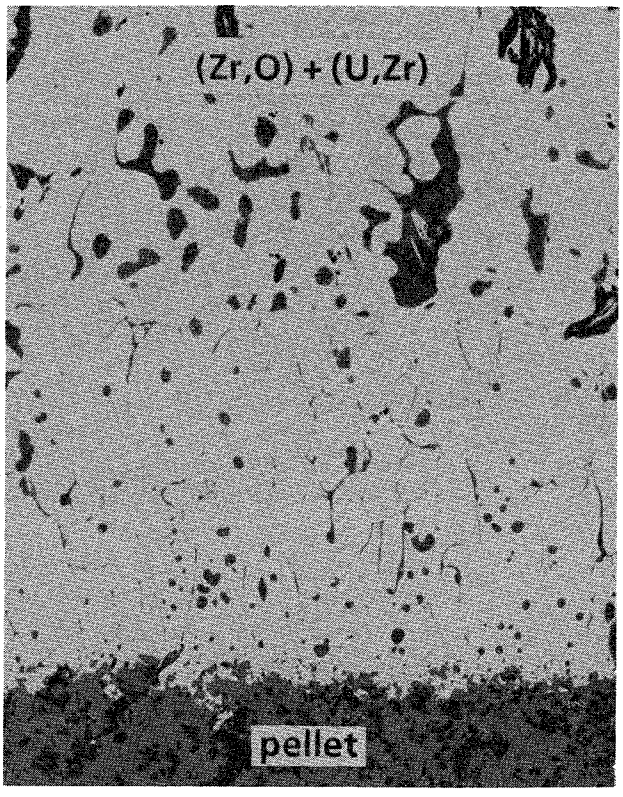

UO_2 dissolution ⟷ 50 µm

Fig. 71. Relocated melt and dissolution of embedded fuel rod at cross section 1 of CORA-3

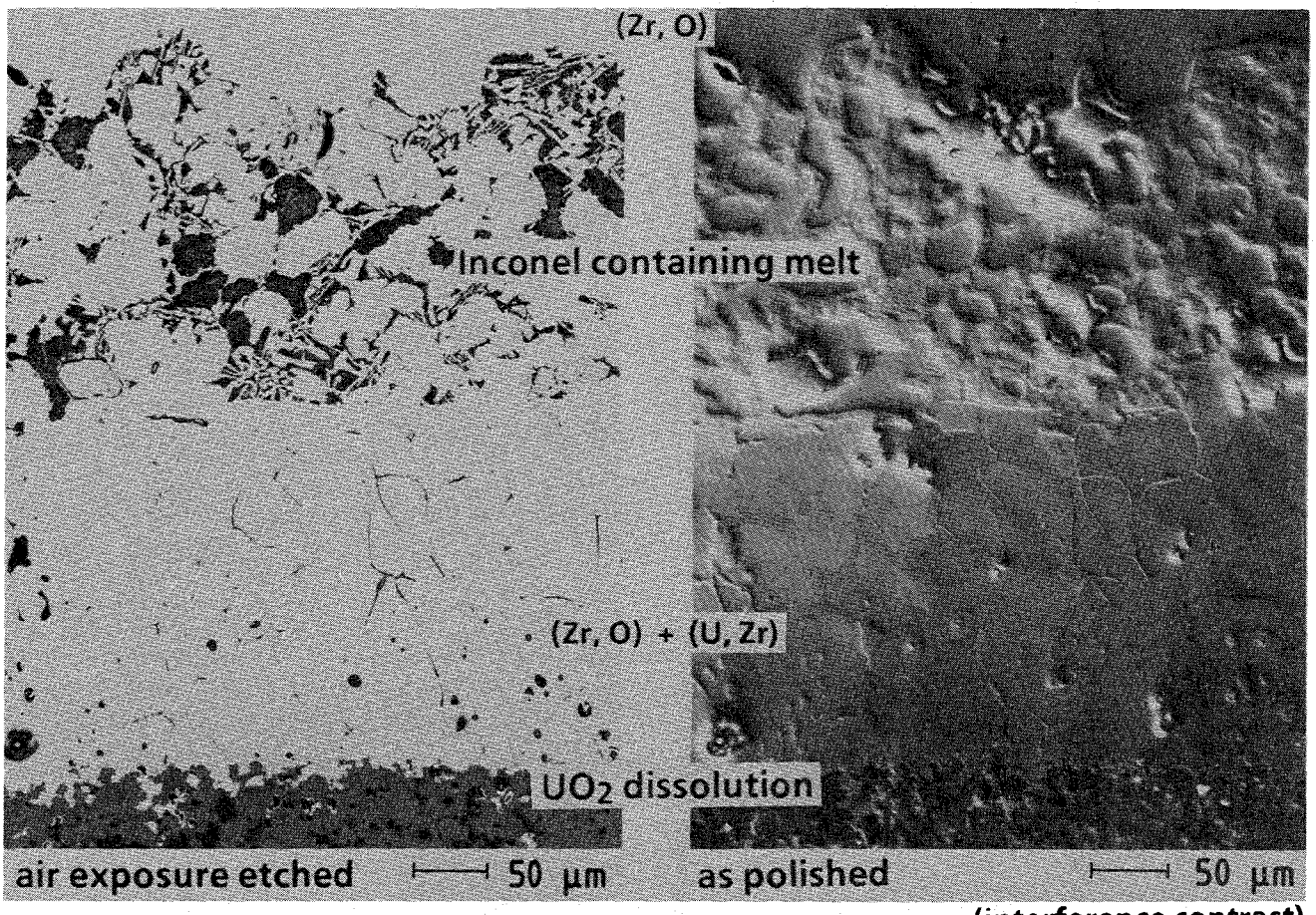

Fig. 72. In situ Zry-UO_2 interaction plus interference with Inconel-containing melt at cross section 1 of CORA-3

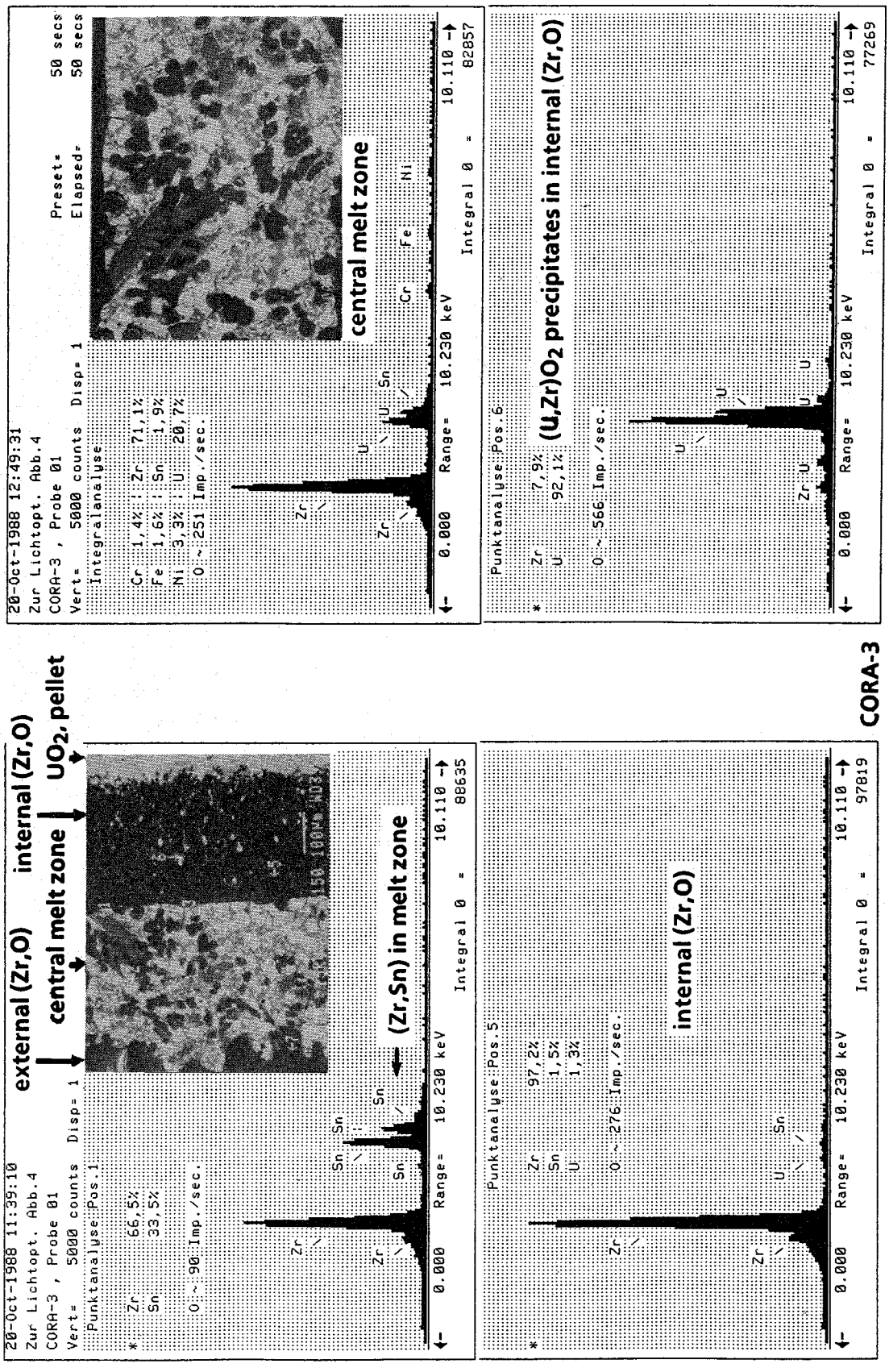

Fig. 73. Melt, containing Inconel spacer material after penetration between cladding and pellet of a partially embedded fuel rod

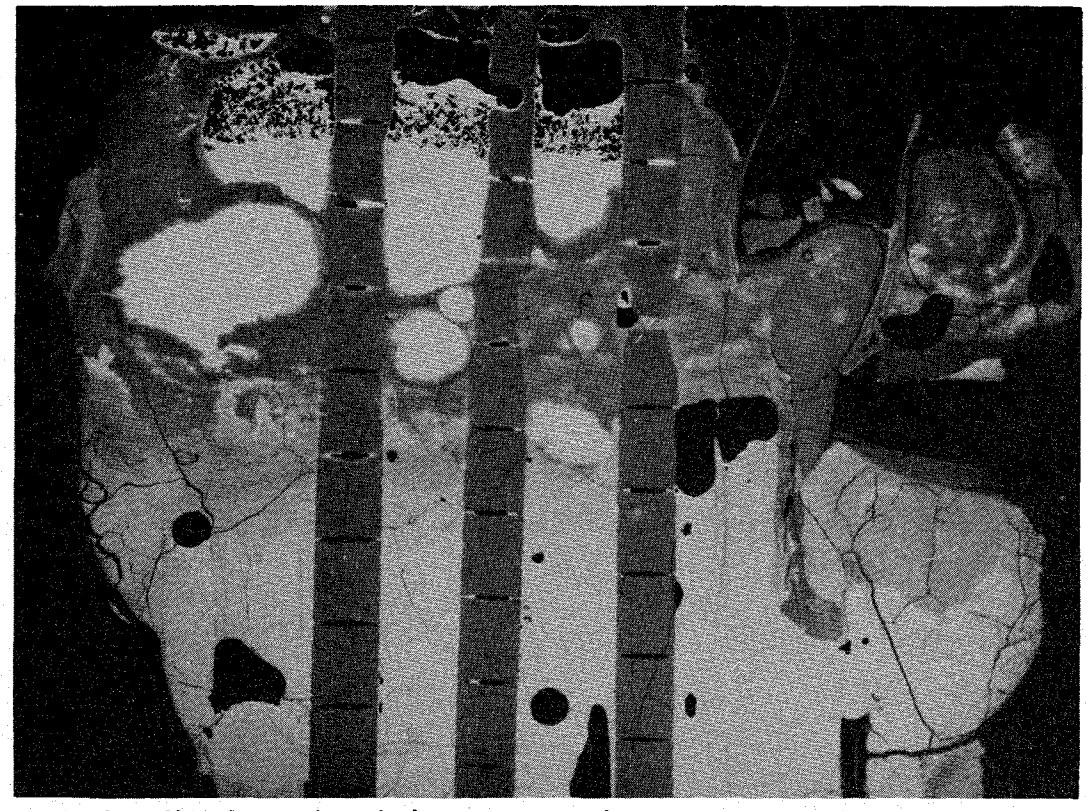

longitudinal section b (67-184 mm) ⟵⟶ 10 mm

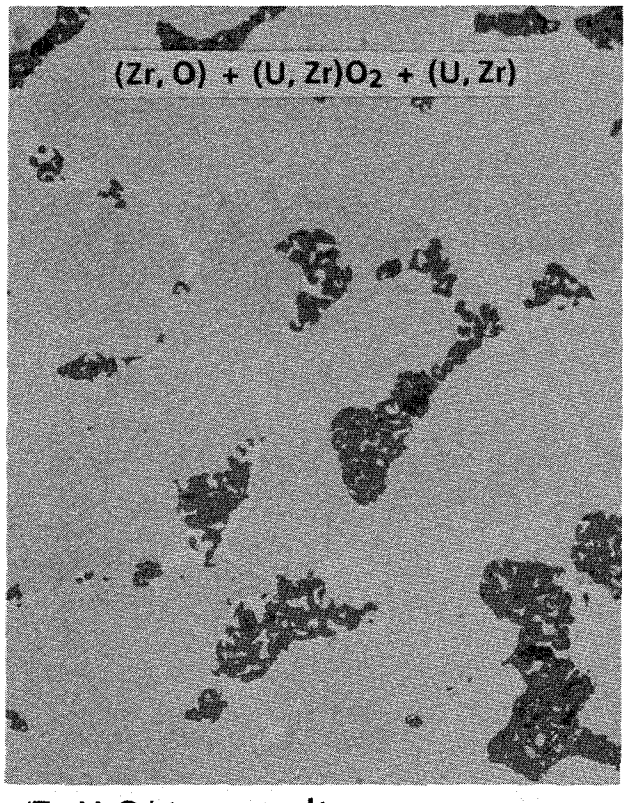

/Zr,U,O/-type melt ⟵⟶ 20 µm

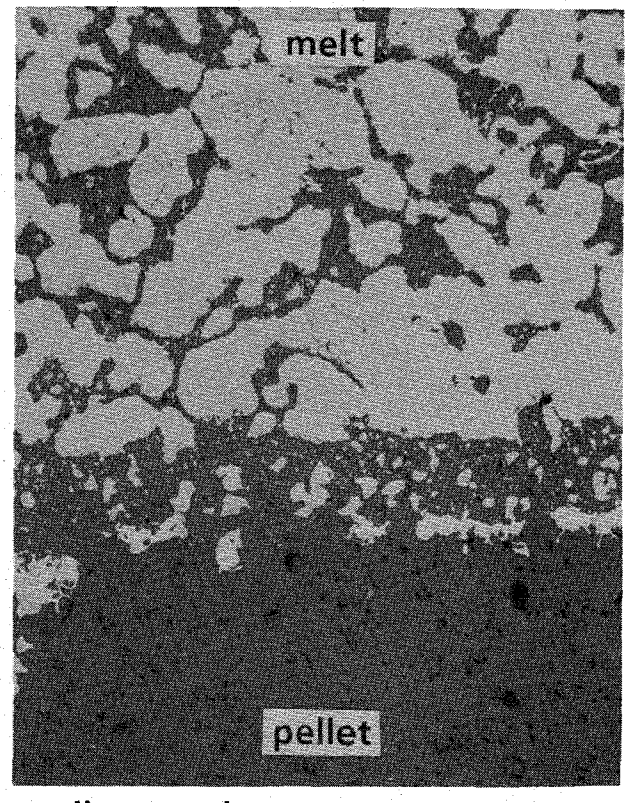

pellet attack ⟵⟶ 50 µm

Fig. 74. Zr-rich ("gray") melt of (Zr, U, O) type and pellet attack at longitudinal section b of CORA-3

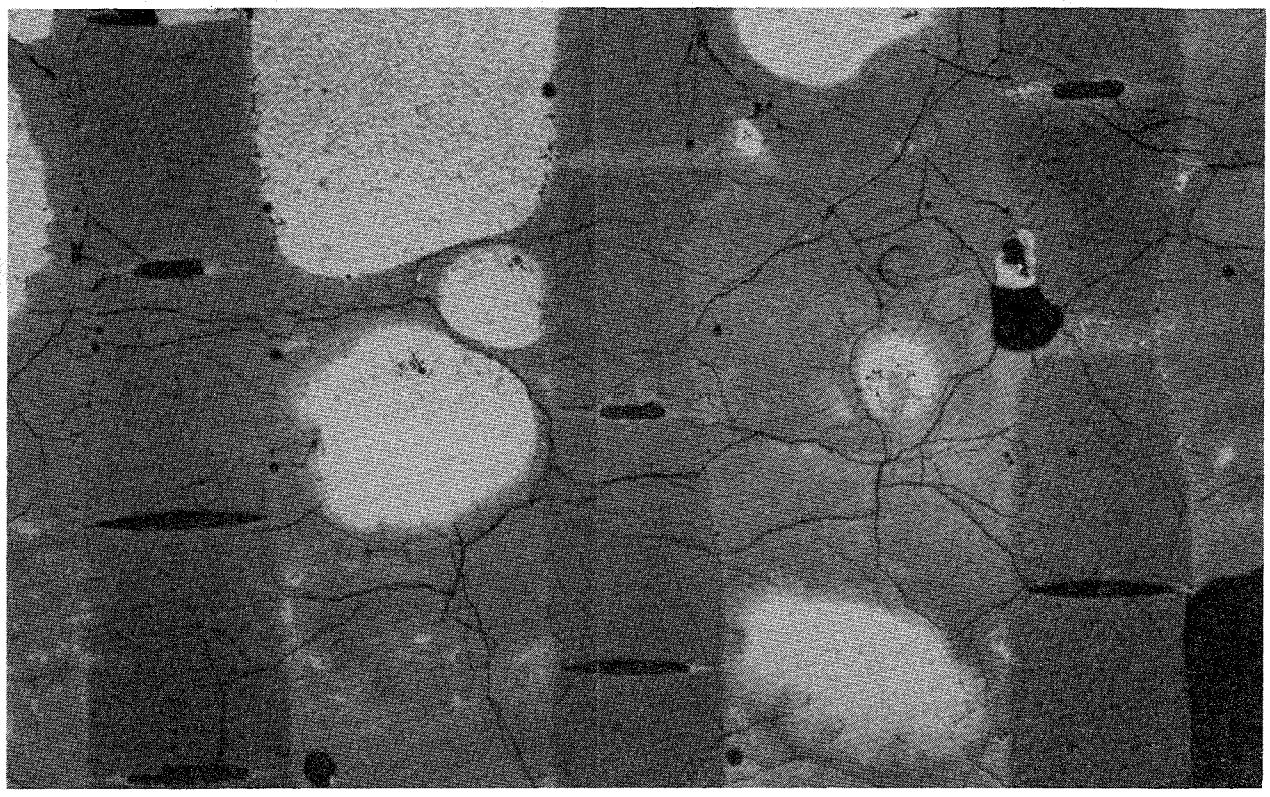

Macrograph from longitudinal section b ⟷ 5 mm

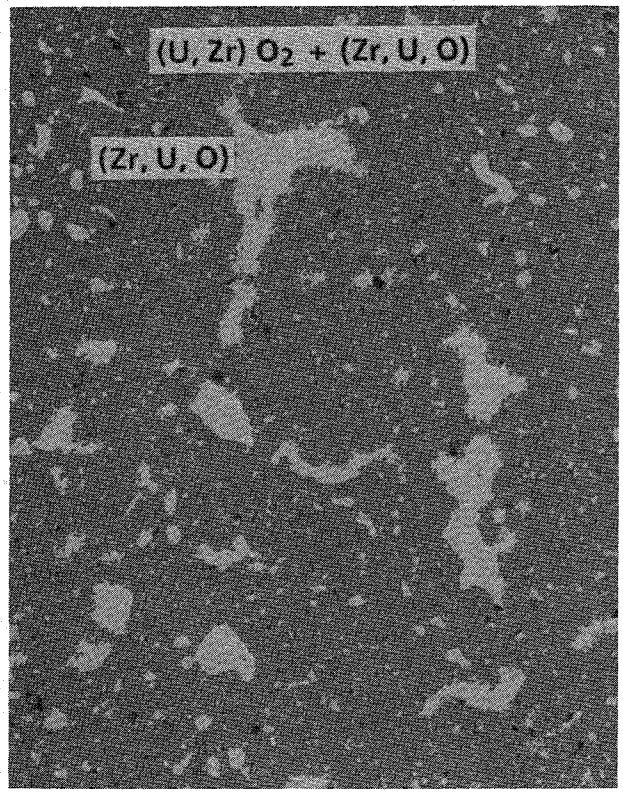

/Zr,U,O/-type melt ⟷ 20 µm

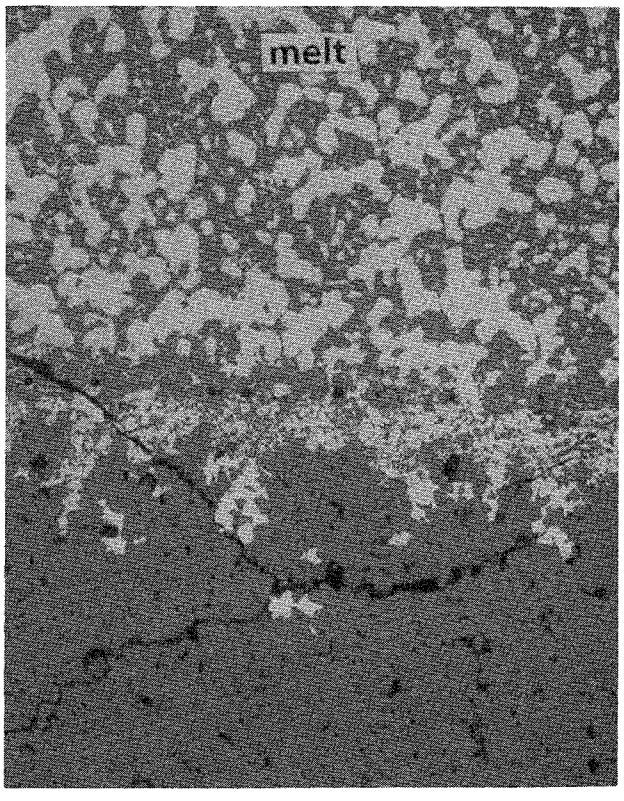

pellet attack ⟷ 50 µm

Fig. 75. U-rich ("dark") melt of (Zr, U, O) type and pellet attack at longitudinal section b of CORA-3

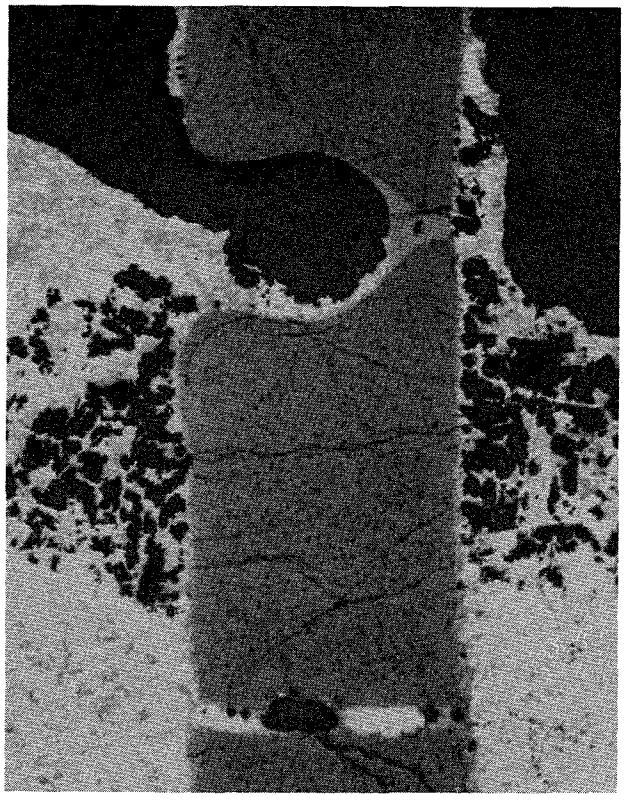

5 mm

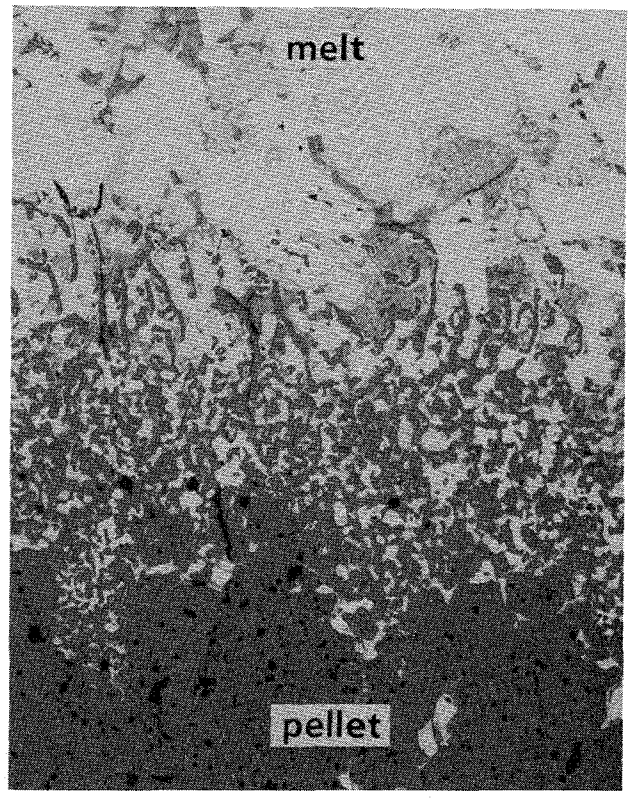

pellet attack 50 µm

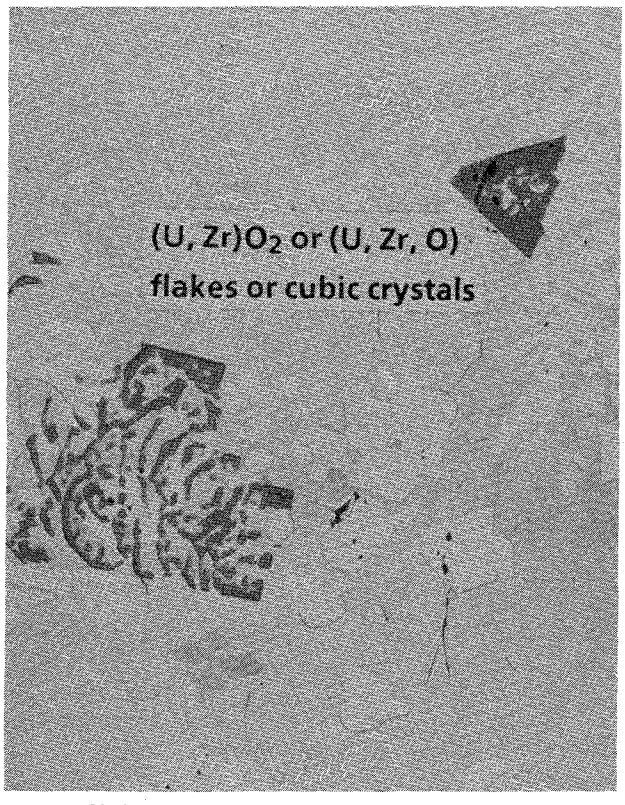

as polished 50 µm

melt

air exposure etched 50 µm

Fig. 76. Mo- and W-rich ("bright") melt, from interference with heater rod electrode, and pellet attack at longitudinal section b of CORA-3

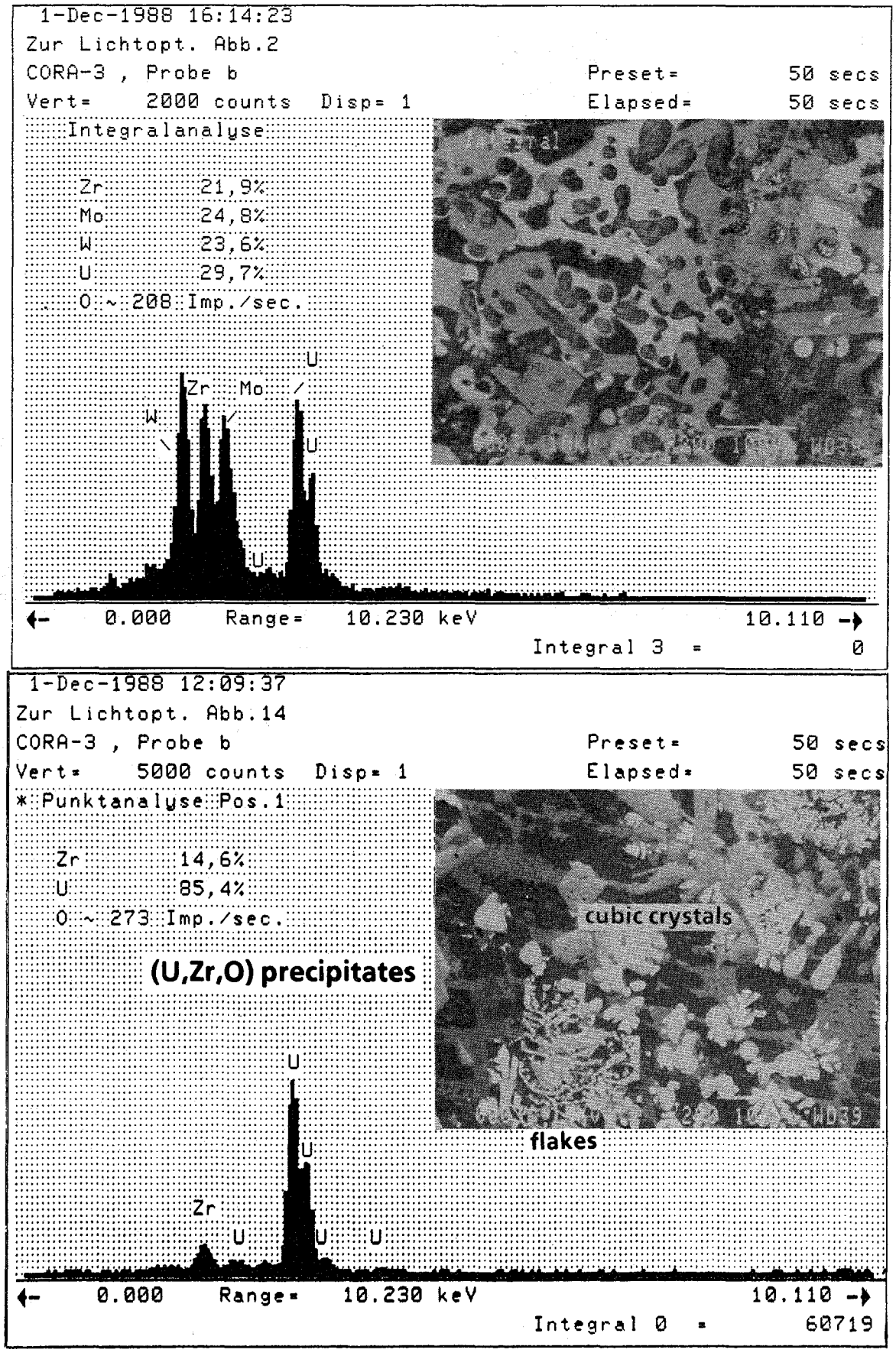

CORA-3

Fig. 77. Analysis of melt from interference with material of heater rod and electrode. Identification of UO_2 dissolution and (U, Zr, O) growth

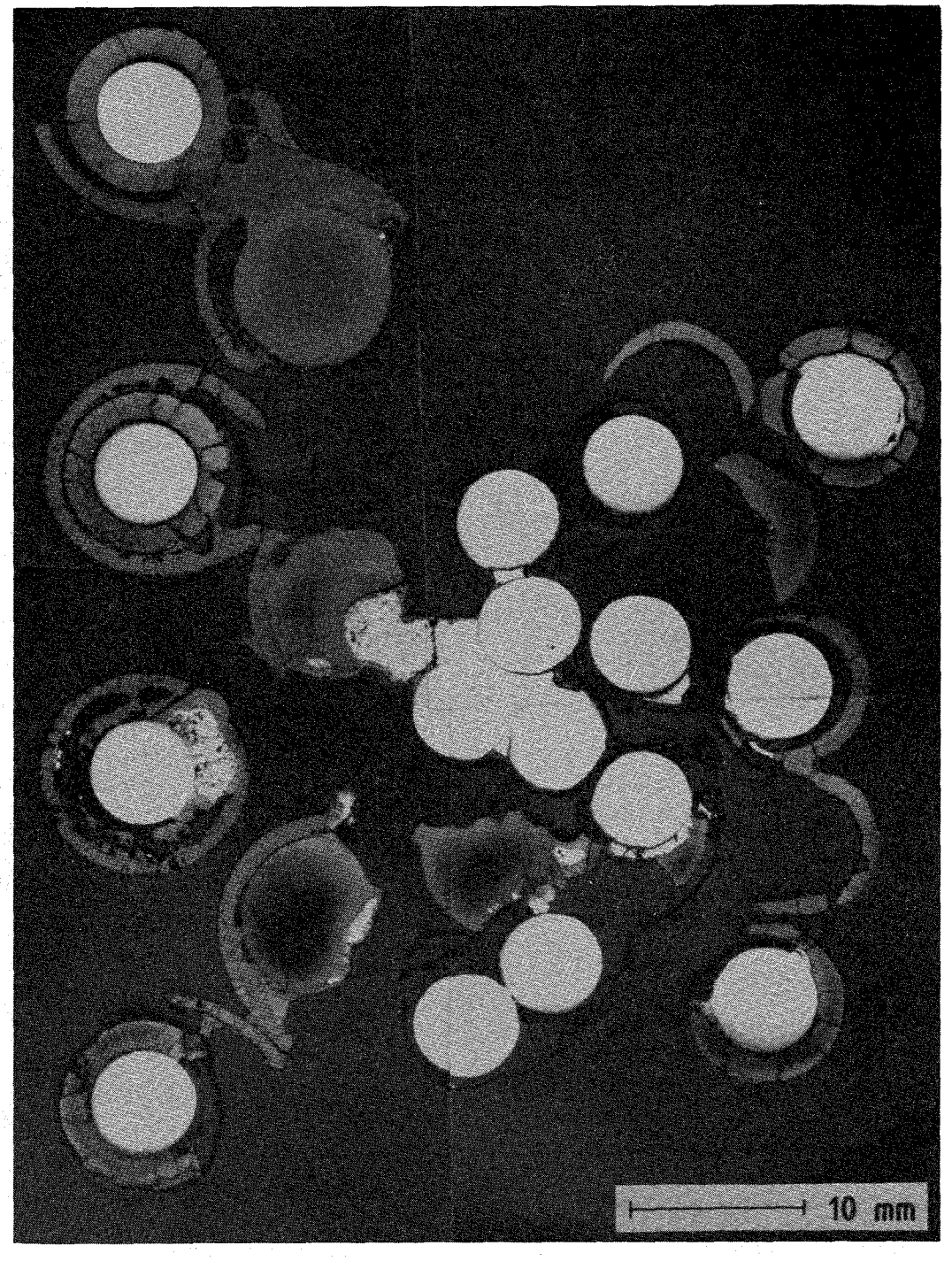

Fig. 78. Macrograph of cross section 14 (798 mm) of CORA-3

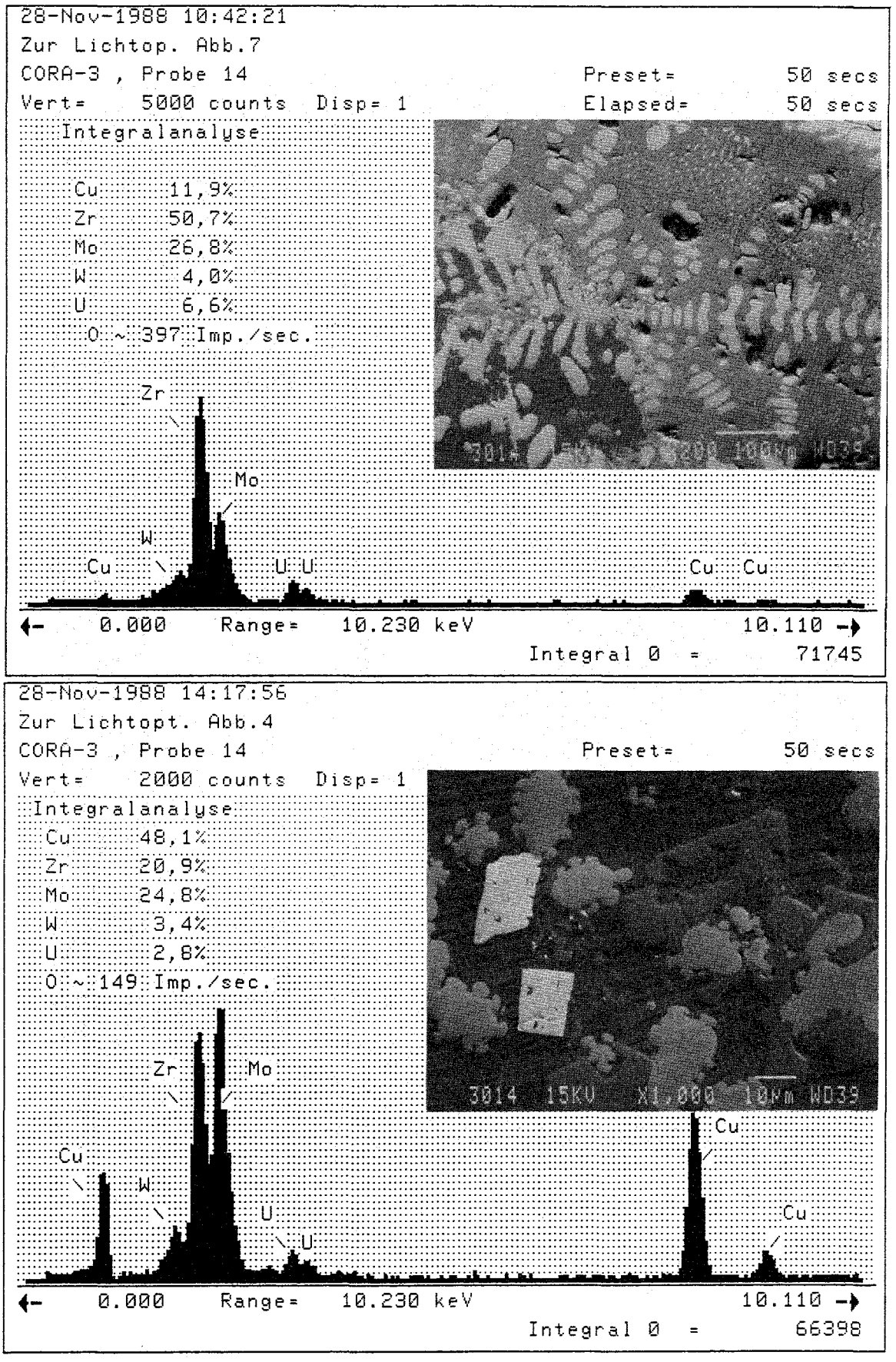

CORA-3

Fig. 79. Late melt formation from interference with heater and electrode materials

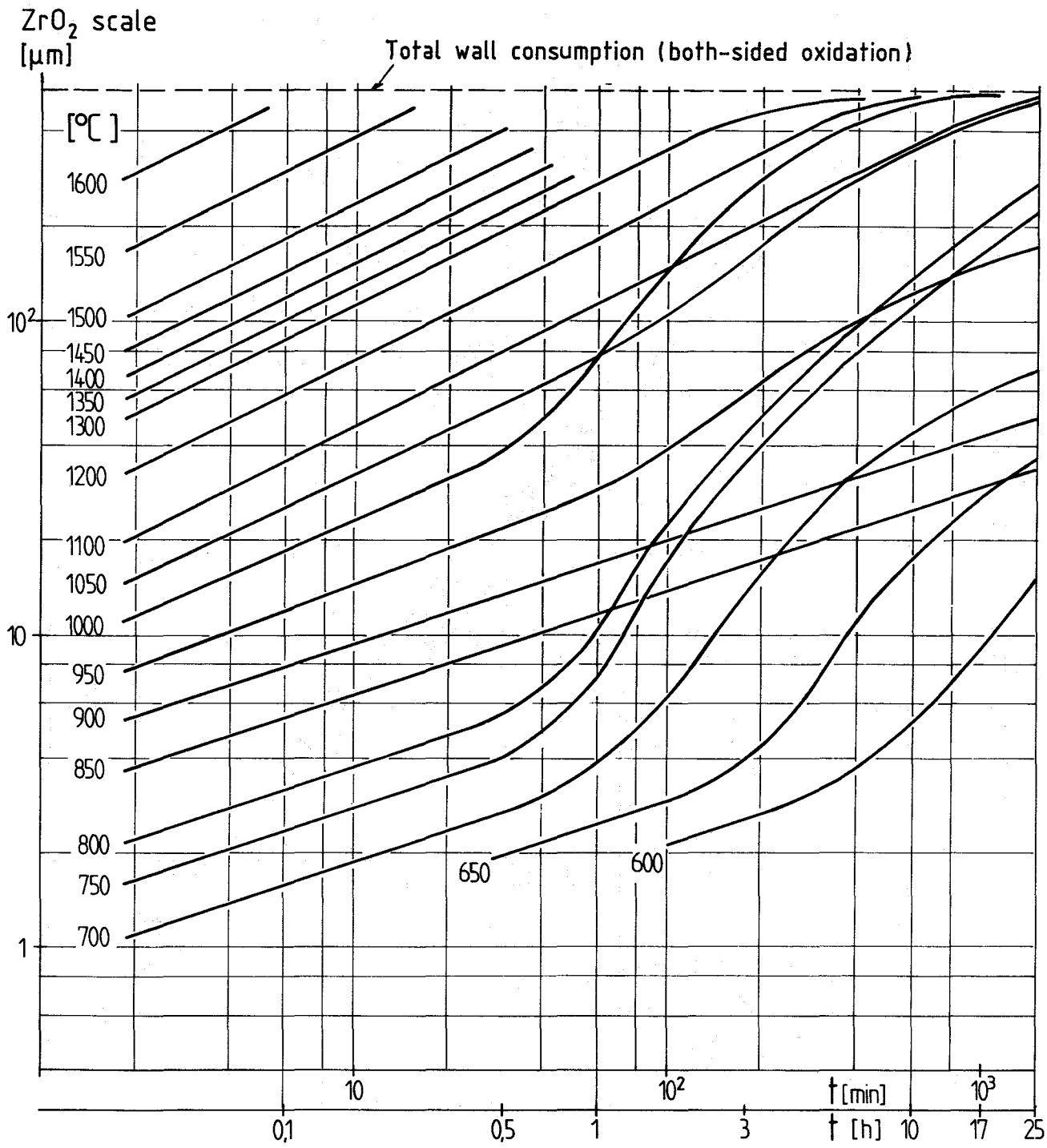

Fig. 80. High-temperature oxidation of Zircaloy-4 cladding material in steam; ZrO_2 scale growth kinetics (600-1600°C, 2 min-25h)

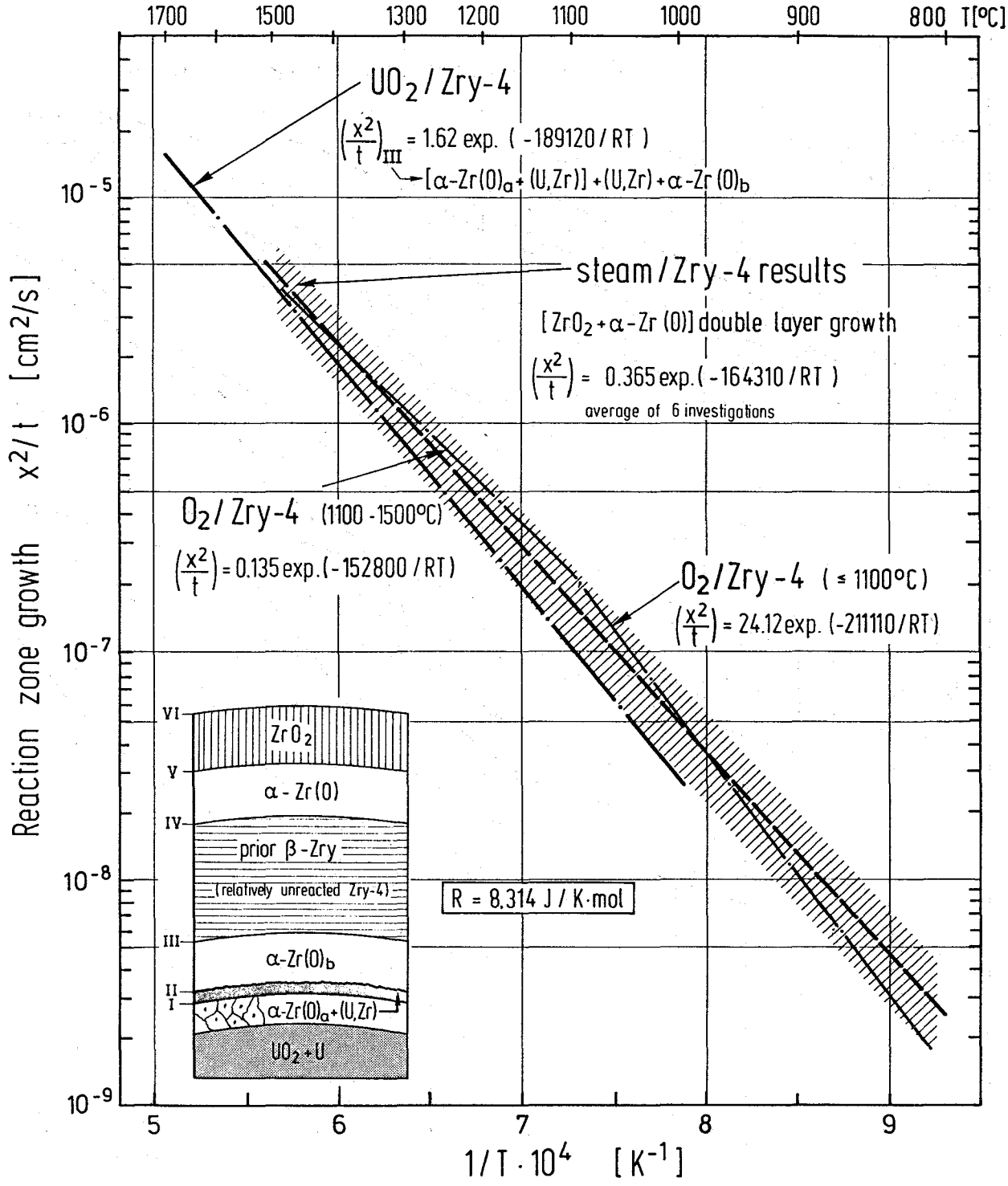

Fig. 81. Comparison of the growth rate equations for reaction systems UO_2/Zircaloy, (Ar + 25 vol.% O_2)/Zircaloy and steam/Zircaloy

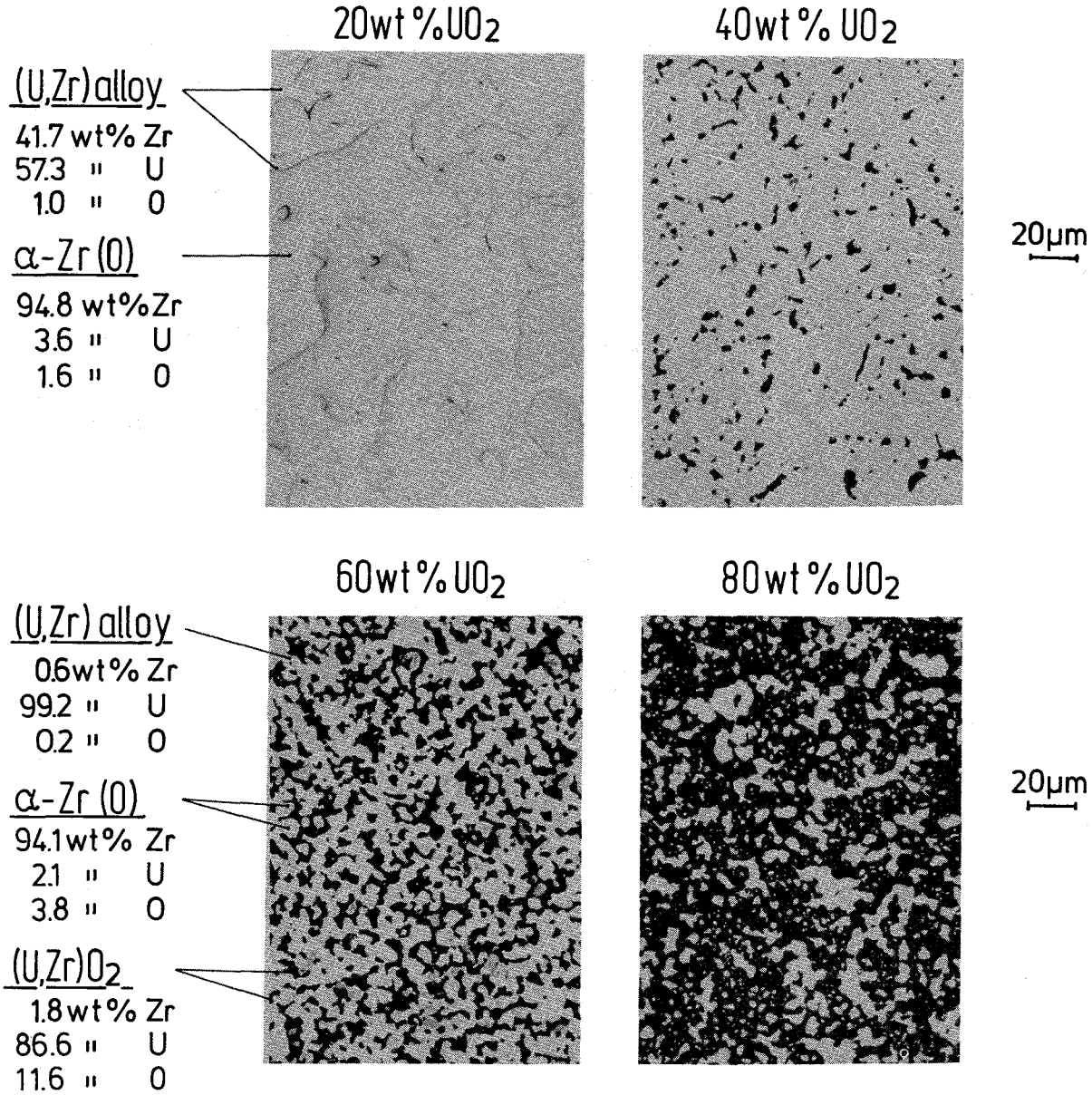

$(U,Zr,O) \rightarrow \alpha\text{-}Zr(O) + (U,Zr)$; $(U,Zr)O_{2-x} \rightarrow (U,Zr)O_2 + (U,Zr)$

melting: arc furnace ; homogenization: 1400 °C / 30 min

Fig. 82. Microstructure of molten UO_2/Zr reference specimens for four different initial UO_2 concentrations. Depending on the UO_2 concentration either two metallic or two metallic and one ceramic phase form on cooldown.

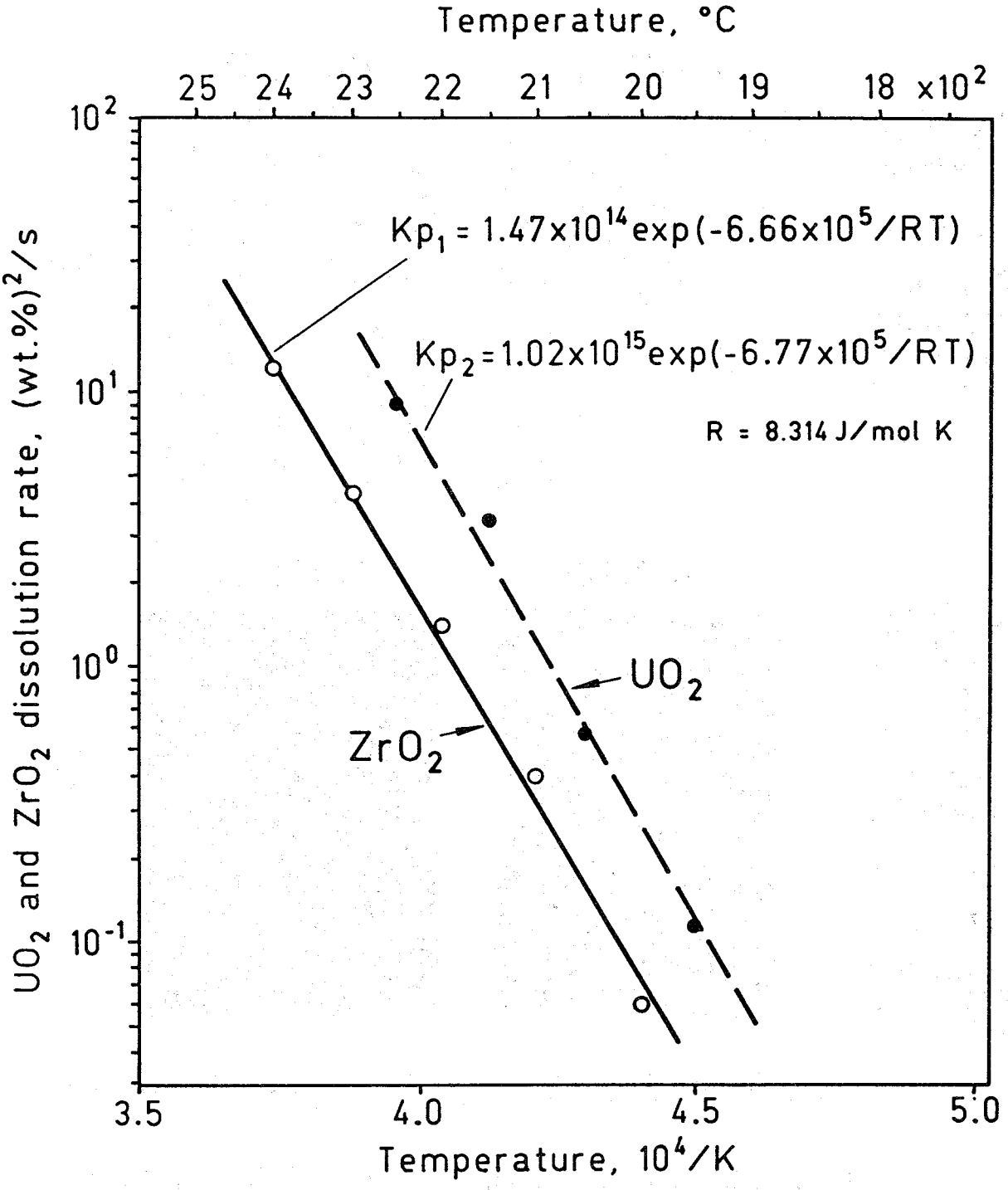

$$Kp = \frac{(wt.\% - a)^2}{t\ [s]} \longrightarrow (wt.\%)_{ZrO_2} = 23.3 + (Kp_1 \cdot t)^{0.5}$$

$$(wt.\%)_{UO_2} = 35.8 + (Kp_2 \cdot t)^{0.5}$$

Fig. 83. Dissolution rates for solid UO_2 and solid ZrO_2 by molten Zircaloy-4

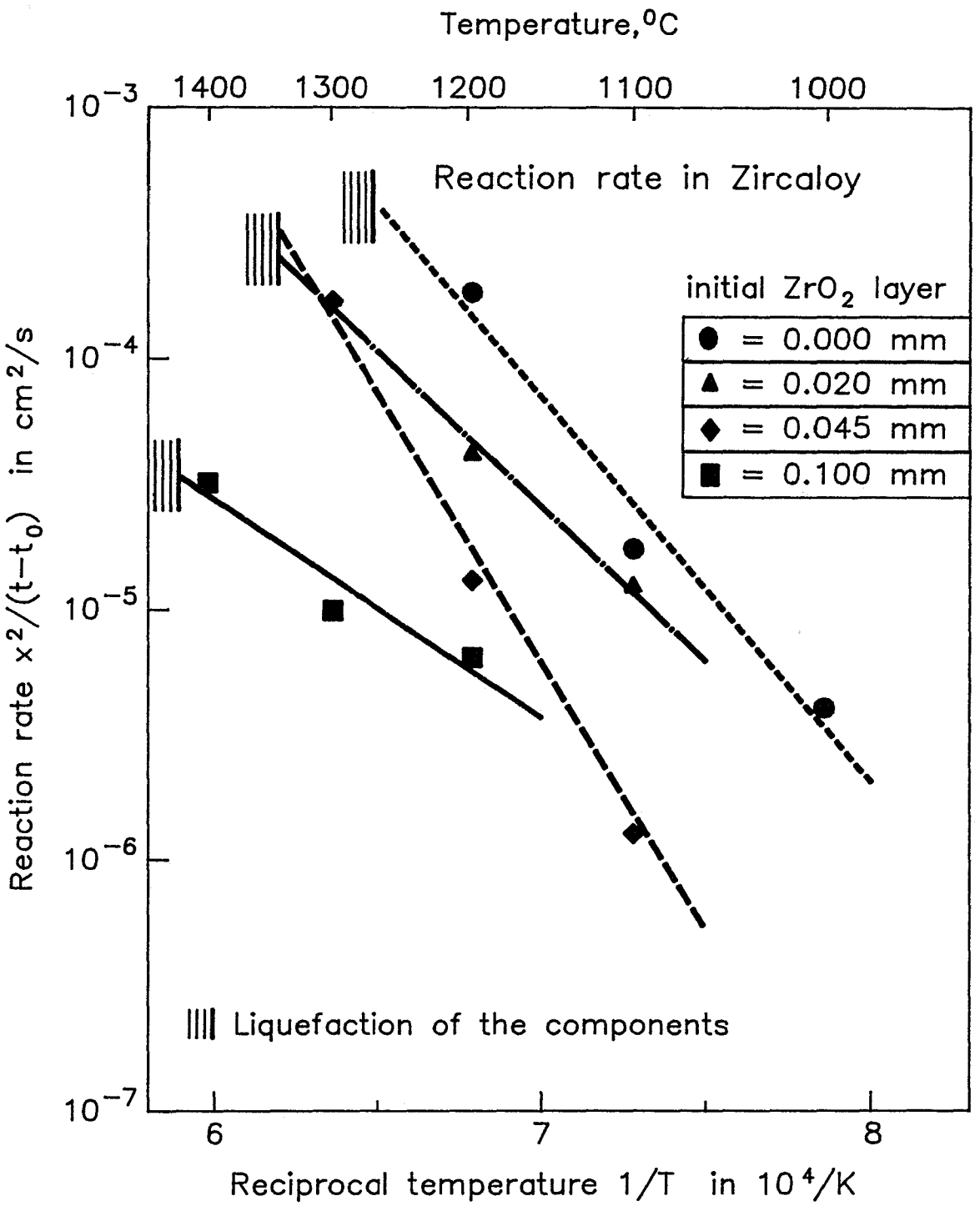

Fig. 84. Reaction rates for the system Inconel 718/Zircaloy-4. Influence of oxide layers on the Zircaloy surface.

Appendix

Appendix

1. Encapsulation of the test bundle

An illustration of the produre for encapsulating the test bundle is shown in Fig. A-1.

2. Cross Sections of CORA-2

The elevations of the sections are given in Table A-1 and are illustrated in Fig. A-2.
The orientation of the vertical cuts of bundle CORA-2 is provided with Fig. A-3.
The cross sections of bundle CORA-2 are given in Figs. A-4 through A-18.

3. Cross Sections of CORA-3

The elevations of the sections are given in Table A-2 and are illustrated in Fig. A-19.
The orientation of the vertical cuts of bundle CORA-3 is provided with Fig. A-20.
The cross sections of bundle CORA-3 are given in Figs. A-21 through A-31.

4. Preparation of the Metallographic Samples

The procedure for the preparation of the metallographic samples is listed in Table A-3.

5. List of Metallographic Samples

The cross sections of CORA-2 and CORA-3 taken for metallographic examinations are listed in Table A-4.

6. List of Fragments Taken from Bundles CORA-2 and CORA-3

The fragments taken from bundle CORA-2 and CORA-3 are provided with Tables A-5 and A-6, respectively.

Table A-1: List of cross sections, CORA-2

Sample (a)		Axial position	General location, remarks
a	bottom top	- 210 mm - 60 mm	Below lower grid spacer "
2-01	bottom top	- 58 mm - 45 mm	" Lower grid spacer (zircaloy)
2-02	bottom top	- 43 mm - 30 mm	" "
2-03	bottom top	- 28 mm - 15 mm	" "
2-04	bottom top	- 13 mm 0 mm	" Above lower grid spacer
2-05	bottom top	+ 2mm 15 mm	" "
b	bottom top	17 mm 134 mm	" (In addition longi- " tudinal cuts of b and c)
c	bottom top	136 mm 253 mm	" " " "
2-06	bottom top	255 mm 268 mm	
2-07	bottom top	270 mm 283 mm	
2-08	bottom top	285 mm 298 mm	
d	bottom top	300 mm 363 mm	(In addition longitudinal cut of d)
2-09	bottom top	365 mm 380 mm	
e	bottom top	382 mm 435 mm	
2-10	bottom top	437 mm 450 mm	Below the central grid spacer Central grid spacer (Inconel)
2-11	bottom top	452 mm 465 mm	" "
2-12	bottom top	467 mm 480 mm	" "
2-13	bottom top	482 mm 495 mm	" "
2-14	bottom top	497 mm 510 mm	Above central grid spacer "

Sample (a)		Axial position	General location, remarks
f	bottom top	512 mm 603 mm	
2-15	bottom top	605 mm 618 mm	
g	bottom top	620 mm 743 mm	
2-16	bottom top	745 mm 758 mm	
h	bottom top	760 mm 840 mm	
2-17	bottom top	842 mm 855 mm	Upper grid spacer (zircaloy) "
2-18	bottom top	857 mm 870 mm	" "
i	bottom top	872 mm 985 mm	
2-19	bottom top	987 mm 1000 mm	Upper end of heated section
j	bottom top	1002 mm 1093 mm	Above heated zone "
2-20	bottom top	1095 mm 1108 mm	" "
2-21	bottom top	1110 mm 1123 mm	" "
k	bottom top	1125 mm -	Remnant

(a) Numbers refer to 13 mm-thick samples; small letters are designation for remnants of different heights.

Table A-2: Sample Locations of CORA-3 Bundle

Sample	Sample length	axial location		Comments
		bottom	top	
3- a	82 mm	- 77 mm	+ 5 mm	Lower grid spacer
Cut	2 mm			
3-01	13 mm	+ 7 mm	20 mm	
Cut	2 mm			
3-02	13 mm	22 mm	35 mm	
Cut	2 mm			
3-03	13 mm	37 mm	50 mm	
Cut	2 mm			
3-04	13 mm	52 mm	65 mm	
Cut	2 mm			
3- b	117 mm	67 mm	184 mm	Longitudinal section
Cut	2 mm			
3-05	13 mm	186 mm	199 mm	
Cut	2 mm			
3-06	13 mm	201 mm	214 mm	
Cut	2 mm			
3- c	122 mm	216 mm	338 mm	
Cut	2 mm			
3-07	13 mm	340 mm	353 mm	
Cut	2 mm			
3-08	13 mm	355 mm	368 mm	
Cut	2 mm			
3- d	130 mm	370 mm	500 mm	
Cut	2 mm			
3-09	13 mm	502 mm	515 mm	
Cut	2 mm			
3-10	13 mm	517 mm	530 mm	
Cut	2 mm			
3- e	136 mm	532 mm	668 mm	
Cut	2 mm			

Sample	Sample length	axial location		Comments
		bottom	top	
3-11	13 mm	670 mm	683 mm	
Cut	2 mm			
3-12	13 mm	685 mm	698 mm	
Cut	2 mm			
3- f	68 mm	700 mm	768 mm	
Cut	2 mm			
3-13	13 mm	770 mm	783 mm	
Cut	2 mm			
3-14	13 mm	785 mm	798 mm	
Cut	2 mm			
3- g	68 mm	800 mm	868 mm	
Cut	2 mm			
3-15	13 mm	870 mm	883 mm	
Cut	2 mm			
3-16	13 mm	885 mm	898 mm	
Cut	2 mm			
3- h	90 mm	900 mm	990 mm	
Cut	2 mm			
3-17	13 mm	992 mm	1005 mm	Upper end of heated zone
Cut	2 mm			
3-18	13 mm	1007 mm	1020 mm	
Cut	2 mm			
3- i	ca. 295 mm	1022 mm		

Note: Elevations were corrected for 20 mm due to downward movement of the fuel rod simulators referred to the shroud.

Table A-3: Procedure for the metallographic preparation of the CORA samples

	Horizontal grinding	Grinding	Lapping	Polishing		
Abrasive	Corrundum disc 120 µm Diamond disc 64 µm	Diamond disc 20 µm	Petrodisc-M or DP Net*)	PAW cloth	PAN-W	NAP cloth
Particle size			Diamond spray 6 µm	6 µm	3 µm	1 µm
Lubricant	Water	Water	W. lubric. **)	W. lub.	W. lub.	W. lub.
Revolutions of disc	300 rpm	300 rpm	150 rpm (Net) or 300 rpm (Petrod.)	150 U/min	150 U/min	150 U/min
Pressure	200-400 N	200-300 N	200 N	100 N	100 N	100 N
Time	to level	25 min	30 min	30 min	60 min	60 min

*) Petrodisc-M and DP Net are registered trade marks of Struers company
**) "White lubricant" of Struers; liquid on an oil/alcohol/glycerin basis

Table A-4: List of Metallographic Samples of Bundles CORA-2 and CORA-3

CORA-2

- Sample 2 - 4	bottom	- 13 mm	Lower grid spacer
- Sample 2 - 6	top	268 mm	
- Sample 2 - 8	top	298 mm	
- Sample 2 - 12	top	480 mm	
- Sample 2 - 18	top	870 mm	Upper grid spacer
- Sample 2 - c		136 mm-253 mm	Vertical section

CORA-3

- Sample 3 - 1	top	20 mm	Blockage region
- Sample 3 - b		67 mm - 184 mm	Vertical section
- Sample 3 - 14	top	798 mm	

Table A-5: List of Fragments Taken from Bundle CORA-2 (Comments in German)

Probe Nr.	Höhe[a]	Umfangsl.[b]	Bemerkung
2-101	300 mm	210°	Schmelzbahn am Eckstab Nr. 7.1. Schmelze dunkelgrau bis schwarz, nicht glänzend; haftete an größerer Schmelzbahn, die den Eckstab umgab.
2-102	390 mm	255°	Schmelznase mit Hüllrohr.
2-103	360 mm	165°	Umverlagertes Hüllstück, gefunden als Schmelzklumpen auf Shroud, vor Stab Nr. 7.5
2-104	240 mm	165°	Doppelwandiges Shroudstück, vertikal unterhalb der Probe 2-103 gelegen.
2-105	360 mm	75°	Vollpellet, vom unbeheizten Stab Nr. 6.6.
2-106	460 mm	75°	Ringpellet-Bruchstücke des Eckstabes Nr. 1.7. Zum Vergleich mit Probe 2-105.
2-107	230 mm	75°	Hülle mit Brennstoff, Oberkante des 200 mm-Fensters (H25), Stab Nr. 5.7.
2-108	900 mm	300°	Bruchstück von Hüllrohr aus oberem Bündelbereich (Fenster H39), stark oxidiert. Probenahme vom 17.8.87.
2-109	80 mm	300°	Schwarzer, teilw. glänzender Schmelzklumpen, der im Fenster H23 an der Shroud erstarrt ist.

a Abst. von Unterkante Heizzone
b Zur Orientierung: Winkel 180°= Dampfeinlaßstutzen

Table A-6: List of Fragments Taken from Bundle CORA-3 (Comments in German)

Probe Nr.	Höhe[a]	Umfangsl.[b]	Bemerkung
3-101	360-390 mm	30°	Vollpellets des Stabes 2.2, zum Stab verbacken
3-102	300-350 mm	30°	Ringpelletstücke von Stab 1.7
3-103	800 mm	30°	Hüllstück des Stabes 1.5, ohne metallische Schmelze
3-104	800 mm	30°	Hüllstück des Stabes 1.7, mit metallischer Schmelze
3-105	500 mm	30°	Erstarrte Schmelztropfen an Stab Nr. 1.3
3-106	150 mm	210°	Shroudstück, nahe Stab 7.7
3-107	150 mm	210°	Shroudstück, nahe Stab 7.5
3-108	100 mm	300°	Schmelzkissen aus Videofenster
3-109	130 mm	210°	Schmelzfragment oberhalb Dampfeintritt

a Abst. von Unterkante Heizzone
b Zur Orientierung: Winkel 180°= Dampfeinlaßstutzen

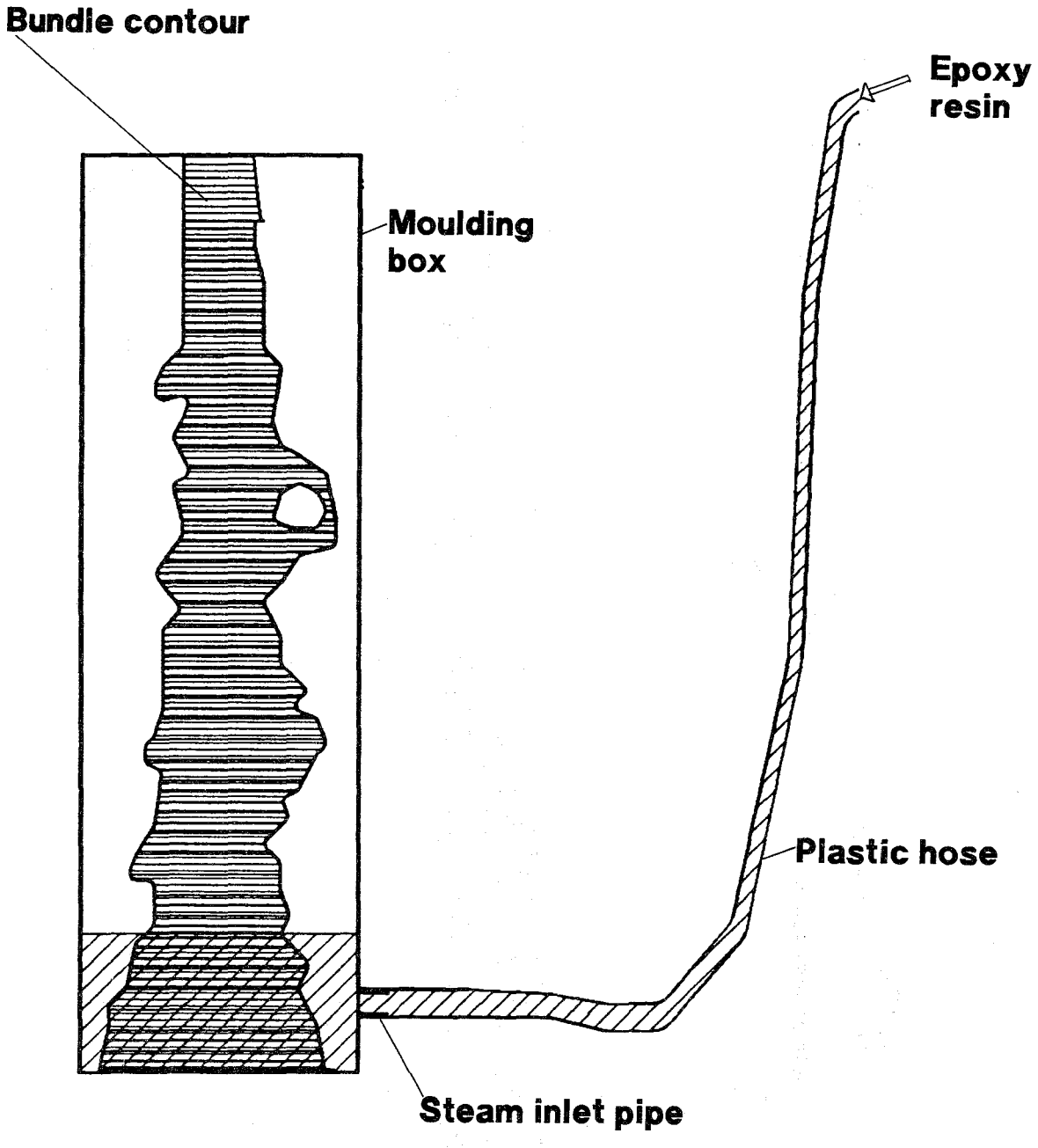

Fig. A-1 Procedure of encapsulation of the tested bundle by using epoxy resin, schematic /10/

Fig. A-2 CORA-2, bundle sectioning

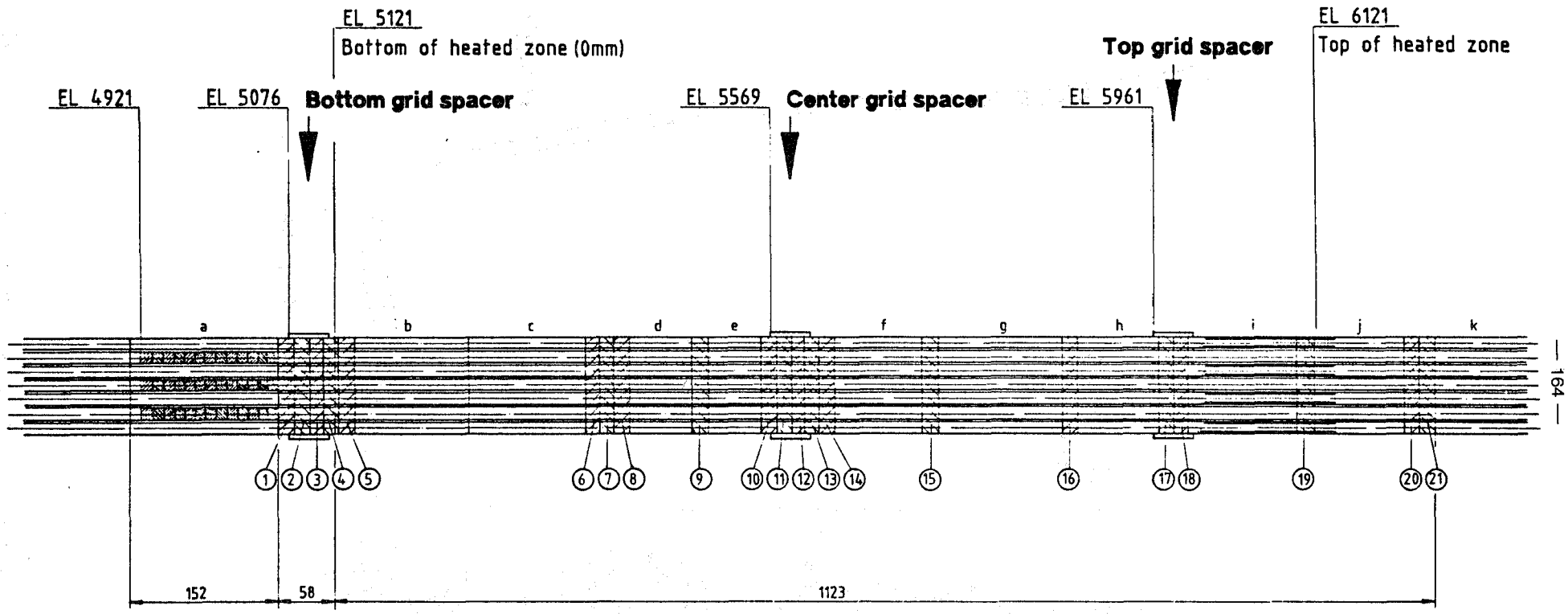

Vertical sections of remnants b, c, d

Height of horizontal sample : 13mm (marking distance = 15mm)

Bundle viewed from 30°, 120°, 210°, and 300°, respectively

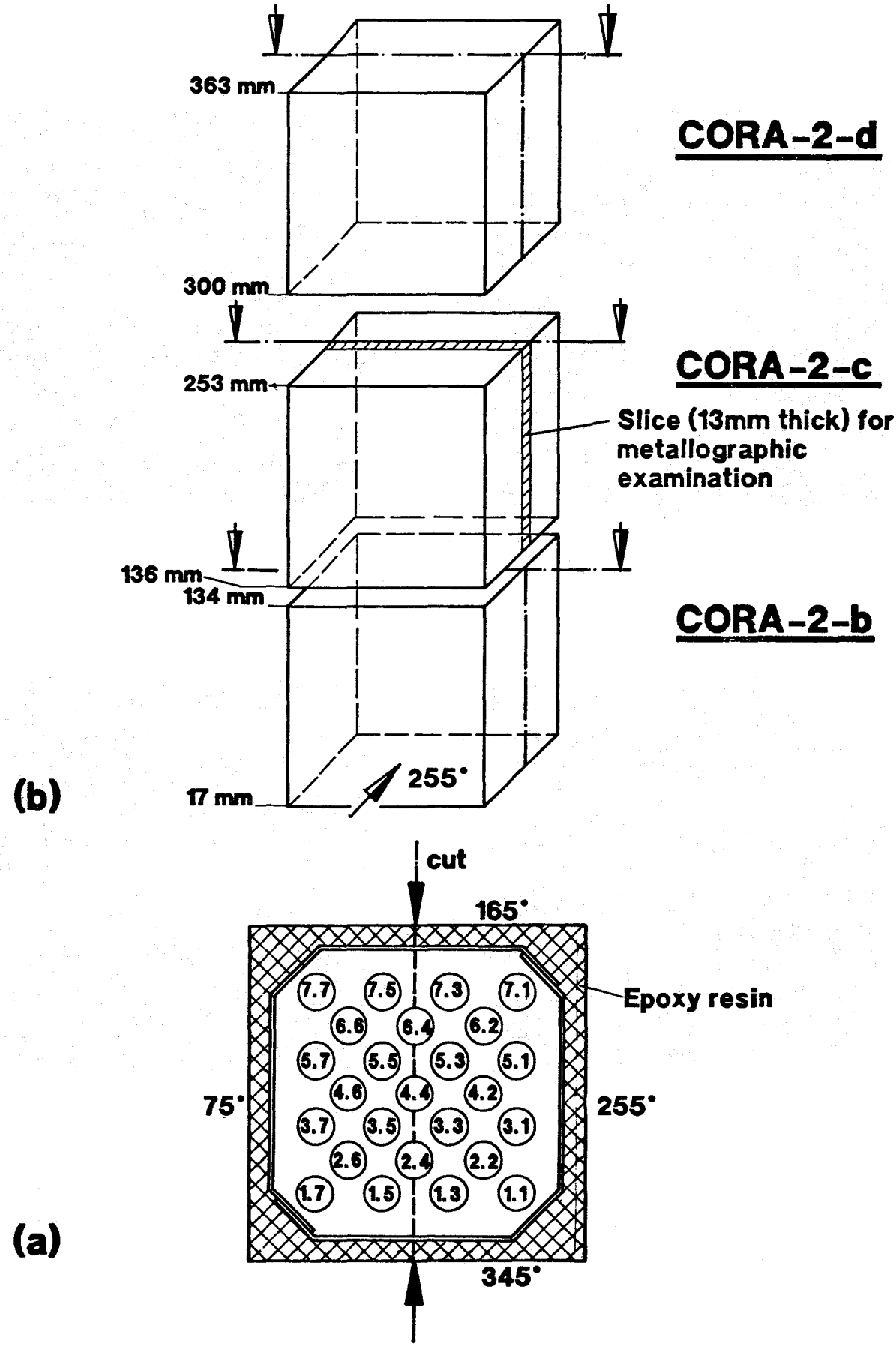

Fig. A-3 CORA-2; Locations of the vertical cuts through sections 2-b, 2-c and 2-d; (a) top view, (b) bundle viewed from 255°

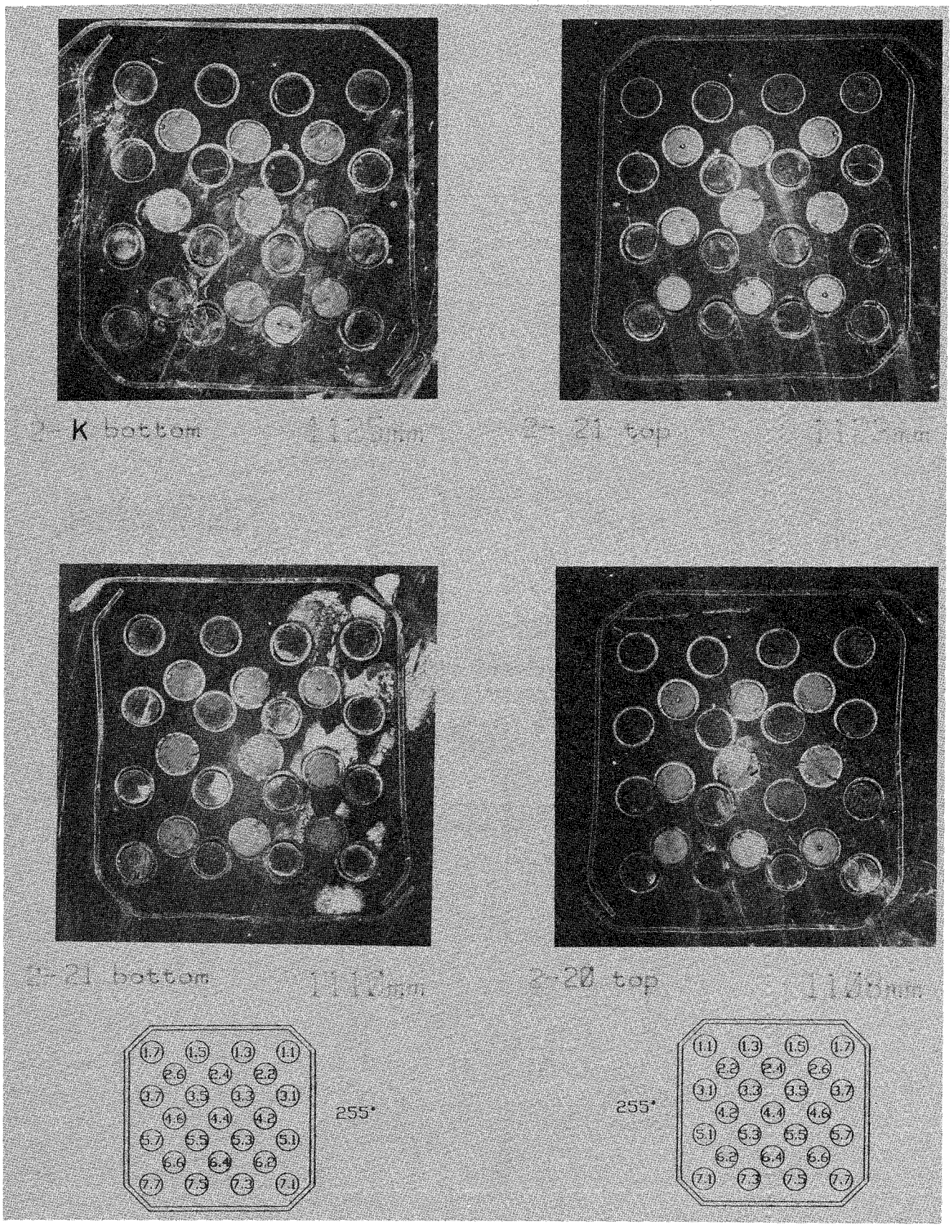

Fig. A-4 Cross sections of the test bundle CORA-2 at elevations indicated

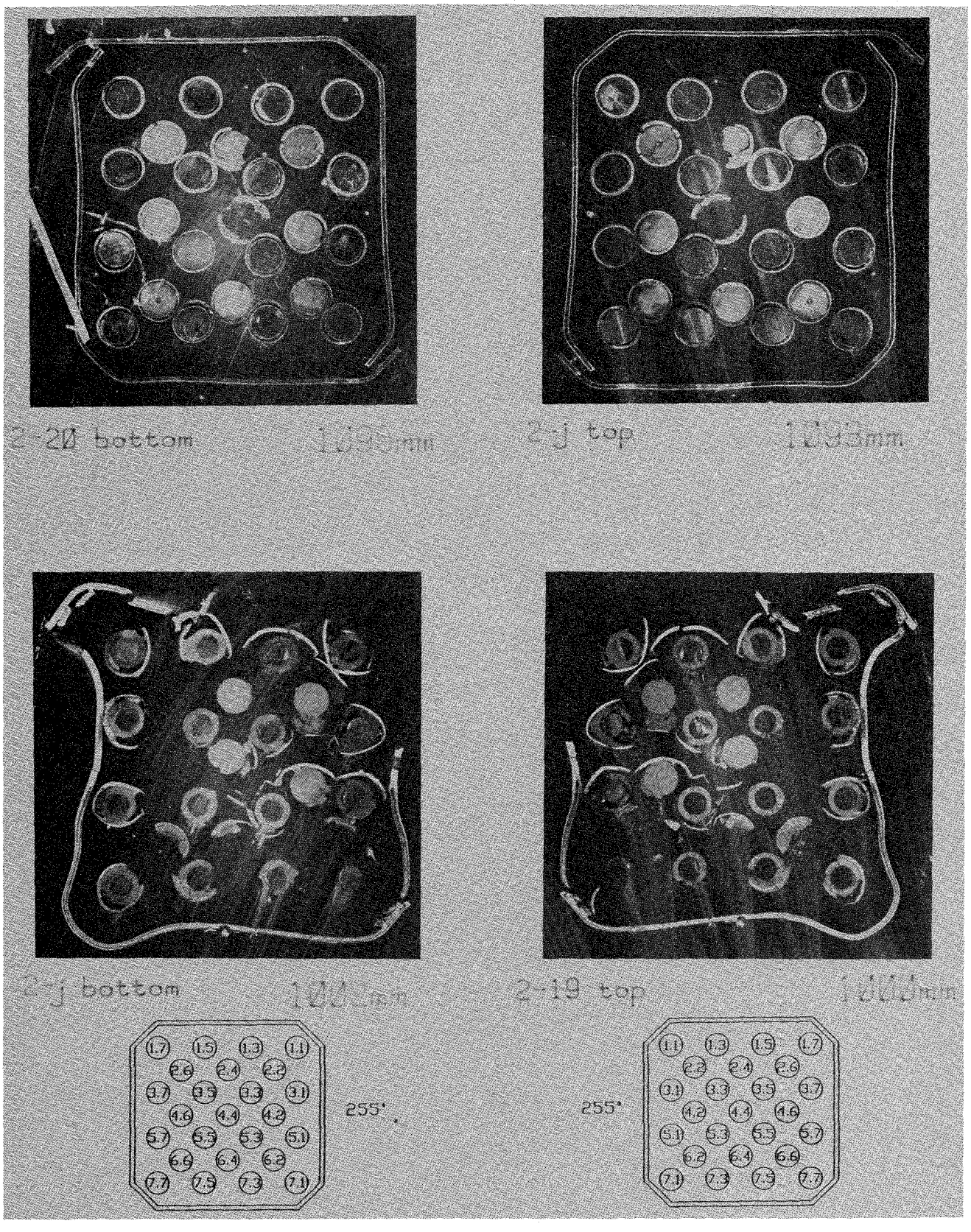

Fig. A-5 Cross sections of the test bundle CORA-2 at elevations indicated

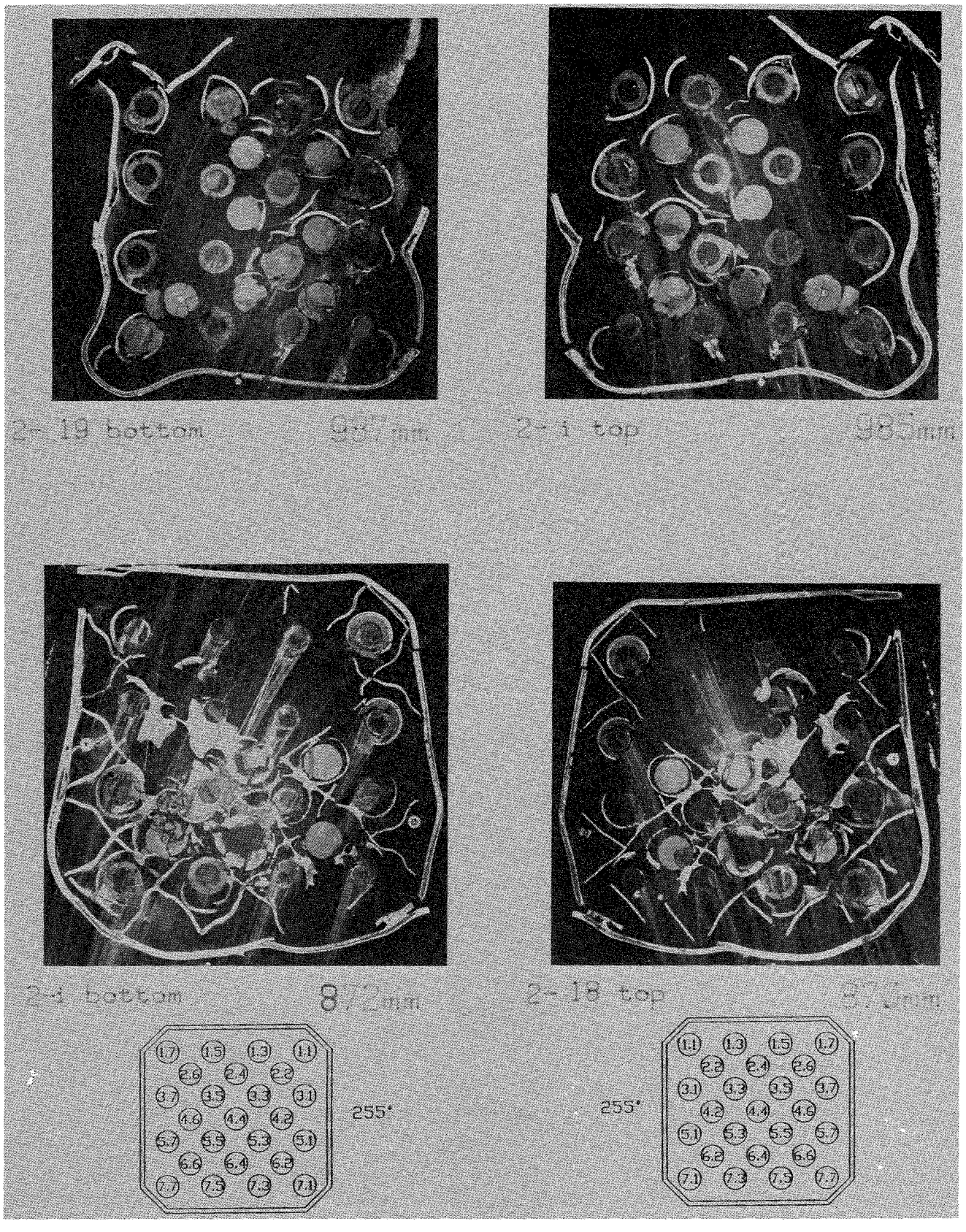

Fig. A-6 Cross sections of the test bundle CORA-2 at elevations indicated

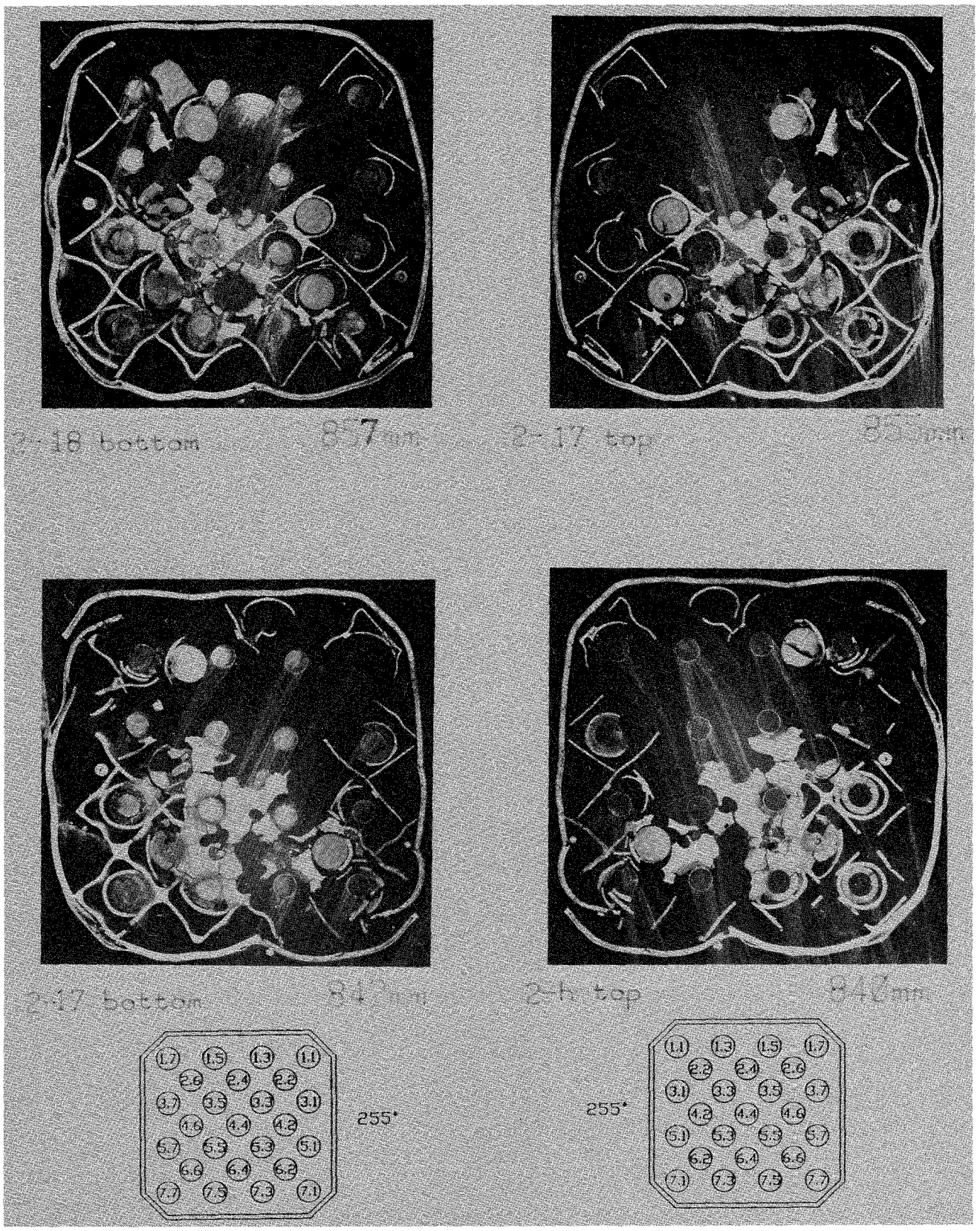

Fig. A-7 Cross sections of the test bundle CORA-2 at elevations indicated

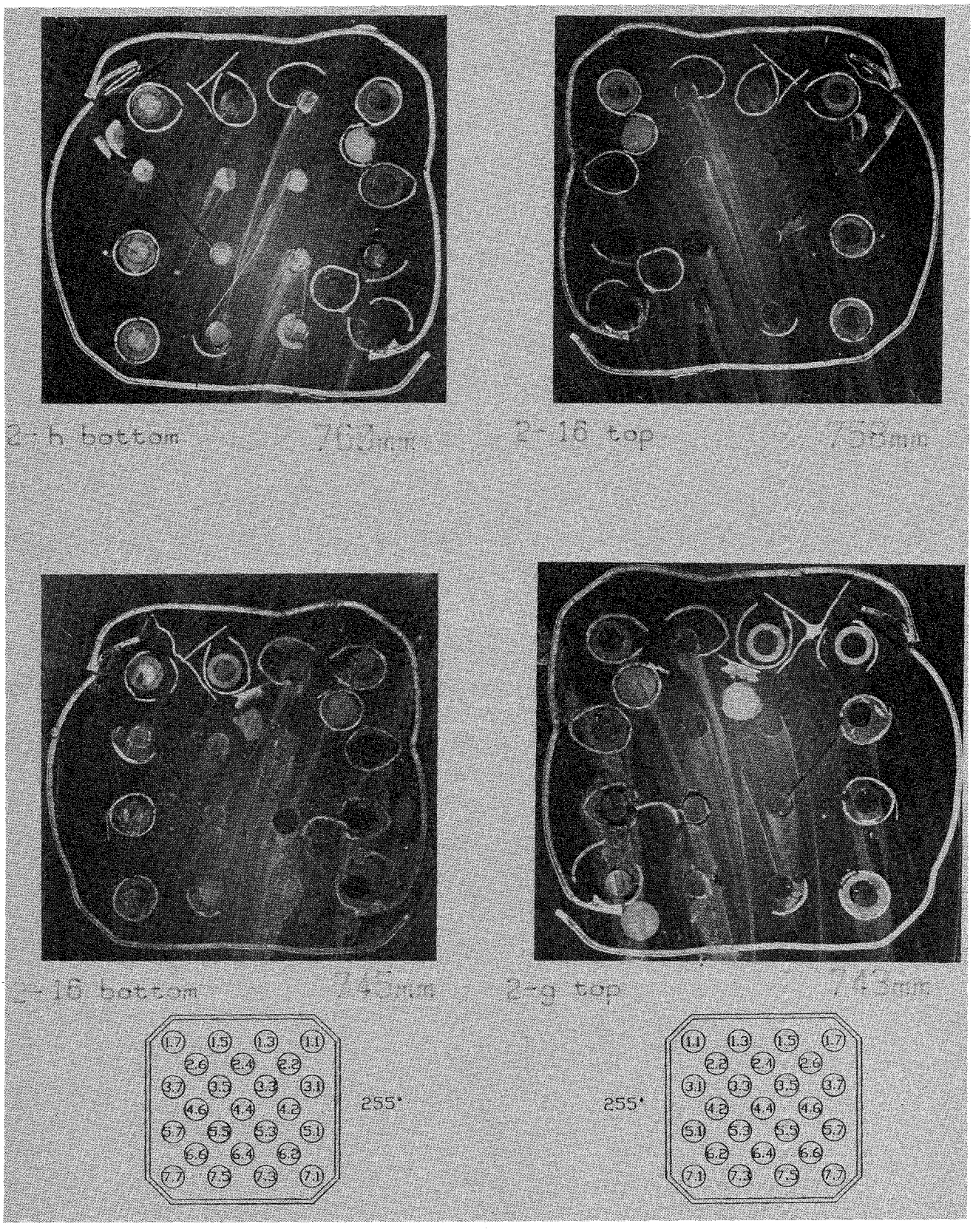

Fig. A-8 Cross sections of the test bundle CORA-2 at elevations indicated

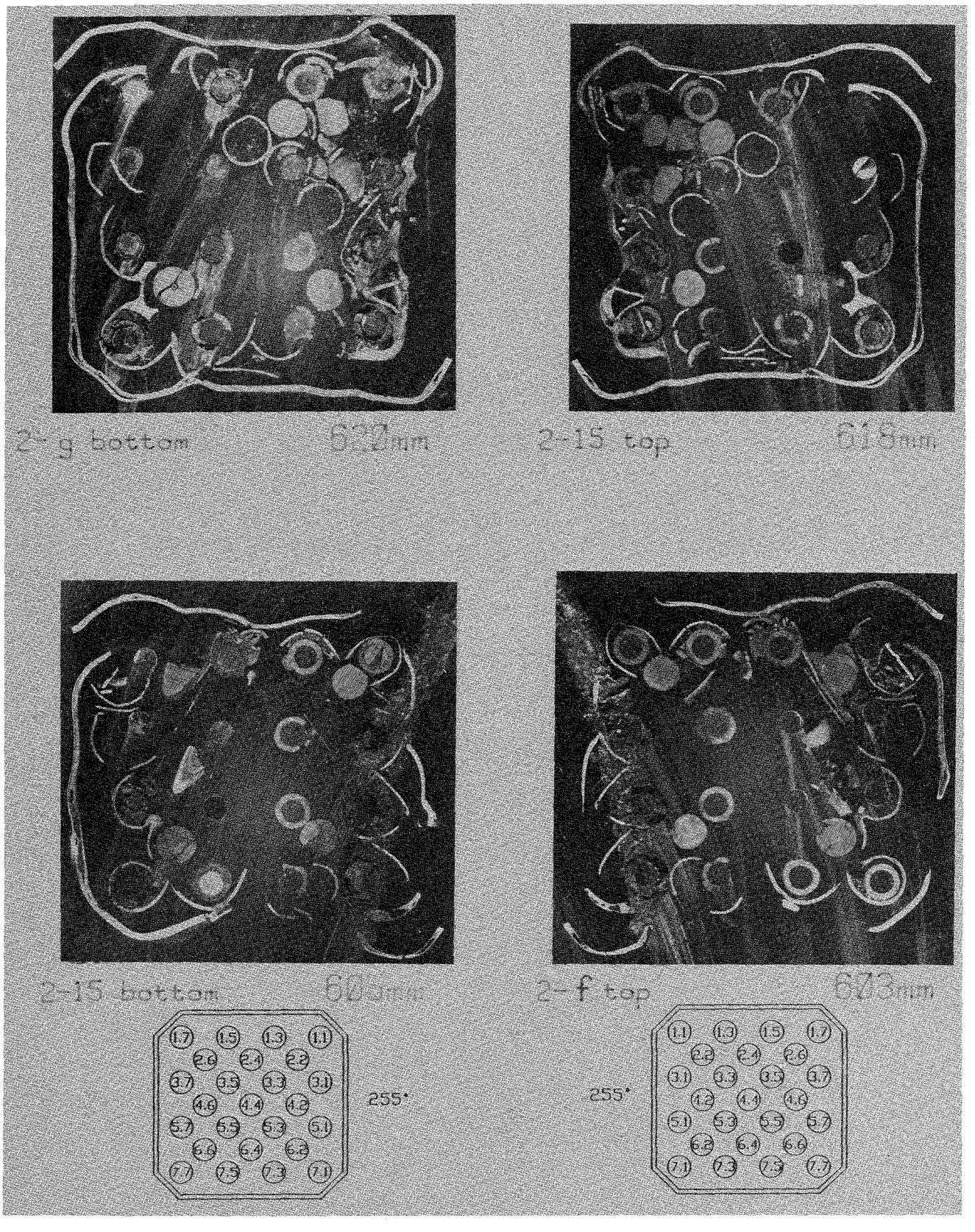

Fig. A-9 Cross sections of the test bundle CORA-2 at elevations indicated

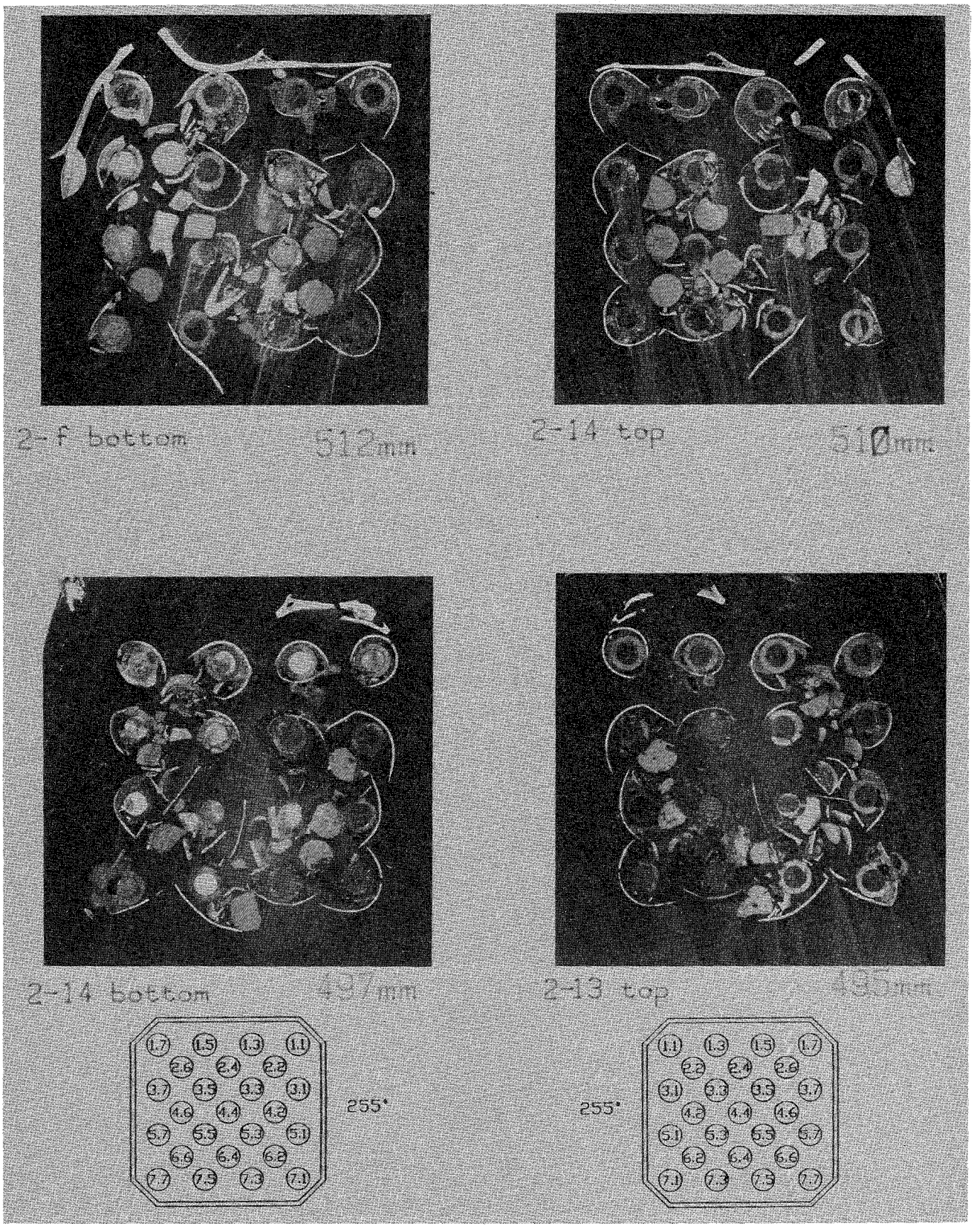

Fig. A-10 Cross sections of the test bundle CORA-2 at elevations indicated

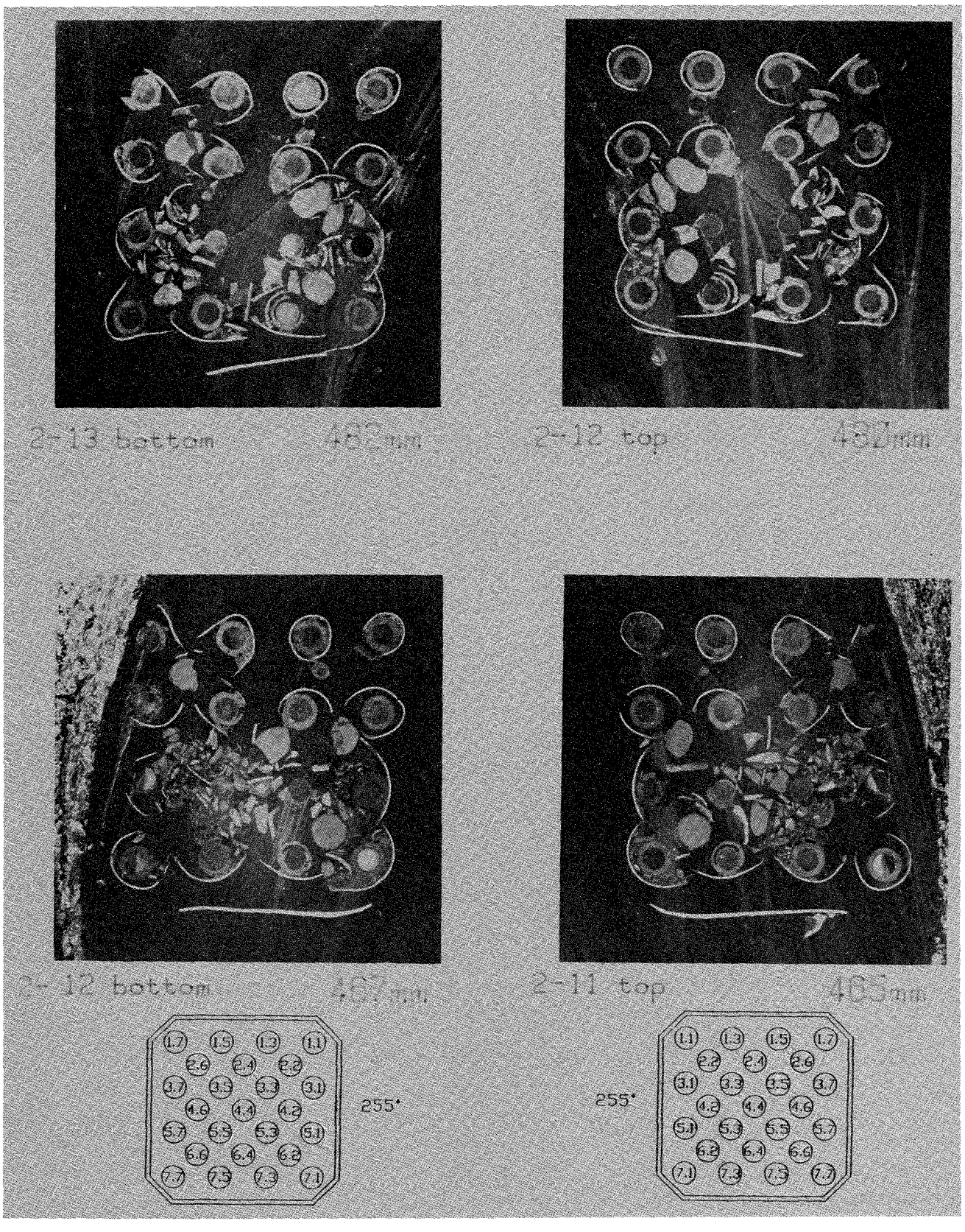

Fig. A-11 Cross sections of the test bundle CORA-2 at elevations indicated

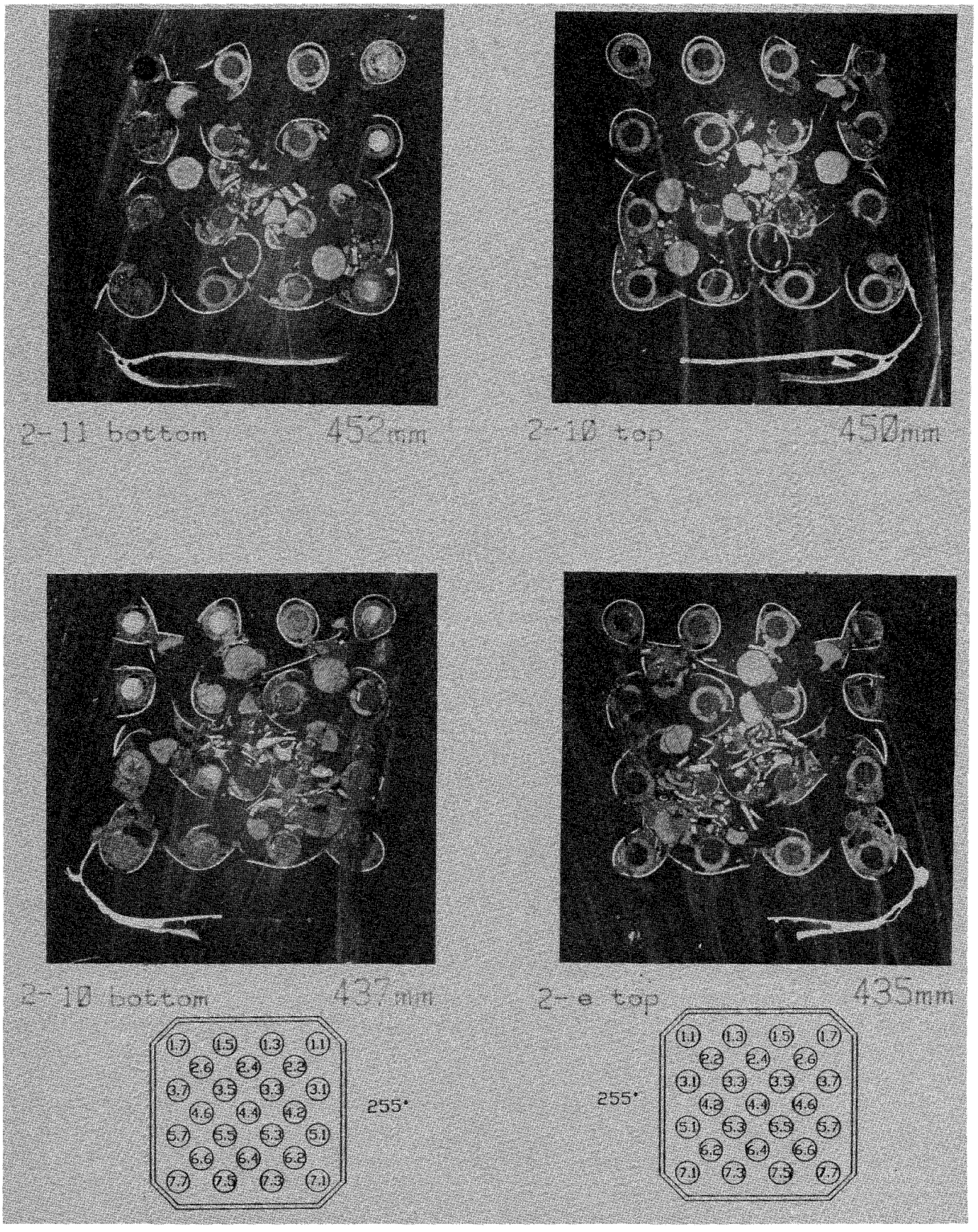

Fig. A-12 Cross sections of the test bundle CORA-2 at elevations indicated

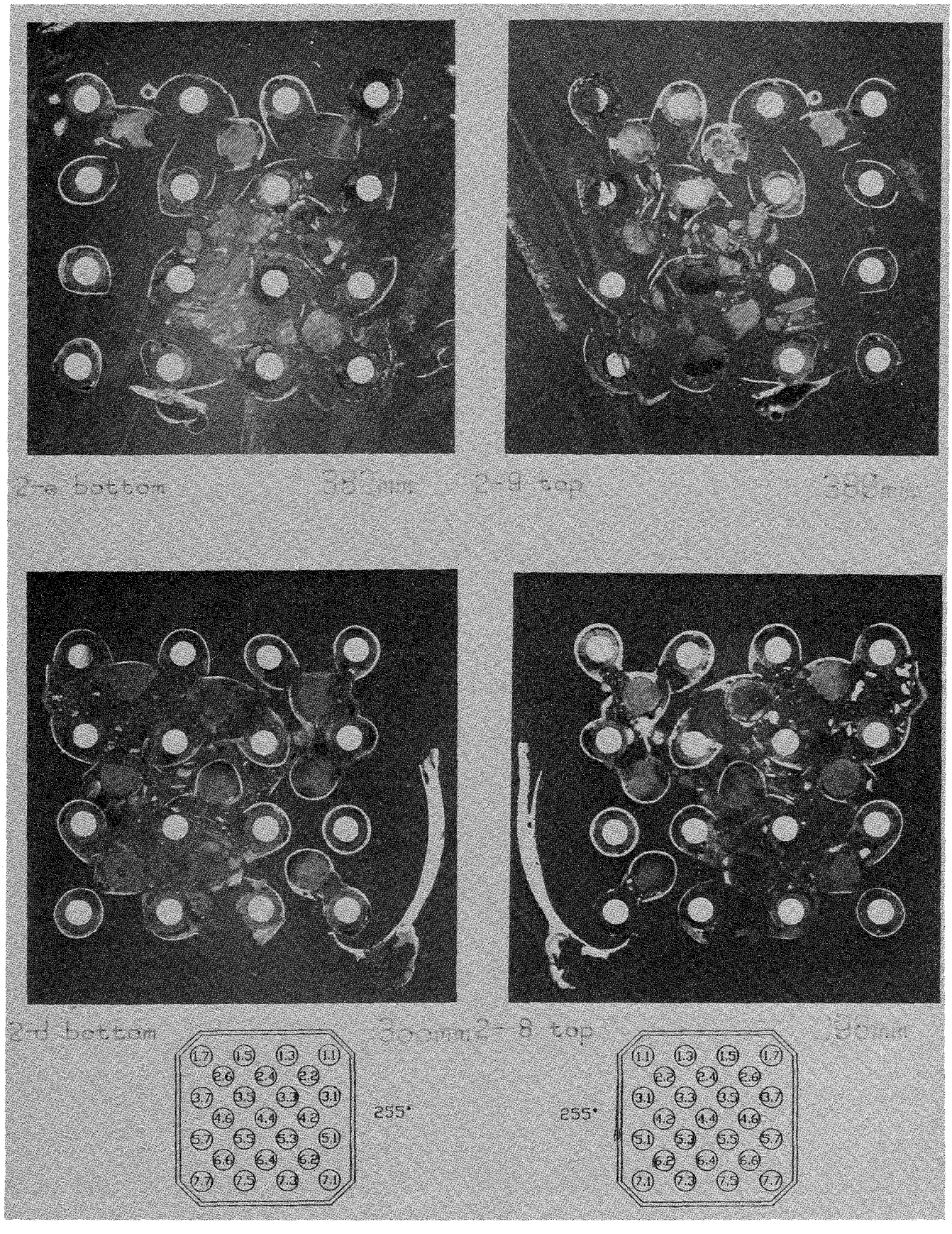

Fig. A-13 Cross sections of the test bundle CORA-2 at elevations indicated

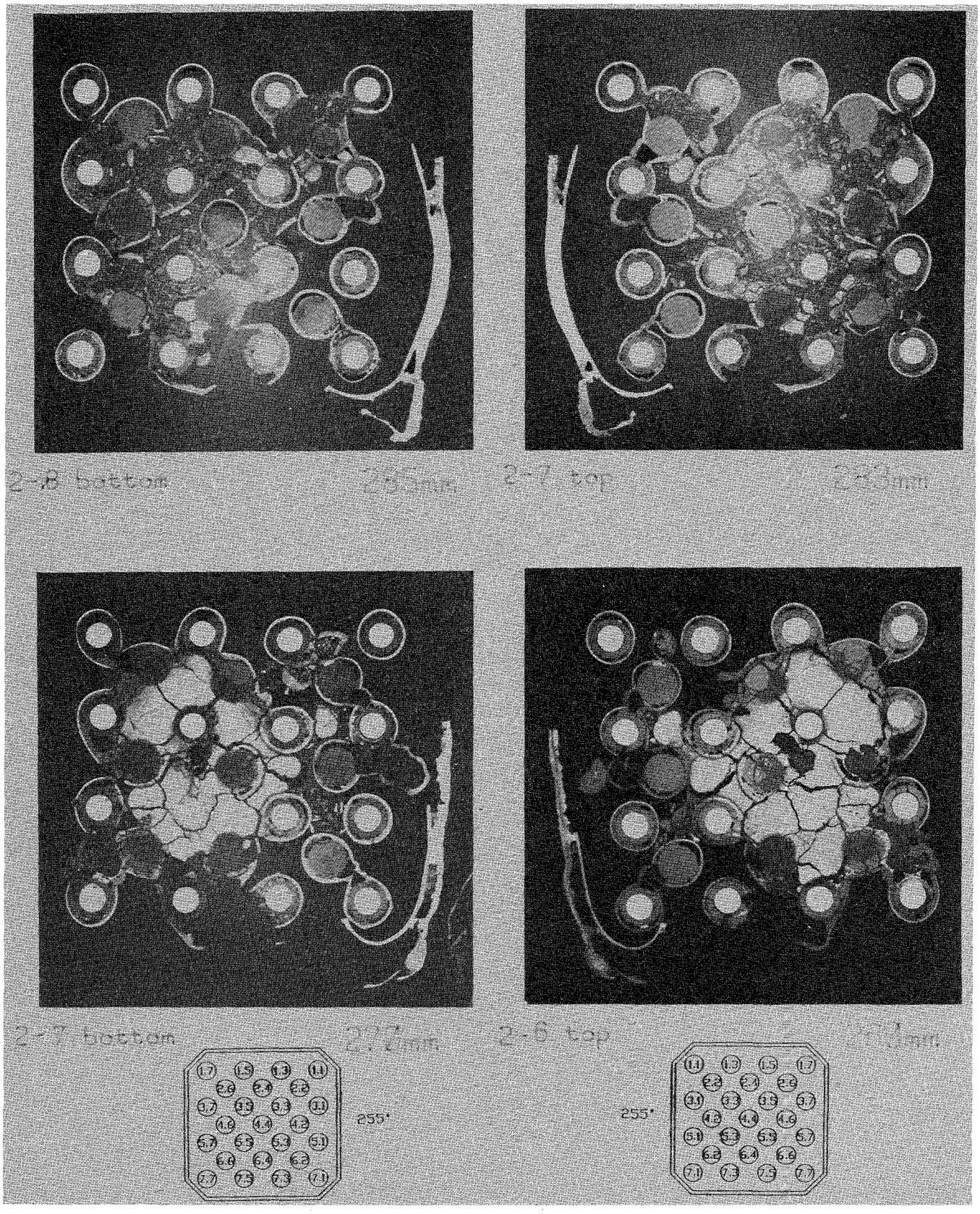

Fig. A-14 Cross sections of the test bundle CORA-2 at elevations indicated

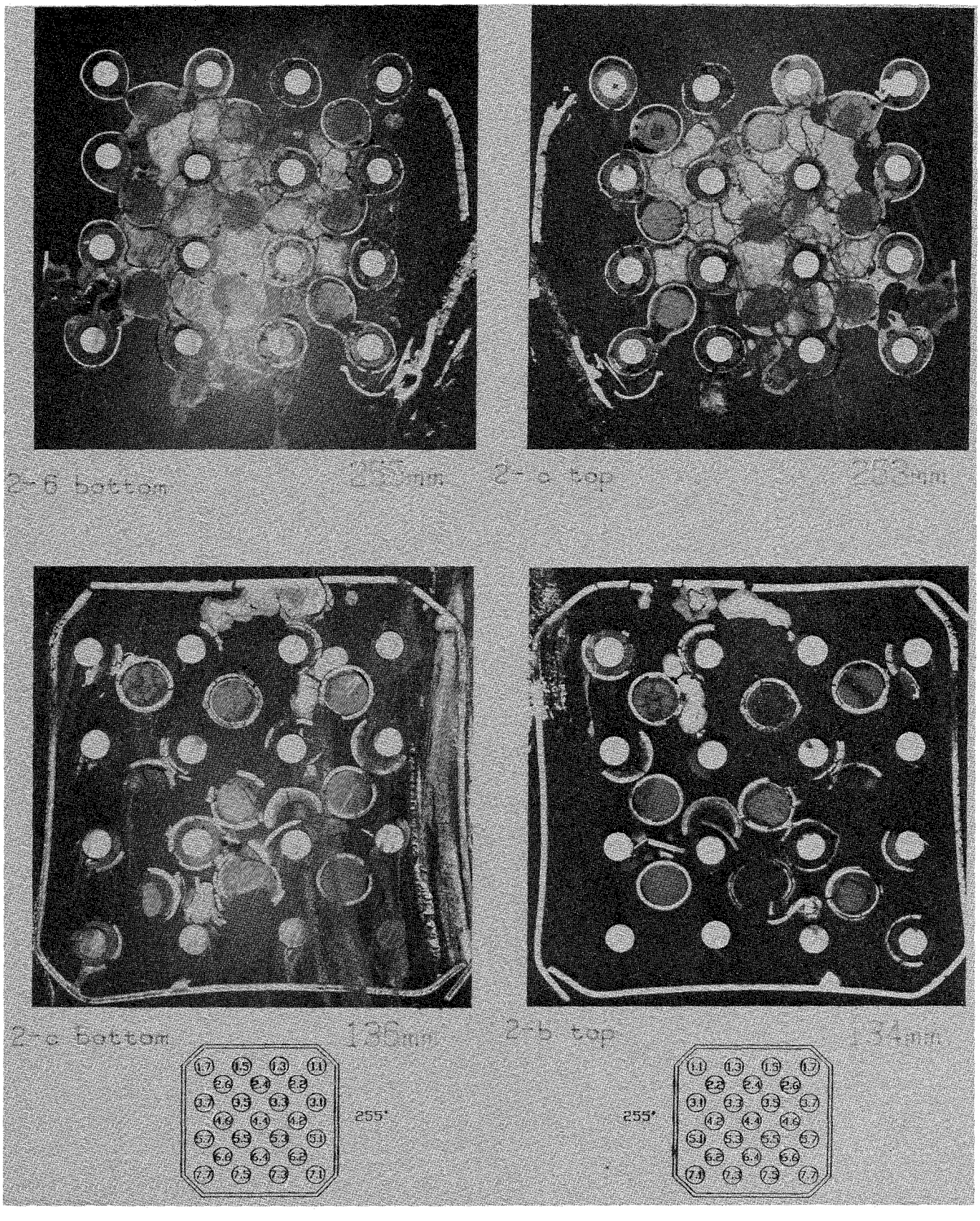

Fig. A-15 Cross sections of the test bundle CORA-2 at elevations indicated

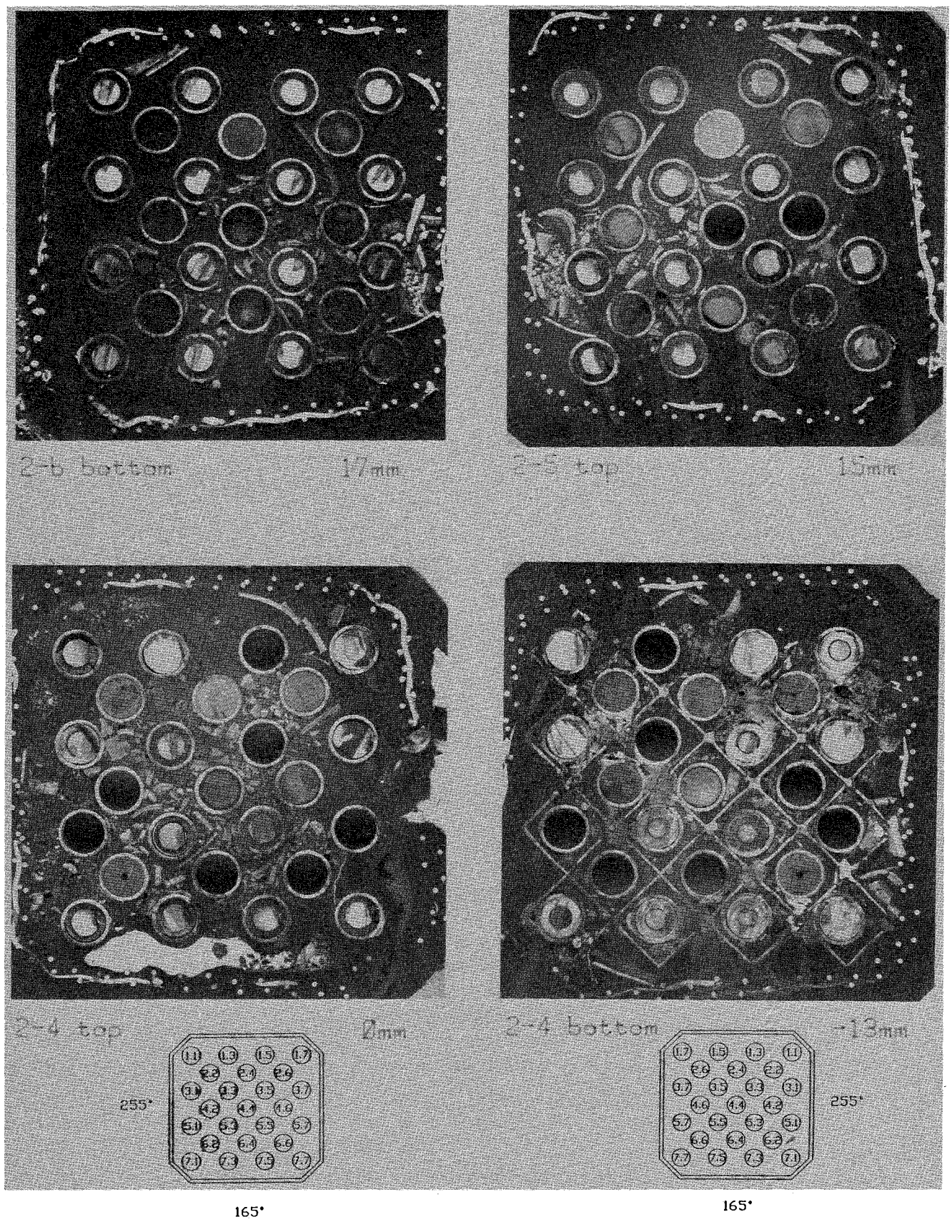

Fig. A-16 Cross sections of the test bundle CORA-2 at elevations indicated

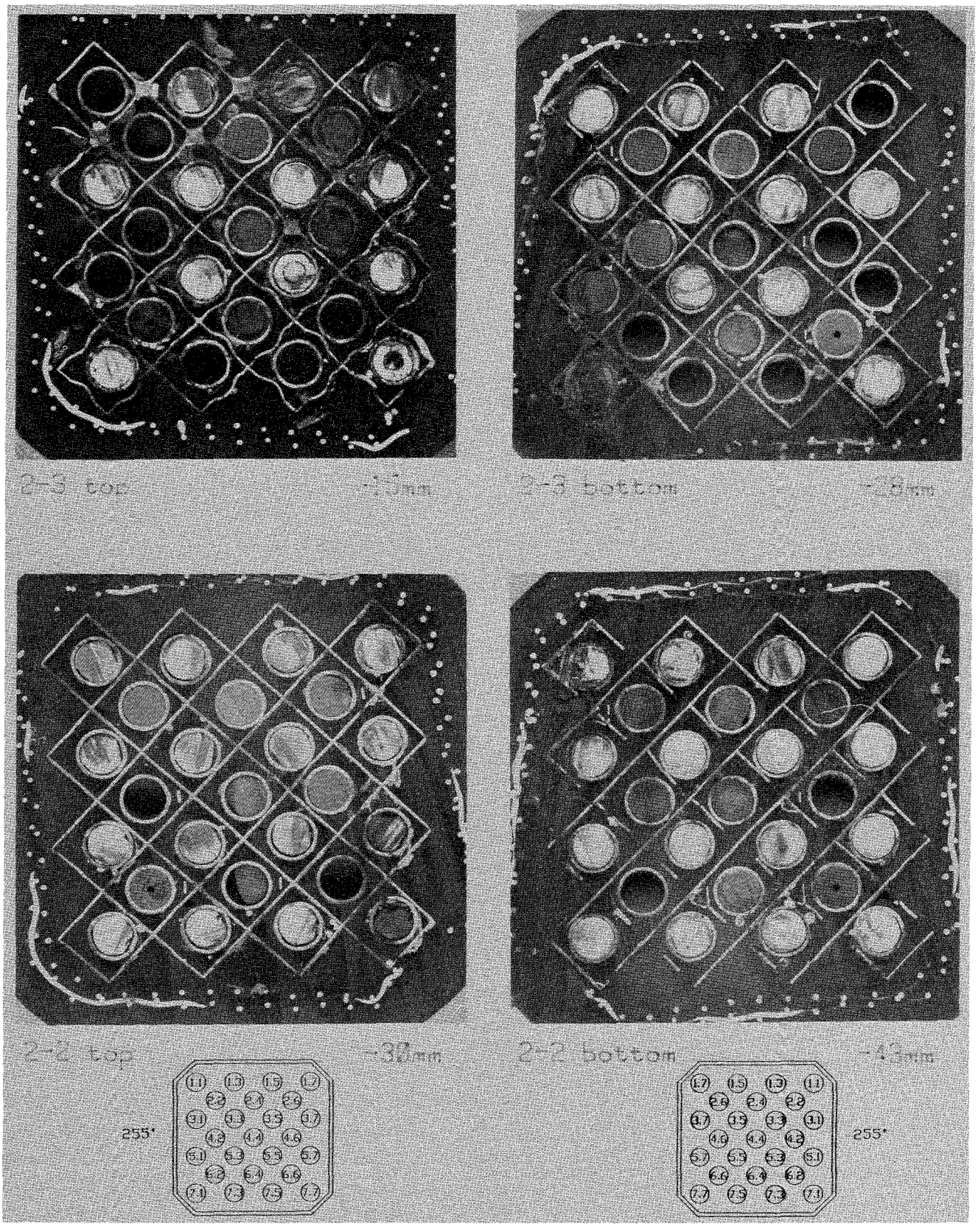

Fig. A-17 Cross sections of the test bundle CORA-2 at elevations indicated

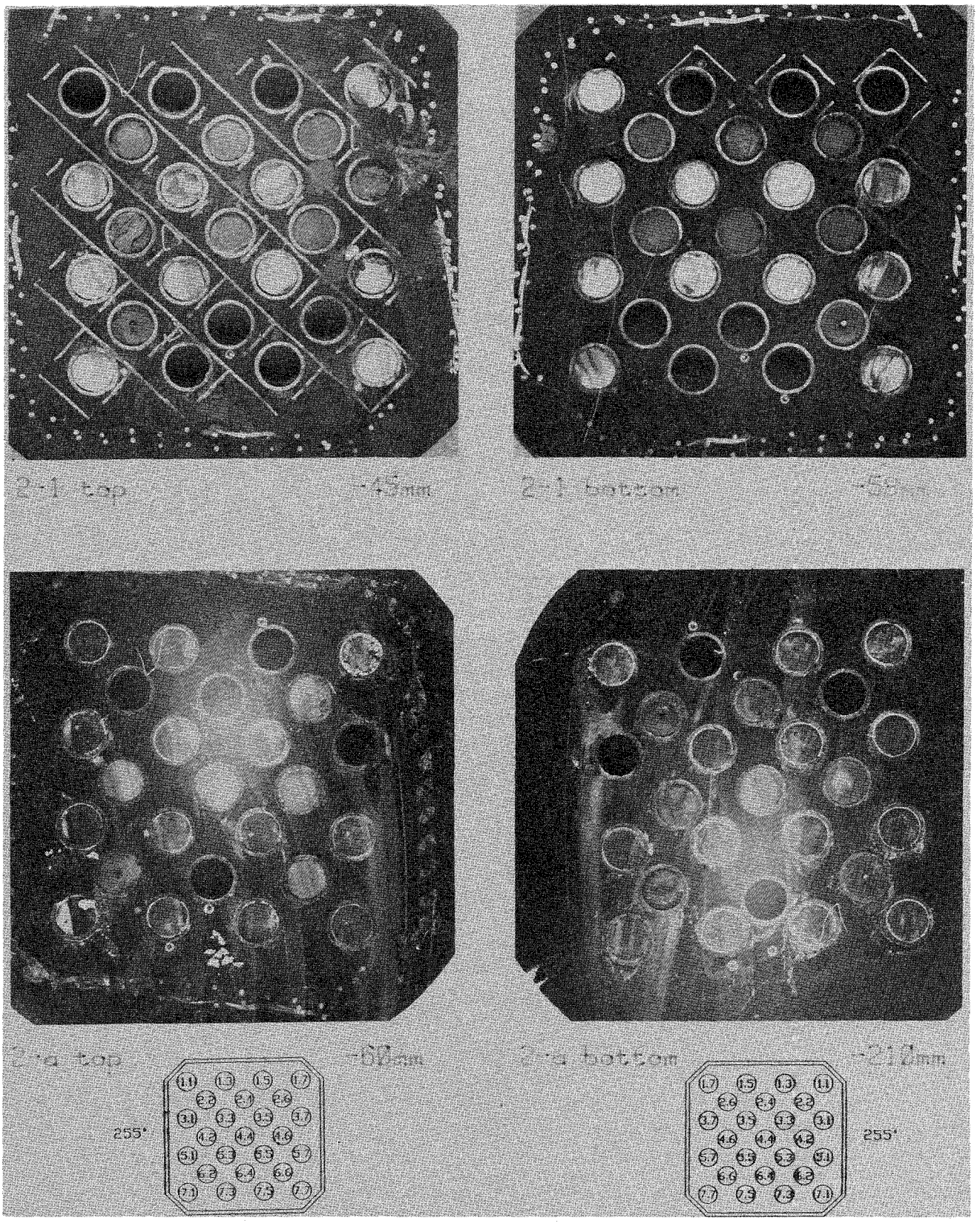

Fig. A-18 Cross sections of the test bundle CORA-2 at elevations indicated

Fig. A-19 CORA-3, bundle sectioning

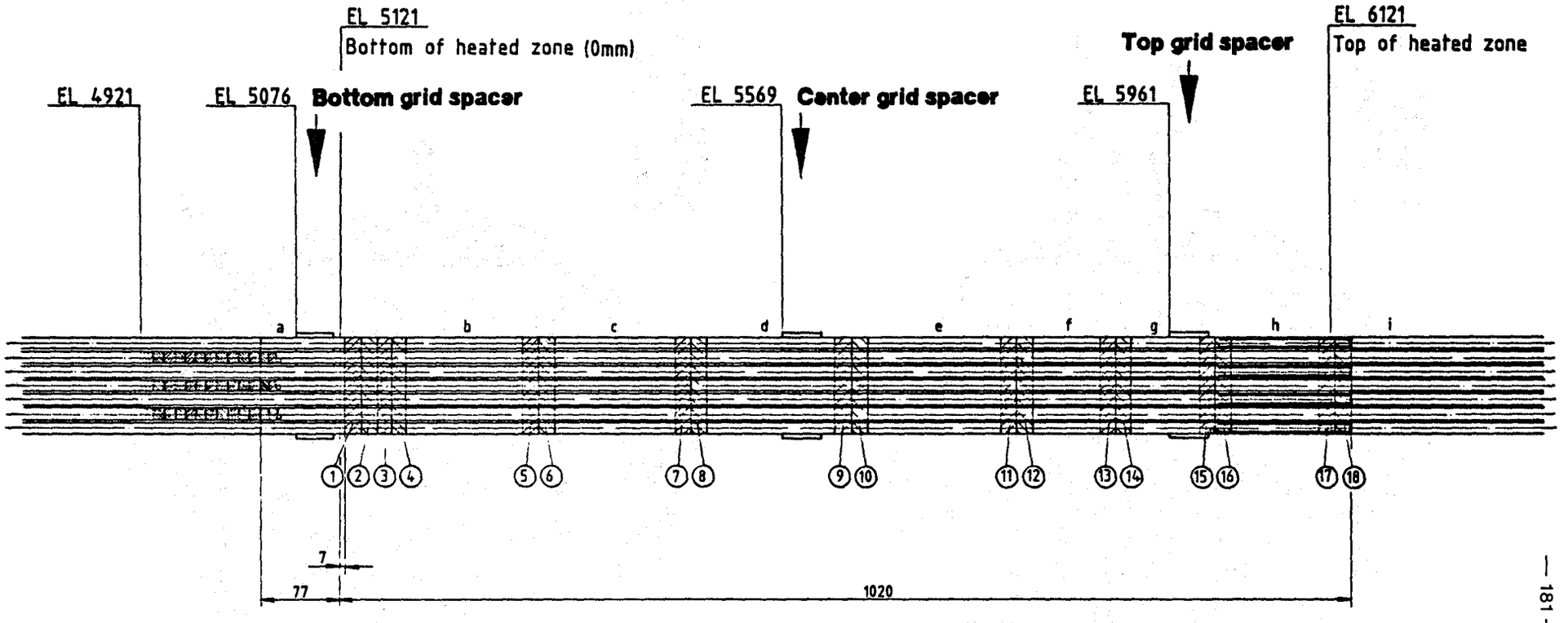

Vertical sections of remnants a, b

Height of horizontal sample : 13mm (marking distance = 15mm)

Bundle viewed from 30°, 120°, 210°, and 300°, respectively

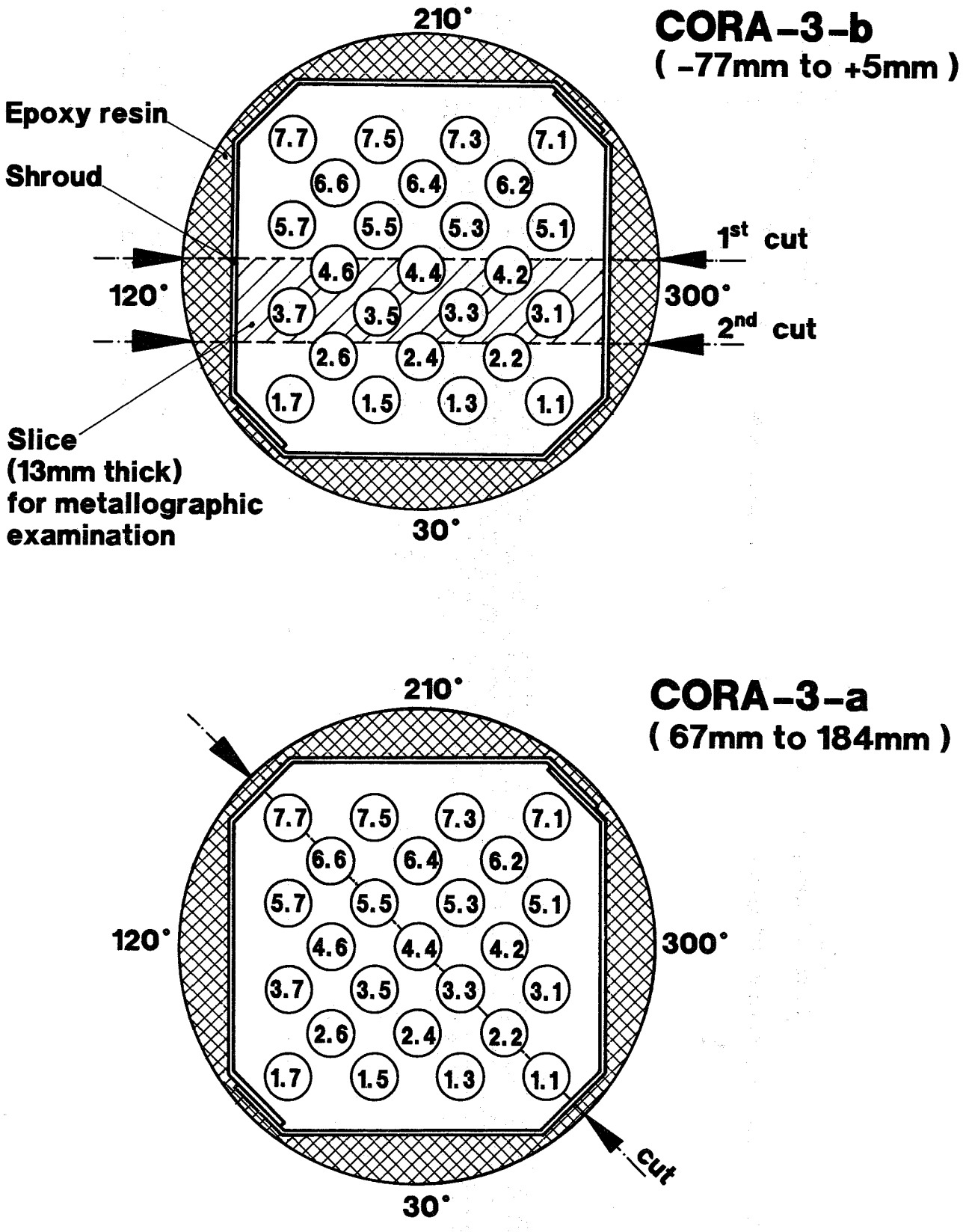

Fig. A-20 CORA-3; Locations of the vertical cuts through sections 3-a and 3-b, top view

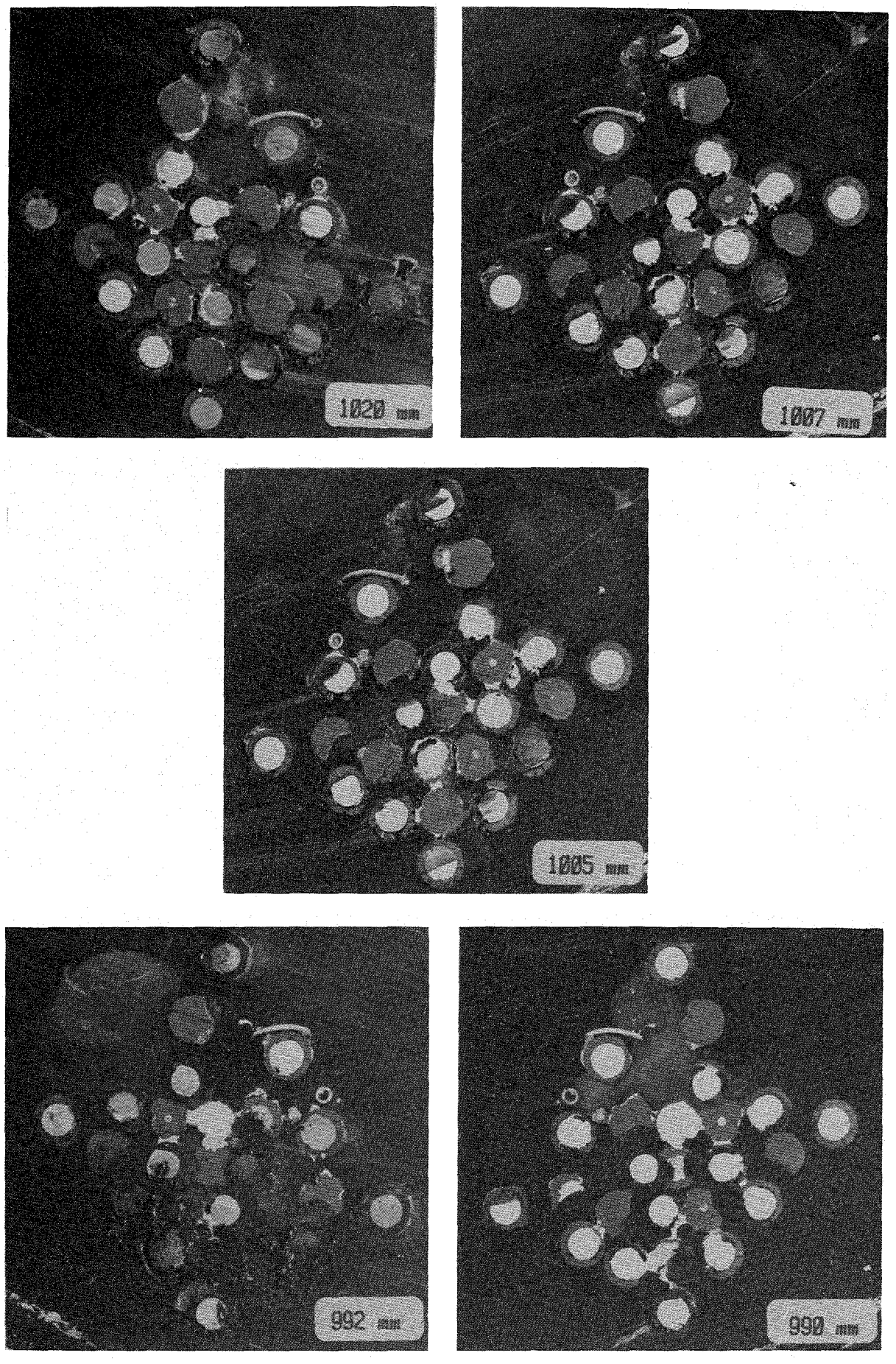

Fig. A-21 Cross sections of the test bundle CORA-3 at elevations indicated

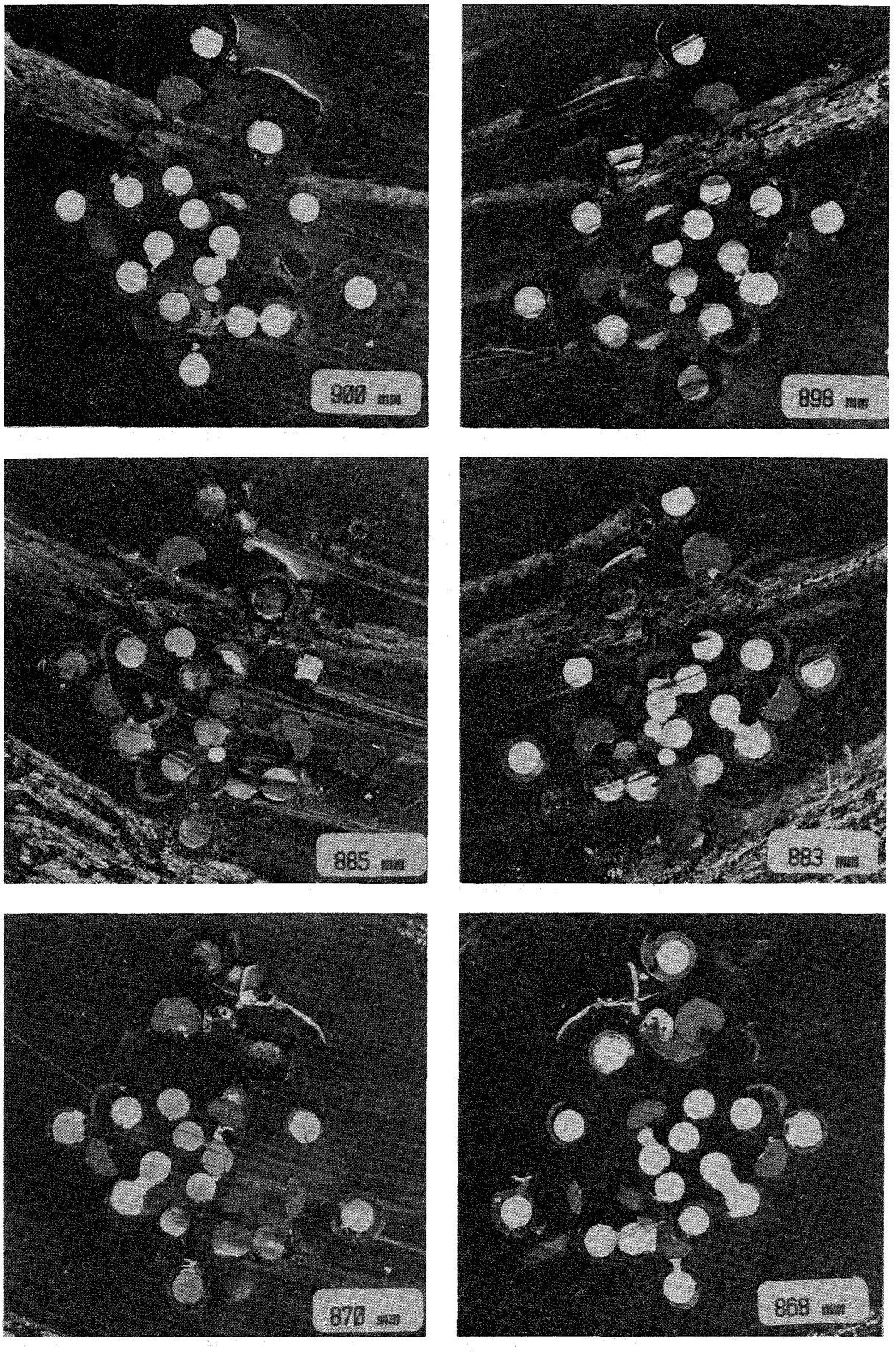

Fig. A-22 Cross sections of the test bundle CORA-3 at elevations indicated

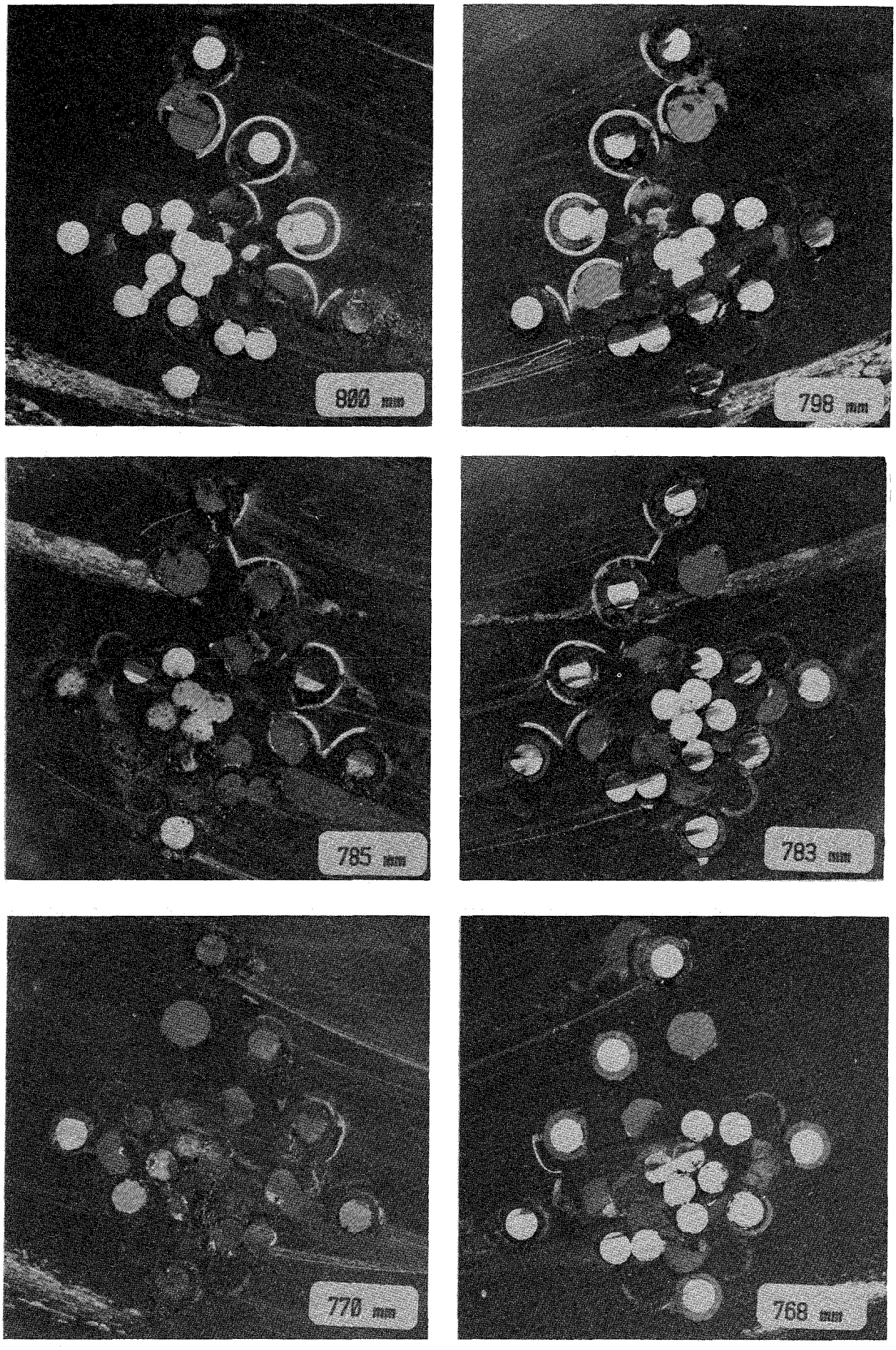

Fig. A-23 Cross sections of the test bundle CORA-3 at elevations indicated

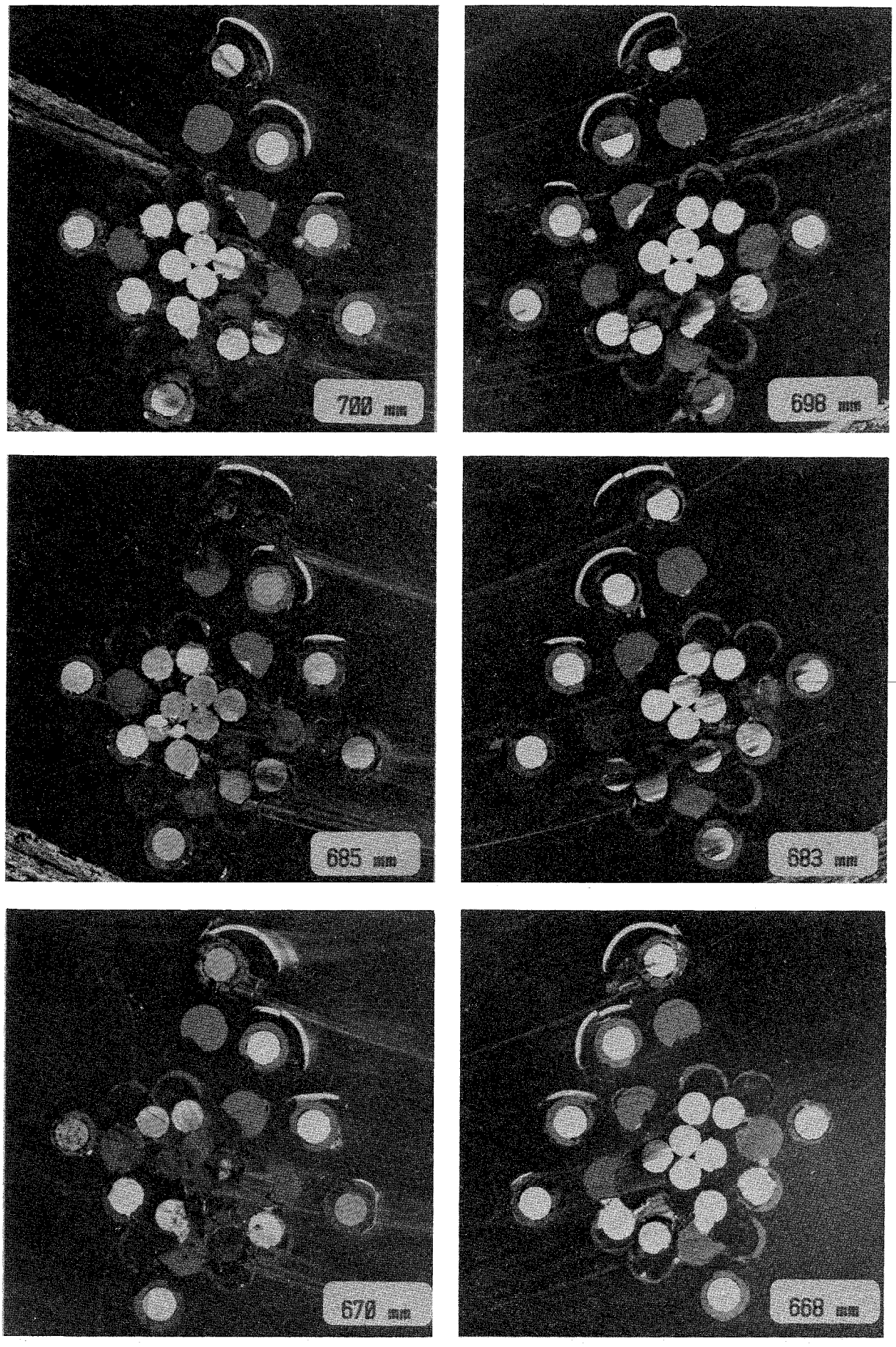

Fig. A-24 Cross sections of the test bundle CORA-3 at elevations indicated

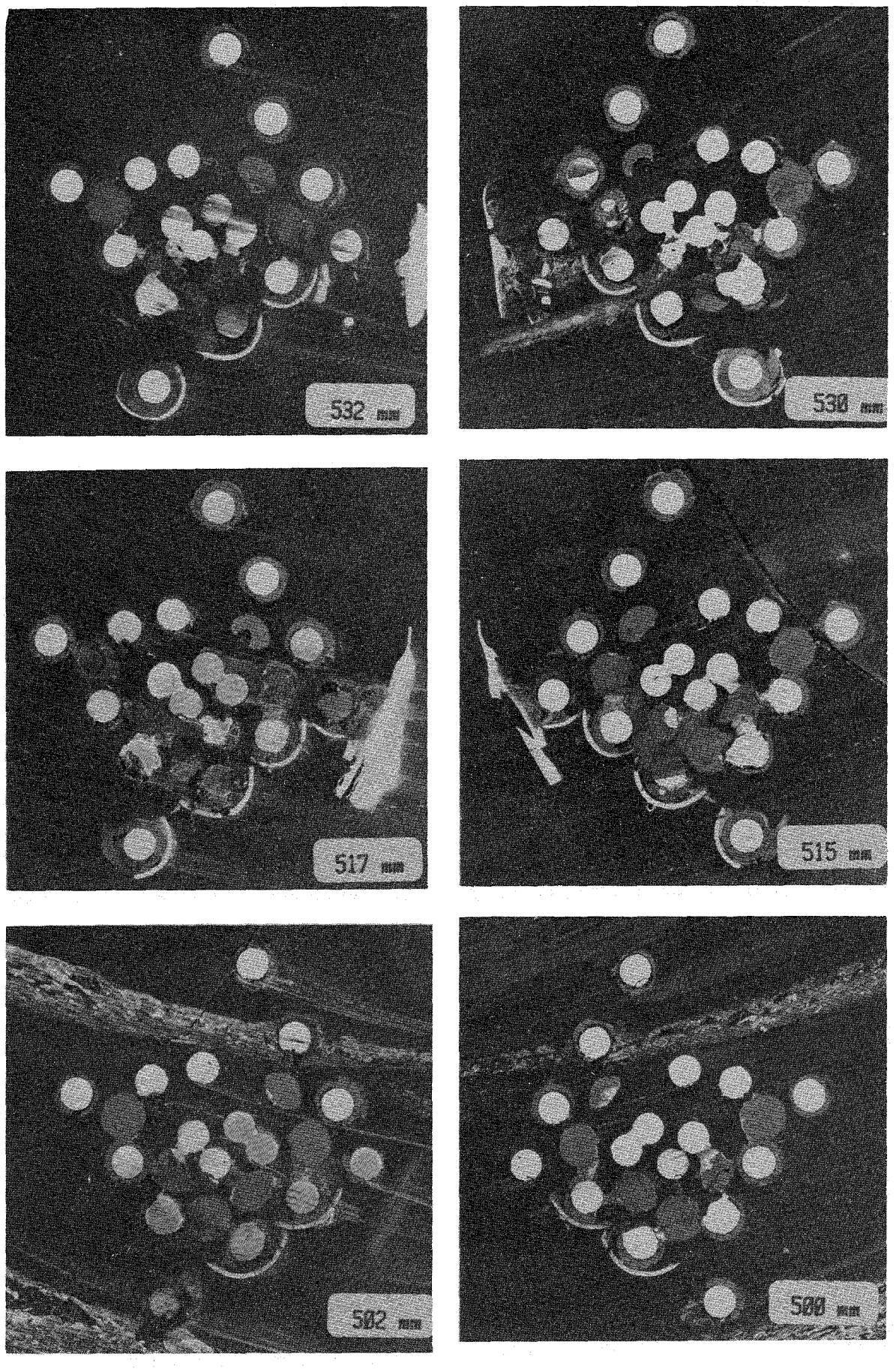

Fig. A-25 Cross sections of the test bundle CORA-3 at elevations indicated

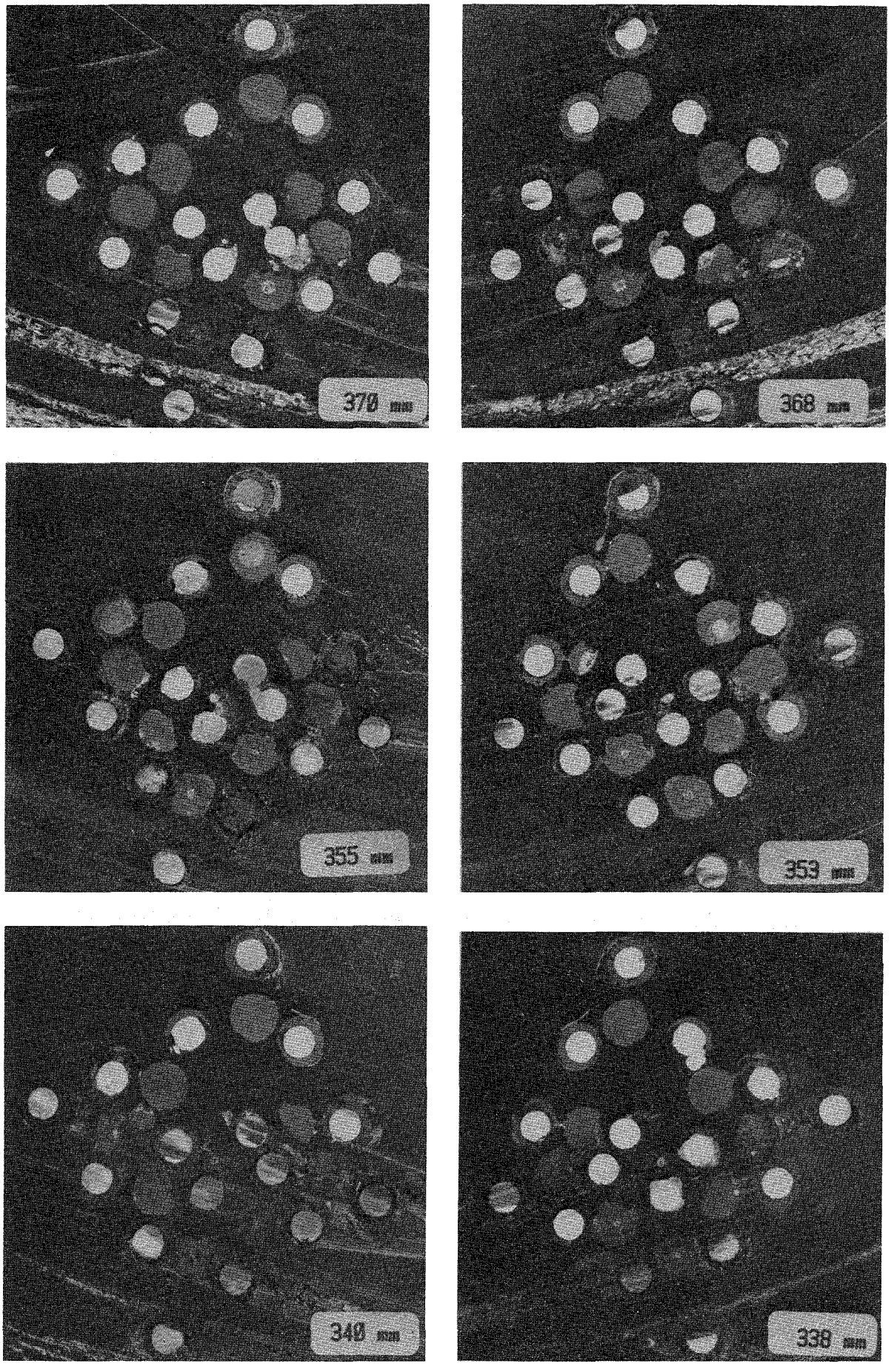

Fig. A-26 Cross sections of the test bundle CORA-3 at elevations indicated

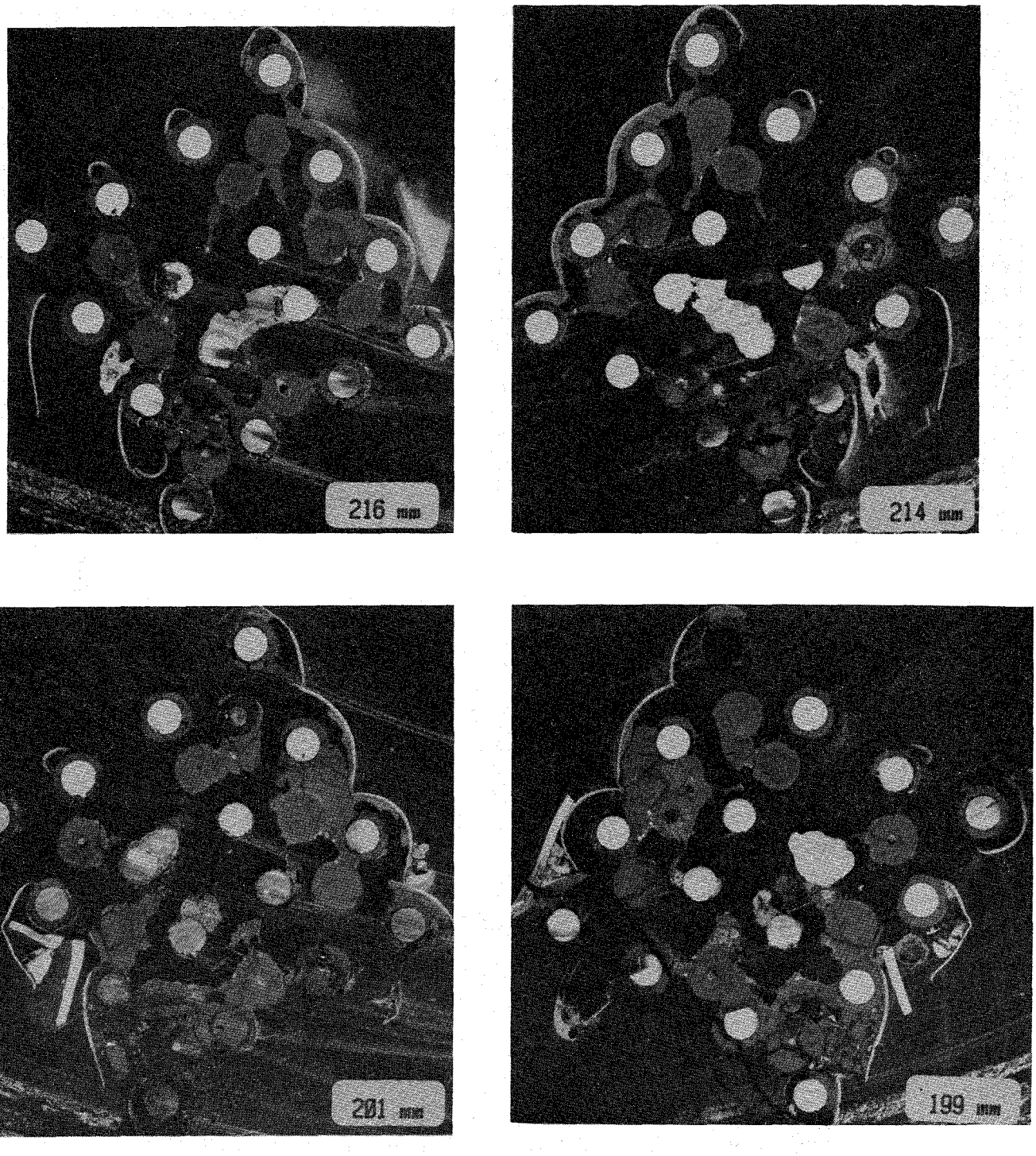

Fig. A-27 Cross sections of the test bundle CORA-3 at elevations indicated

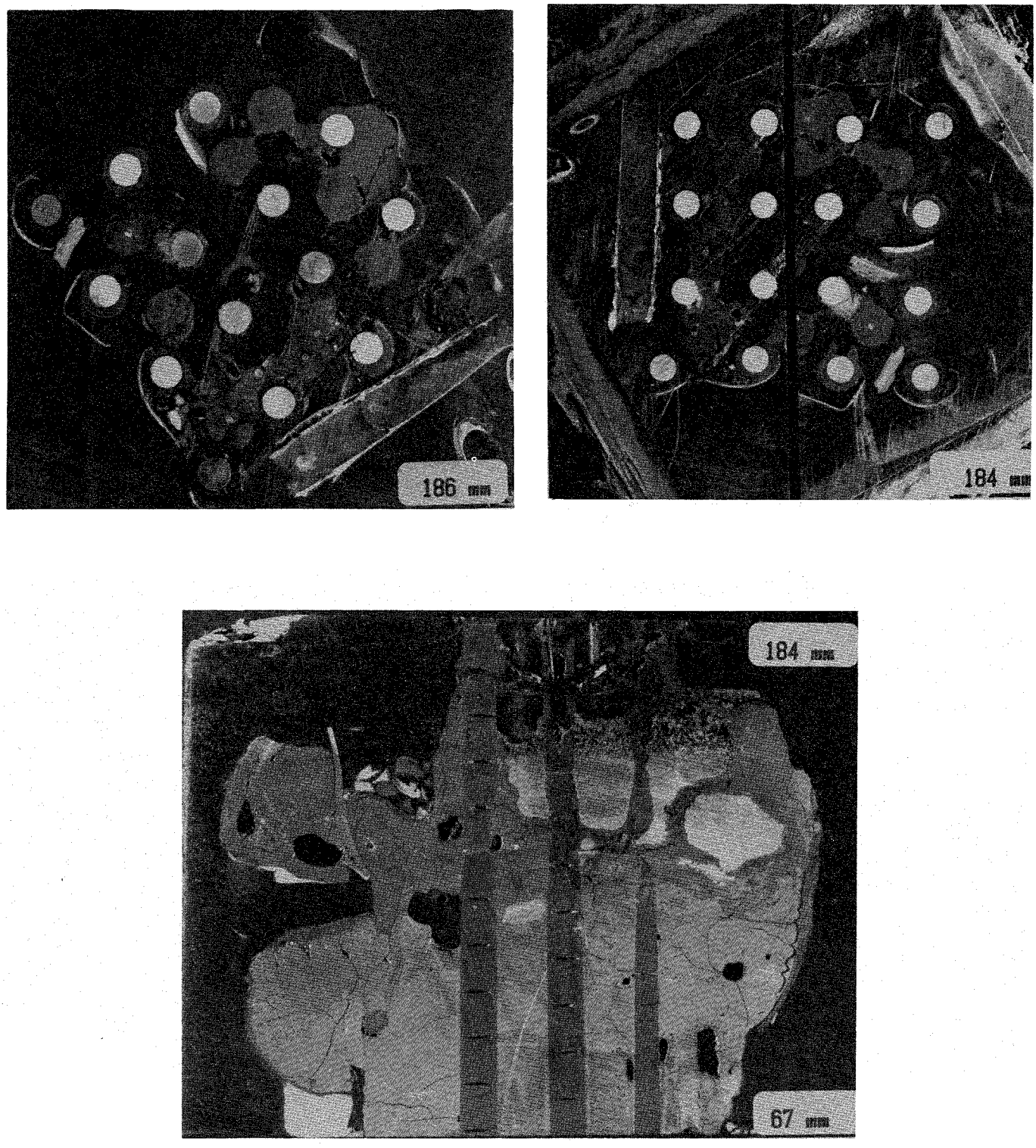

Fig. A-28 Cross sections of the test bundle CORA-3 at elevations indicated

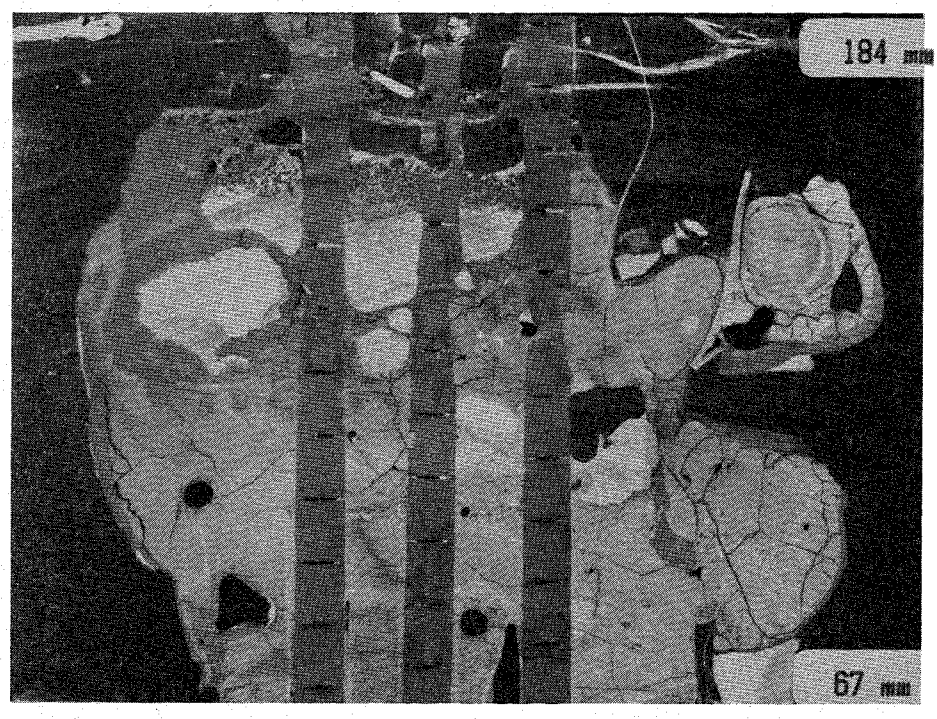

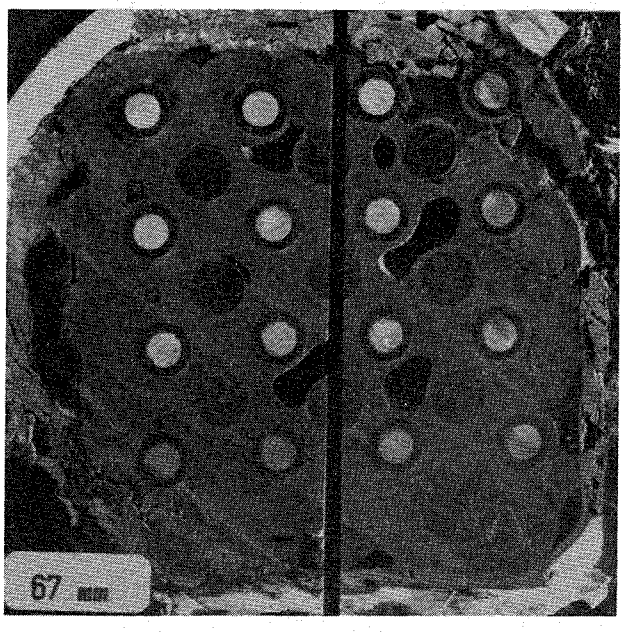

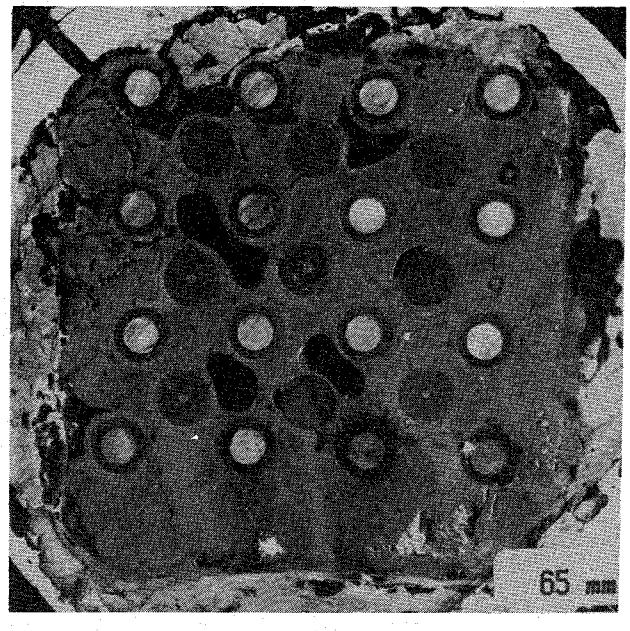

Fig. A-29 Cross sections of the test bundle CORA-3 at elevations indicated

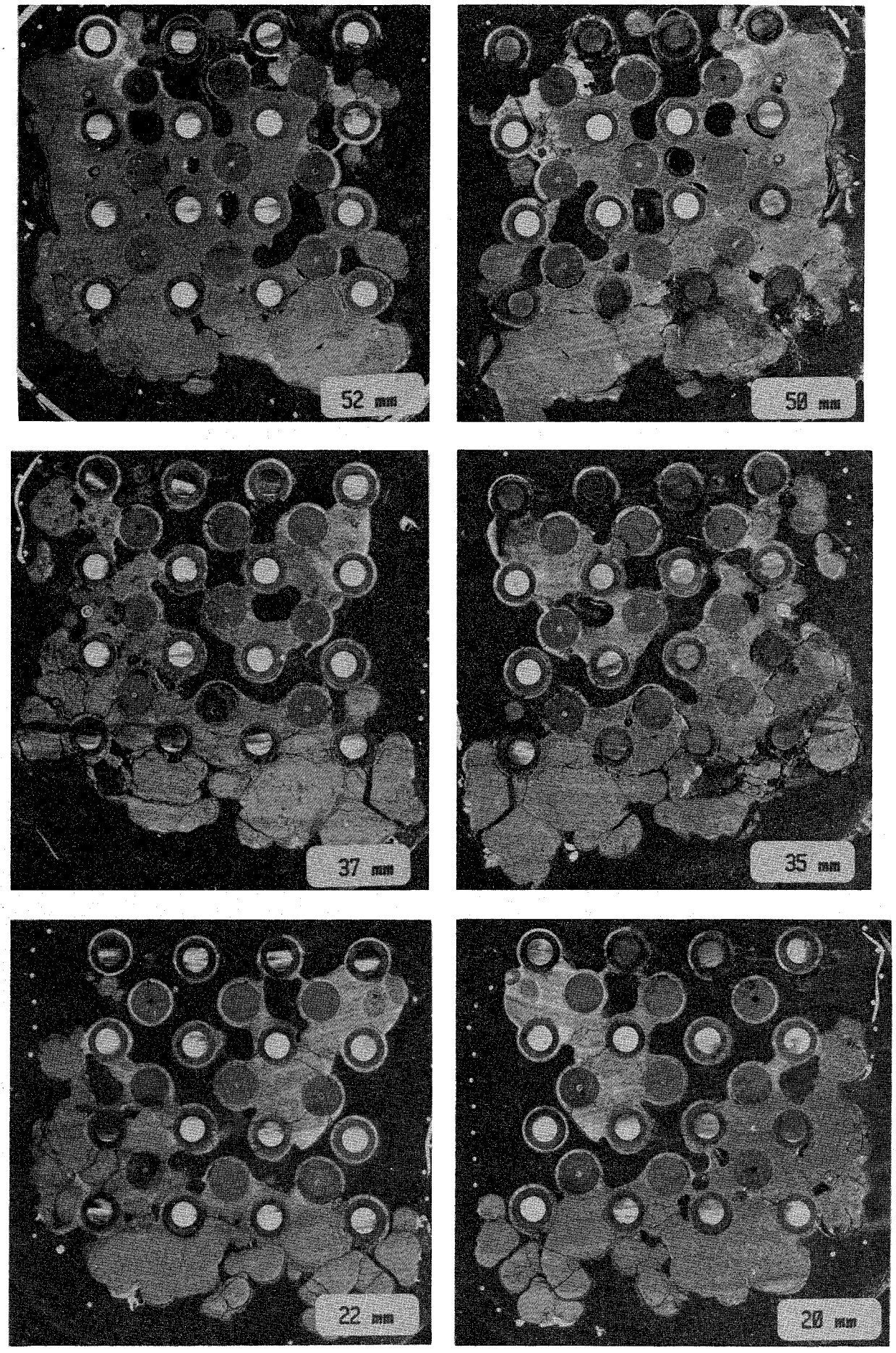

Fig. A-30 Cross sections of the test bundle CORA-3 at elevations indicated

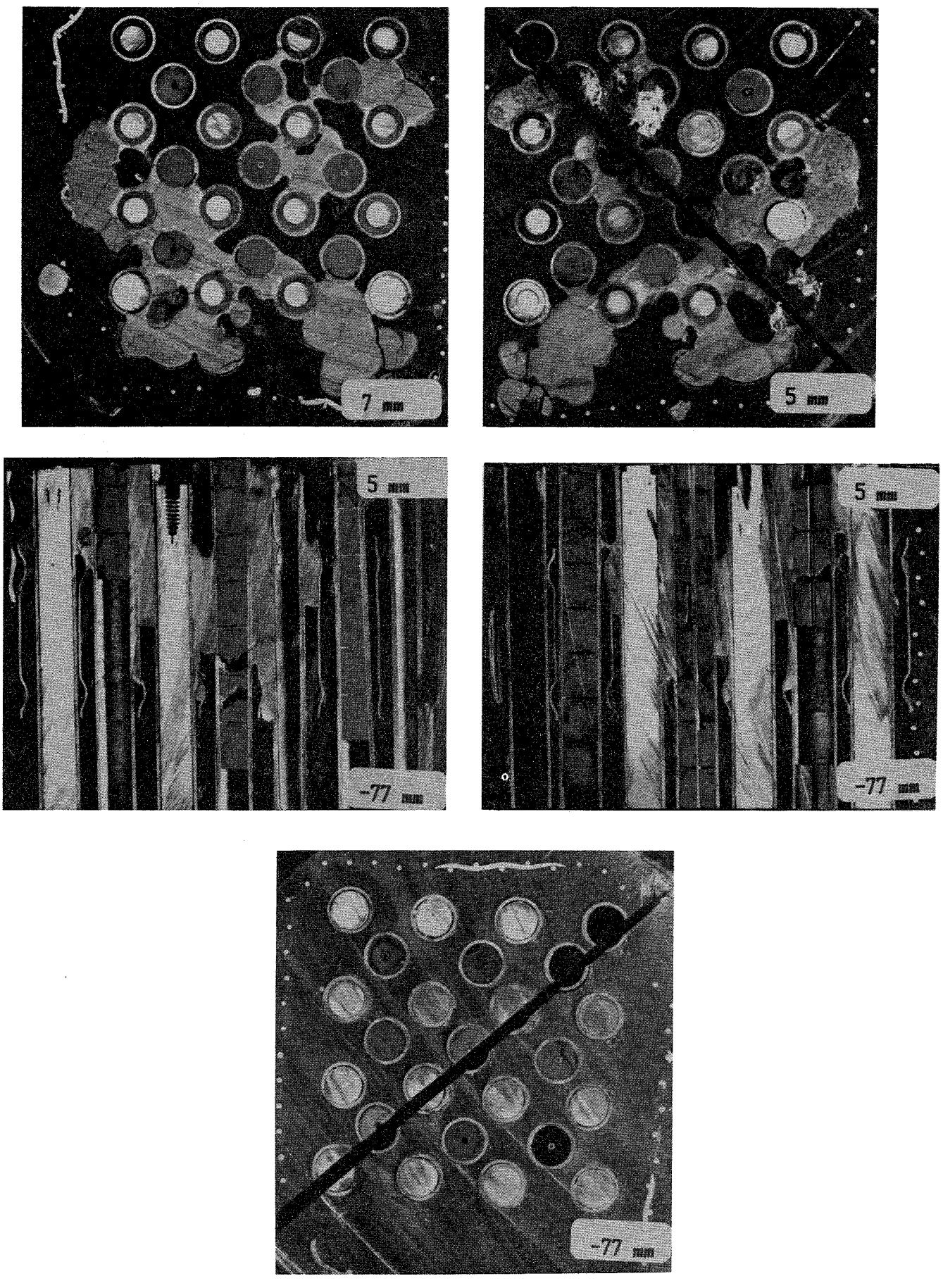

Fig. A-31 Cross sections of the test bundle CORA-3 at elevations indicated